DOUBLE ROTOR SWITCHED RELUCTANCE MACHINE WITH SEGMENTED ROTORS

DOUBLE ROTOR SWITCHED RELUCTANCE MACHINE WITH SEGMENTED ROTORS

By

TENG GUO, B.Eng.

A Thesis

Submitted to the School of Graduate Studies

In Partial Fulfillment of the Requirements

for the Degree of

Master of Applied Science

McMaster University
© Copyright by Teng Guo, December 2014

Master of Applied Science (2014)	McMaster University
(Mechancial Engineering)	Hamilton, Ontario, Canada

TITLE:	Double Rotor Switched Reluctance Machine with Segmented Rotors
AUTHOR:	Teng Guo
SUPERVISORS:	Dr. Ali Emadi & Dr. Nigel Schofield
NUMBER OF PAGES:	xvii, 203

ABSTRACT

Double rotor machines, appearing in versatile forms and configurations thanks to the great flexibility of having a pair of rotors, are seen in a number of applications. Double rotor machines show promising prospect in the application of advanced hybrid electric vehicle powertrains due to the requirement of dual electro-mechanical ports in such systems. Integrating these powertrain systems with double rotor machines not only brings design freedom of laying out components, but also reduces number of parts and thus improves compactness. The switched reluctance type double rotor machines, offering unique characteristics of having a simple structure and no permanent magnets, are strong candidates for high performance applications.

In this thesis, a family of double rotor switched reluctance machine with segmented rotors is proposed and studied. Compared to double rotor switched reluctance machines with a more conventional structure, the proposed designs exhibit potentials of achieving higher compactness and performance. A prototype double rotor machine of the segmented rotor design is constructed and tested to benchmark an existing double rotor switched reluctance machine. The experiment results show that the proposed design is able to achieve the same output with similar or higher efficiency than the benchmark machine, while occupying only about 60% of overall volume. The double segmented rotor switched reluctance machine demonstrates to be a promising double rotor topology and is worth further research.

ACKNOWLEDGEMENTS

This research was undertaken, in part, thanks to funding from the Canada Excellence Research Chairs Program.

The research presented in this thesis is an outcome of generous help and support from a number of people. I would like to thank you all for making the work possible.

First I would like to thank my supervisors, Dr. Ali Emadi and Dr. Nigel Schofield for their supervisory of my master degree research. With his abundant knowledge and experience as well as rigorous academic attitude, Dr. Emadi mentored me to become a capable researcher. His broad vision in hybrid electric vehicle technologies enlightened my research ideas and his trust and encouragement helped me to progress through obstacles and finally achieving a meaningful research work. I am equally grateful for Dr. Schofield. During the course of the project, Dr. Schofield offered me numerous advices on electric machine design, manufacturing and testing. With his expertise and vast experience in electric machines, Dr. Schofield not only taught me the techniques but also the art of electric machine design. His questions and critics refined my research focus and led to the completion of a contentful and well-supported thesis. I really appreciate the time he spent with me on problem discussion, machine testing and thesis editing.

I would like to thank Edward Kries of Kries Manufacturing Inc, Chris Procter of Procter Precision Ltd and John Steinman of Brant Custom Grinding Ltd for their help on machining the various components of the prototype machine. The high quality of work, as well as valuable consultancy they offered had made the prototype construction a success.

I would also like to thank all my colleagues and friends from McMaster Automotive Resource Center. My special thanks go to Fei Peng, who designed the power electronics and control of the prototype machine. Without his huge amount of effort devoted to debugging and monitoring the machine drives, the experiments would not be possible. I would like to thank Earl Fairall, Hao Ge, Jianing Lin and Yinye Yang for giving me valuable machine design advices, inspirations and support throughout the research.

I want to thank technicians Ron Lodewyks, Terry Wagg, John Colenbrander and Michael Lee from the Department of Mechanical Engineering at McMaster University for their support and consultancy on component design and machining of a number of fixtures and jigs.

Finally, I would like to thank my parents and friends for their constant support and love, which accompanied me through the difficulties in finishing this work. Their encouragement and trust make me aim higher objectives and stay stronger when facing setbacks.

TABLE OF CONTENTS

LIST OF FIGURES

LIST OF TABLES

CHAPTER 1 INTRODUCTION

A normal electric machine usually has two parts: a stationary component called the stator and a rotatory component called the rotor. The double rotor electric machine represents a unique electric machine family that employs a pair of rotors instead of one. The concept of double rotor machines is not new, with machines reported back in 1969, for example, when a double rotor induction motor was proposed[1]. For many applications (especially the hybrid electric vehicle powertrain), double rotor machines have demonstrated benefit over conventional machines[2]-[5]. This thesis focuses on a double rotor machine of the switched reluctance (SR) type, and integrates the unique stator flux path sharing capability of double rotor switched reluctance machines with segmented rotors. A novel segmented rotor double rotor machine is proposed, studied in detail and prototyped. The concept machine demonstrates compactness and performance improvement when compared to a double rotor machine having a more conventional magnetic structure. This Chapter gives an overview of past double rotor machine research, which inspired and motivated this thesis research study.

1.1. Double Rotor Machine Applications

The double rotor arrangement allows for a variety of machine configurations. For example, depending on whether the two rotors are independent, the machine can be of a double independent output type or a single coupled output type. Geometrically, the rotors can be axially or radially displaced and have one rotor embedded within another. These variations offer a lot of flexibility in electric machine design for complicated systems, as will be shown in this Chapter, along with the benefits of a number of design topologies.

1.1.1. Application in hybrid electric vehicle (HEV) powertrain

One of the most promising applications of the double rotor machine is in integrated hybrid electric vehicle (HEV) powertrain. Before going into details of double rotor machine applications, it is necessary to be familiar with fundamental knowledge of HEV powertrains. Unlike a conventional vehicle powertrain where all traction power comes from an internal combustion engine (ICE) or diesel engine (DE), an HEV powertrain has additional power output via an electric traction motor. Because of the added electric power path, HEVs can save energy by:

(i) shutting down engine at idling or low vehicle speed

(ii) recovering kinetic energy through regenerative braking

(iii) allowing engine to operate near speeds of optimal efficiency

As an intermediate stage of development between conventional combustion engine powertrains and fully electrified powertrains, the hybrid electric powertrain provides a viable solution to reduce transportation energy demand and achieve long term sustainability. According to the United States EPA/NHTSA final rule in 2012 on fuel economy standards, passenger cars and light trucks are required to achieve an average of 54.5 miles per gallon by 2025[6]. HEV technologies will play a critical role in fulfilling fuel economy targets because of its increasing worldwide acceptance and vehicle volumes. As of October 14th 2014, a leading HEV manufacturer, Toyota Motor Co., announced its cumulative sales of HEVs passed 7 million units, accounting for about 70% of all hybrid vehicles sold worldwide [7].

While there are a number of hybrid powertrain architectures, series and parallel are the two most basic, as illustrated in Figure 1.1. In a series hybrid powertrain the engine is decoupled from vehicle load, which achieves optimal engine efficiency. However, it suffers from loss at higher vehicle speeds due to added energy conversion stage (the mechanical energy output from the engine could have been directly delivered to the drive shaft)[8]. On the contrary, the parallel hybrid couples outputs from both the engine and electric machine at the drive shaft. The added mechanical power path improves efficiency at higher vehicle speeds. However, the coupling also leads to wider engine operating speed range, making it no longer possible to maintain optimal engine efficiency[9].

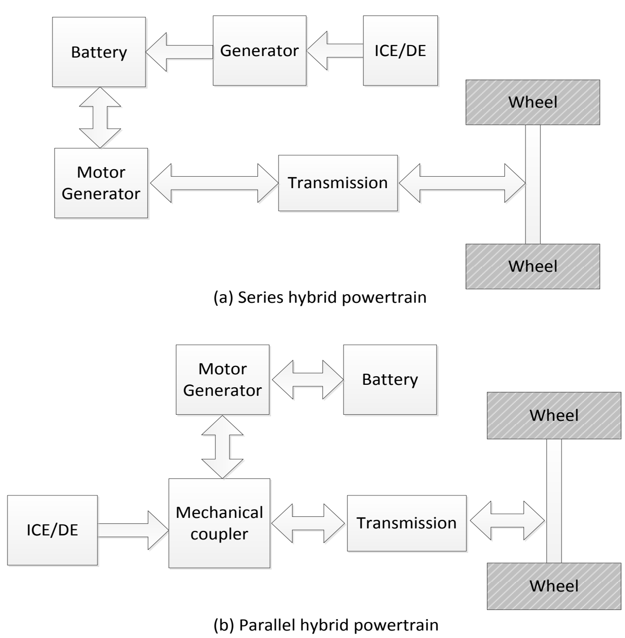

Figure 1.1 Series and parallel HEV powertrain architectures

To overcome the drawbacks of the series and parallel hybrid powertrains, a more complex architecture with more modes of operation is required, leading to the development of a complex hybrid electric powertrain, sometimes also called series-parallel hybrid powertrain. The complex hybrid powertrain achieves highest overall efficiency and is used in most advanced hybrid electric vehicles. The currently most popular HEV model Toyota Prius is based on the complex hybrid powertrain architecture and achieves 40% fuel saving[10].

In a complex powertrain architecture, drive shaft output consists of outputs from both a mechanical path and an electric path as in a parallel hybrid; however, in the meantime the engine load is decoupled from drive load demand as in a series hybrid. This is achieved by splitting engine power with the help of electric machines. There are two engine power split structures: the input split and the compound split. The Toyota Hybrid System (THS) and GM Allison Two-mode hybrid are examples of the input split and compound split hybrid powertrains, respectively, see Figure 1.2.

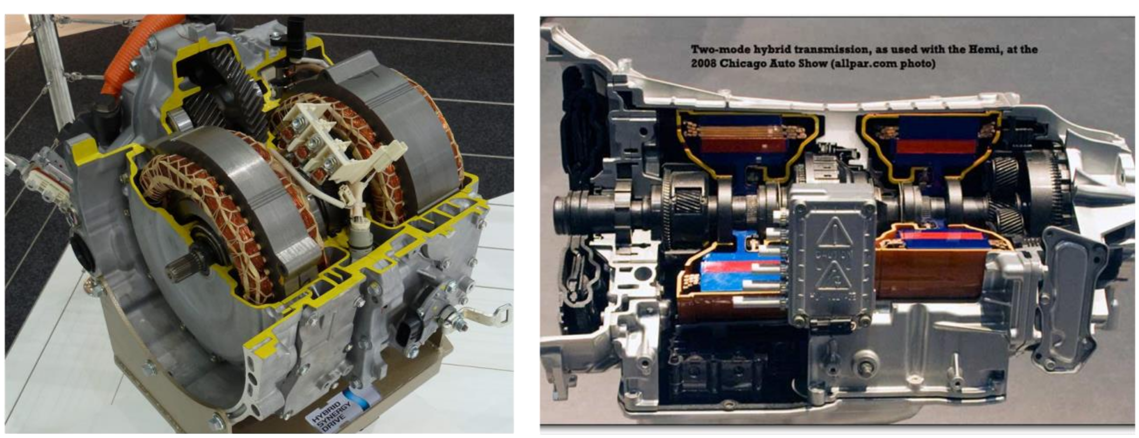

(a) Toyota Hybrid System – Input split

(b) GM Allison Two-mode Hybrid System – Compound split

Figure 1.2 Photographs of complex HEV powertrain models[11][12]

For both split modes, the powertrain requires two electric machines, one high speed machine coupled with engine output shaft for engine power split, and one high torque machine coupled with the output drive shaft to supplement output based on driving load condition. As an example, the THS input split hybrid is briefly discussed here. Figure 1.3 shows a schematic diagram of the powertrain structure. Major components include the battery, an internal combustion engine (ICE), two electric machines, either of which is able to run as a motor or generator (designated "M/G1" and "M/G2"), a planetary gear set unit ("R", "C" and "S" in the diagram designate ring gear, carrier and sun gear, respectively) and final drive (designated by "FD"). As the name suggests, engine power split is at the input port, where the ICE is coupled with M/G1 through the carrier and sun gear. Together, they determine the speed at the ring gear, which is directly connected to the final drive. By controlling the speed of M/G1, the speed of the output drive shaft can be adjusted to match the vehicle drive requirement with engine speed unaffected. Most of the time, M/G1 works as a generator that splits off excess engine power and converts it into electricity to be stored in the vehicle on-board battery. However, having M/G1 only ensures vehicle speed demand is matched at the drive shaft. To also satisfy the torque demand, a second electric machine M/G2 is added at the ring gear, directly supplementing torque to the drive shaft. In comparison, the compound power split powertrain uses two planetary gear sets and additional brakes and clutches to realize more modes of operation. Nevertheless, the underlying principle is similar between both types that two electric machines are employed for splitting engine power and meeting road speed and torque demands. A detailed review of complex hybrid electric powertrain architectures is given in [10].

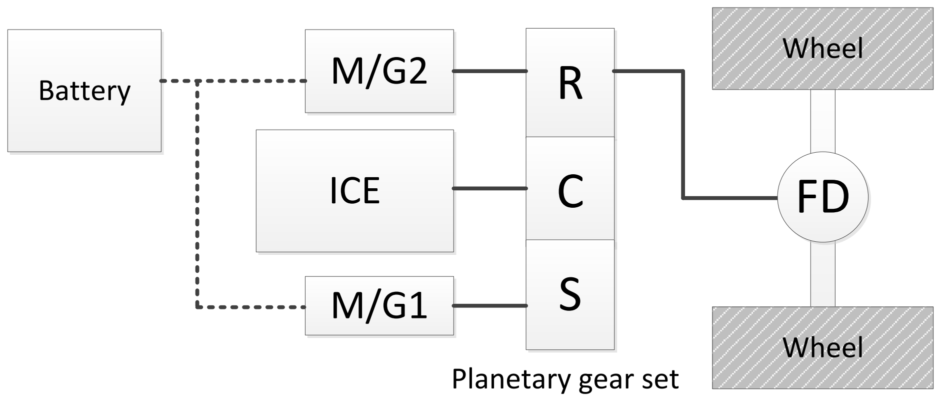

Figure 1.3 Toyota input split hybrid system

The double electric machine arrangement in the complex hybrid electric powertrain systems allows the use of a double rotor machine (independent outputs type) to replace the two individual machines. As an integrated machine, the double rotor machine provides various opportunities of system improvement through a higher degree of integration. Opportunities include, but are not limited to, reducing the total number of components, improving electric and thermal efficiency through integrated wiring and cooling system design and increased compactness through reduction of redundant parts with design integration. The various double rotor machine configurations that will be discussed in Chapter 2, also allow for much greater design flexibility in powertrain component layout, which is critical in implementing hybrid powertrains on existing automotive platforms. Few research is found on integration of double rotor machine in complex hybrid electric powertrains. In his thesis on integrated electro mechanical transmission, Yang proposed an integrated double rotor machine for the GM Allison

Two-mode Hybrid powertrain[2]. Notably, Yang demonstrated in his work that integration of the double rotor machine reduces powertrain mechanical components by 1 clutch, 1 brake and 1 planetary gear set, which greatly reduces system complexity. This proves that integration of double rotor machine in HEV powertrain achieves system wide benefit. In this thesis, the research focus is purely on the electric machine, rather than the complete powertrain system.

Another advanced hybrid electric powertrain architecture is the electric variable transmission (EVT). The EVT is based on a special configuration of double rotor machine, with magnetically coupled rotors. The EVT attracts great interest in double rotor machine research[3][13]. Figure 1.4 shows a system diagram of a typical EVT. At the center of the transmission is a double rotor machine with an external stator and two concentrically enclosed rotors. The interior rotor is connected to the engine output shaft and has slip-rings that conduct electrical current to the rotor windings. The exterior rotor envelops the interior rotor and is connected to the vehicle final drive. Usually, in published works [3][14]-[17], the exterior rotor contains two layers of permanent magnets that interact with interior rotor field and external stator field. Similar to a complex hybrid powertrain, engine power is split at the input with the interior rotor functioning as a generator most of the time. The external stator field is synchronized with output shaft speed and supplements torque according to road demand. The EVT is very attractive because it achieves variable transmission with minimal amount of powertrain components. Compared to a complex hybrid powertrain, the EVT eliminates the planetary gearing, clutches and the engine flywheel (the interior rotor can be designed to have the same function).

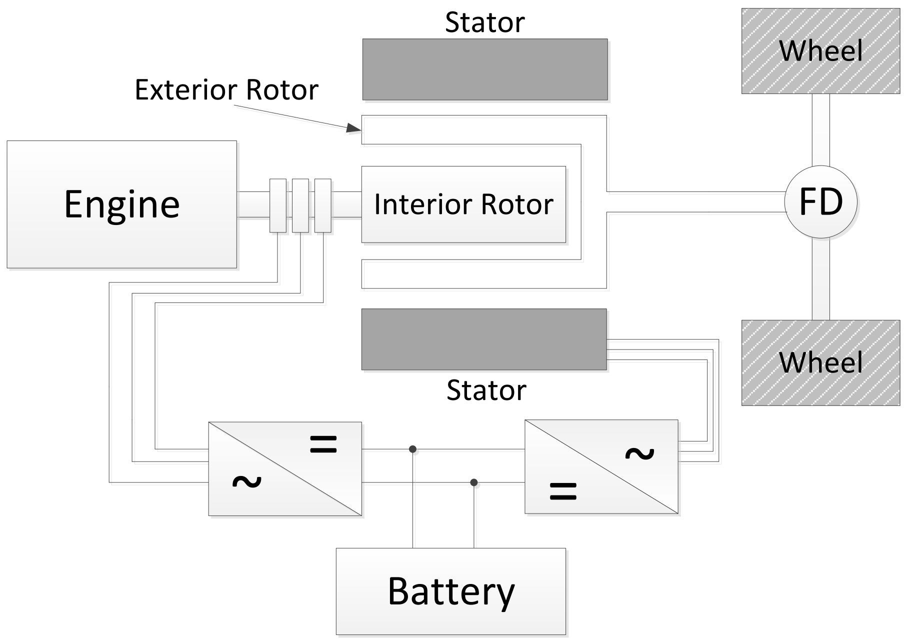

Figure 1.4 System diagram of an electric variable transmission (EVT)

The EVT concept was first introduced by Norlund et al in 2002 [3]. Norlund proposed and constructed the first permanent magnet double rotor machine for EVT and named it a four quadrant energy transducer (4QT). The study[3] simulated system performance of EVT on a light truck and concluded that higher efficiency is gained without an increase in vehicle total weight. The operation modes of the 4QT in an HEV is discussed and analysed in [18]. The design parameters and characteristics of the 4QT is studied in [14][15][19]. These studies show that the magnetic coupling between the two rotors is low in 4QT, which is critical in achieving accurate powertrain control of HEVs. A complete experimental evaluation of a 4QT is reported in [16], where it is reported that the enclosed structure of the 4QT makes machine cooling more challenging than the case for conventional machines. The cooling system of 4QT systems was later investigated in [20], while [21] proposes a method for determining machine size based on vehicle load requirements.

A number of variations of the 4QT are investigated in literature, for example, Hoeijmakers proposed the first double rotor induction machine for hybrid electric powertrains[22], generalizing the two mechanical port and single electrical port transmission system and named it EVT. A prototype machine was built and tested as proof of concept. A permanent magnet (PM) double rotor design with single layer of magnets was proposed and tested in [23], see Figure 1.5(a). The 4QTs introduced so far all feature a wound interior rotor with slip-rings and brushes, making the mechanical construction complicated. In [24], a design with two stators and two rotors, each with one layer of permanent magnets was proposed as a brushless version of the 4QT, see Figure 1.5(b). Another brushless PM 4QT design having magnets located on the interior rotor was proposed in [25], for which the exterior rotor is made of claw shaped lamination stacks. Figure 1.5(c) shows a diagram of the rotor structure. Designs with axially displaced rotors have also been investigated for 4QT, for example, [26] proposes an axial flux double rotor PM machine that features disk shaped rotors, see Figure 1.5(d), while [27] studies another axially displaced rotor PM 4QT design that has two separate stators, see Figure 1.5(e). Because neither rotor has windings, this design is also brushless. A design with permanent magnets placed on machine yokes, which results in a magnet free exterior rotor is proposed in [28], see Figure 1.5(f). The exterior rotor is made of steel laminations and features salient poles, resembling a switched reluctance machine.

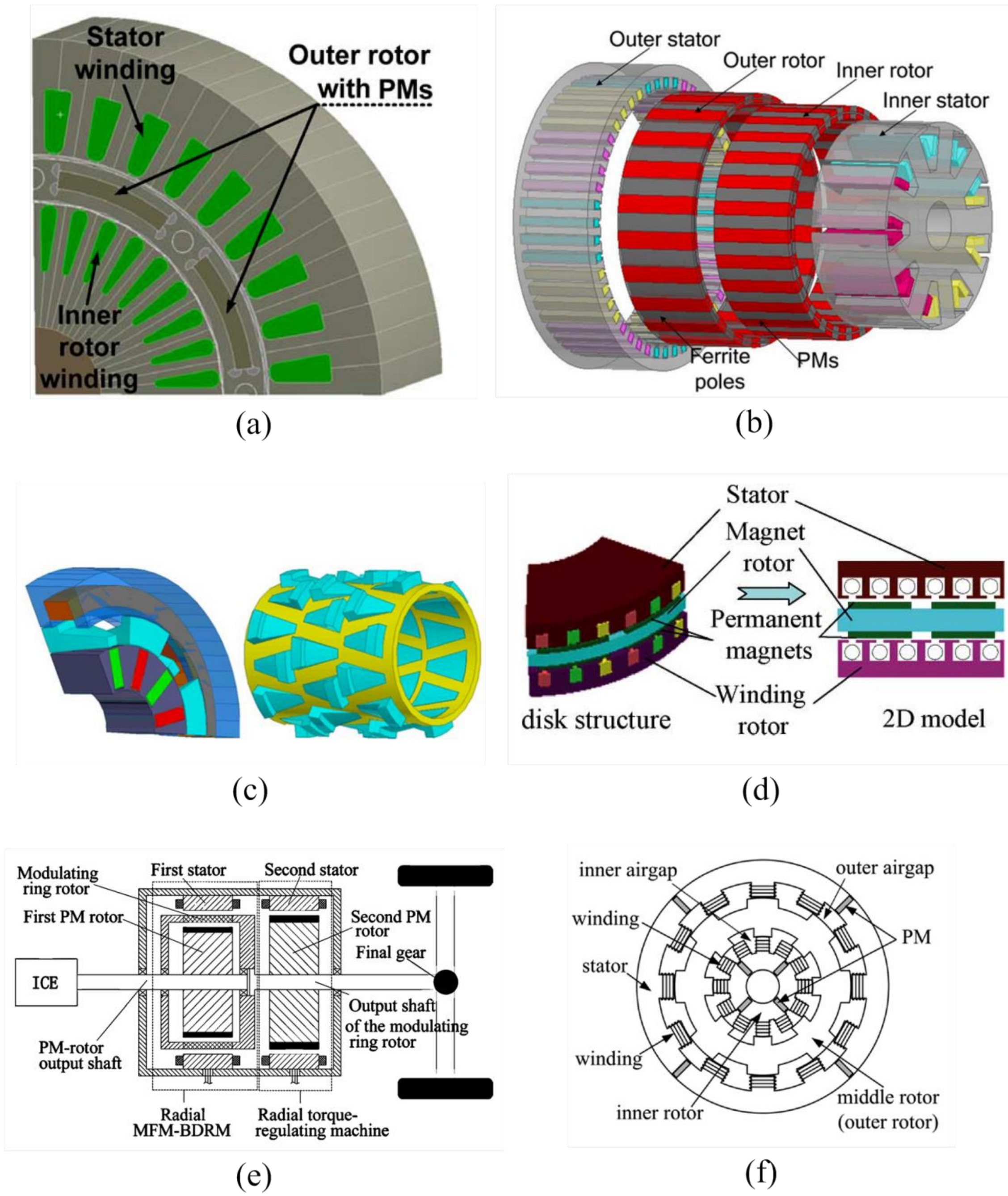

Figure 1.5 Examples of different double rotor 4QT designs

1.1.2. Other applications.

Apart from HEV powertrains, double rotor machines are also seen in many other applications. Qu et al. proposed double rotor PM machine designs with a central wound stator structure, see Figure 1.6. The double rotors are mechanically connected to deliver a single output, which can replace any conventional single rotor electric machines. The design exploits spatial advantages of the double rotor structure and achieves increased torque density. According to the author[4], the machine is able to achieve twice as much torque density as a conventional IPM (internal mounted permanent magnet machine). In [29], Qu studied characteristics of key design parameters and provided design equations for such machines. It is reported that higher torque density can be achieved for this machine by introducing stator current harmonics[30].

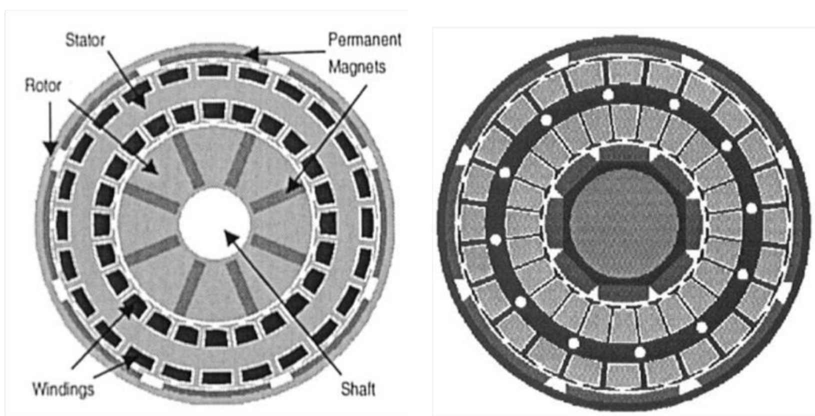

(a) (b)

Figure 1.6 PM double rotor machines with central wound stator

If the stator iron is removed from the previously presented double rotor PM machine, we have an air-cored double rotor machine. Figure 1.7 shows a diagram of such a machine design [31]. Permanent magnets are mounted on both rotors and interact with stator coils to produce torque. Elimination of the stator core brings benefits of improved winding installation and zero cogging torque. However, winding retainment becomes a challenging issue and this design suffers from low magnet utilization due to the much increased effective air gap length. Such a design framework is presented in [32].

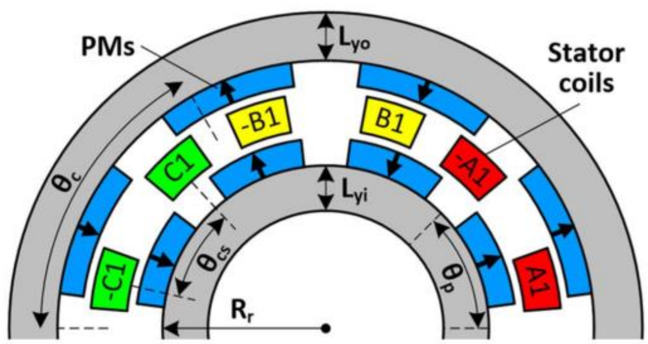

Figure 1.7 Air-cored double rotor machine

Another interesting application of double rotor machines is magnetic gears. Unlike mechanical gearing which relies on direct contact between teeth of two gears to transmit torque, magnetic gearing utilizes magnetic coupling between input and output rotors, achieving non-contact transmission. A proposed high performance magnetic gear design is reported in [33]. The exterior rotor contains 22 permanent magnet (PM) pole pairs and the interior rotor contains 4 PM pole pairs. Because of the interaction of PM fields, each pole-pair switch of the exterior rotor also corresponds to a pole-pair switch of the interior rotor. As a result, the exterior rotor rotates slower and the interior faster due to the pole number difference. The magnetic gear has no contacting components and therefore has less friction, vibration and noise than a conventional mechanical gear [33][34]. When a stator is added, we have an electric machine with integrated gearbox[35], as illustrated in Figure 1.8. Such a machine can be applied to wind power generation because gearbox is usually used to increase output speed for higher generation efficiency.

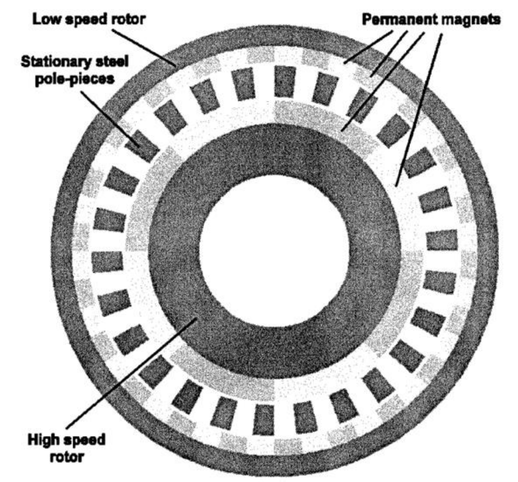

Figure 1.8 Example of a magnetic gear design[35]

Double rotor machines with dual outputs are also seen in literature. In [5], a PM dual output double rotor machine is designed and manufactured. The design features a central toroidally wound stator, sandwiched by two exterior and interior rotors embedded with permanent magnets. This machine is designed to be used in an air conditioner to replace two individual machines for the condenser and the evaporator.

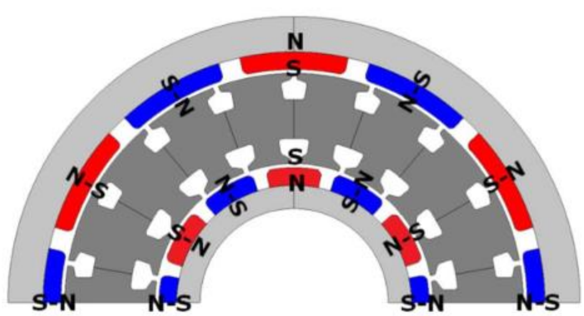

Figure 1.9 Diagram of half cross section of a double rotor dual output PM machine[5]

1.2. Double Rotor Switched Reluctance Machine

Switched reluctance machine (SRM) is a special type of electric machine that works on reluctance torque. An SRM does not have any source of magnetic excitation on the rotor. This characteristic gives SRM advantages over other brushless electric machines. Compared to induction machines, SRMs do not have induced AC magnetic field on the rotor, which leads to lower loss on the rotor and thus higher efficiency. Compared to permanent magnet machines, SRMs do not contain magnets, which require expensive rare earth elements for high performance applications.

It should be noted that despite of these benefits, SRMs are also subject to problems of having lower torque density as well as increased vibration and noise than PM machines. Currently, PM machine are the most widely applied electric machine type in HEVs and EVs. However, SRMs, offering lower cost, fault-tolerant capability and extended constant power operation range, are seen as a promising alternative for future HEV/EV powertrain propulsion system[36]. Recently, extensive research has been focused on SRM for vehicle traction applications[9][37]-[40]. These studies demonstrate that SRM is a viable solution for traction application. It has been previously shown in section 1.1 that HEV powertrain is one major application area of double rotor machines. Double rotor switched reluctance machine appears to be a good candidate with high potential for the realization of integrated HEV powertrains.

Only two previous publications have discussed double rotor SRMs. To have a comprehensive overview of the dual electric machine design, double stator SRMs are included here in the discussion as a special type of double rotor SRM. In fact, a double stator machine can be viewed as a double rotor machine with two rotors bonded together. In [41], Peng et al. designed and manufactured a bearingless double stator SRM. The machine has a ring shaped toothed rotor, sandwiched by exterior and interior stators, see Figure 1.10(a). The exterior stator supplies excitation for torque production and the interior stator provides a direction controlled magnetic pulling force, which suspends the rotor and is thus bearingless. In [42], Fahimi et al proposed and prototyped a unique double stator SRM design, see Figure 1.10(b). This design also has a pair of stators on the exterior and interior, facing a cup shaped rotor. The windings on the two stators are connected and provide excitation in unison. The double stator design allows for better utilization of space which increases winding area and hence excitation, consequently allowing for higher torque [43].

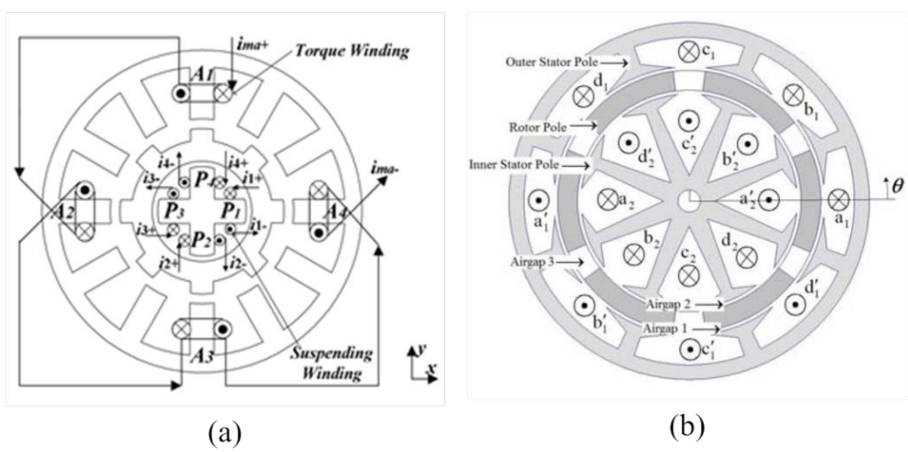

Figure 1.10 Two double stator SRM designs[41][42]

The above designs show some inspirations of novel SRM design. However, neither of the two double stator machines has two rotors and therefore is not applicable to an integrated HEV powertrain. Cui et al [44] presents the only research found on a double rotor SRM for EVT application, a 4QT. Figure 1.11 shows the (a) cross and (b) longitudinal section views of the 4QT. The machine has windings on external stator and interior rotor. The outer rotor is just a tube shaped iron core with toothed poles on both the interior and exterior. The machine is based on conventional toothed SRM design, which results in a bulky outer rotor occupying almost half of the total machine volume. The design is evaluated using FEA, but not validated by a machine prototype.

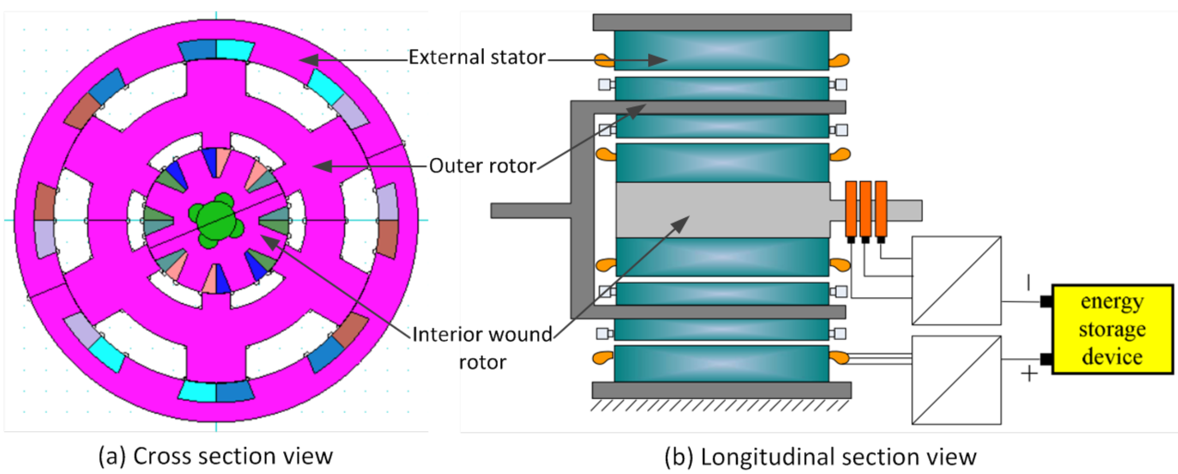

Figure 1.11 Double rotor SRM for EVT

Yang in his thesis[2] conducted a comprehensive study on a number of double rotor SRMs and proposed and constructed a double rotor SRM with central wound stator, see Figure 1.12. The machine is part of a proposed integrated electro-mechanical transmission system that is able to achieve the same functions as that of a GM Allison two-mode hybrid powertrain, but with less mechanical components. The design is also based on conventional toothed SRM structures. In the stator, there is a very thick yoke occupying a significant amount of machine interior volume because it needs to accommodate flux from both exterior and interior windings. In order to reduce the magnetic coupling effect between the exterior and interior machine, Yang introduced flux barriers (known as "bridges") along the center of the stator yoke, see Figure 1.13, which result in a mechanically weak structure. This machine is used to benchmark the segmented rotor double rotor SRM proposed in this thesis.

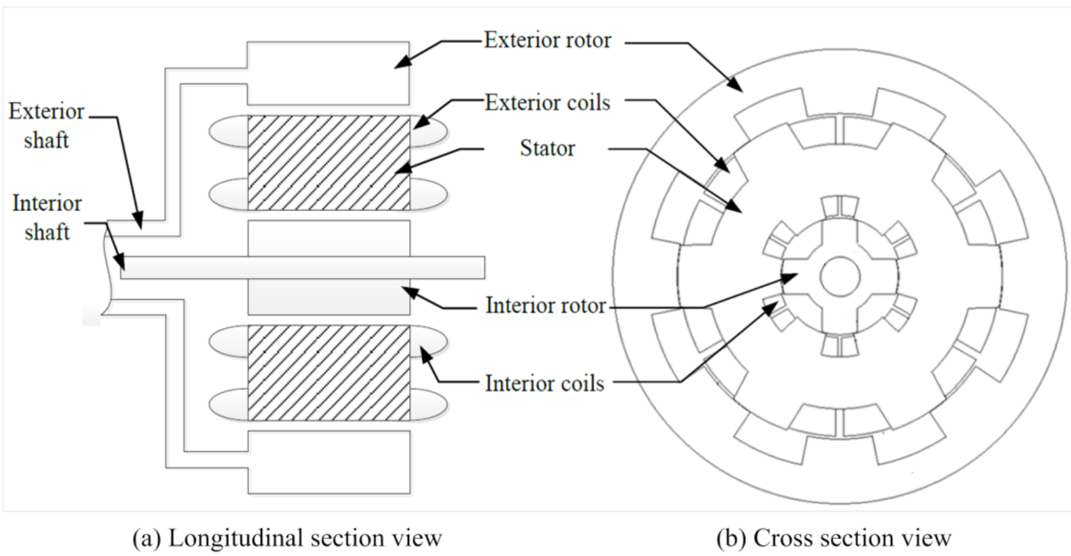

Figure 1.12 Double rotor SRM with central wound stator

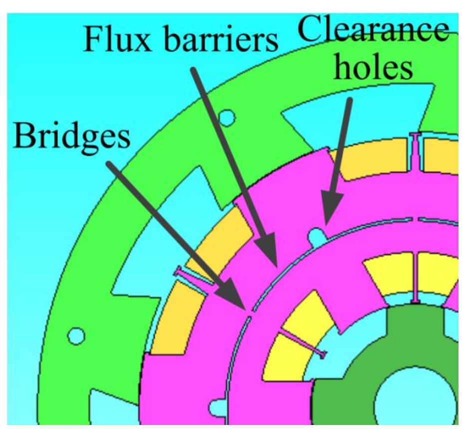

Figure 1.13 Diagram illustrating flux barrier in stator

1.3. Novelty and Contribution

This thesis research contributes several original developments and electric machine design novelties. These are presented in the thesis and are summarized here for clarity.

In this thesis, the segmented rotor SRM structure is applied to the design of double rotor electric machines. So far, no research has been found on double rotor machine with a segmented rotor SRM structure. The machine is studied and a family of radial flux double rotor switched reluctance machines with segmented rotors is established. Because of the unique structure of the segmented rotor design, higher compactness can be achieved compared to a conventionally structured double rotor SRM.

The various applications of double rotor electric machines are investigated and two major applications are identified for series-parallel HEV powertrains and 4QT of EVT, which lead to the design with wound central stator and another with wound external stator and inner rotor, respectively.

Stator yoke flux path sharing in double segmented rotor SRMs is another novel aspect of this thesis. By introducing flux path sharing in the stator yoke, yoke thickness can be significantly reduced, leading to increased machine compactness and reduced weight, which in turn improves torque and power density of the machine as a whole.

1.4. Thesis Outline

This thesis consists of 6 Chapters. In Chapter 1, applications of double rotor machine are reviewed with a focus on HEV powertrains. An introduction to HEV powertrain architectures is given to provide some fundamental knowledge required to understand the system. Then applications of double rotor machines in advanced HEV powertrains are discussed, followed by other applications. The advantage and suitability of applying SRM in double rotor machine is discussed and the thesis contribution stated.

In Chapter 2, fundamental knowledge on SRM and SRM with segmented rotor is presented. The various double rotor SRM configurations are then proposed. Chapter 3 covers the design of double segmented rotor SRMs. Various radial flux segmented double rotor designs are introduced and discussed. The central wound stator design is chosen for prototyping and the design process associated is presented. The capability of the machine for stator flux path sharing is thoroughly investigated. Details on modelling, simulation and parameter determination of the prototype are also presented.

Chapter 4 documents the manufacturing process of the chosen prototype machine. The complete mechanical design, along with associated machining processes are explained and discussed. Chapter 5 presents experiment results of the prototype machine, which are compared to the finite element analysis (FEA) simulations of Chapter 3 and the overall machine performance is evaluated. Finally, Chapter 6 summarises the major findings of the research and suggests areas of future research.

CHAPTER 2
FUNDAMENTALS AND BACKGROUND

2.1. Switched Reluctance Machine Fundamentals

2.1.1. Basic operation

A switched reluctance machine (SRM) is an electro-magnetic energy conversion device that operates purely on changes to magnetic circuit reluctance and the interaction thereof with supplied currents to produce torque in a rotary machine or force in a linear machine. Unlike permanent magnet and induction machines where torque generation is mainly due to the interaction between rotor and stator magnetic fields, a switched reluctance machine does not have any source of excitation on the rotor. Both the stator and the rotor of an SRM are made of soft magnetic material and only the stator has windings for current excitation. Torque generation of an SRM relies on the tendency of rotor teeth aligning with excited stator teeth, such that the excited electro-magnetic circuit tends towards minimum magnetic reluctance or maximum inductance.

To illustrate the basic operation of an SRM, a standard 6/4 machine is shown in Figure 2.1. The 6/4 designation indicates that this machine has 6 stator teeth (poles) and 4 rotor teeth (poles). This topology lends itself to a three-phase winding implemented via 2 coils per phase on the 6 stator teeth. Considering phase A, the two most important rotor positions are shown in Figure 2.1, the unaligned or minimum inductance position (a), where excited stator teeth point towards the mid-point of two adjacent rotor teeth, and (b) the aligned or maximum inductance rotor position, where excited stator teeth are aligned with rotor teeth. Because air has a much higher magnetic reluctance than the soft magnetic material on the machine rotor and stator, the total reluctance of the magnetic circuit is dominated by the reluctance of the air gap. The saliency of the rotor and stator teeth causes the air gap size to change as a function of rotor position. At the unaligned position, the air gap is largest and hence the machine magnetic reluctance is highest or inductance a minimum. As the rotor teeth start to align with stator teeth, the air gap becomes smaller and reluctance reduces or inductance maximized.

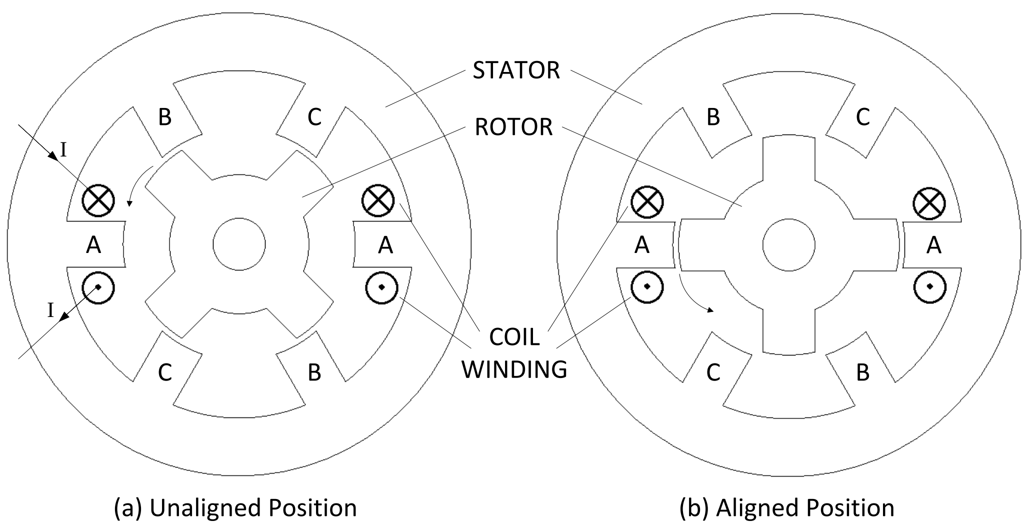

Figure 2.1 Standard 6/4 SRM Operation

Suppose current excitation is turned on for phase A just after rotor teeth pass the unaligned position, Figure 2.1 (a), torque will be developed in the direction of rotation as shown because of the tendency of the soft magnetic material to orient itself with minimal total magnetic reluctance. Torque will reduce to zero at the aligned rotor position, Figure 2.1 (b), because minimum reluctance is reached. From the aligned position to the next unaligned position, a negative torque that is opposite to the direction of rotation shown in

Figure 2.1 (b) will be developed. The region from the unaligned position to the aligned position is called the motoring region where the machine draws energy from the electric circuit to output mechanical work. The region from aligned to unaligned position is called the generating region where mechanical energy input is electro-magnetically connected to electricity in the stator coils. By sequentially exciting the corresponding stator phases as the rotor rotates, the machine can continuously operate as either a motor or generator. Usually, this sequential excitation is achieved by switching on and off different phases, hence the switched reluctance machine. Normally, the machine characteristic is analysed by the magnetic inductance L, which is inversely proportional to reluctance for constant current excitation. Figure 2.2 shows the inductance and torque profile of a typical SRM under constant current excitation.

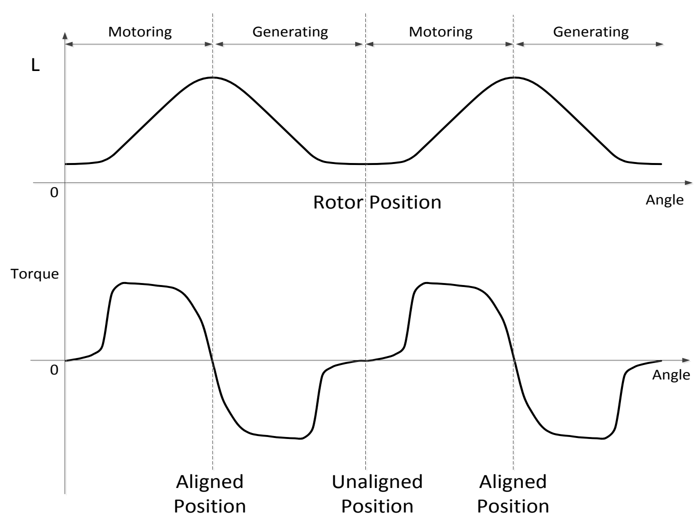

Figure 2.2: Typical inductance and torque profile of an SRM

2.1.2. Torque generation mechanism

The torque generation mechanism of an SRM can be explained by considering the electromagnetic energy conversion in the machine. If the losses are neglected, by applying the law of conservation of energy, we have

$$W_e = W_f + W_m \tag{2.1}$$

where W_e represents the electrical energy inputted into the machine, W_f is the magnetic field energy stored in the excited coils and W_m is mechanical energy output.

Because electrical energy equals the integral of instantaneous electrical power P_e, which is the product of induced voltage and excitation current, we have

$$W_e = \int P_e\, dt = \int Vidt = \int \frac{d\lambda}{dt} idt = \int id\lambda \tag{2.2}$$

in which V is input voltage, i is input current and λ is flux linkage.

A flux linkage versus excitation current diagram can be used to illustrate the energy conversion process. Figure 2.3 shows the flux linkage characteristics of a typical SRM. For each rotor position, there is a characteristic curve showing the relationship between flux linkage and excitation current. Because the aligned and unaligned positions have maximum and minimum inductance, they also define maximum and minimum flux linkage of the machine. Plots of all other rotor positions should fall within the boundary defined by the aligned and unaligned curves.

Consider two intermediate positions 1 and 2 on the rotor path as the rotor rotates from an unaligned position to an aligned position. The magnetic field energy is given by:

$$W_f = \int i d\lambda \tag{2.3}$$

which is essentially the area above the flux likage versus current curve. Therefore, the field energy of rotor position 1 is designated by area OBEO and the field energy of position 2 is designated by area OCDO. The area under the curve is termed "coenergy":

$$W_C = \int \lambda di \tag{2.4}$$

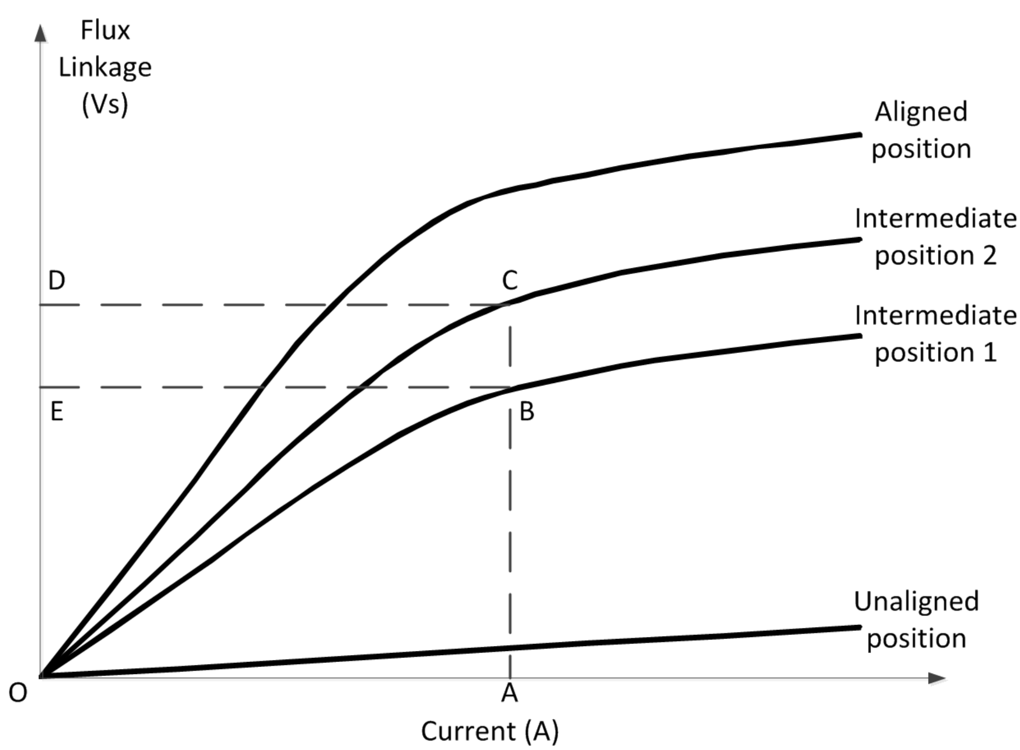

Figure 2.3: Flux linkage vs. excitation current characteristics for a typical SRM

For a finite change from rotor position 1 to rotor position 2, we have

$$\delta W_e = \delta W_f + \delta W_m \tag{2.5}$$

Suppose excitation current is constant, which means points A, B and C are on the same vertical line. The equation for change of electrical energy becomes:

$$\delta W_e = i\int_{\lambda_1}^{\lambda_2} d\lambda = i(\lambda_2 - \lambda_1) \tag{2.6}$$

The change of electrical energy input is then the rectangular area BCDEB. And the change of field energy is area difference between OCDO and OBEO.

$$\delta W_m = \delta W_e - \delta W_f \tag{2.7}$$

$$\delta W_m = area(BCDEB) - \big(area(OCDO) - area(OBEO)\big) = area(OBCO)$$

Thus, the mechanical work produced is the area enclosed by the flux linkage curves at the two positions. Note this area also equals the difference between coenergy W_C at the two positions. Hence, for constant excitation,

$$\delta W_m = \delta W_c \tag{2.8}$$

$$W_C = \int \lambda di = \int L(\theta, i) i di \tag{2.9}$$

$$T = \frac{\delta W_m}{\delta\theta} = \frac{\delta W_c}{\delta\theta} = \frac{\delta W_c(\theta, i)}{\delta\theta}\bigg|_{i=constant} = \frac{i^2}{2}\frac{dL(\theta, i)}{d\theta} \tag{2.10}$$

where T is mechanical torque output.

Two important characteristics of an SRM can be seen from the derived torque equation. First is that torque is proportional to current squared. This means change of current direction will have no impact on direction of rotation, which is usually not the case for other types of machines. Secondly, torque generation depends on the rate of rotational inductance change. As can be observed from the inductance profile, Figure 2.2, the inductance profile is not always linear with angular position, making derivation of a closed-form steady state torque solution not possible for SRMs.

Generally, mutual inductance between phases can be neglected [45], thus the torque equation of an SRM can also be derived from a simple equivalent circuit as shown in Figure 2.4.

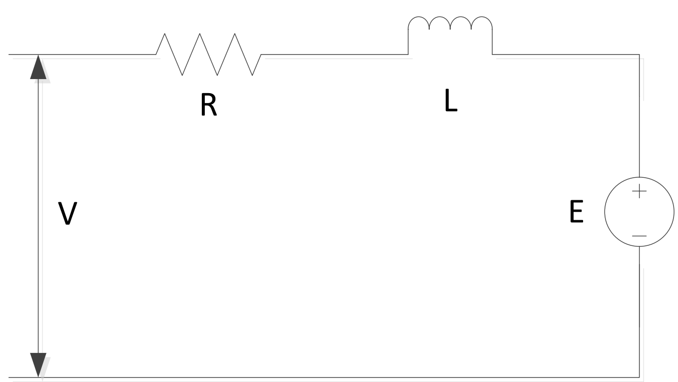

Figure 2.4: Single phase equivalent circuit of an SRM

The phase voltage should equal the sum of the resistance voltage drop and the induced voltage by the magnetic field. The induced voltage is basically the rate of change of flux linkage with time. The phase voltage can be expressed:

$$V = iR + \frac{d\lambda(\theta, i)}{dt} \tag{2.11}$$

in which i is phase current, R is phase resistance and λ is flux linkage, being a function of both rotor position and current. The flux linkage can also be represented by:

$$\lambda(\theta, i) = iL(\theta, i) \tag{2.12}$$

Then the phase voltage can be written as

$$V = iR + \frac{d[iL(\theta, i)]}{dt} = iR + \frac{di}{dt}\, L(\theta, i) + i\frac{dL(\theta, i)}{dt} \tag{2.13}$$

The total electrical power input P_e is the product of phase instantaneous voltage and current:

$$P_e = i^2R + i\frac{di}{di}\, L(\theta, i) + i^2\frac{dL(\theta, i)}{dt} \tag{2.14}$$

The last term can be rewritten based on the following relationship:

$$\frac{d}{dt}\left(\frac{1}{2}i^2L(\theta, i)\right) = \ i\frac{di}{di}\, L(\theta, i) + \frac{1}{2}i^2\frac{dL(\theta, i)}{dt} \tag{2.15}$$

which gives:

$$P_e = i^2R + \frac{d}{dt}\left(\frac{1}{2}i^2L(\theta, i)\right) + \frac{1}{2}i^2\frac{dL(\theta, i)}{dt} \tag{2.16}$$

From left to right, the three terms of equation 2.16 are resistive power loss, rate of change of field energy and air gap power. Only the last term contributes to mechanical work [46]. Let the rotational speed of the machine be ω, which is also the ratio of finite change of angular position over time. The air gap power can be reformulated as:

$$\frac{1}{2}i^2\frac{dL(\theta,i)}{dt}=\frac{1}{2}i^2\frac{dL(\theta,i)}{d\theta}\frac{d\theta}{dt}=\frac{1}{2}i^2\ \frac{dL(\theta,i)}{d\theta}\omega \tag{2.17}$$

Neglecting iron losses, mechanical power P_m is the product of torque output T and rotational speed which also equals the product of induced EMF and phase current:

$$P_m=\frac{1}{2}i^2\ \frac{dL(\theta,i)}{d\theta}\omega=T\omega \tag{2.18}$$

Rearranging the equation also gives:

$$T=\frac{1}{2}i^2\ \frac{dL(\theta,i)}{d\theta} \tag{2.19}$$

2.1.3. Drive and control

An SRM is connected to a direct current (DC) power supply via a power electronic converter stage, a typical configuration of which is shown in Figure 2.5. As mentioned previously, current direction has no impact on the direction of rotation, hence the control of the machine is relatively simple. For motoring, a phase winding is excited during the period as rotor moves from unaligned to aligned position to produce torque. The generating region covers the other half period of rotation and a short period of excitation current is given at the beginning of aligned position to initiate the coil flux linkage. The power electronic converter unit is a system of power electronic components (e.g. transistors and diodes). There are a number of converter topologies for SRM control.

One of the most popular is called an asymmetric bridge converter, a diagram of this converter structure for a three phase SRM is shown in Figure 2.5. For each phase, there are two transistors and two diodes, designated by “T” and “D”, respectively, on the diagram as shown in Figure 2.5. When the two transistors are turned on, e.g. T1 and T2, current flows out of the power supply and excites the phase coils. When the transistors are off, the diodes allow current to be fed back to the supply and thus the coils are de-energized.

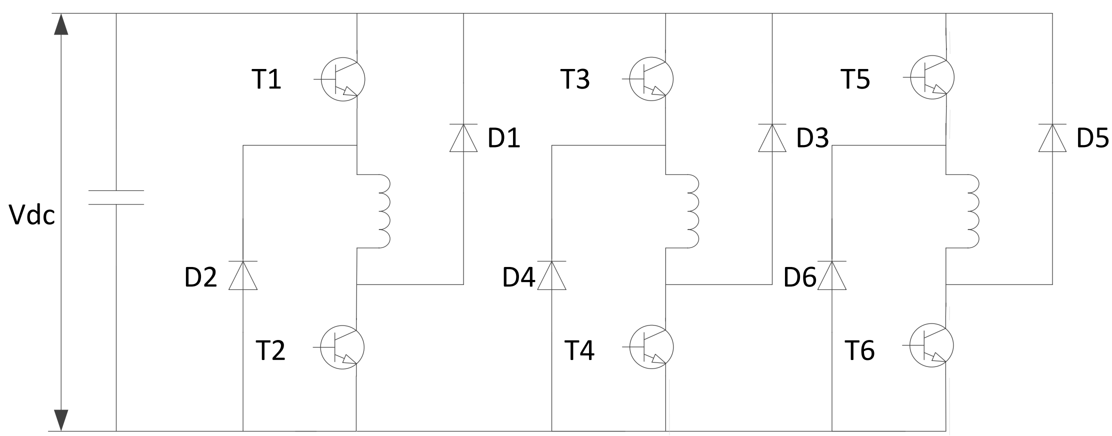

Figure 2.5: Asymmetric bridge converter for a 3 phase SRM

The strong dependency of SRM operation on rotor position requires positional feedback sensors to be installed and linked to the power electronic control unit, from which signals are sent to the transistors for switching control. Because motoring and generating regions keep alternating as the rotor rotates in an SRM, torque production for each phase is of an intermittent fashion. As a result, higher torque ripple is often observed for SRMs. To reduce torque ripple, switching is controlled so that there is an overlap between the conduction periods of adjacent phases. Figure 2.6 shows typical phase current waveforms for a 6/4 SRM. The constant current regions are normally achieved by applying a hysteresis band control or current chopping. Because of the transient dynamics when coils are energized and de-energized, current waveforms are of a trapezoidal shape. At low speeds, the transient regions are smaller and the current waveforms can be approximated as a rectangular pulse.

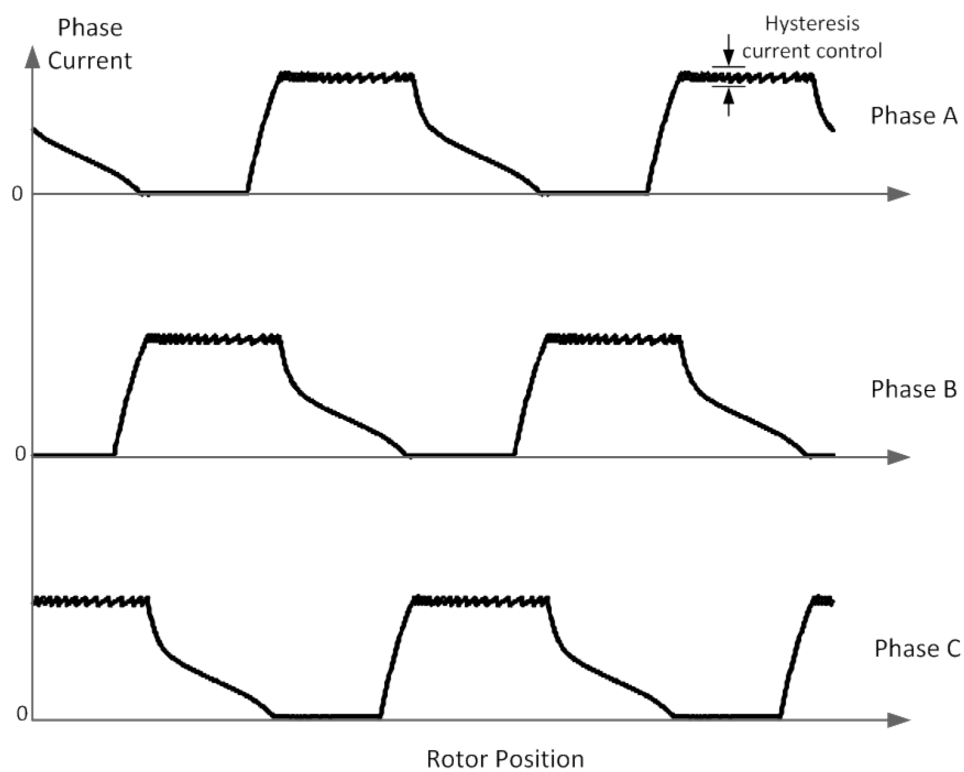

Figure 2.6: Typical phase current waveform for a 6/4 SRM

The design and control of conventional SRM is a well-studied subject in literature, references [45][46][47] give more details on the design procedure and control theory of switched reluctance machines.

2.2. Switched Reluctance Machine with Segmented Rotor

2.2.1. Summary of past research

Switched reluctance machines with segmented rotors (SSRM) were first introduced by Mecrow et al. in [48]. Although other researchers have developed different segmental rotor SRM designs [49][50][51], the design proposed by Mecrow [52] is by far the most successful. In [50] Higuchi et al. designed a segmental rotor machine with a 6/4 topology, see Figure 2.7(a), however the machine suffers from high torque ripple. Many techniques were studied by Higuchi's group to enhance machine performance, including increasing phase number [53], a rotor with a 2-step structure [54] and rotor segments made of special grain-oriented electric steel [55]. In [49], Vandana et al. proposed a flower-shaped stator geometry, as illustrated in Figure 2.7(b). The stator structure provides ideal flux path but reduces effective winding area and increases manufacturing difficulty. In [51], a 5 rotor pole machine is designed, which inherently suffers from unbalanced rotor radial force.

In [52], Mecrow proposes and compares two different segmental rotor SRM designs; a 12/8 machine with full pitch winding (c) and a 12/10 machine with concentrated single tooth winding (d) as illustrated in Figure 2.7. Even though both machines produce similar output torque for the same copper loss, the design with the single tooth winding has smaller end windings [56], and thus results in a shorter and more compact machine. This characteristic makes the later machine design more favorable for large diameter-to-length ratio machines, such as the case of a double rotor machine configuration.

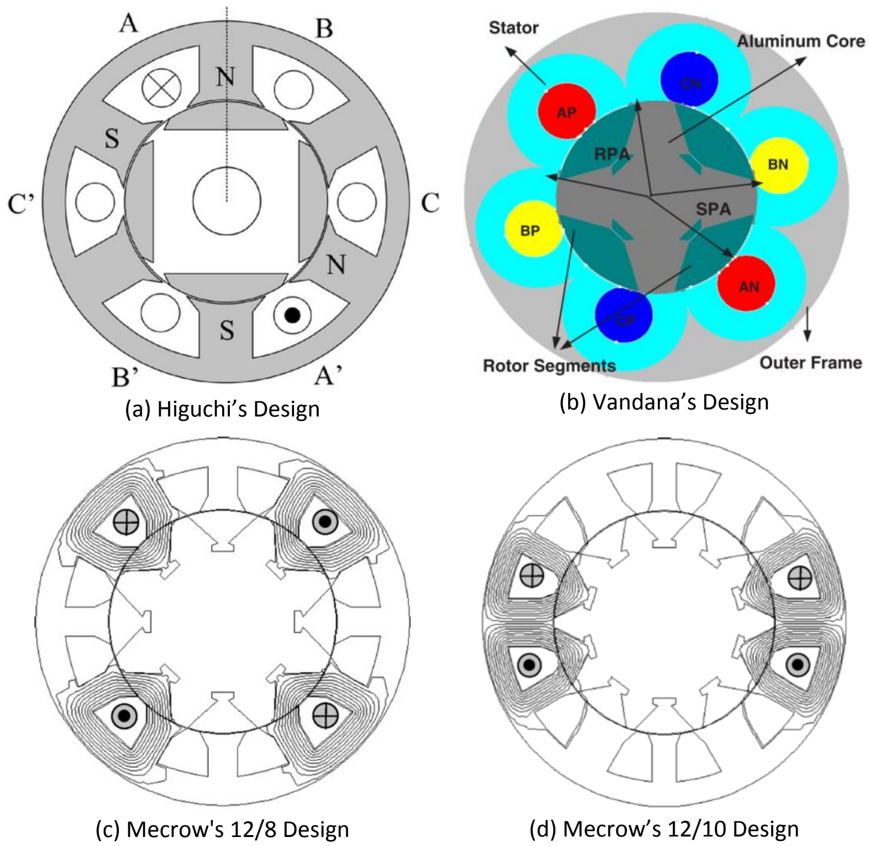

Figure 2.7 Examples of published schemes of segmented rotor SRM

Several studies [52][57][58][59] have shown SRMs with segmented rotors have higher torque-to-copper loss ratio than conventional SRMs. In [52], a conventional SRM was compared to a segmental rotor SRM with most design parameters being held equal. In [59], a genetic optimization algorithm was used to find designs with maximal average torque. Both studies were validated by experiments. In [60], an 80kW segmented rotor SRM was designed and optimized for automotive traction. A prototype is being constructed for performance validation.

The segmental rotor SRMs discussed so far all have a conventional structure with stator on the exterior and internal rotor. Designs with the rotor on the exterior and internal stator have also been reported. For example, Vandana et. al proposed an external rotor design in [61]. The external rotor configuration achieves good torque output, which is good for in-wheel propulsion application where high torque is demanded. A prototype was designed and manufactured in [62]. The authors also found increasing the number of phases and number of rotor poles both contributed to increased average torque [62][63]. Similar conclusions were found for internal segmental rotor SRMs [64].

In [65], Madhavan et al. developed an axial flux segmented rotor SRM that has two mechanically coupled rotor disks. An angle displacement was introduced to reduce torque ripple of the machine in [66]. As in radial-flux segmental SRMs, torque capability at low speed can be enhanced by increasing rotor pole number [67].

The only publication that relates to radial-flux double/dual segmental rotor SRM is [68], which analyzed a toroidally wound stator with two mechanically coupled segmental rotors. The authors claimed that this design suffered from significant flux leakage at stator coil ends. The design was not validated by a prototype machine.

2.2.2. Structure and operation

Figure 2.8 shows cross section diagrams of rotor and stator of a 12/10 segmented rotor SRM. Unlike a conventional SRM whose rotor is made up of single continuous soft magnetic material, a segmented rotor structure consists of an array of segments (dark wedges on left diagram of Figure 2.8) made of soft magnetic material and a filler piece (white regions on left diagram of Figure 2.8) made of non-magnetic material. Because the poles (segments) are disconnected from each other, the segmented rotor does not have a rotor yoke. The stator geometry of a SSRM is more similar to a conventional SRM. Note that even though there are 12 stator poles (teeth), the machine effectively operates as a conventional 6 stator pole machine. This is because only the six phase poles (ones with wide teeth) are wounded with coils. The other six thinner stator poles, having half of the width of phase poles, are for flux bypass only.

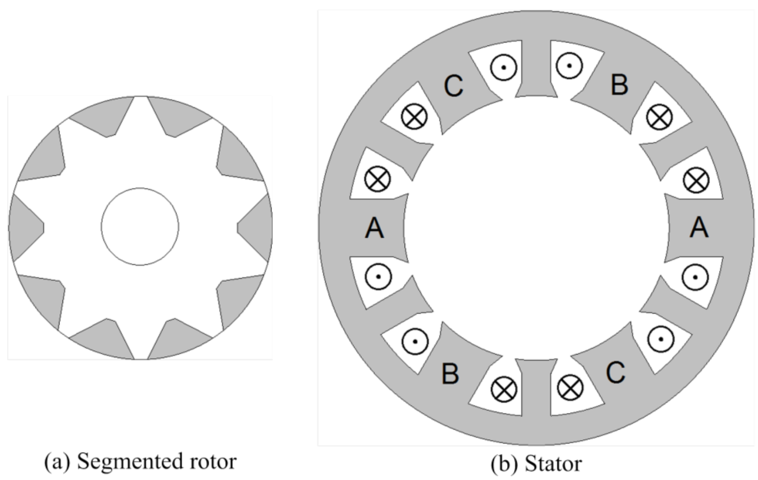

Figure 2.8: Rotor and stator sturctrue of a 12/10 segmented rotor SRM

Segmental rotor SRMs have a very different magnetic flux loop compared to conventional SRMs. In a conventional tooth SRM, a magnetic conducting loop is created by aligning two pairs of rotor and stator tooth, as illustrated in Figure 2.9(a). To allow pathways for magnetic flux between conducting rotor teeth and stator teeth, there are both a stator yoke and a rotor yoke in these machines. In a segmental rotor SRM, the rotor is formed by an array of magnetically isolated segments. A magnetic conducting loop is formed when a rotor segment spans over two adjacent stator poles and bridges an excited slot, see Figure 2.9(c). Because each magnetic conducting loop is within one rotor segment, no pathways are required between segments and therefore there is no rotor yoke in a segmental rotor SRM. Note that contrary to intuition, rotor pole/segment actually aligns with stator pole at the magnetic unaligned position for a SSRM; and at the magnetic aligned position, segments are geometrically unaligned with stator poles, as illustrated in Figure 2.9(c) and Figure 2.9(d).

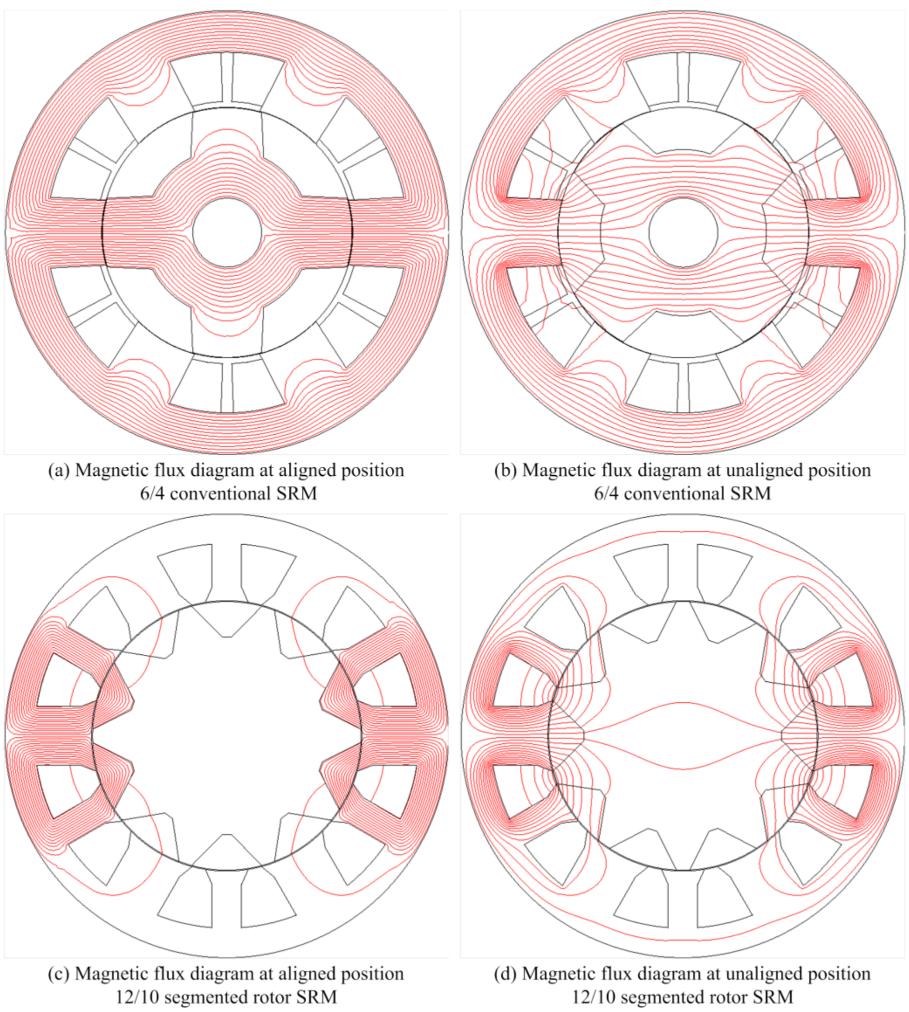

(a) Magnetic flux diagram at aligned position 6/4 conventional SRM

(b) Magnetic flux diagram at unaligned position 6/4 conventional SRM

(c) Magnetic flux diagram at aligned position 12/10 segmented rotor SRM

(d) Magnetic flux diagram at unaligned position 12/10 segmented rotor SRM

Figure 2.9: Magnetic flux diagram of conventional and SSRMs

The increased torque capability of a segmental rotor SRM is attributed to shorter flux path and higher stator tooth width to pitch ratio [48]. In a conventional SRM, tooth width is not only constrained by available winding area, but also the spacing between teeth. Normally the spacing between teeth needs to be larger than one tooth width so that there is enough air gap (between rotor and stator teeth) at unaligned position. As a result, the tooth width to pole pitch ratio is less than 0.5 for a conventional SRM. For a segmental rotor SRM at unaligned position, conducting stator poles align with rotor segments (see Figure 2.10). The effective air gap equals the spacing between two adjacent stator poles, which allows a higher tooth width to pole pitch ratio. In fact, the ratio is only constrained by available winding area and can reach 0.7.

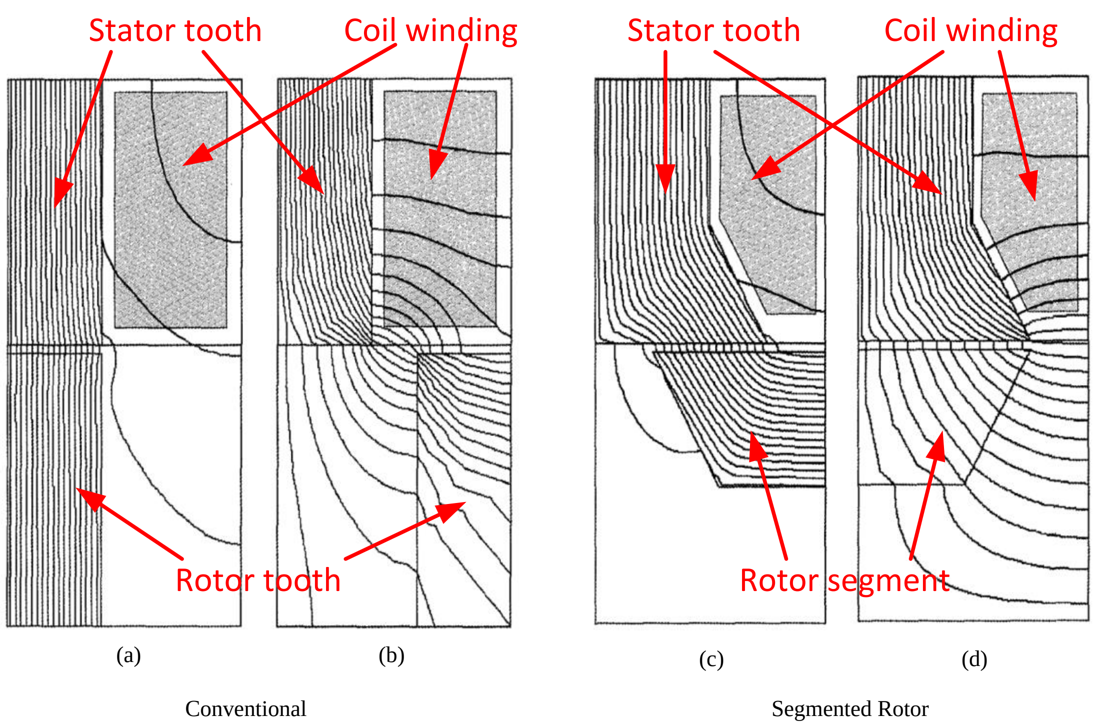

Figure 2.10: Comparison of flux loops at aligned and unaligned positions of a conventional SRM and a segmental rotor SRM [48]

Apart from structural differences, the operation and control of an SSRM is largely similar to a conventional SRM. Torque generation still exclusively relies on reluctance torque. Direction of rotation is controlled by sequential excitation of stator coils. What is unique about this type of machine is that changing reluctance profile is not due to tooth saliency. This can be best observed by comparing the flux diagrams at the unaligned positions, see Figure 2.10(b) and Figure 2.10(d). In a conventional SRM, maximal air gap is in the radial direction, between the rotor yoke and top of stator pole. In an SSRM, maximal air gap is created when segment aligns with stator pole. The gap is in the tangential direction and covers regions between adjacent segments and a portion of the winding slot. As a result, long rotor teeth are not required to achieve a high reluctance at unaligned position for SSRM, which leads to less rotor soft magnetic material usage and a more compact rotor structure for external rotor configuration. This reduction is very beneficial for double rotor machines.

2.3. Double Rotor SRM Configurations

A double rotor machine consists of a minimum of three parts: two rotatory pieces (called rotor) and one stationary piece (called a stator). When radial flux machines are concerned, as in this thesis, there are four general arrangements that can be designated by the relative position of the rotor/stator, as illustrated in Figure 2.11, showing the longitudinal section views of double rotor machine arrangements. Radially from center to exterior, we can have rotor-rotor-stator, Figure 2.11(a), rotor-stator-rotor, Figure 2.11(b), stator-rotor-rotor, Figure 2.11(c) and lastly two rotors enclosed by a double layer stator, Figure 2.11(d).

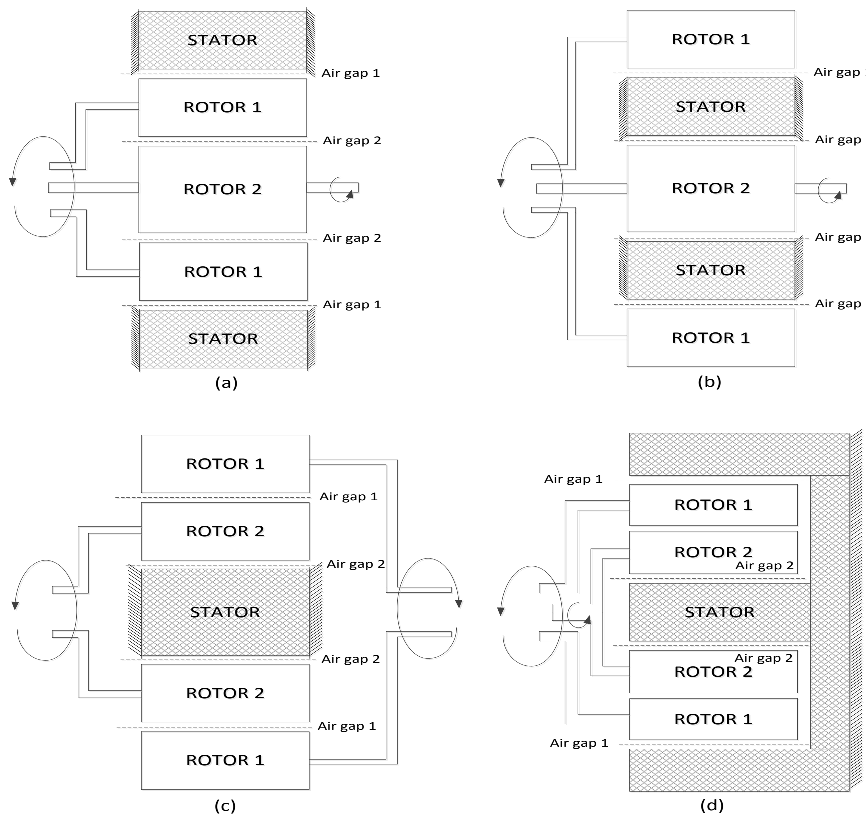

Figure 2.11: General arrangements of radial flux double rotor machine

So far only SRMs with windings on the stator have been considered. It is important to note that coils can also be wound on the rotor. In this case, rotor and stator pole combination will be opposite to that of a wound stator machine to accommodate phase windings on the rotor. For example, a standard wound stator 6/4 SRM is equivalent to a wound rotor 4/6 SRM. In addition, for wound rotor machines, slip-rings are required to conduct electricity to the rotating windings.

Because either the rotor or the stator can be wound in an SRM, variations of arrangement arise due to different winding set-up. Of the two sides of the air gap, one side should be wound while the other not. In a double rotor machine, there are two air gaps, which give two by two, four different winding configurations for each rotor-stator position arrangement. The four general double rotor SRM arrangements now expand to 16 configurations. A simple diagram of the longitudinal section view of each configuration is shown in Figure 2.12. In the diagram, "S" designates stator and "R1" and "R2" designates the two rotors. Note only the top half of a section view is shown. The machine center axis is denoted in a dashed line. Besides machine component blocks, a "w" means the component is wound with coils and a "u" means the component is unwound.

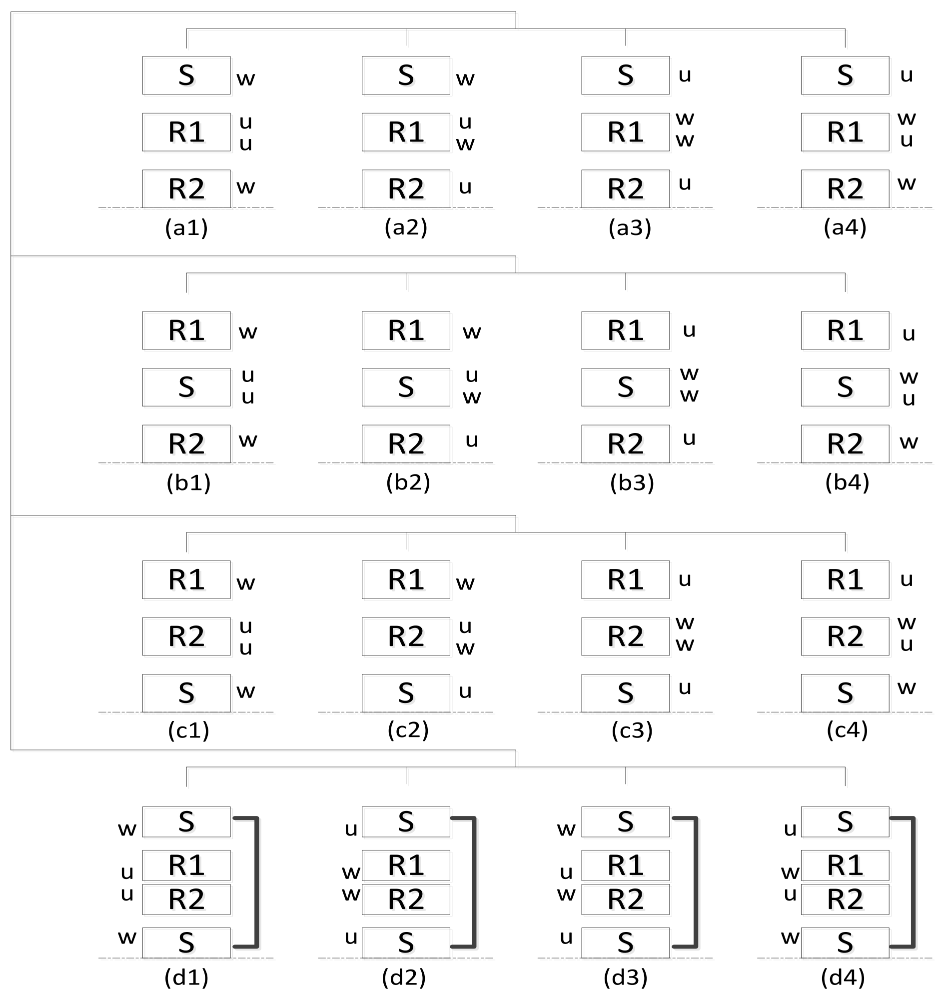

Figure 2.12: Double rotor SRM configurations

For the first three categories (a), (b) and (c), the middle piece, be it a rotor or stator, interacts with both air gaps. This means the middle piece is essentially an integrated part with two sets of poles responding to different excitations. Either set of poles can be wound or unwound. In the last category (d), the integrated part is the double layer stator, which interacts with both air gaps.

Even though all 16 configurations can deliver two independent rotor outputs and have viable topologies, not all of them are wise choices from a machine design point of view. For example, having a rotating coil increases machine complexity and makes cooling more difficult. Configurations that have both sets of coils rotating greatly increase system complexity and should be avoided (configurations a3, a4, b1, c2, c3 and d2).

Of the four categories, (a) and (c) have magnetically coupled rotors (air gap exists between the rotors) and can be used for an electrical variable transmission (EVT) system. Normally, cooling is most easily applied to the exterior and center shaft, making configuration a1 most commonly seen in such applications. In a2, cooling of R1 will be a challenging task. Configuration c1 is similar to a1, however, having a wound exterior rotor results in large rotating mass, which makes the mechanical design more challenging.

Category (b) features a center stator with rotors on exterior and interior. Having a wound rotor only adds complexity in these configurations. the better choice would be configuration b3, where both sets of coils are on the stator. This arrangement is good for any independently controlled double output applications.

Category (d) also has magnetically uncoupled rotors, making wound rotor unnecessary (configurations d3 and d4 should be avoided). For configuration d1, sometimes the rotors can be mechanically coupled together. Some researchers call this arrangement a double stator machine [69], [70].

2.4. Summary

This Chapter introduces fundamental knowledge of switched reluctance machines and double rotor machine configurations. Basic operation principle and control scheme of conventional SRM are explained first. Then one of the key elements of this thesis, switched reluctance machines with segmented rotors, is introduced and discussed. Compared to conventional SRM, the segmented rotor SRM features short flux paths and a high tooth width to tooth pitch ratio, which reduces magnetic reluctance and hence greater flux under same field excitation. Moreover, the segmented rotor design eliminates rotor back iron, which improves the compactness of the machine. Especially for exterior rotor machines, reduced rotor back iron leads to overall machine dimension reduction and material saving. To set the stage for specific design discussions in Chapter 3, general double rotor SRM configurations are also introduced. All possible rotor/stator arrangements for the radial flux type of double rotor SRM are identified and briefly discussed.

CHAPTER 3

DOUBLE SEGMENTED ROTOR SWITCHED RELUCTANCE MACHINE DESIGN

3.1. Double Segmented Rotor SRM Configurations

In Chapter 2, a total of 16 possible arrangements of double rotor SRMs (rotors radially displaced) are discussed. Omitting the 8 overly complex arrangements, i.e. those having windings on one or both of the rotors, and the following 8 configurations are interesting for further study:

a) External stator and wound inner rotor

b) External stator and wound exterior rotor

c) Wound central stator

d) Central stator and wound external rotor

e) Central stator and wound inner rotor

f) Inner stator and wound external rotor

g) Inner stator and wound central rotor

h) Double layer stator

For each configuration, a double segmented rotor SRM (DSRSRM) design has been developed and briefly discussed in the following section of this Chapter.

3.1.1. DSRSRM with External Stator and Wound Inner Rotor

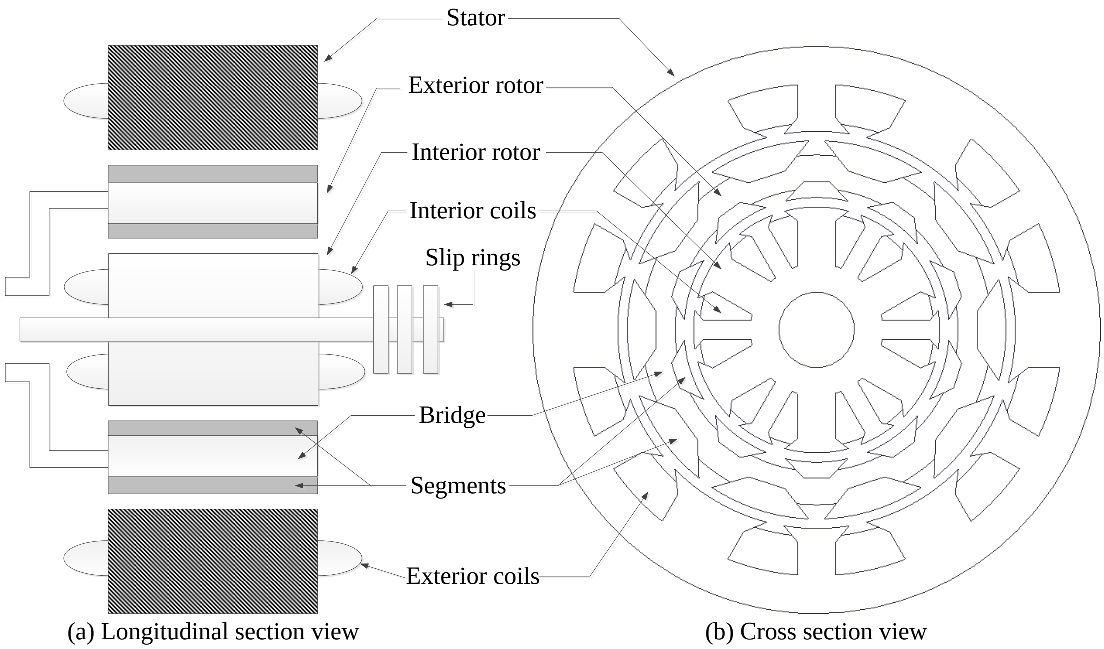

Figure 3.1 DSRSRM with external stator and wound inner rotor

This configuration features an external wound stator with two rotors enclosed. The interior rotor is wound with coils and thus requires slip-rings to maintain electrical connection to the power supply. The exterior rotor consists of two sets of segments made of magnetic conducting electric steel laminations. The segments are located on a bridge made of magnetic non-conductive material, which also serves as a flux separator.

The interior rotor rotates relative to the exterior rotor and this configuration can be effectively used in an electrical variable transmission (EVT) without mechanical gears [22], sometimes called a four quadrant energy transducer (4QT). The external wound stator offers advantage in cooling due to its big surface area. The interior wound rotor can be cooled through a fluid channel in shaft center. The cooling of the exterior rotor is most challenging due to double air gaps on the inside and outside. This creates problems for PM machines using this configuration [20], where the exterior rotor usually contains magnets. In an SRM, cooling of the exterior rotor may not be necessary since the rotor is magnet free and can thus be subject to much higher temperature.

The interior wound rotor double rotor SRM was previously proposed by Cui et al. [44] and Yang [2]. In their design the machine is of a conventional straight toothed SRM structure, as illustrated in Figure 3.2. Compared to the newly proposed segmented rotor design, the conventional design has a bigger exterior rotor due to the need to maintain saliency and a thick rotor yoke. This results in smaller available winding area of the phase coils.

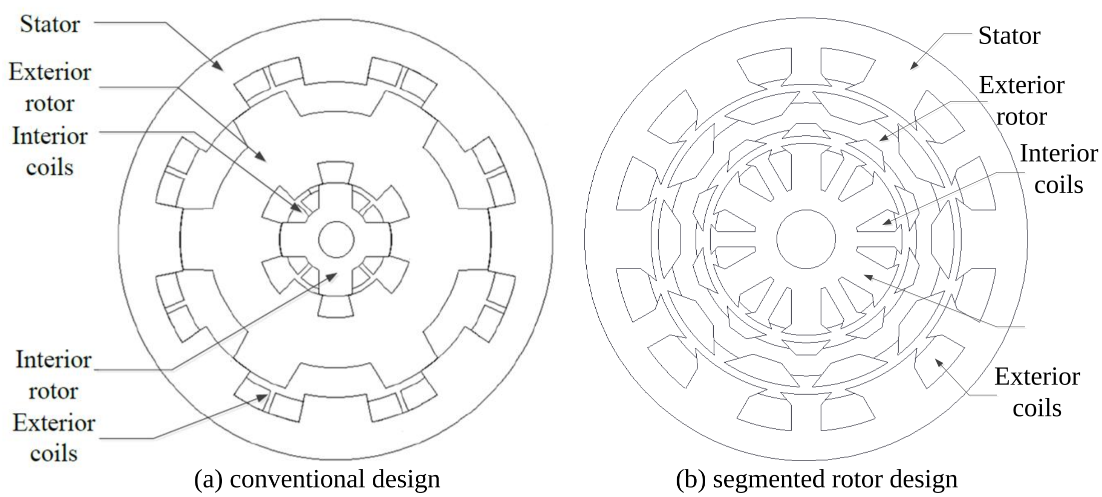

Figure 3.2 Comparison between conventional and segmented rotor designs

3.1.2. DSRSRM with External Stator and Wound Exterior Rotor

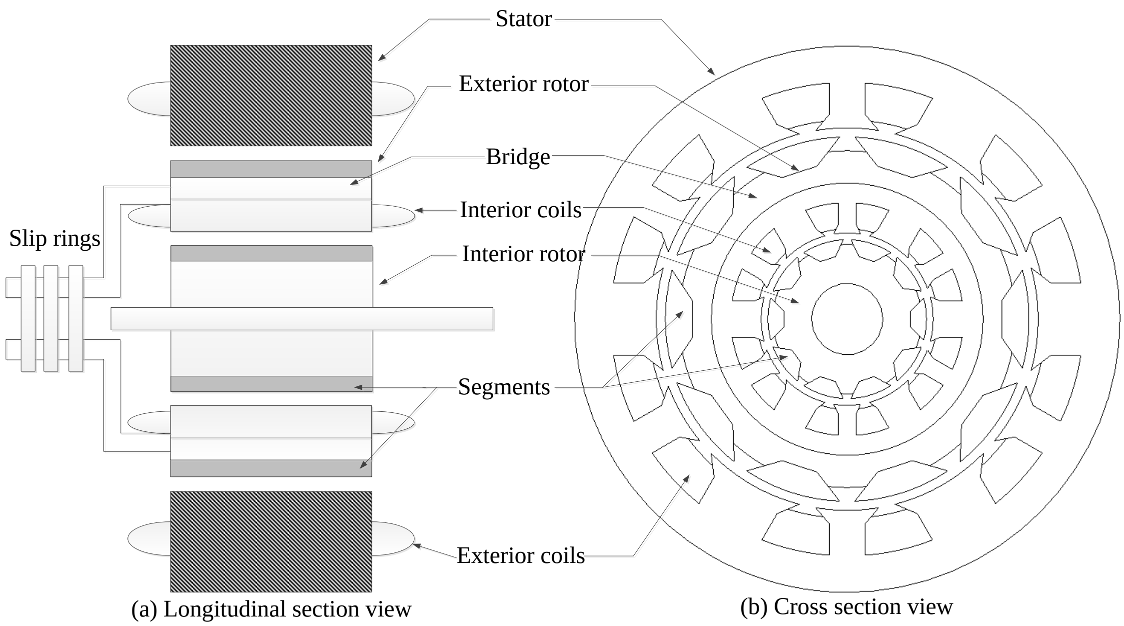

Figure 3.3 DSRSRM with external stator and wound exterior rotor

This topology has the same stator-rotor-rotor arrangement as the design shown in section 3.1.1, but the interior coils are on the exterior rotor, forming a tubular exterior rotor that has electric steel segments on the outside and wound coils on the inside. As a result, slip-rings are needed on the exterior rotor shaft to provide electric connection to the interior coils. A non-magnetic conductive bridge is required to hold the segments and to minimize flux coupling.

This configuration can also be used as a 4QT. However, cooling of the interior coils will be a challenge since heat transfer is least efficient for the exterior rotor due to the double air gaps. In a 4QT, the interior rotor is often connected to input load[3]. Transferring coils to the exterior rotor increases rigidity and reliability of the interior rotor, which can potentially be beneficial for high speed input load applications. Note the interior winding placement also affects the inertia of the two rotors, which may be of concern for particular applications.

3.1.3. DSRSRM with Wound Central Stator

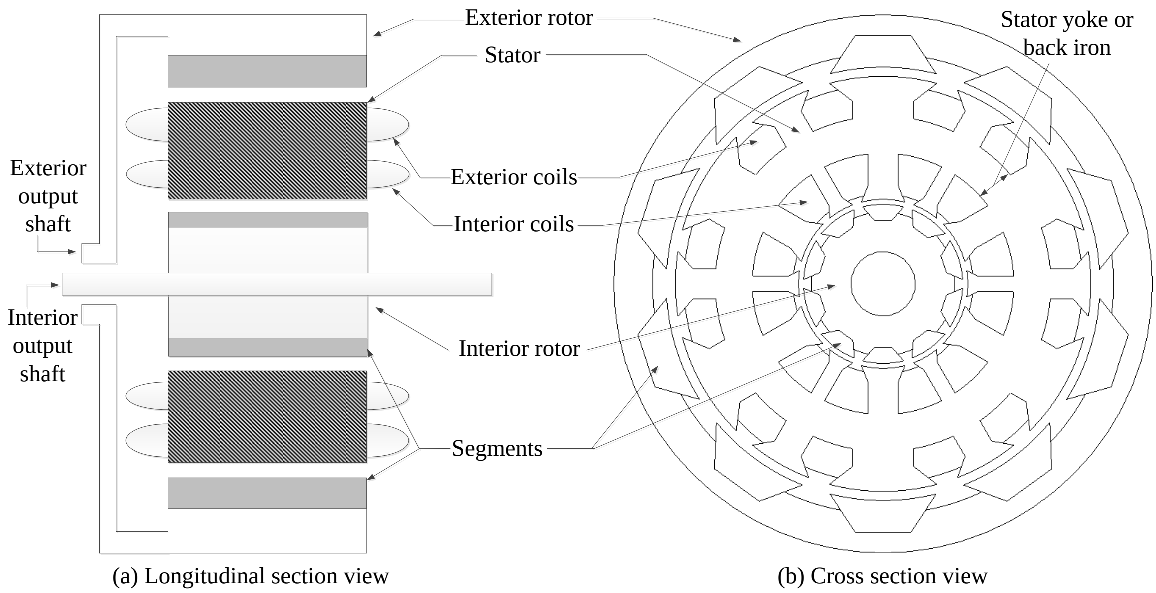

Figure 3.4 DSRSRM with wound central stator

In a central stator double rotor arrangement, the stator is located in the center, sandwiched by the rotors on the outside and inside. Because there are no magnetic force interactions between the two rotors, configurations with a central stator arrangement cannot be used as a 4QT. The two rotor outputs are independent and essentially either of them forms a switched reluctance machine with one side of the stator. The central stator double rotor machine configuration can be applied to most power split type HEV powertrains, where two independent output shafts are required[10]. Yang demonstrated in his work on an integrated electro-mechanical transmission, that by integrating a central stator double rotor machine into the GM Allison two-mode hybrid powertrain, the total number of mechanical components could be reduced [2].

In the above configuration, both exterior and interior coils are located on the central stator. No coils are on either of the rotors, eliminating the need for slip-rings and reducing system complexity. However, since all coils are in the center of the machine, cooling is not as efficient as in a conventional external wound stator machine where large surface area can be utilized and the machine can be air cooled. Liquid cooling will probably be necessary for this configuration for high power operations[2].

Note in this configuration, stator poles on the exterior and interior share the same stator yoke. It is discovered in this thesis that the segmented rotor design allows flux path sharing of the stator yoke between the exterior and interior, which reduces the size of the stator and hence the overall size of the machine. Details will be shown later in section 3.2.1.

3.1.4. DSRSRM with Central Stator and Wound External Rotor

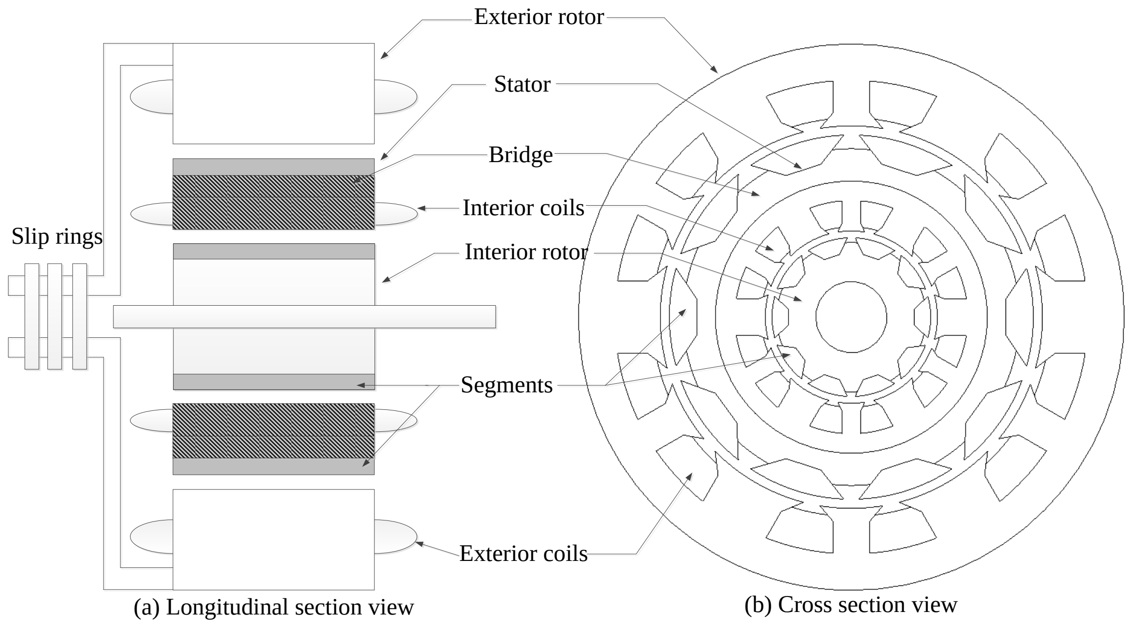

Figure 3.5 DSRSRM with central stator and wound external rotor

This configuration has exterior windings on the external rotor. The cross section of the machine is identical to the configuration shown in section 3.1.2. Similar to machines that have an external wound stator, this configuration allows the use of the complete outer surface area of the machine for heat dissipation of the exterior coils. This increases the cooling capacity of the exterior coils, which makes the exterior machine suitable for high power operations. However, slip rings are needed for electric connection, increasing complexity. The exterior coils also make inertia of the external rotor significantly larger.

3.1.5. DSRSRM with Central Stator and Wound Inner Rotor

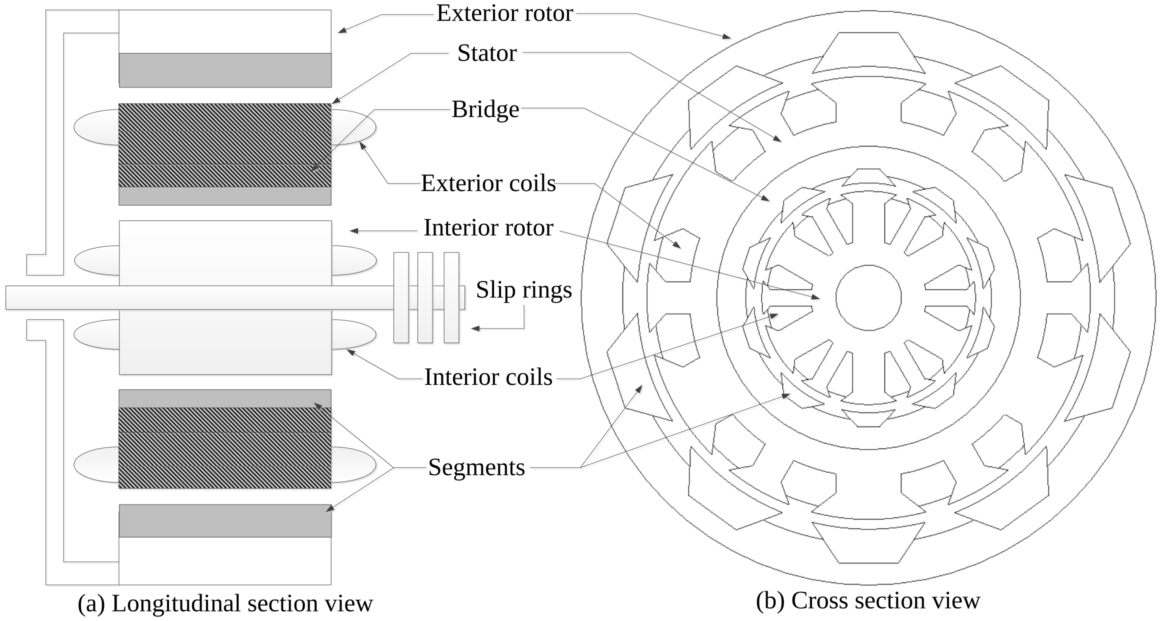

Figure 3.6 DSRSRM with central stator and wound inner rotor

The interior coils can also be wound on the inner rotor, giving the configuration shown in Figure 3.6. Slip-rings are needed on the inner rotor shaft for electrical conduction. The central stator consists of coils on the outside and electrical steel lamination segments on the inside, with a non-magnetic conductive bridge separating the two. Again, fluid cooling is necessary for both exterior and interior coils since neither is close to the machine surface.

3.1.6. DSRSRM with Inner Stator and Wound External Rotor

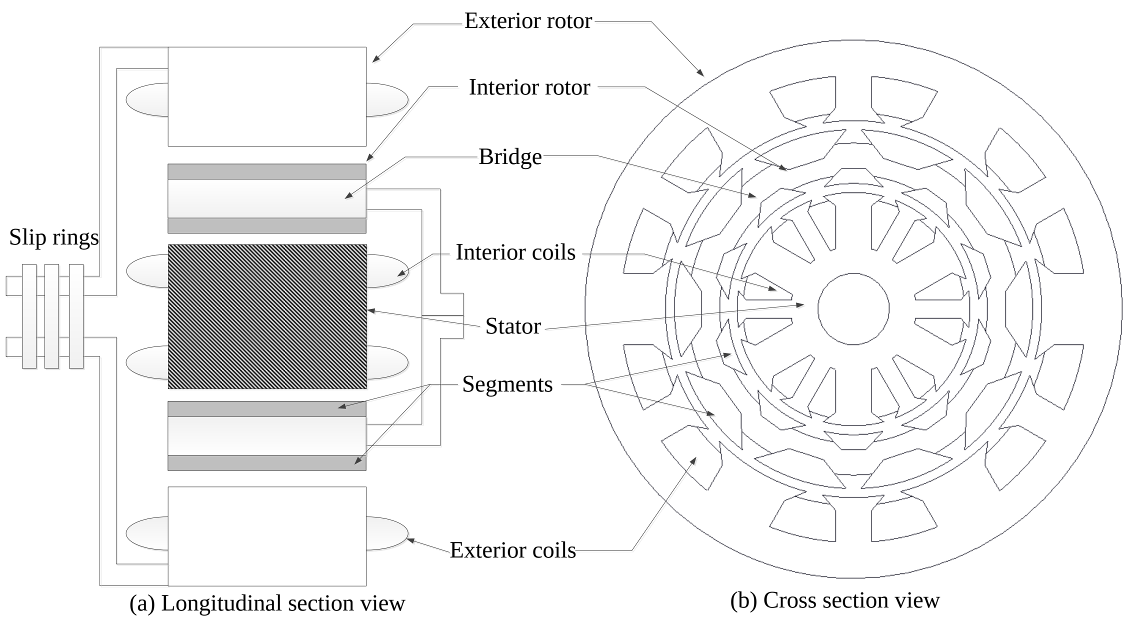

Figure 3.7 DSRSRM with inner stator and wound external rotor

An alternative of the machine configuration of section 3.1.1 is to have the exterior coils rotary and the interior coils stationary, forming an inner stator double rotor machine. Because the placement of coils is not changed, this design has a cross section identical to that of the machine of section 3.1.1. Due to the coils on the exterior rotor, rotor inertia is significantly larger. This configuration can be applied to a 4QT.

3.1.7. DSRSRM with Inner Stator and Wound Central Rotor

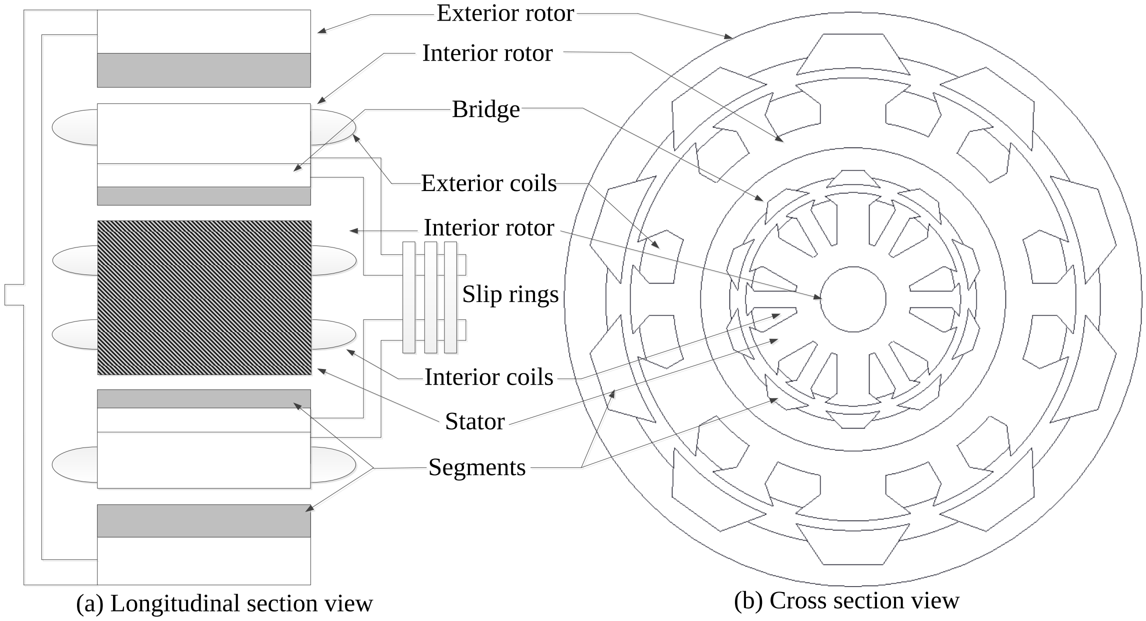

Figure 3.8 DSRSRM with inner stator and wound central rotor

If the central stator of machine configuration shown in section 3.1.5 is rotary and the wound rotor is held stationary, we have the configuration shown in Figure 3.8. The two rotors are coupled through magnetic forces across the outer air gap, making this configuration suitable for a 4QT application. The interior rotor inertia is expected to be large considering the mass of the structure.

3.1.8. DSRSRM with Double Layer Wound Stator

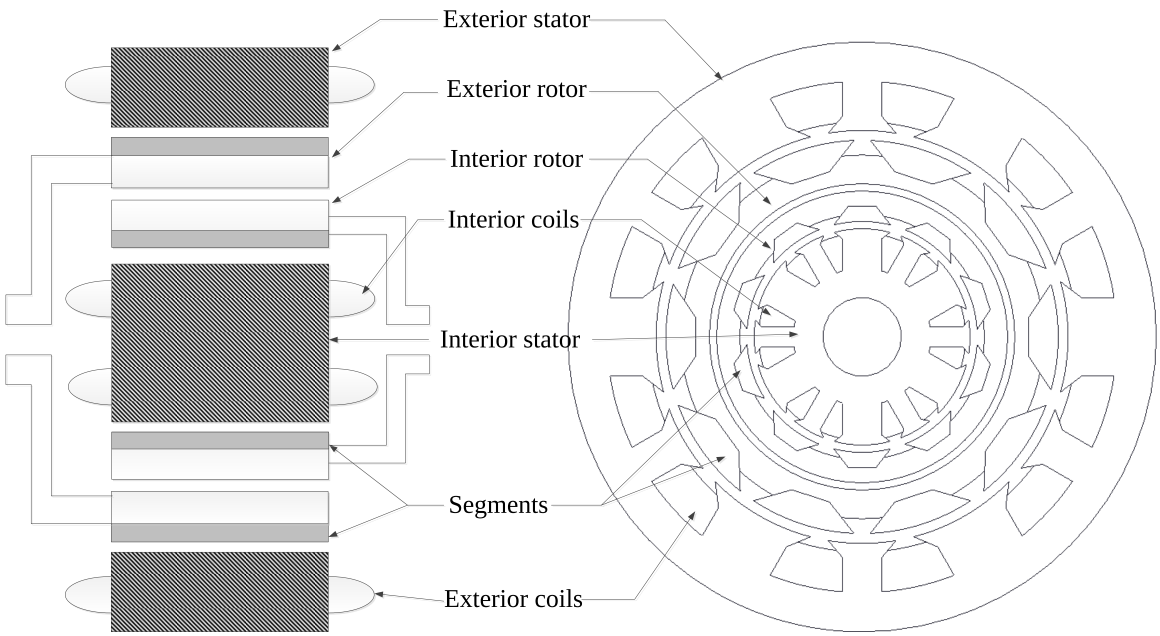

Figure 3.9 DSRSRM with double layer wound stator

Finally, one could have implemented two layers of wound stator on the exterior and interior of the machine, sandwiching two tubular segmented rotors. No slip rings are required since all coils are stationary. Because the rotors are uncoupled, this configuration is able to deliver two independent outputs as the machine configuration in section 3.1.3. Unlike the central stator arrangement, this configuration has the stator on the outside, which makes cooling more efficient. However, this configuration has an additional air gap and the stator is not as compact, which will likely increase the mechanical complexity of the machine.

Note a variation of this design is to have the two rotors mechanically coupled together to deliver a single output. A layout diagram is shown in Figure 3.10. The two sets of rotor segments are located on the outside and inside of the rotor sleeve, made of non-magnetic conducting material. In the single output configuration, the exterior and interior coils excitations are to be synchronized to give a steady torque output. A similar design with cage shaped rotor was proposed in [42] where the machine was called a double stator SRM, as illustrated in Figure 3.11.

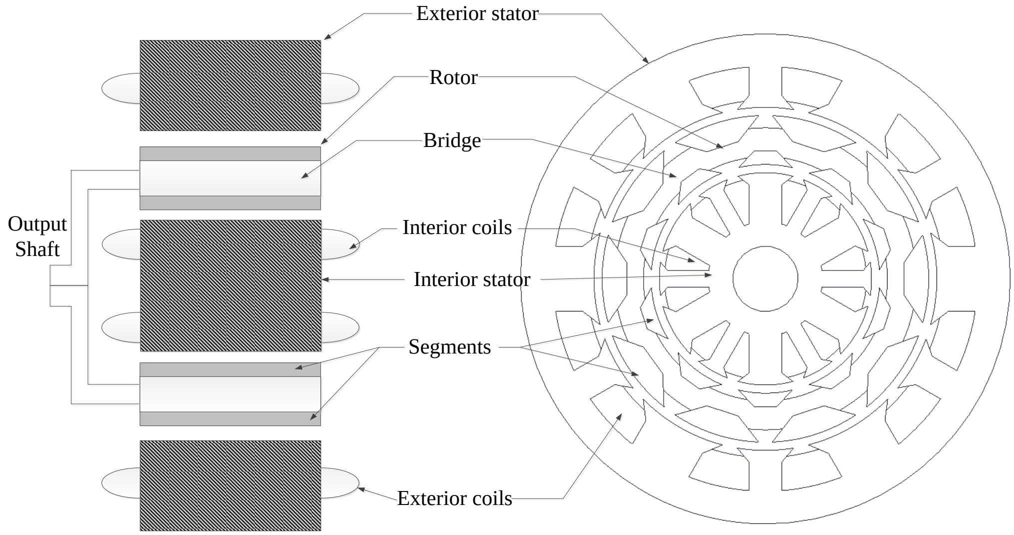

(a) Longitudinal section view (b) Cross section view

Figure 3.10 Double layer stator with single output

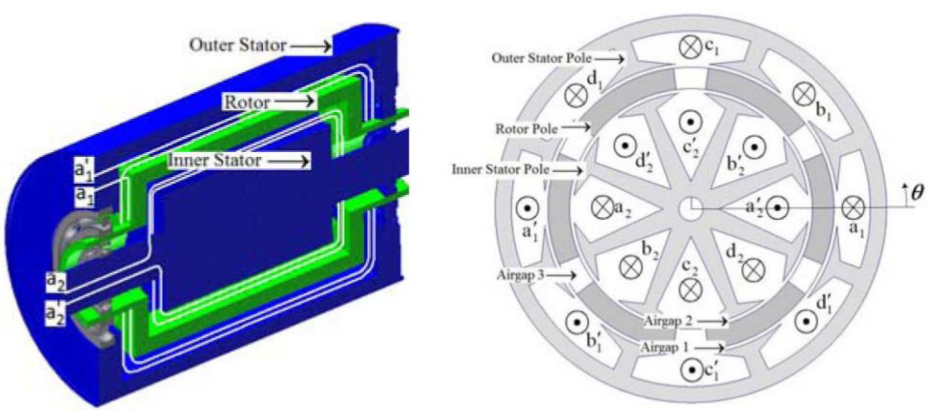

(a) Longitudinal section view (b) Cross section view

Figure 3.11 Double stator SRM [42]

3.1.9. Summary

In summary, a family of double segmented rotor SRMs have been proposed and discussed. SRMs with segmented rotor have a very compact structure, which are very suitable for double rotor machine configurations where space is often one of the biggest limitations. Of the 8 DSRSRM configurations discussed, the external stator and wound inner rotor configuration in section 3.1.1 and the wound central stator configuration in section 3.1.3 are the least complex and are suitable for automotive hybrid powertrain applications. The former can be used in an EVT (a hybrid powertrain without planetary gear sets). The latter can be incorporated into a power split type hybrid powertrain.

The attributes of the machine topologies discussed in sections 3.1.1 to 3.1.8 are presented in Table 3.1.

Table 3.1 Summary of attributes of DSRSRM topologies

	3.1.1	3.1.2	3.1.3	3.1.4	3.1.5	3.1.6	3.1.7	3.1.8
Slip rings	√	√	x	√	√	√	√	x
Shared stator	x	x	√	x	x	x	x	x
External surface cooling of coils	√	√	x	√	x	√	x	√
External diameter reduction	√√	√	√	√	√	√√	√	√
Coupled rotors	√	√	x	x	x	√	√	x
Exterior rotor mass	small	large	small	large	small	large	small	small
Interior rotor mass	large	small	small	small	large	small	large	small

The machine configuration discussed in section 3.1.3, i.e. having a wound central stator, segmented rotors, offers a very compact and simple structure. It has both windings on the stator, eliminating the need for slip-rings. Clearly, this topology has a single stator section and is therefore has the potential for stator yoke sharing. This feature reduces stator yoke thickness and improves machine compactness, hence this configuration is selected for prototyping and performance validation.

3.1.10. Benchmarking

One design motivation of the proposed DSRSRM is to improve the performance of existing double rotor SRMs. Yang [2] designed and manufactured the first double rotor SRM (DRSRM) prototype that can be integrated into an automotive electro-mechanical transmission system. Having a structure very similar to the proposed DSRSRM, the DRSRM design by Yang is selected for benchmarking.

To make a fair comparison, the following parameters of the DSRSRM are kept the same as Yang's DRSRM prototype, as presented in Table 3.2.

Table 3.2 Fixed design parameters for prototype implementation

Power supply voltage	300V
Number of phases – exterior machine	3
Number of phases – interior machine	3
Air gap length – exterior machine	0.3mm
Air gap length – interior machine	0.3mm
Interior machine air gap diameter	80mm
Interior machine stator tooth height	17mm
Stack length	50mm
Exterior machine power rating	500W
Interior machine power rating	500W
Stator yoke thickness	15mm

Note the DSRSRM has a shared stator yoke between exterior and interior machines. The thickness of the shared yoke is selected to be equal to the interior layer of stator (for the interior machine) in Yang's DRSRM. The DSRSRM design is also subject to the constraints detailed in Table 3.3. The DSRSRM should achieve same output at rated speeds with equal or higher efficiency, as summarised in Table 3.4.

Table 3.3 DSRSRM design constraints

Max flux density in the middle of stator teeth	1.8T
Overall length smaller than	160mm
Overall diameter smaller than	302mm
Peak phase current (exterior) smaller than	5A
Peak phase current (interior) smaller than	6A
Slot fill factor (exterior) not greater than	39%
Slot fill factor (interior) not greater than	35.5%
RMS Current density less than	$5A/mm^2$

Table 3.4 DSRSRM output requirement

Exterior machine			Interior machine		
Speed (RPM)	Torque (Nm)	Efficiency %	Speed (RPM)	Torque (Nm)	Efficiency %
500	8	82.0	2000	2	83.0
750	6.57	82.0	2400	1.81	84.2
837	5.57	77.5	3000	1.63	81.0
1000	3.57	78.0	4000	1.47	89.0

In this benchmarking study, both air gap diameter and stator tooth height are kept the same for the interior machine, which makes the case for a justified comparison. However, this is not done for the exterior machine because the stator yoke sharing feature introduced in the DSRSRM design significantly reduces machine overall size, hence affecting the air gap diameter of the exterior machine.

3.2. Design of the Double Segmented Rotor Switched Reluctance Machine

A wound central stator DSRSRM prototype is designed and manufactured for validation purposes. The basic structure of the machine is described in section 3.1.3. Recall that in this configuration, both exterior coils and interior coils are located on the outside and inside of the central stator, sandwiched by external and inner segmented rotors. The two rotors are independent in operation and are excited separately by associated phase coils. Essentially, the machine can be viewed as two SRMs integrated on the same stator. For simplicity, in the preceding discussion the exterior portion of the DSRSRM will be referred to as the "exterior machine" and the interior portion be referred to as the "interior machine".

3.2.1. Stator yoke flux path sharing

Stator yoke flux path sharing is utilized as a novel technique for reducing the overall size of the DSRSRM. The stator yoke (or stator back iron) is the annular portion of the stator connecting stator poles, both inner and outer, as illustrated in Figure 3.4 for clarity. In an SRM, the stator yoke not only provides structural support but also serves as conduits of magnetic flux. Similar to copper wires conducting current in an electric circuit, stator yoke conducts magnetic flux in the electric machine with minimum impact on total magnetic circuit reluctance. In all machine design, the stator yoke must be of a certain minimum thickness to avoid magnetic saturation and to reduce iron loss [46].

In a conventional SRM, the whole stator yoke conducts magnetic flux, as shown in Figure 3.12. The red lines represent magnetic flux. The solid dark lines designate major magnetic flux loops. The arrows designate magnetic flux directions. Current directions in the winding are represented using the cross (into the page) and dot (out of the page) symbols. It is seen that for conventional SRMs, flux lines occupy the complete stator yoke when a phase is excited. Another observation is that when excitation changes from phase to phase, magnetic flux direction reverses at some locations on the stator yoke. Such regions are outlined in dotted lines.

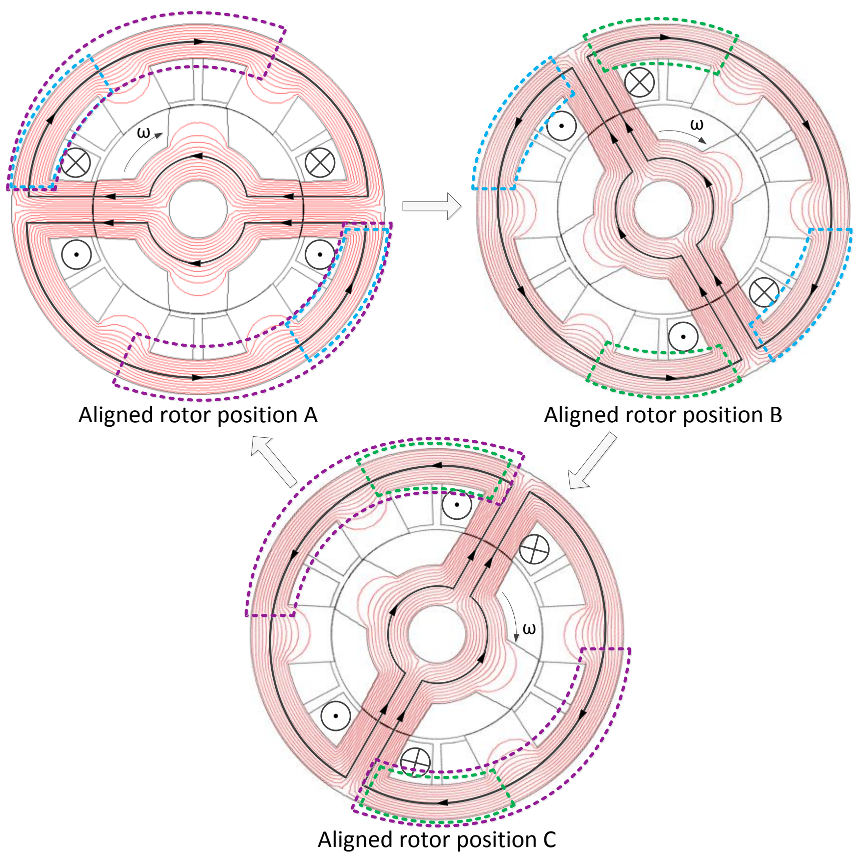

Figure 3.12 Diagrams of magnetic flux at aligned rotor positions of a 6/4 SRM

The above characteristics require a conventional double rotor central stator SRM to have separate stator yoke regions to accommodate magnetic flux of both exterior and interior machines. In other words, it is not possible to achieve stator flux path sharing in a conventional DRSRM. Moreover, as shown by Yang [2], considerable amount of flux coupling between the exterior and interior exists in a conventionally structured DRSRM. Yang suggested the use of a flux barrier (a 2mm thick air gap separating the stator yoke) to reduce the coupling effect between the two machines, as shown in Figure 3.13. It should be noted that even though the flux barrier effectively controls flux coupling, it also increases total stator yoke thickness, reducing available winding area. The added air gap weakens the mechanical rigidity of the stator, which may lead to increased vibration and noise, or even mechanical failure.

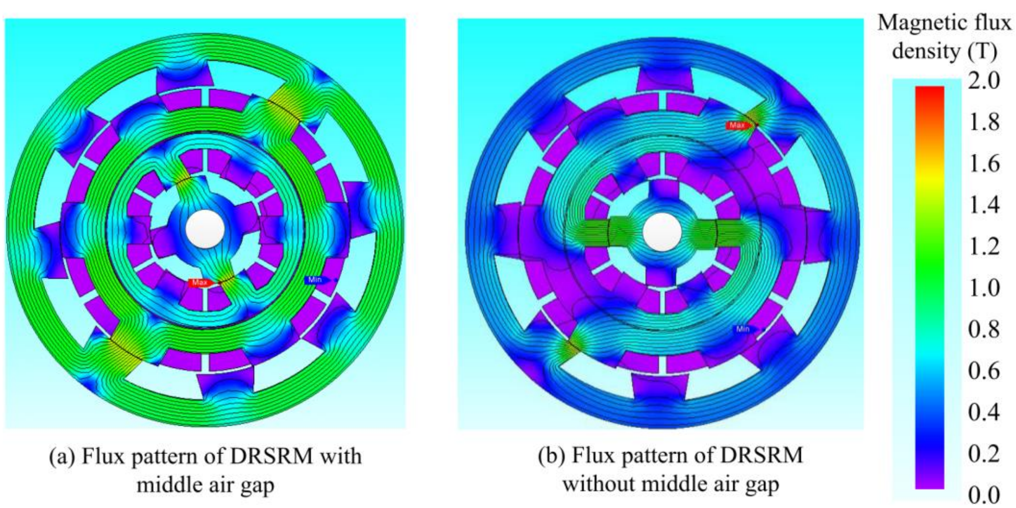

Figure 3.13 DRSRM flux coupling reduction using air gap in stator[2]

In comparison, the segmented rotor SRM has a very different stator yoke flux pattern. Figure 3.14 shows magnetic flux diagrams at different aligned rotor positions of a

12/10 segmented rotor SRM. The red lines represent magnetic flux. The solid dark lines designate major magnetic flux loops. The arrows designate magnetic flux directions. Current directions in the winding are represented using the cross (into the page) and dot (out of the page) symbols. Different from conventional SRMs, segmented rotor SRMs have short flux loops. Two unique flux pattern characteristics can be observed: (a) each time a phase is turned on, only one third of the stator yoke conducts magnetic flux; (b) magnetic flux directions in the stator yoke never change.

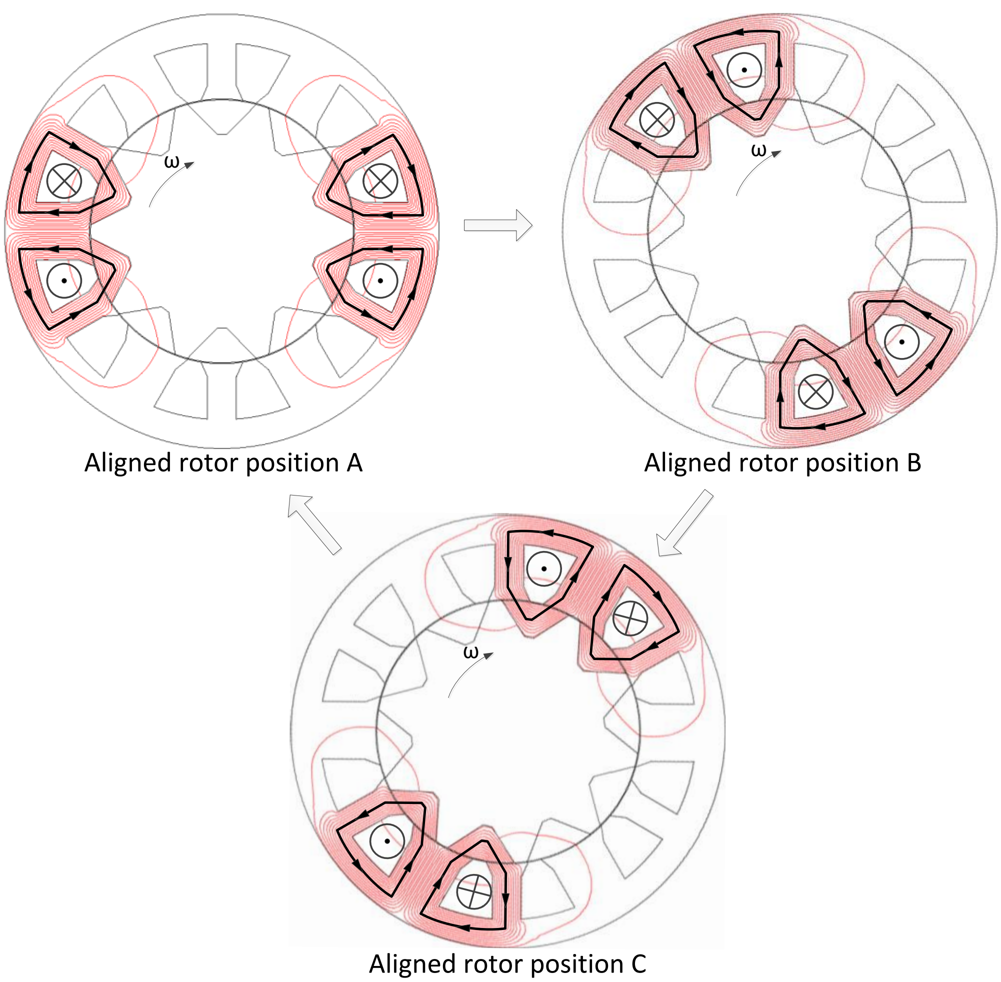

Figure 3.14 Diagrams of magnetic flux at aligned rotor positions of a 12/10 segmented rotor SRM

By exploiting the unique flux pattern of segmented rotor SRMs, it is possible to design the DSRSRM to have shared stator yoke for magnetic flux conduction of both the exterior and interior machines. Because only 1/3 of stator yoke conducts flux when a phase is excited in a segmented rotor SRM, phase excitations can be manipulated such that the exterior and interior machines use different portions of the stator yoke, hence sharing the yoke. Figure 3.15 (a) shows magnetic flux diagram of a DSRSRM with both exterior and interior phase excited and sharing the stator yoke. In comparison, flux diagram of a conventional DRSRM is shown in Figure 3.15 (b). For simplicity, here the example uses equivalent linear models, which can be interpreted as the circular rotors and stator being rolled out flat and the rotors traversing instead of rotating. The red lines represent magnetic flux and the arrows designate flux directions. Current directions in the winding are represented using the cross (into the page) and dot (out of the page) symbols.

Comparing the two topologies, it is seen that stator yoke thickness can be reduced by more than half in a segmented rotor design due to stator flux path sharing and elimination of flux barrier. Moreover, FEA analysis has shown that the shared stator yoke configuration will not increase flux density. To see the difference in magnetic flux pattern and flux density, three cases were modelled, one for DSRSRM with both exterior and interior windings excited, one for an isolated exterior machine and one for an isolated interior machine. Figure 3.16 and Figure 3.17 compare magnetic flux density contours of the DSRSRM to isolated interior and exterior machines with same geometry and current excitation. The flux contours are almost identical, which suggests stator yoke flux path sharing should have negligible impact on machine operation (this will be proved in subsequent analysis on magnetic coupling between the exterior and interior machines).

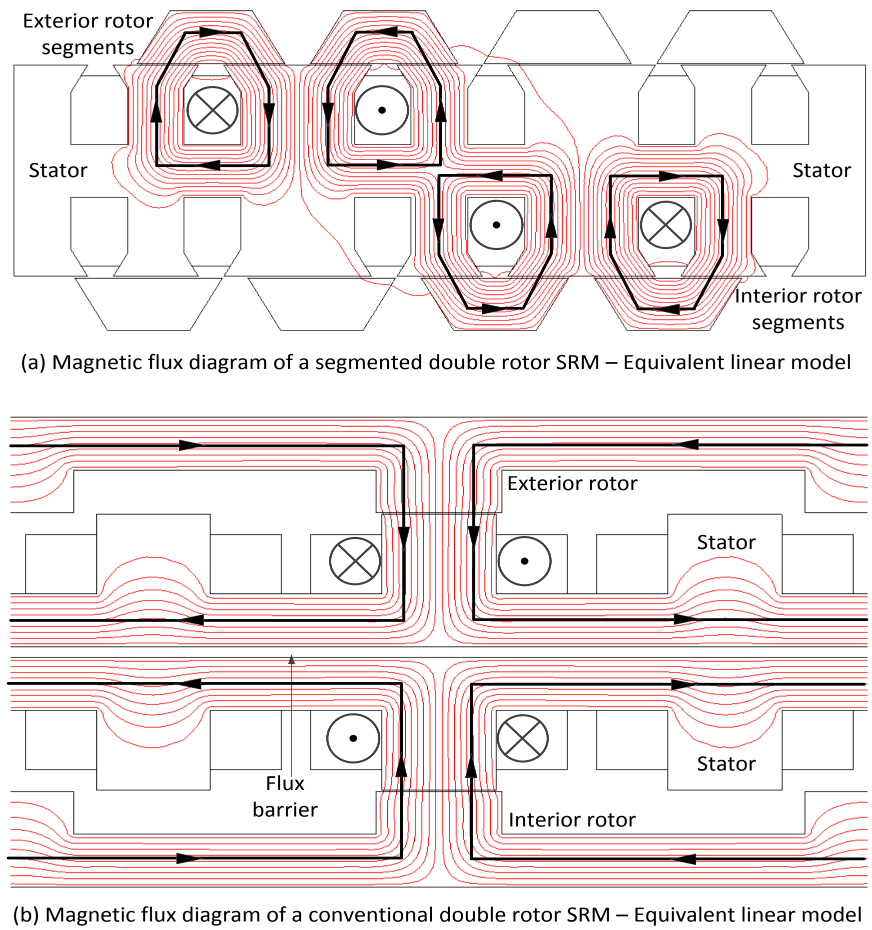

Figure 3.15 Magnetic flux diagrams of equivalent linear models of different double rotor SRMs

Note the biggest flux pattern difference is observed at the junction where exterior flux loops meet with interior flux loops, forming a low flux density region. This is due to the fact that magnetic fluxes of the two machines are in opposite directions at the junction. If the coil winding polarity is switched for either the interior or the exterior machine, the fluxes will have same direction at the junction, resulting in higher flux density. The opposite flux direction configuration is purposely implemented here to avoid magnetic saturation and iron loss increase at the junction.

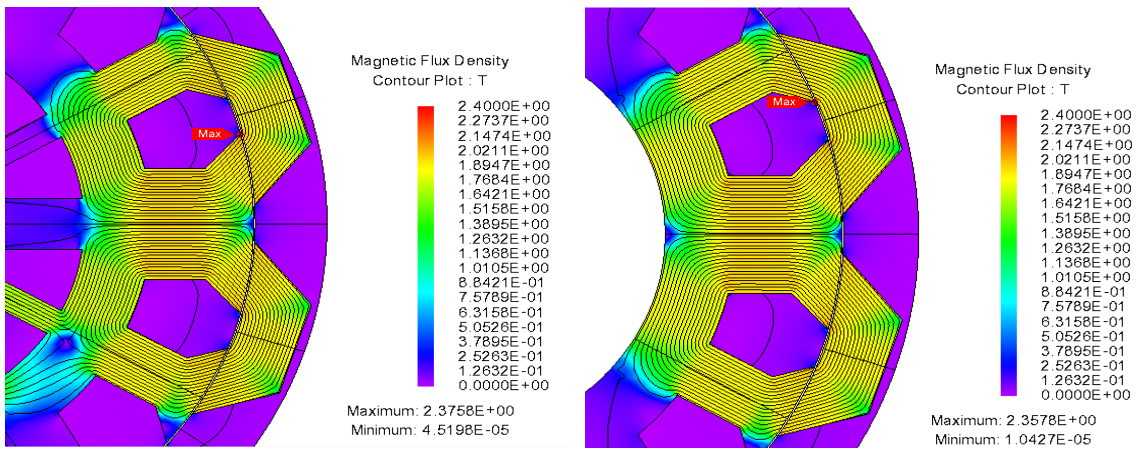

(a) Magnetic flux density contour plot (DSRSRM) (b) Magnetic flux density contour plot (exterior machine only)

Figure 3.16 Magnetic flux density comparison between exterior machine only and DSRSRM

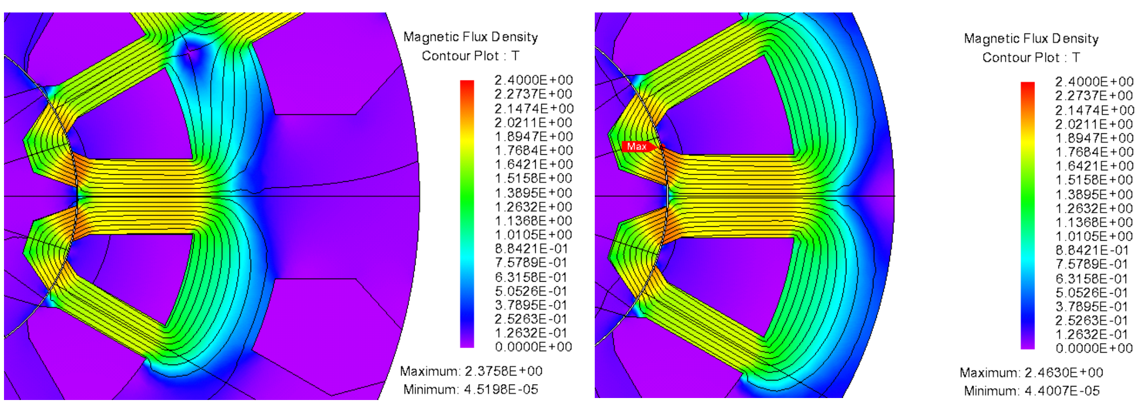

(a) Magnetic flux density contour plot (DSRSRM) (b) Magnetic flux density contour plot (interior machine only)

Figure 3.17 Magnetic flux density comparison between interior machine only and DSRSRM

It should be noted that the above stator sharing scheme only allows two adjacent phases, for example interior phase A and exterior phase B or phase C (but not exterior phase A), to be excited at the same time, which only works when two rotors rotate at same speed. To have independent rotor outputs, unavoidably there will be moments when same phases are excited on both exterior and interior machines, requiring the excited portion of stator yoke to carry both interior and exterior machine fluxes at the same time. Again, the winding polarity can be designed such that magnetic flux directions in the stator yoke are opposite between exterior and interior machine, making flux density in the yoke lower than a single rotor machine, as shown in Figure 3.18 (compares the exterior) and Figure 3.19 (compares the interior).

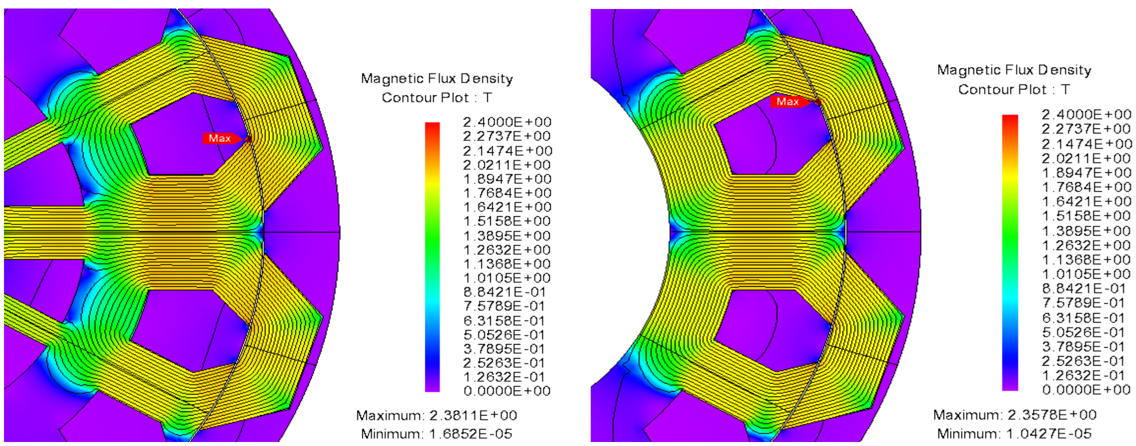

(a) Magnetic flux density contour plot (DSRSRM) (b) Magnetic flux density contour plot (exterior machine only)

Figure 3.18 Magnetic flux density comparison between exterior machine only and DSRSRM

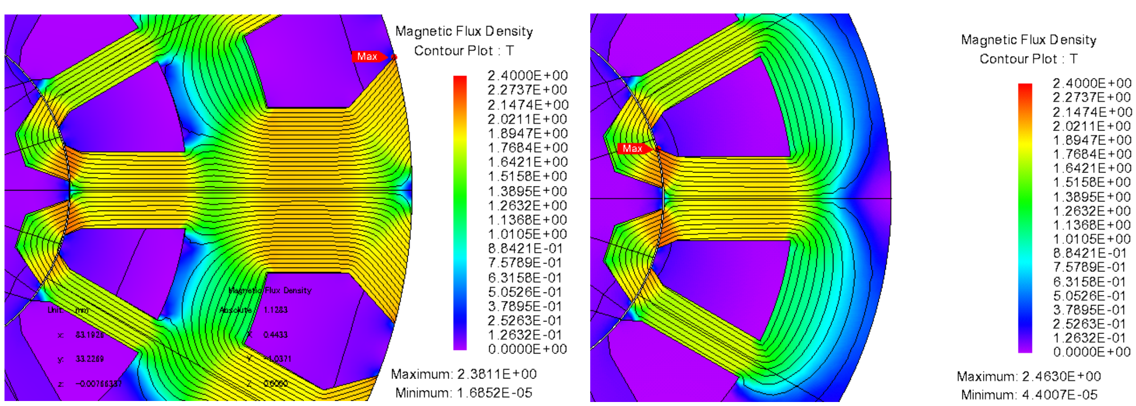

(a) Magnetic flux density contour plot (DSRSRM) (b) Magnetic flux density contour plot (interior machine only)

Figure 3.19 Magnetic flux density comparison between interior machine only and DSRSRM

The FEA simulation results show that apart from the stator yoke, flux density and pattern remain largely the same on other parts of the machine. This stator sharing scheme also has negligible impact on machine operation, as will be shown later in the coupling analysis of DSRSRM.

To implement the above mentioned two stator yoke sharing schemes, the stator coil winding directions can be designed in the arrangement shown in Figure 3.20. The diagram shows the cross section of a DSRSRM, where stator and rotor iron is in blue and windings are colored in orange. The arrows denote phase current directions. Two rules should be followed when determining the winding polarity. First, the interior machine winding polarity should be identical to the exterior, so that when same phase is excited, fluxes in the stator yoke are in opposite directions. Second, at the junctions of adjacent exterior and interior phases, winding polarity should also be same to have opposite fluxes.

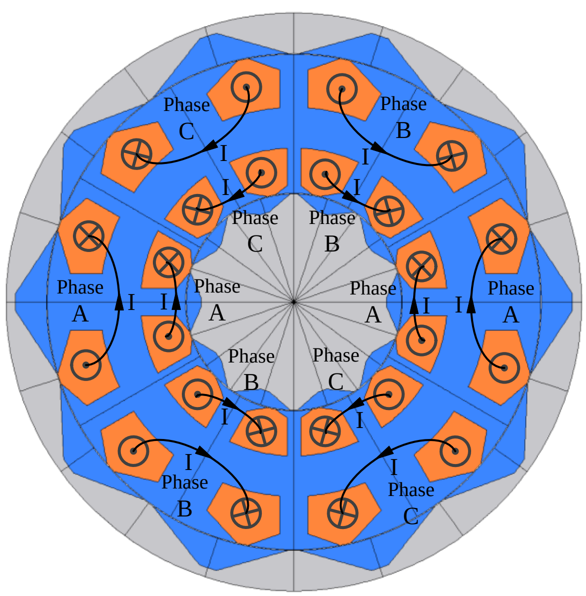

Figure 3.20 Winding diagram of DSRSRM

3.2.2. Magnetic Coupling Effect Analysis

Limiting magnetic coupling between the two machines is of great importance in the design of DSRSRM because either machine is required to deliver an independent output. It has been observed in previous section that stator yoke flux path sharing causes small but noticeable changes on magnetic flux patterns of the exterior and interior machines. To gain a quantitative measure of the impact of magnetic coupling on machine magnetic characteristic, static torque and phase inductance of the proposed DSRSRM are studied using FEA. The results are compared to isolated exterior and interior machines (see Figure 3.21) with same dimension and excitation.

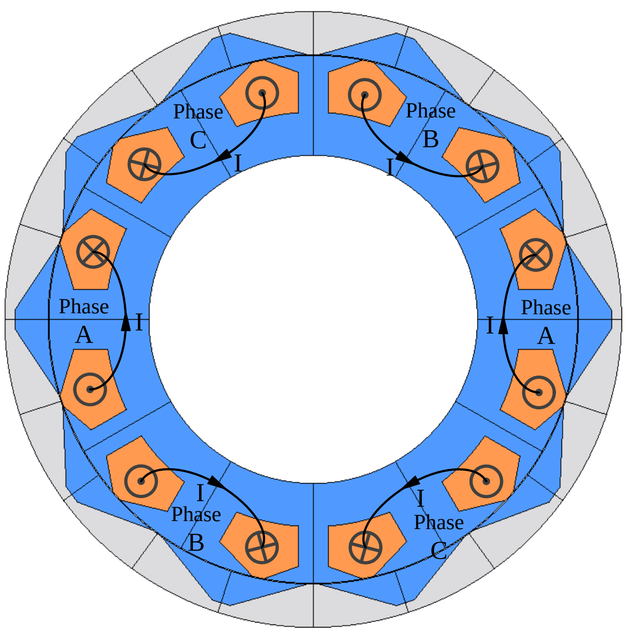

(a) Isolated exterior machine

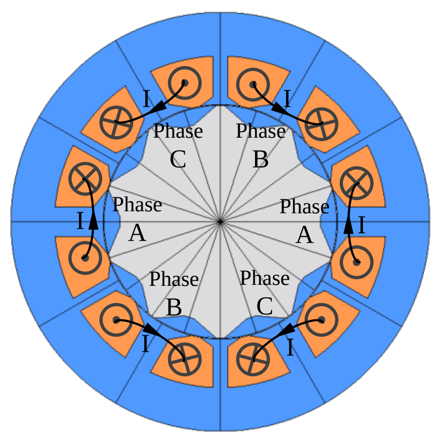

(b) Isolated interior machine

Figure 3.21 Cross sectional diagrams of isolated exterior and interior machines

As discussed previously, two excitation conditions exist in the proposed DSRSRM: adjacent phases excited (e.g. exterior phase A and interior phase B) and same phases excited (e.g. exterior phase A and interior phase A). Either excitation condition is studied separately with static torque and phase inductance of both exterior and interior machines calculated at all rotor positions. The results are compared to isolated cases and the differences are plotted in Figure 3.22-Figure 3.25. To cover the full range of rotor position combinations, both the exterior and interior rotor positions are varied from 0 to 36 mechanical degrees with 1 degree interval in the analysis. Note 0 degree corresponds to the start of an unaligned position and 36 degree corresponds to the next unaligned position. At 18 degree, the rotor is at aligned position. The FEA calculations are conducted under constant excitation current that is similar to rated machine operation level.

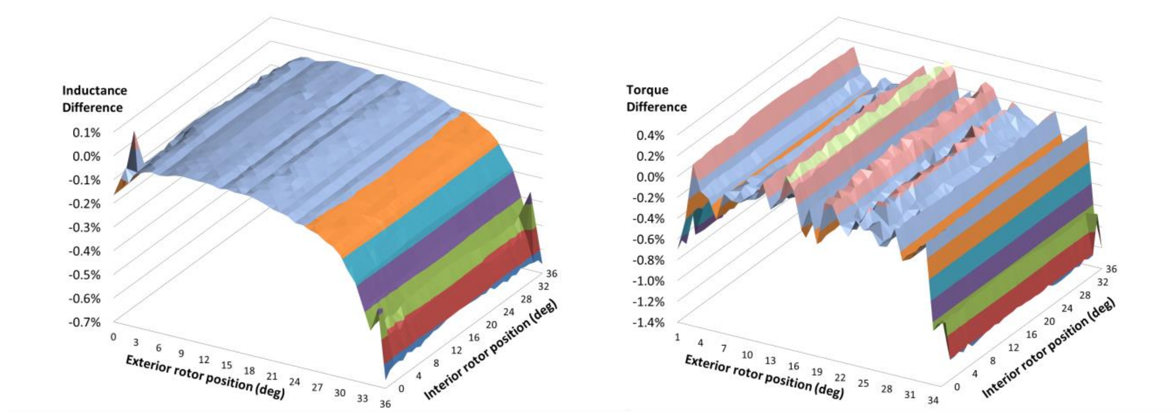

(a) Exterior machine inductance comparison

(b) Exterior machine static torque comparison

Figure 3.22 Coupling effect on exterior machine characteristics (adjacent phases excited)

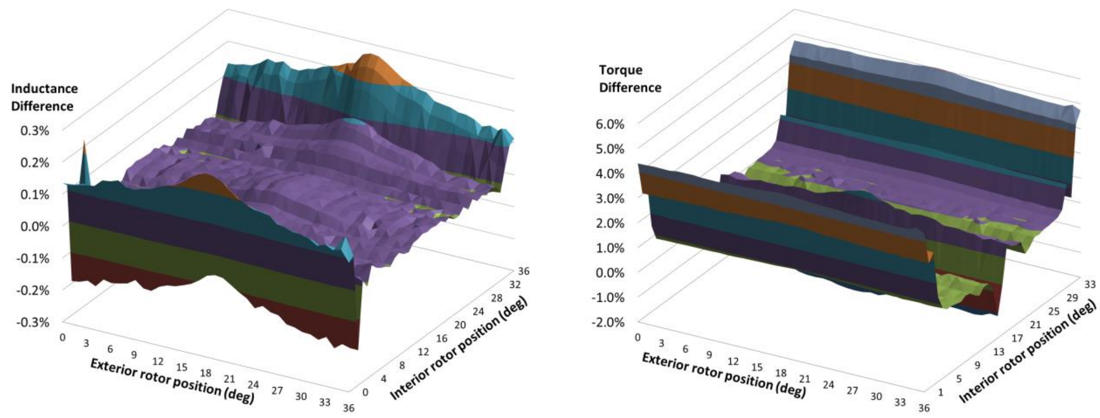

(a) Interior machine inductance comparison

(b) Interior machine static torque comparison

Figure 3.23 Coupling effect on interior machine characteristics (adjacent phases excited)

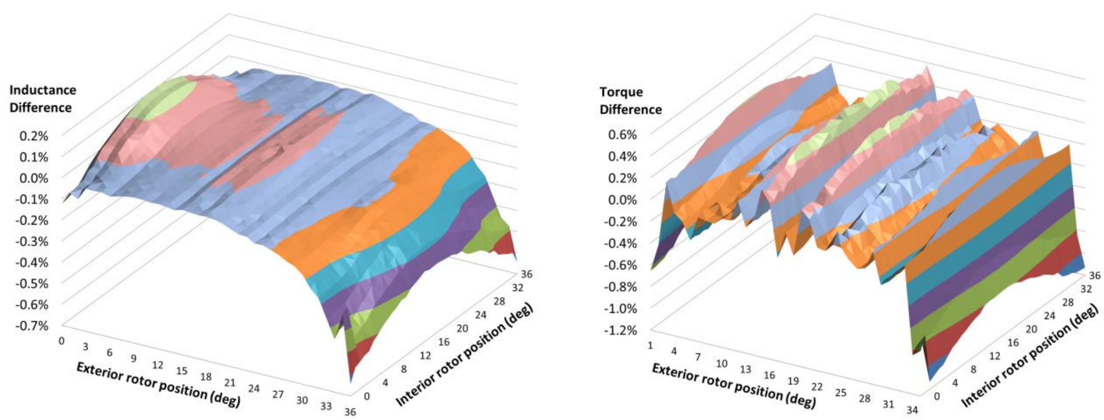

(a) Exterior machine inductance comparison

(b) Exterior machine static torque comparison

Figure 3.24 Coupling effect on exterior machine characteristics (same phases excited)

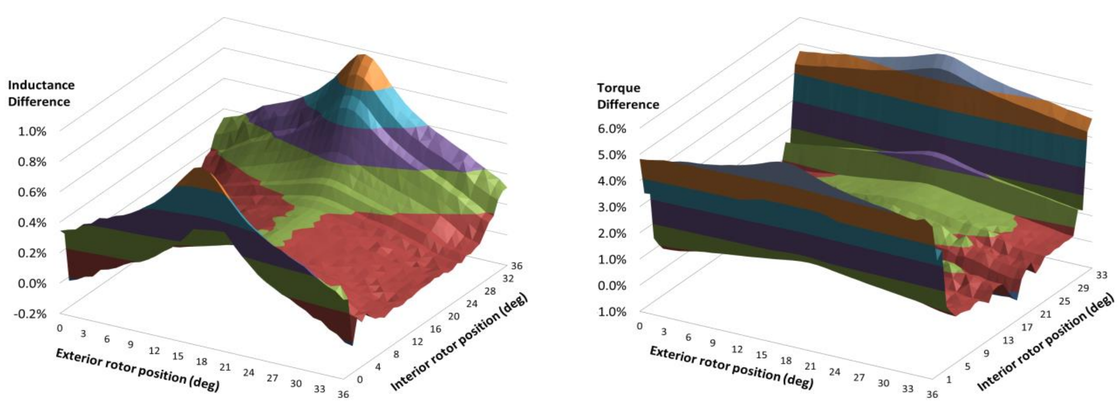

(a) Interior machine inductance comparison

(b) Interior machine static torque comparison

Figure 3.25 Coupling effect on interior machine characteristics (same phases excited)

Summarizing the above plots, the differences in static torque and phase inductance are fairly small for both exterior and interior machines, regardless of the excitation condition. For both machines, the difference in phase inductance is within 1% and the torque difference within 5%. In fact, torque difference is within 1% for most rotor positions. Bigger difference is only observed near unaligned positions where torque is low and more strongly affected by calculation error. Because the change of flux pattern is small, it is difficult to relate the observed pattern of difference variation to rotor position changes. However, generally it is observed that variation of difference is smaller along the rotor position axis of the other machine (the color coded difference bands are uniform along these axes in the diagrams). In other words, machine magnetic characteristic is almost invariant to changes of rotor position of the other machine. This indicates that coupling between the two machines is negligible in the DSRSRM. Because the differences between isolated models and the DSRSRM are so small, the isolated models can be relied on for reasonable accurate estimation of machine performance. The isolated models are used frequently to simplify machine design optimization.

3.3. Modelling and Simulation

In Chapter 2 we have shown that modelling of SRM is difficult due to the non-linearity in its magnetic characteristics. Moreover, the machine characteristics are strongly affected by geometry, which further complicates the problem. Even though researchers have developed a number of analytical models that achieve reasonable estimation accuracy[71]-[74], the models are based on assumed magnetic flux distribution of conventional SRMs, and thus cannot be applied to segmented rotor SRMs. Models based on Finite Element Analysis (FEA), on the other hand, are good at handling geometry differences and give solutions with satisfactory accuracy. The FEA technique is used throughout the design process of the DSRSRM for parameter tuning and performance evaluation.

FEA technique provides acceptable results but is computationally intensive. To save time and computation effort, model simplifications are usually applied. For example, a 2D cross section model is often used instead of a 3D model, which can significantly reduce mesh number and improve calculation convergence. For electric machines with large length to diameter ratio, end effect is usually small and so is the difference between 2D and 3D analysis. In the design of the DSRSRM, 2D analysis is used predominantly in the determination of most design parameters, while 3D analysis is used for verification of the final design. In section 3.2.1 it is shown that magnetic flux coupling between the exterior and interior machines is negligible. Therefore, the two machines are designed separately with isolated models (refer to Figure 3.21). Moreover, a simplified machine geometry that omits features that insignificantly affect machine performance (e.g. mounting holes, shaft, rotor segment dovetails) is used in the preliminary design phase to reduce model complexity.

3.3.1. FEA modelling of the electromagnetics

The commercial electromagnetic simulation software JMAG[75] is used throughout the study for both 2D and 3D finite element electromagnetic analysis. The section below covers major settings and simulation parameters of the FEA model.

Geometry and Material

Three 2D models are used extensively in the design process,

(a) isolated exterior machine, Figure 3.26(a)

(b) isolated interior machine, Figure 3.26(b)

(c) DSRSRM, Figure 3.26(c)

Because the machine geometry is 180° rotational symmetric with itself, half models are used to reduce calculation time. Taking into account of winding polarities, 180° anti-periodic boundary condition is applied on the symmetric plane.

In the models, the blue region designates rotor and stator iron core, which is made of laminated soft magnetic steel. The yellow region designates copper coil windings. The grey region designates non-magnetic material that serves as structural support. The iron core laminations are manufactured with AK M15 Gauge29 silicon steel. The JMAG software library does not contain specification of the M15 silicon steel. Instead, equivalent electrical steel, 35JN300, having very similar characteristic and produced by JFE Steel Corp. is used in all the simulations. The material magnetic property is validated in Chapter 5, section 5.1.3. A 95% stacking factor is set for all the steel laminations.

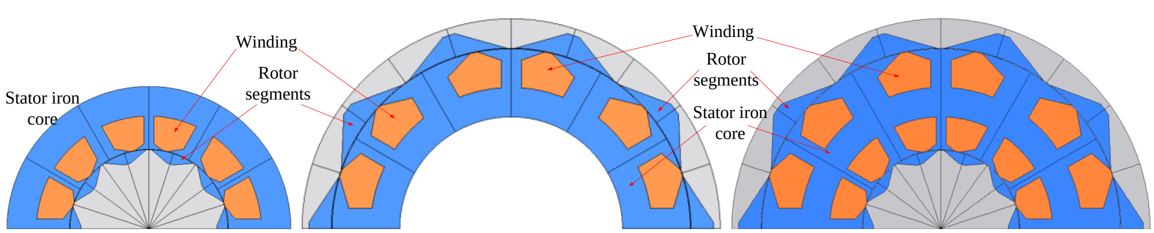

(a) interior machine model (b) exterior machine model (c) DSRSRM model

Figure 3.26 2D FEA model geometry

Finite element mesh

FEA meshes in JMAG are generated in a semi-automatic manner where the user defines regions and sets meshing constraints and the software creates and optimizes final meshing. For rotating machinery, a sliding mesh is often created on the air gap between rotor and stator. The sliding mesh consists of several thin layers of quadrilateral meshes that are able to rotate against each other when rotor and stator relative position changes. The sliding mesh allows other mesh to stay unchanged when rotor position changes, avoiding re-meshing of the whole model between time steps, which significantly reduces calculation time.

Figure 3.27 shows the meshing diagram of the DSRSRM model. Both air gap regions have 4 layers of sliding mesh. Because the air gap magnetic characteristics have the biggest impact on machine performance, mesh density is highest in these regions to ensure model accuracy. An element size constraint of 0.5mm is applied to the edges of the air gap regions. To keep a reasonable mesh aspect ratio, the interior air gap sliding mesh is divided into 1440 circumferential divisions and the exterior air gap into 3360 divisions. The iron cores conduct majority of magnetic flux and are therefore critical in the calculation. A 2mm element size constraint is applied to the steel lamination regions. Outside the machine model, there is an air boundary that defines the boundary of the FEA model. This boundary is 30% of the machine external diameter and has zero magnetic vector potential on the outside surface. This air region is to ensure that the model solves correctly for any leakage flux from the machine, which should be negligible to zero. A 5mm element size constraint is applied to the air boundary region.

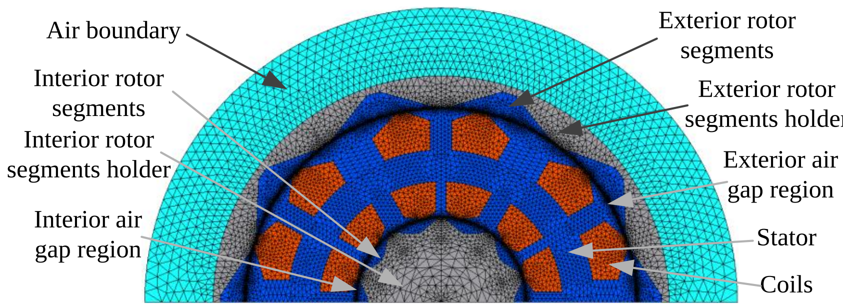

Figure 3.27 Meshing diagram of DSRSRM

The above meshing control parameters are determined based on a mesh sensitivity analysis. Figure 3.28 shows the result of a sensitivity study on the isolated exterior machine. Phase inductance at various rotor positions of a fine mesh model and a coarse mesh model are compared to the selected mesh model. The mesh size characteristics are summarized in Table 3.5. The comparison shows that a finer mesh will not noticeably improve solution convergence and a coarser mesh introduces considerable amount of error near unaligned positions.

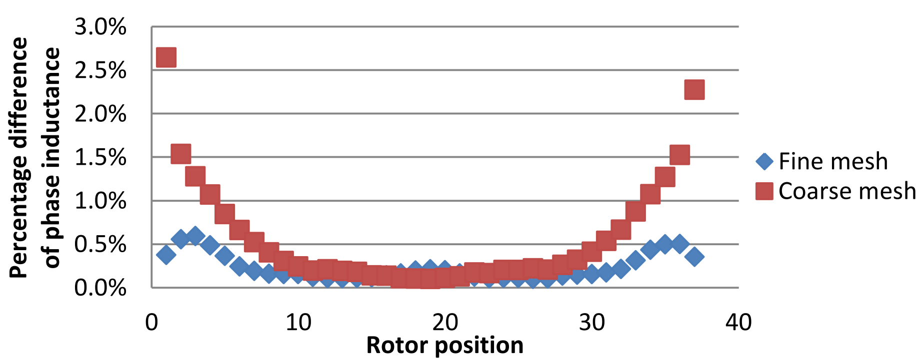

Figure 3.28 Comparison of calculated phase inductance of models with different mesh sizes

Table 3.5 Mesh size characteristics of different models

	Selected	Fine	Coarse
Number of elements	28154	51332	11783
Number of nodes	17545	29404	7229

Circuit and excitation

Two circuit models are used in the analysis,

i. constant current excitation model

ii. asymmetric bridge converter model

The former model, see Figure 3.29, simlifies the analysis by omiting circuit dynamics and assuming a constant excitation current. This model is helpful in calculating static torque and magnetic inductance, which can be used to form a look-up table for a motor drive simulation (details will be illustrated in section 3.3.3).

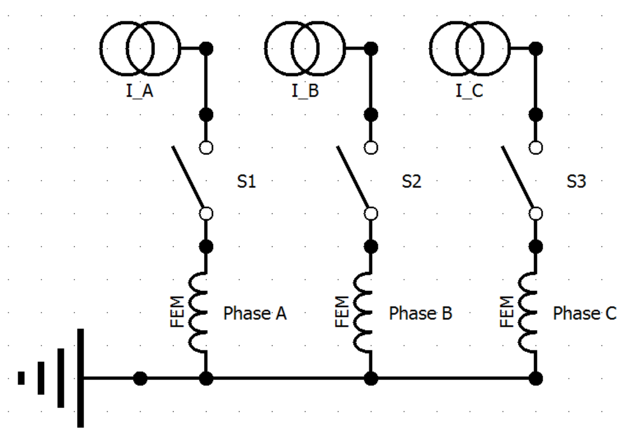

Figure 3.29 Constant current excitation circuit model

The asymmetric bridge circuit model, see Figure 3.30, gives a more realistic simulation of machine operation. Supply voltage (300V as in the design specification) is fixed in the model and phase current is calculated at each time step by performing a circuit analysis. On each phase, there is a pair of current limit switches that constraints peak current. The other pair of switches controls the excitation angle and duration. Being able to simulate phase current waveform, this model gives much more accurate estimate of instantaneous torque. However, to get reasonably accurate simulation of circuit dynamics, a small time step is required which results in large number of steps and makes the model very computationally demanding. For this reason, the asymmetric bridge circuit model is only used for design verification and calculation of final design iron loss.

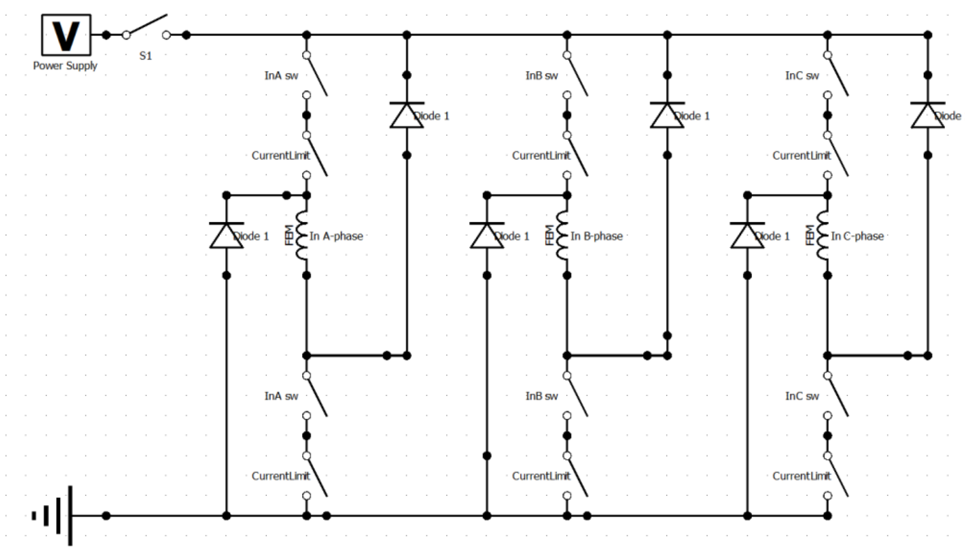

Figure 3.30 Asymmetric bridge converter circuit model

The above circuit models are for single machines only, therefore only having three phases. To simulate a DSRSRM operation, three more phases are added to enable control of both machines.

3-dimentional (3-D) model

2-dimensional (2D) analysis gives fast solutions, which is good for comparing alternatives in the design process. However, 2D simplification fails to capture 3D effects such as end winding flux leakage and fringing effect. A 3D model shown in Figure 3.31 is created for design verification purposes. Because the DSRSRM is symmetrical about its central plane in both the radial and longitudinal directions, a 1/4 model is sufficient to represent the whole machine. 3D mesh is generated by extruding 2D mesh in the axial direction. The end winding geometry is also simplified to uniform cross section bars to ease mesh generation in the axial direction. Note the air boundary mesh surrounding the machine model is not shown in the figure to allow better illustration of the machine mesh model.

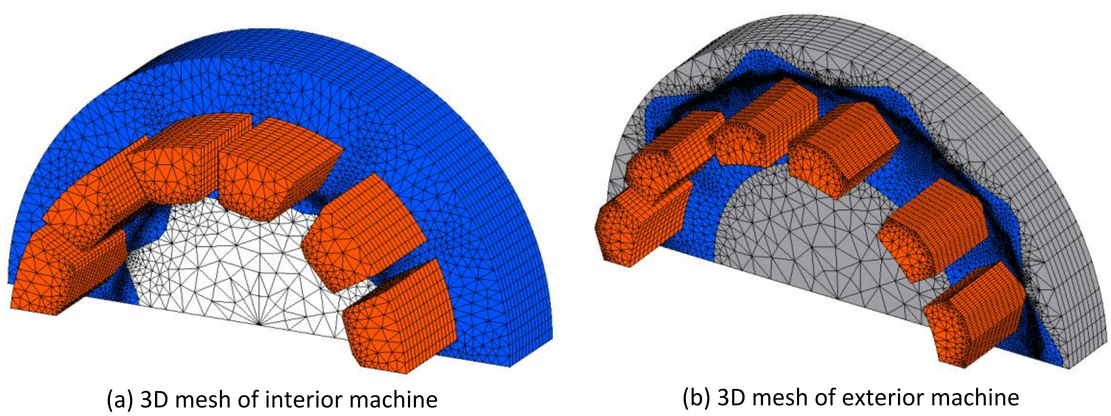

Figure 3.31 3D mesh models of interior and exterior machine

3.3.2. Losses

Apart from mechanical losses such as windage and friction, two major losses associated with electric machine operation are copper loss and iron loss. The analysis methods of the two losses are presented below.

Copper loss results from resistance heating of the copper coil windings when conducting electrical current. According to ohm's law, the instantaneous copper loss of a phase coil is:

$$P_{\text{copper,ph}} = {I_{rms}}^2 R_{ph} \tag{3.1}$$

where I is the phase root-mean-square (RMS) current and R is phase electrical resistance. Note an equivalent AC resistance should be used due to the pulsation of the excitation current. A factor of 1.05 is applied to the DC resistance to get the AC resistance [76]. The total machine copper loss is then (3.1) multiplied by the number of phases.

In the preliminary design stage, both phase current waveform and phase electrical resistance are difficult to determine. The following simplifications are applied to enable the estimation of copper loss. Assuming the current waveforms are rectangular and each phase is turned on for 1/3 of the time (for a three phase machine), the RMS current of each phase is then 1/√3 of peak current I_{pk}.

$$P_{copper} = 3I^2R = 3\left(\frac{1}{\sqrt{3}}I_{pk}\right)^2 R = {I_{pk}}^2 R \tag{3.2}$$

Let phase turn number be N and phase magnetomotive force be $\mathcal{F}$, then

$$I_{pk} = \frac{\mathcal{F}}{N} \tag{3.3}$$

According to electrical resistance formula of conductors

$$R = \rho \frac{\mathrm{L}}{A} \tag{3.4}$$

where ρ is resistivity (0.0168μΩm for copper), L is conductor length and A is conductor cross sectional area.

For the phase coils, L equals number of turns multiplying average turn length L_{turn} and A equals total available copper area, which is the product of slot area A_{slot} and slot fill factor SF, divided by number of turns.

Combining the above relationships, equation 3.2 becomes

$$P_{copper} = (\frac{\mathcal{F}}{N})^2 \rho \frac{NL_{turn}}{\frac{A_{slot}SF}{N}} = \frac{\rho}{SF} \frac{\mathcal{F}^2 L_{turn}}{A_{slot}} \tag{3.5}$$

The average per turn coil length is estimated as

$$L_{turn} = 2[(1 + 2 \times 10\%)W + L_{stk}] \tag{3.6}$$

where W is the distance between the geometric center of two slots of a phase, approximating the width of a coil turn, and L_{stk} is machine stack length, which is 50mm. An additional 10% of width is added on both sides of a stator pole to compensate length increase due to end winding.

Iron loss

Iron loss, or core loss, consists of eddy current loss and hysteresis loss. It is induced by changing magnetic field in the laminated iron core. Unlike copper loss, estimation of iron loss is not as straight forward because it depends on flux density changes along various flux paths and the frequency of the changes. The JMAG software contains an iron loss analysis package. To validate the iron loss solver, an analysis based on the method of reference [77] is conducted on an interior segmented rotor SRM. The results are compared to the JMAG solution.

Based on the magnetic flux pattern, the segmented rotor SRM iron core is divided into the following four sections: stator yoke, stator pole teeth, stator inter-pole teeth and rotor segment. Within each section, flux waveform is assumed to be uniform. Figure 3.32 shows the calculated flux waveforms of the four sections for one complete rotor rotation.

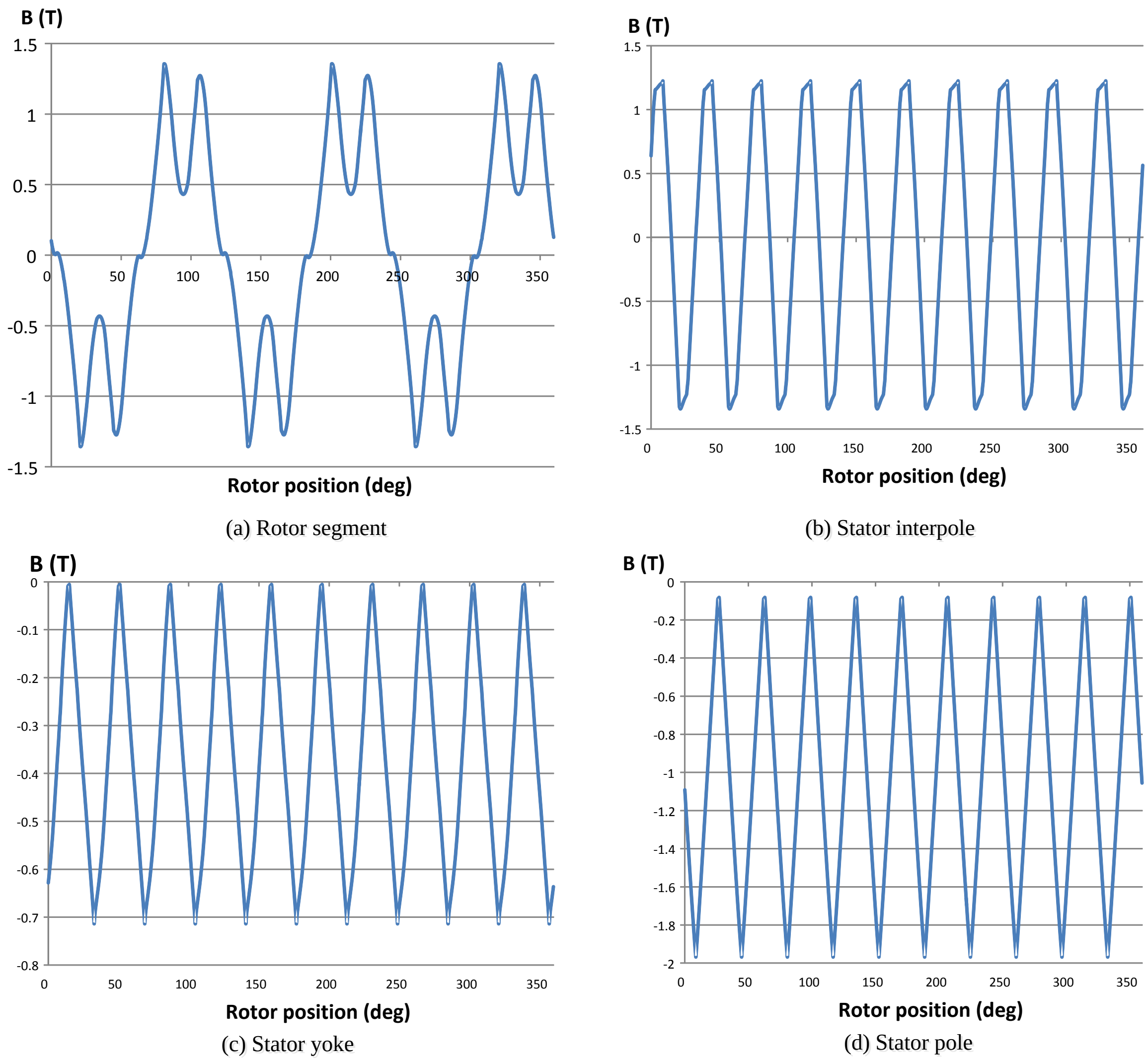

Figure 3.32 Flux waveforms of different sections in a segmented rotor SRM

Same loss model, see equation 3.7, as in [2] is used for the current analysis because the lamination material is the same. In the loss equation, P is in loss per volume, B is magnetic flux density and f is frequency of magnetic flux change.

$$P = log^{-1}[1.9\log(B) + 0.64\ln(f) + 1.37] \tag{3.7}$$

Note the loss equation assumes sinusoidal excitation, which is hardly the case as shown in the flux waveforms. To be able to apply the iron loss equation, the flux waveforms can be decomposed into different orders of harmonics using Fourier transformation. Then for each harmonic, the iron loss

$$P_n = log^{-1}[1.9\log(B_n) + 0.64\ln(f_n) + 1.37] \tag{3.8}$$

The total loss is the summation of losses of all harmonic orders

$$P_{total} = \sum_{n=1}^{\infty} P_n(B_n\,, f_n) \tag{3.9}$$

Figure 3.33 compares iron loss estimation between the JMAG solver and the current study. Generally, good correspondence is observed. Significant iron losses almost always appear at the same harmonics. Total stator iron loss estimation difference is about 3% between the two analyses. Note the JMAG solver gives higher rotor iron loss than the validation study at all harmonics. In the validation study, flux is assumed uniform along each section to simplify the calculation. This assumption is true for the stator sections where flux density variation is relatively small. The rotor segments, on the other hand, have considerably higher flux density variation. The simplified calculation overlooked high flux density areas on the segments and results in underestimated iron loss for the rotor segments. The comparison study shows that the JMAG iron loss solver gives satisfactory loss estimation. The solver is used throughout the thesis for iron loss calculations.

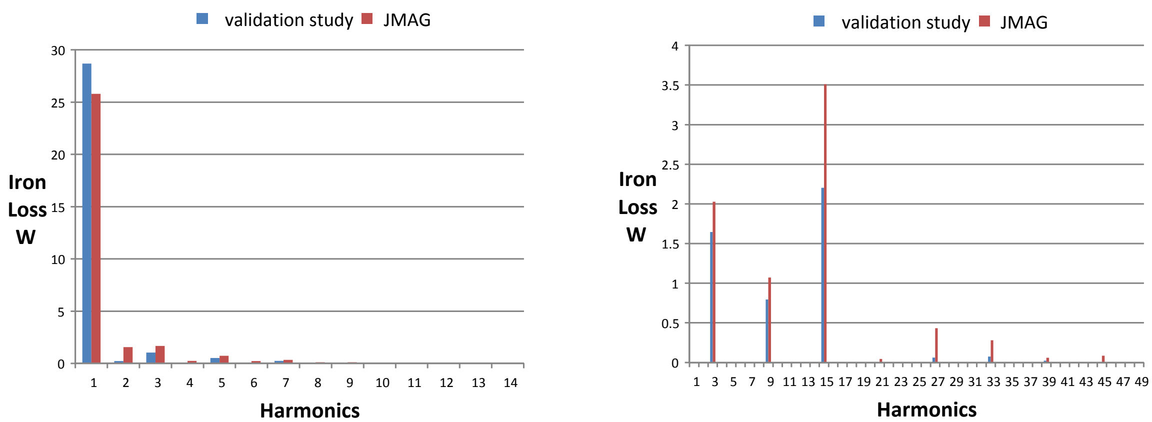

(a) Stator iron loss estimation comparison

(b) Rotor iron loss estimation comparison

Figure 3.33 Comparison of iron loss estimation

3.3.3. Drive simulation

Electromagnetic FEA is capable of providing high fidelity field solutions of electric machines. Combined with a sophisticated electric circuit model (for example, the asymmetric bridge circuit model in section 3.3.1), FEA can even output transient analysis solutions that take into account of control and drive dynamics. However, the computational effort involved in such analysis is substantial. This is contrary to the requirement of machine drive analysis, where fast solutions are necessary for solving the tremendous volume of simulation cases and conditions.

One way to significantly reduce calculation time is to generate a numeric model of the machine and have all drive analysis based on the numeric model, thus eliminating the need for FEA calculation in each simulation. Often, the numeric model can be developed by conducting FEA and creating a machine characteristic look-up table. For SRMs, important machine characteristics are torque and flux linkage. They are both functions of rotor position and current. To generate a look-up table, torque and flux linkage are calculated using FEA at various positions and current levels covering the whole range of machine operation. The results are interpolated for positions and current levels that differ from the pre-defined points.

Because the numeric models calculate very fast, they are sometimes called "real time" models for being able to realize real time control. The JMAG software contains a real time model generator module "JMAG-RT", which automates the numeric model generating process. The RT module is used to generate numeric models for drive simulations in this study. Again, the exterior and interior machines are individually studied and modelled because coupling is proved to be negligible (see 3.2.1). Effects of mutual inductance are neglected in the model and torque and flux linkage calculation is for single phase excitation. To reduce interpolation error, a fine step change is selected for model generation (0.5 mechanical degree for position and 0.25A for current). The FEA calculations are based on same mesh and material settings as described in 3.3.1.

Once the numeric model is attained, it can be incorporated into a complete drive model for machine drive simulations. A three phase SRM drive model, shown in Figure 3.34, is available from JMAG application notes library[78]. This simulink model has been previously validated in Yang's thesis[2] and is applied in the current study for drive simulation. The Simulink model consists of four parts: machine numeric model, electric circuit, switch control and simulation output.

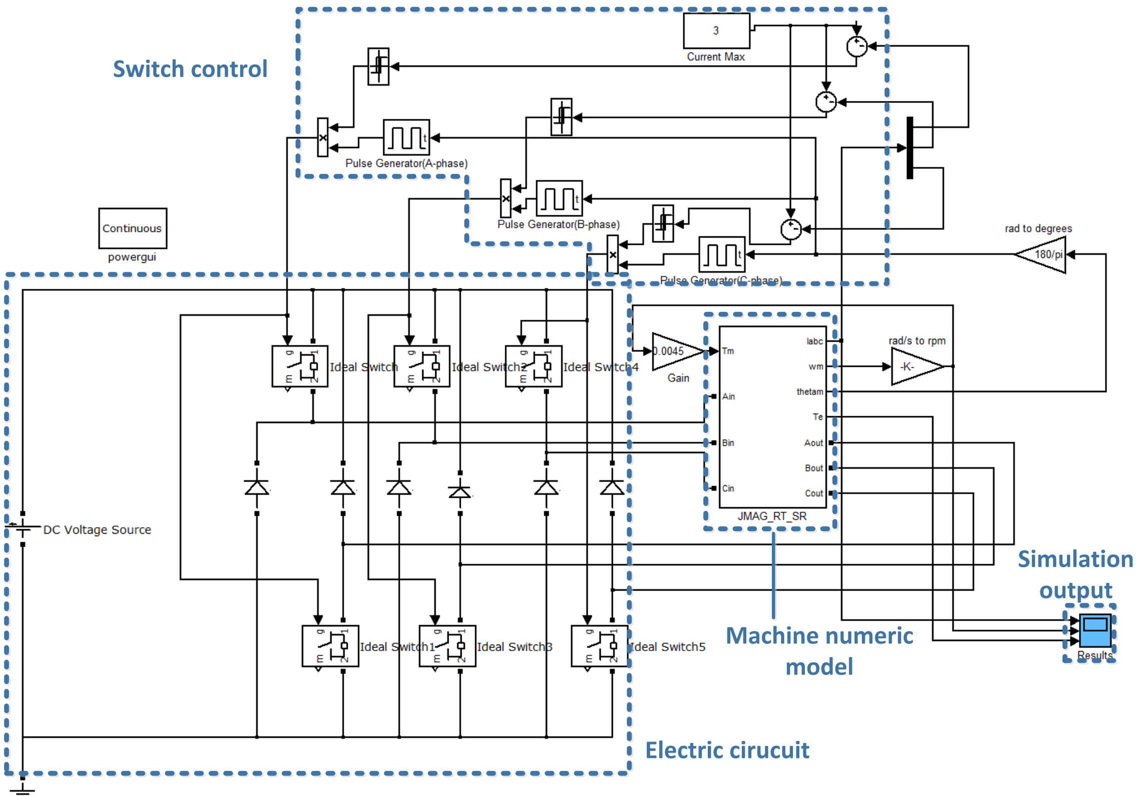

Figure 3.34 Matlab Simulink model for machine drive analysis

The machine model is created by the JMAG-RT module (see Figure 3.35 for block diagram), which contains a look-up table of torque and flux linkage characteristic of the machine. The phase voltage V, phase current i and flux linkage λ are linked in equation 3.10.

$$V = iR + \frac{d\lambda}{dt} \tag{3.10}$$

Because supply voltage is fixed and the rate of change of flux linkage can be found by derivative calculation on the flux linkage look-up table, phase current can be solved. With current determined, output torque can be obtained from the torque look-up table. Note the JMAG-RT machine model also includes a kinematic model that can be used to simulate machine operation under different mechanical loads. Parameters such as inertia and friction can be modified to study steady state or start up drive characteristics of the machine.

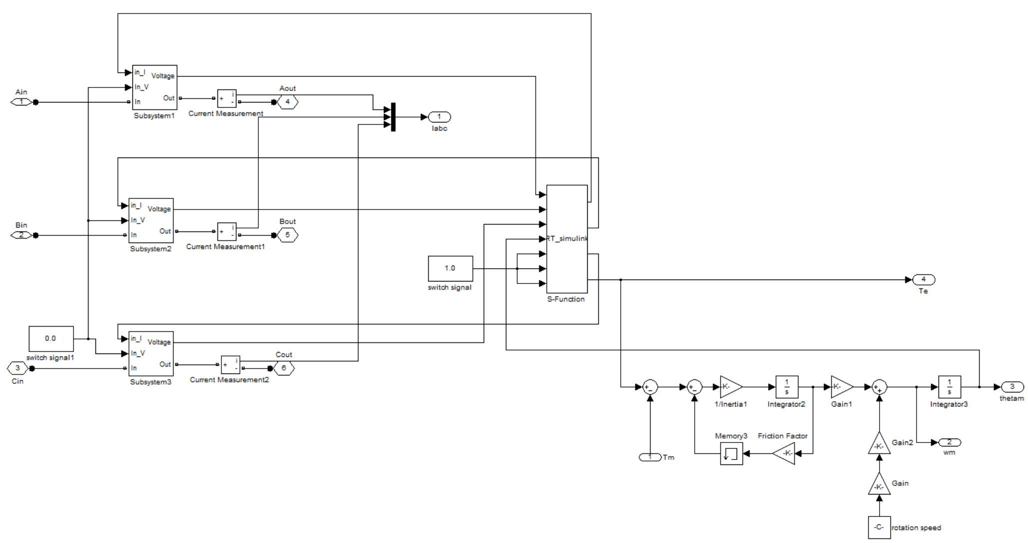

Figure 3.35 JMAG-RT model

The electric circuit model simulates an asymmetric bridge converter, which is in consistent with FEA dynamic analysis. DC voltage source and diodes settings are also kept the same. Ideal switches are assumed in the model with switching loss neglected. The switch control model determines the turn-on and turn-off states of the switches. The periodic switching behaviour is simulated by a pulse wave using the pulse generation module. Hysteresis current control is also implemented by comparing output current to a pre-set limit and applying a hysteresis band. The simulation output is monitored using a scope function. Three parameters, phase current, rotational speed and torque, are recorded and plotted. As an example, a diagram with typical simulation result is shown in Figure 3.36.

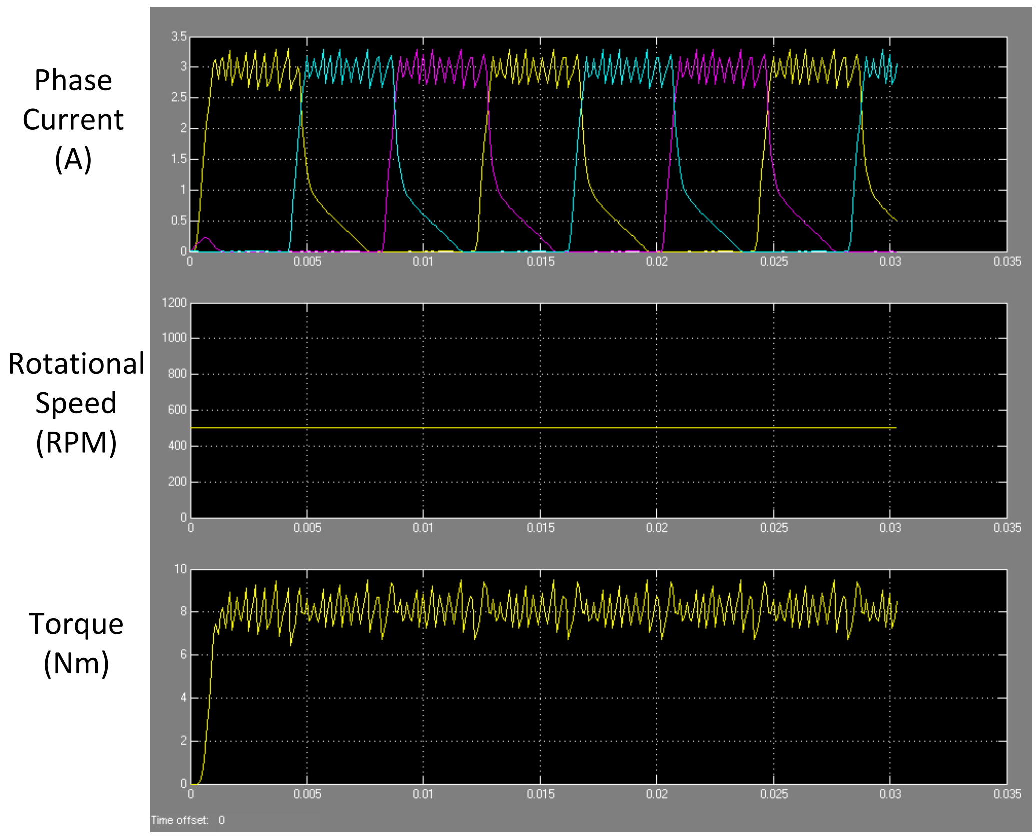

Figure 3.36 Example simulation result from JMAG-RT analysis

Even though drive simulation produces fast solutions (calculation time of each simulation is usually within a second), it requires a significant amount of calculation time generating the machine numeric model. For the specific machine in the current study, model generation takes about 3 hours on a four core desktop computer. Because any change to the FEA model necessitates the generation of a new numeric model, it is impractical to link machine magnetics design to drive simulation due to the high volume of calculations involved. In this thesis, machine drive simulation is not applied to any machine magnetics design optimization, but used solely for control parameter optimization and design performance verification purposes.

3.4. Design Parameter Determination

Optimization of an electric machine design is a very challenging task. On one hand, electric machine designs usually contain a large number of variables, making the optimization a very high dimensional problem. On the other hand, formulation of the design objective is extremely difficult because the designs often have multiple, sometimes even conflicting, objectives. Few studies [60][64][79] have been found in literature on the subject of segmented rotor SRM (SSRM) design optimization. Only [60] and [64] (both by Widmer) attempted global optimization of an SSRM. Widmer' optimization uses an evolutionary strategy algorithm for design case generation and involves large number of simulation cases, which requires substantial amount of computing power. Moreover, the optimization is not suitable for multi-objective problems. For the above reasons, global optimization is not implemented in the parameter selection of the current DSRSRM design. To simplify the problem, geometric relationships between parameters are assumed, mostly based on considerations of the electromagnetics characteristics. The simplification reduces design variables to a smaller set. Then depending on the impact of the variables on performance, they are optimized in groups or individually. A case study is conducted to understand the characteristics of some unique design parameters of SSRM.

3.4.1. Design parameters

The geometry of an SSRM can be defined by a set of parameters listed in Table 3.6. For better illustration, most of the geometric parameters are indicated in Figure 3.37, which shows the cross sectional half model of an SSRM.

Table 3.6 Major geometric parameters of an SSRM

Parameter Symbol	Description
H1	Stator tooth height
H2	Rotor segment height
H3	Stator yoke thickness
W1	Stator phase pole width
W2	Stator interpole width
D	Air gap diameter
a1	Stator phase pole top width
a2	Stator interpole top width
a3	Rotor segment width
a4	Stator phase pole tip taper angle
a5	Stator interpole tip taper angle
a6	Rotor segment tip taper angle
Lstk	Stack length
Lg	Air gap length

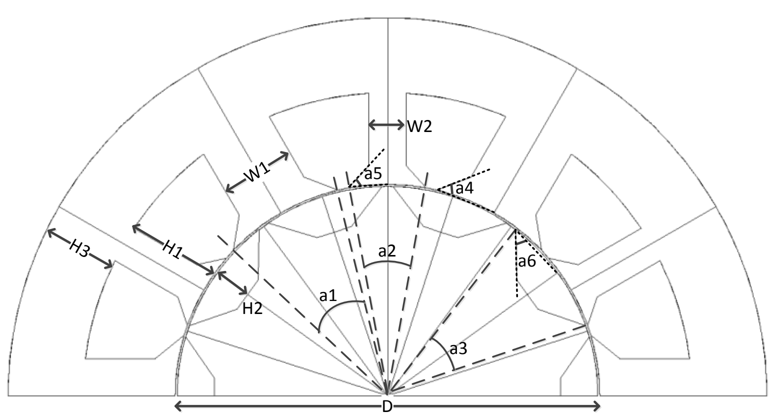

Figure 3.37 Diagram of major geometric parameters of a SSRM

There are as many as 14 geometric parameters in an SSRM design. Luckily, not all of these parameters are independent. Based on the magnetic flux characteristic of SSRM, geometric relationships between some of the parameters can be derived. For example, as suggested in [56], at the unaligned position, to maximize the air gap region so that inductance is minimalized, the stator slot gap should fully align with rotor segment gap. This requires the following two relationships:

$$a1 = a3 \tag{3.11}$$

$$\frac{360°}{12} - \frac{a1}{2} - \frac{a2}{2} = \frac{360°}{10} - a3 \tag{3.12}$$

Therefore both a2 and a3 depend on a1 and can be written as

$$a3 = a1, \qquad a2 = a1 - 12° \tag{3.13}$$

Another rule of thumb of the electromagnetics design is to maintain a uniform iron cross section along major magnetic flux paths at the aligned position so that localized flux saturation is minimized. Figure 3.38 shows magnetic flux of an SSRM at the aligned position. The black arrows indicate major flux paths of the machine. The machine iron core should have uniform cross section along these paths. Similar to a conventional SRM, the stator yoke conducts half of the flux through the phase pole, hence its thickness should be at least half of the width of phase pole (thicker yoke is often designed to reduce iron loss):

$$H3 \geq 0.5W1 \tag{3.14}$$

The stator interpole and rotor segment also conduct half of the flux through the phase pole, therefore interpole width and segment height should be half of the phase pole width:

$$W2 = 0.5W1 \tag{3.15}$$

$$H2 = 0.5W1 \tag{3.16}$$

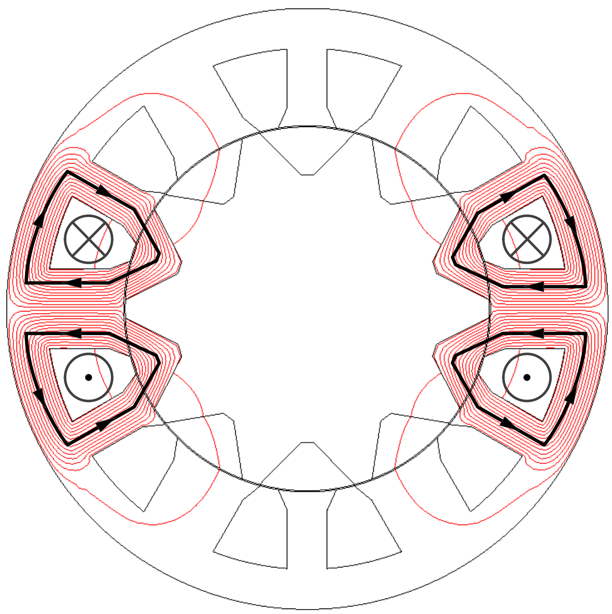

Figure 3.38 Magnetic flux of a 12/10 SSRM at aligned rotor position

The minimum distance between pole tip and rotor segment tip edges, shown in Figure 3.39(a), should also be half of phase pole width to ensure a uniform flux passage. To derive the geometric relationship, the circular air gap can be approximated to be linear to enable simple trigonometric calculations, see Figure 3.39(b). The edges of segment and pole tips can be assumed to be parallel, thus segment tip angle should equal pole tip angle, which gives

$$a5 = a6 = a4 \tag{3.17}$$

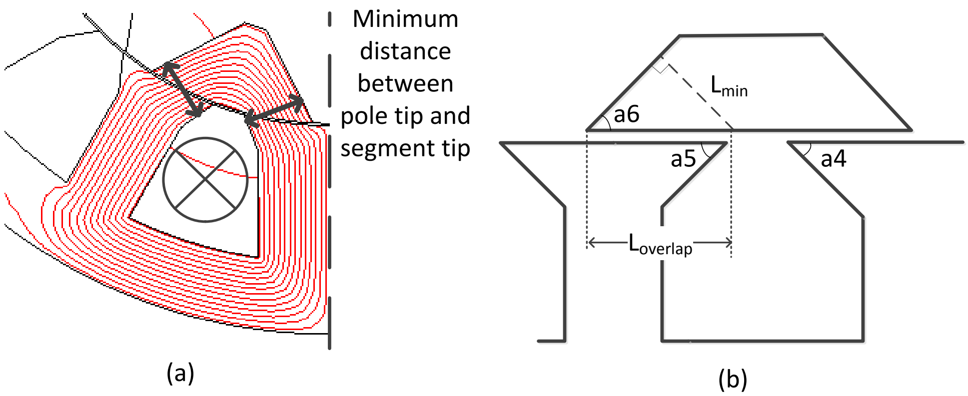

Figure 3.39 Geometric relationship between tip angles

The minimum distance between the two edges L_{min} is then the perpendicular distance between the parallels, which equals

$$L_{min} = L_{overlap}\sin(a6) \tag{3.18}$$

where $L_{overlap}$ is the length of the overlapping section between segment and stator pole. The overlapping section length equals half of the difference between segment width and stator slot gap width:

$$L_{overlap} = \frac{1}{2}\left[a3 - \left(\frac{360°}{12} - \frac{a1}{2} - \frac{a2}{2}\right)\right]\left(\frac{\pi}{180°}\frac{D}{2}\right) \tag{3.19}$$

Substitute equation 3.13 for a2 and a3, equation 3.19 becomes

$$L_{overlap} = \frac{1}{2}\left[a1 - \left(\frac{360°}{12} - \frac{a1}{2} - \frac{a1 - 12°}{2}\right)\right]\left(\frac{\pi}{180°}\frac{D}{2}\right) = (a1 - 18°)\frac{\pi D}{360°} \tag{3.20}$$

Combine equation 3.20 and 3.18, and let L_{min} equal half phase pole width, then tip angle can be calculated as:

$$a6 = \arcsin\left[\frac{0.5W1}{(a1 - 18°)\frac{\pi D}{360°}}\right] \tag{3.21}$$

Based on the above simplifications, independent design parameters reduce to W1 (phase pole width), a1 (phase pole top width), D (air gap diameter), L_g (air gap length) and L_{stk} (stack length).

3.4.2. Characteristic analysis of unique design parameters of SSRM

An SSRM is in many ways similar to a standard SRM, see [56] for a more detailed comparison. For a number of design parameters, similar characteristics observed in an SRM can be expected and applied to the SSRM design. For example, a shorter air gap length is preferred in both types of machines to reduce total magnetic reluctance. And torque capability is positively linked to air gap diameter and stack length. Selection of tooth width needs to balance the requirement of both winding area and magnetic loading for both machine types. It should be noted that apart from the similarities, the segmented rotor SRM also exhibits unique design parameters that result from the machine's unique geometry. Unlike conventional SRMs, segmented rotor SRMs feature segmented rotors and large angled tips on stator poles.

As a relatively new machine topology, SSRM has not been studied as thoroughly as the conventional SRM. No dedicated research has been found on the design parameter characteristics of an SSRM. A characteristic analysis on the unique design parameters of an SSRM is conducted to gain understanding of the importance and characteristics of different design parameters in an SSRM. The study is based on FEA analysis of two particular SSRMs (one with exterior rotor and the other with interior rotor). The details of the two machines are summarized in Table 3.7. The unique design parameters studied are: H2 (rotor segment height), a1 (stator phase pole top arc), a4 (stator pole tip taper angle) and a6 (rotor segment tip taper angle).

Table 3.7 Dimensions of case study machines

	Interior rotor SSRM	Exterior rotor SSRM
Pole configuration	12/10	12/10
Stator teeth root diameter	100mm	194mm
Air gap diameter	70mm	240mm
Stack length	50mm	50mm
Air gap length	0.5mm	0.5mm
Back iron thickness	20mm	21mm
Stator phase pole width	12mm	40mm
Stator inter pole width	6mm	20mm

Rotor segment height

Rotor segment height is varied for both the exterior and interior SSRMs under constant current excitation to study its impact on machine torque and inductance. The results are plotted in Figure 3.40. For the exterior rotor SSRM, height is varied from 16mm to 26mm and for the interior rotor SSRM, 4mm to 10mm. Except for very low segment heights (16mm for exterior and 4mm for interior) where large inductance difference is observed near the aligned rotor position, difference is generally insignificant between cases of different segment height. The reduced inductance for the low height cases is probably due to localized magnetic saturation and should be avoided. As a general design guideline, segment height should be at least equal to half of machine phase pole width to reduce saturation effect.

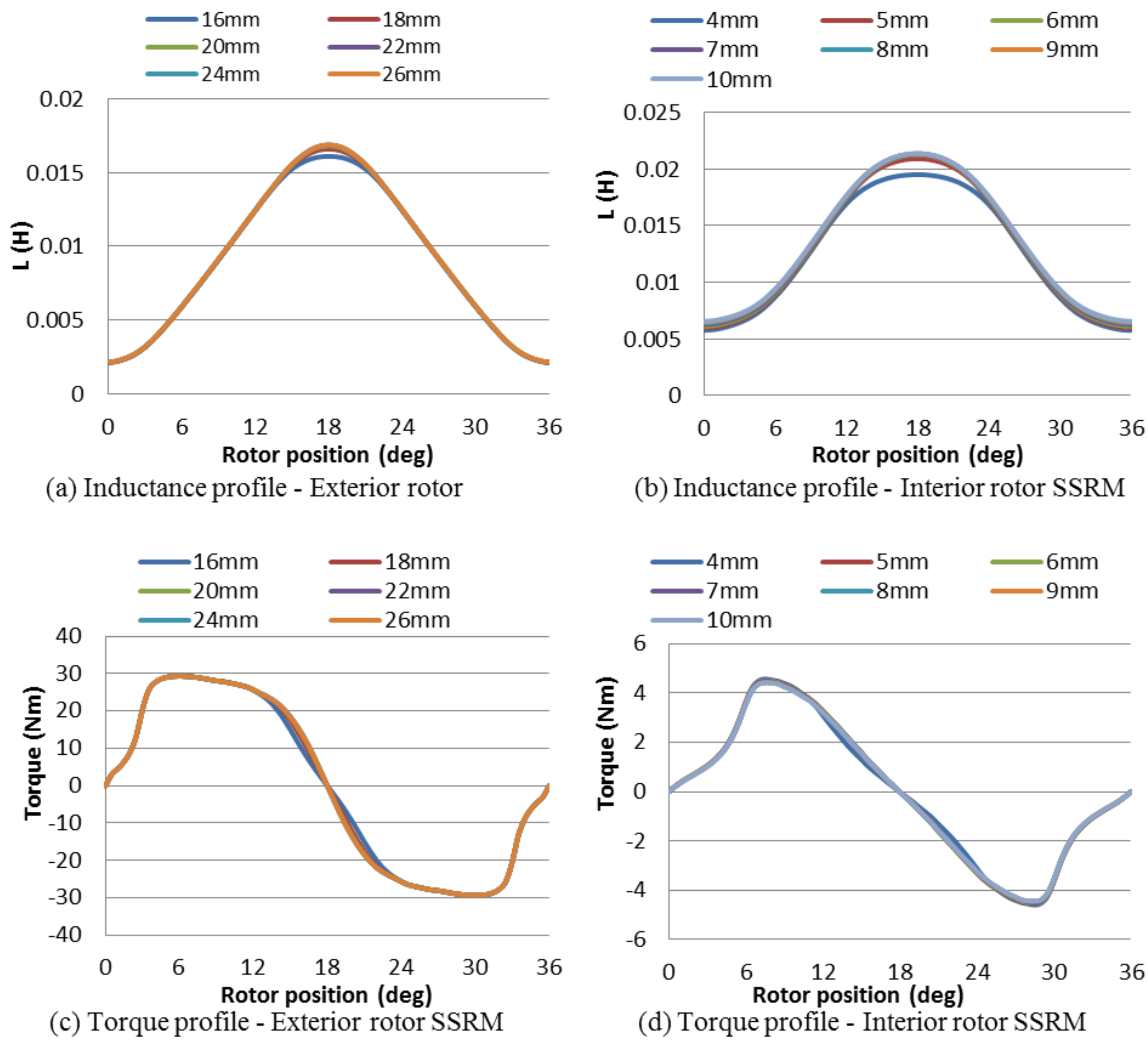

Figure 3.40 Torque and inductance profiles of exterior and interior rotor SSRMs with varying segment height

Stator phase pole top arc

Varying the stator phase pole top arc results in changes to both the torque and inductance profiles of SSRM, see Figure 3.41. Pole top arc is varied from 29° to 35° for the exterior rotor SSRM and from 28 ° to 33 ° for the interior SSRM. A higher pole top arc angle increases width of air gap, which results in an increased phase inductance at all rotor positions, as shown in Figure 3.41 (a) and (b). Larger pole top arc also leads to a smoother inductance increase from the unaligned to the aligned position, which greatly affects the static torque profiles of the machines. Generally, it is observed that larger pole top arc advances the angle where peak torque is reached and extends the peak torque region, giving a more uniform torque waveform.

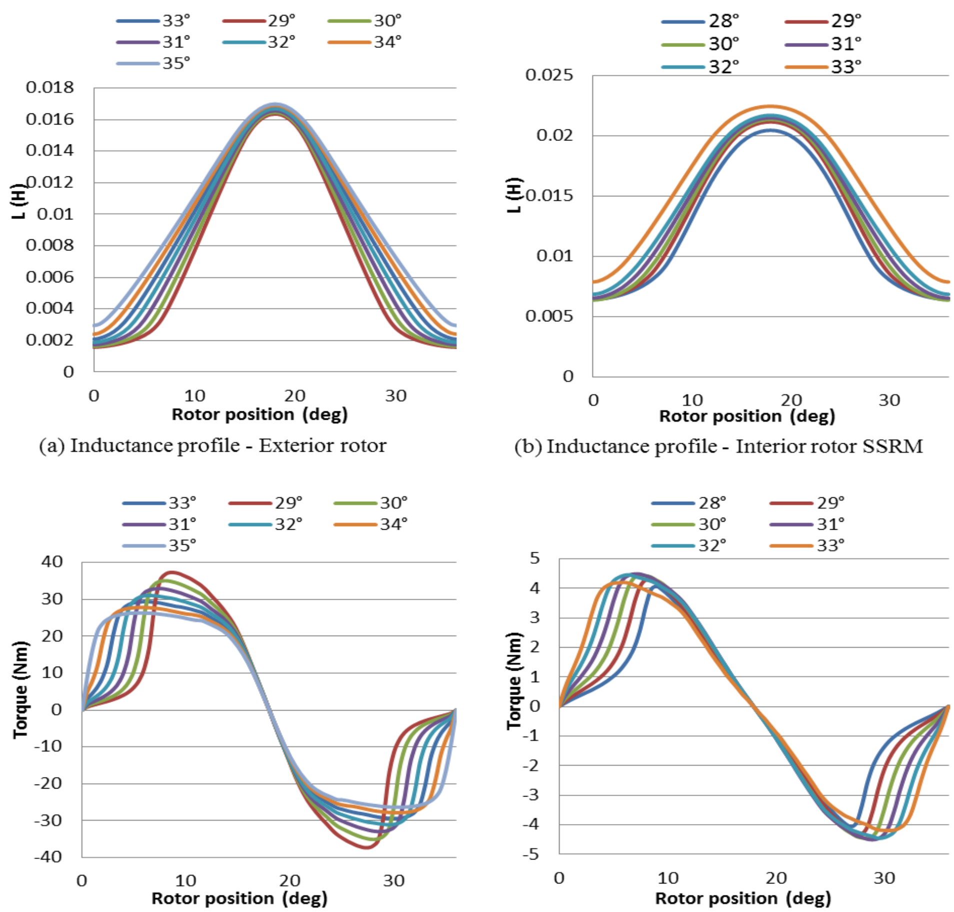

(a) Inductance profile - Exterior rotor
(b) Inductance profile - Interior rotor SSRM
(c) Torque profile - Exterior rotor SSRM
(d) Torque profile - Interior rotor SSRM

Figure 3.41 Torque and inductance profiles of exterior and interior rotor SSRMs with varying stator pole top arc

To see the impact of torque waveform difference on steady state machine output, average torque and torque ripple is estimated by optimizing current excitation angles using the method described in section 3.4.3. The results are shown in Figure 3.42. Generally, a larger pole top arc gives smaller torque ripple. However, average torque suffers for very large arc width. A compromise needs to be made when selecting the optimum arc width. Having a big impact on machine output, stator phase pole top arc should be recognized as a critical design parameter in the machine design process.

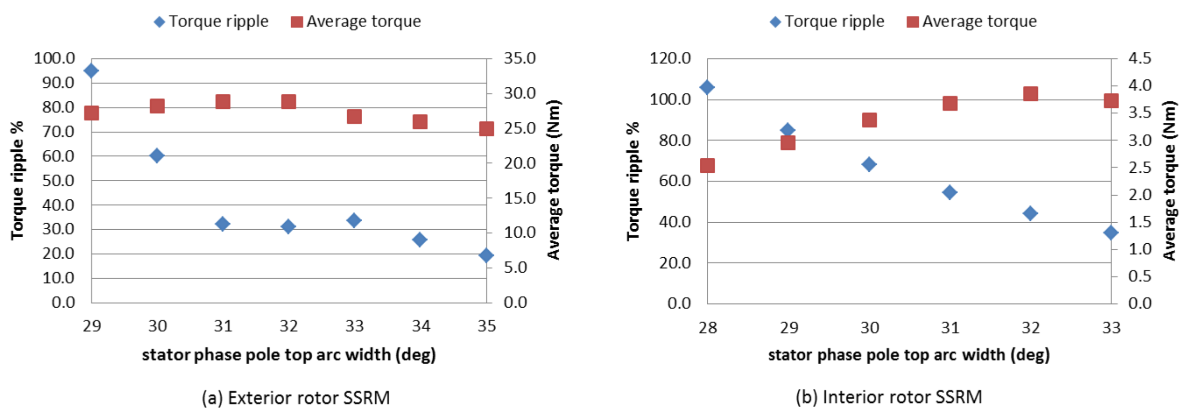

Figure 3.42 Average torque and torque ripple for various pole top arc widths

Rotor segment tip taper angle

Figure 3.44 shows torque and phase inductance profiles for various rotor segment tip taper angles. Segment tip taper angle is varied from 30° to 65° for the exterior rotor SSRM and from 45° to 70° for the interior SSRM. For the interior rotor SSRM, tip taper angle has negligible impact on torque and inductance waveforms; hence optimization of the taper angle is not necessary. For the exterior rotor SSRM, tip taper angle has a significant impact on phase inductance and torque. A smaller tip taper angle is associated with lower and more linear inductance near aligned rotor position. As a result, the static torque profile is more uniform and has a lower peak, which is good for reducing torque ripple but also lowers average torque, see Figure 3.43. A trade-off needs to be made between average torque and torque ripple when deciding the optimal taper angle for exterior rotor SSRMs. Note the 38.8° taper angle is determined using the assumed tip geometry relationship in 3.4.1 and achieves a middle ground between conflicting average torque and ripple requirements. Therefore, it is recommended that the assumed tip geometry relationship be applied in preliminary design parameter selection. Once the high-impact parameters are determined, taper angle can be locally optimized.

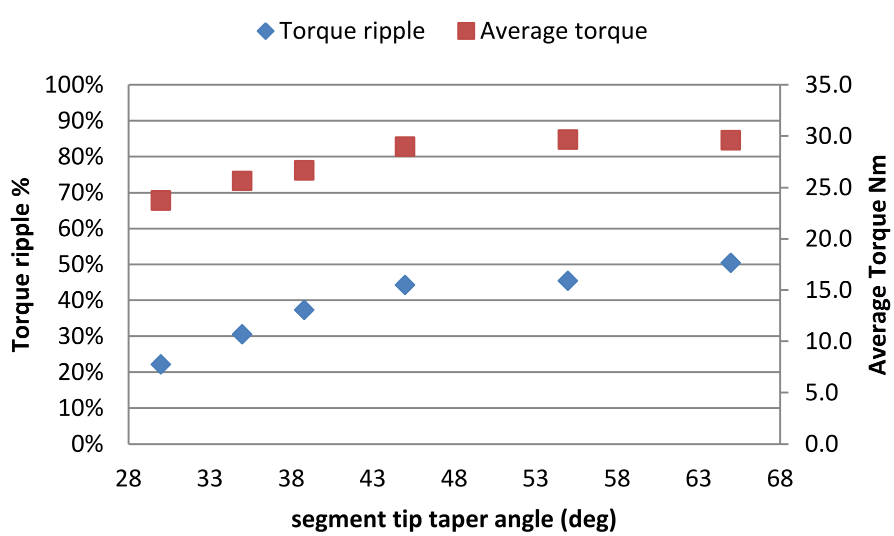

Figure 3.43 Average torque and torque ripple for various rotor segment tip angles of the exterior rotor SSRM

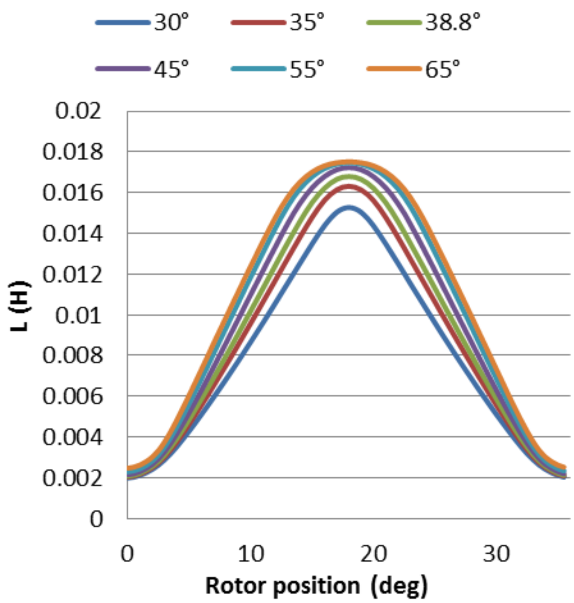

(a) Inductance profile - Exterior rotor

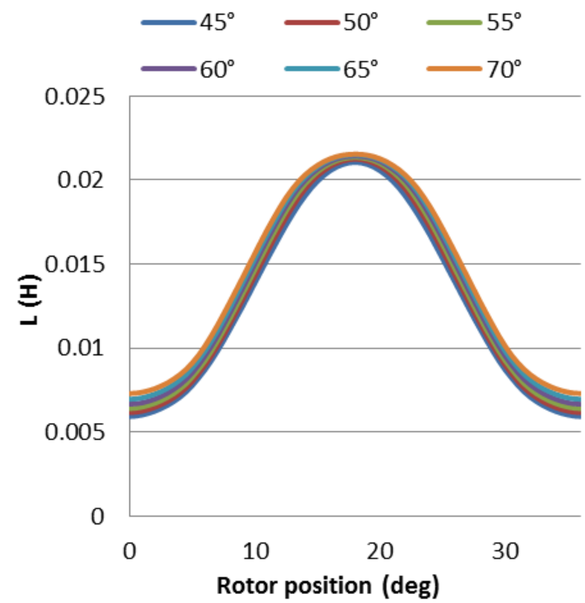

(b) Inductance profile - Interior rotor SSRM

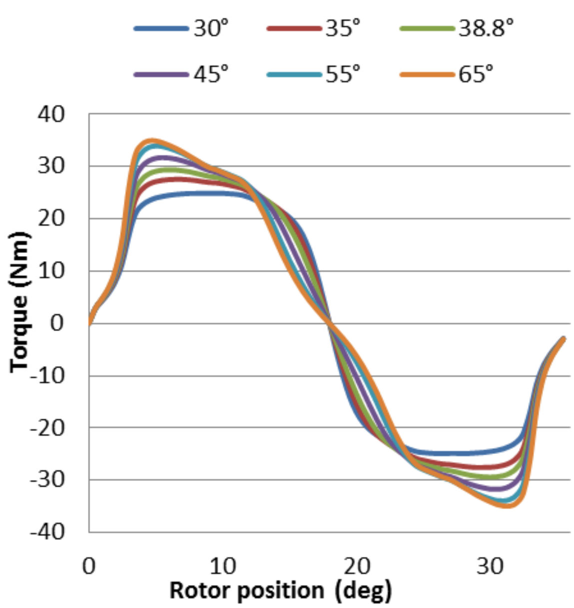

(c) Torque profile - Exterior rotor SSRM

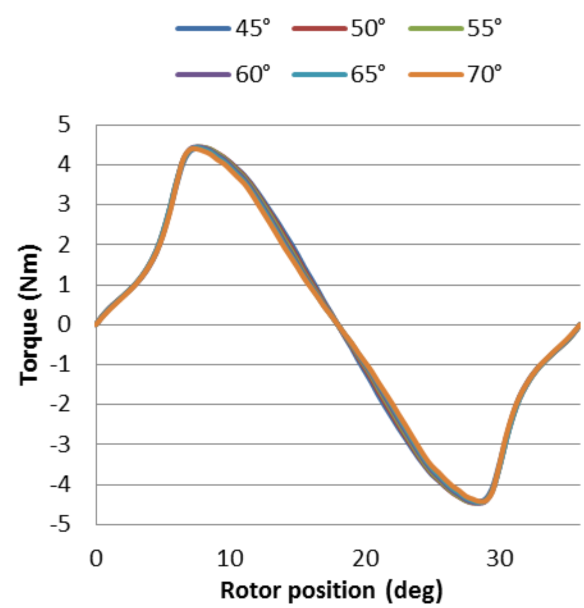

(d) Torque profile - Interior rotor SSRM

Figure 3.44 Torque and inductance profiles of exterior and interior rotor SSRMs with varying rotor segment tip angle

Stator pole tip taper angle

Stator pole tip taper angle is varied from 30 ° to 60 ° for the exterior rotor SSRM and from 45 ° to 65 ° for the interior SSRM. Compared to the segment tip taper, the stator pole tip taper has a very similar impact on torque and inductance waveforms, see Figure 3.46. Again, impact of the taper angle on the interior rotor SSRM is negligible. For the exterior rotor SSRM, a bigger taper angle increases inductance near aligned rotor position and leads to a torque waveform with higher peak but narrower peak region. Same trend is observed for average torque and torque ripple. Bigger angle contributes to higher torque but also higher ripple. The variation is smaller between different angles than that of the segment tip taper in general, see Figure 3.45. Unlike rotor segment tip taper, stator pole tip taper directly affects available winding area. Large taper angles should be avoided because they can greatly reduce slot area, which leads to higher winding resistance and hence increased copper loss.

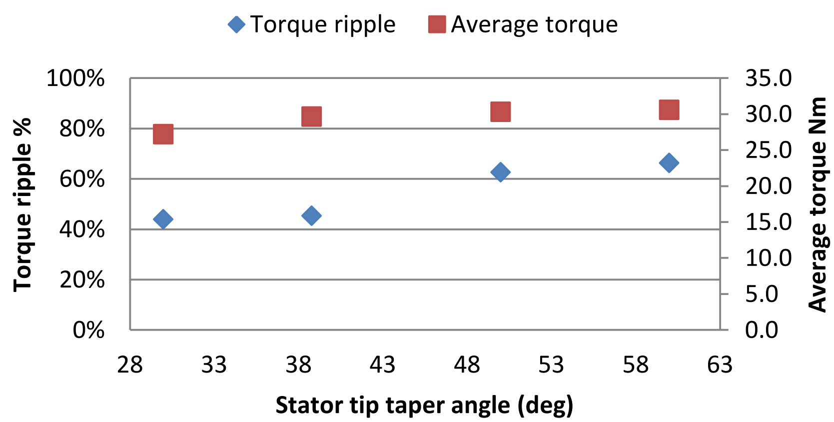

Figure 3.45 Average torque and torque ripple for various stator pole tip angles of the exterior rotor SSRM

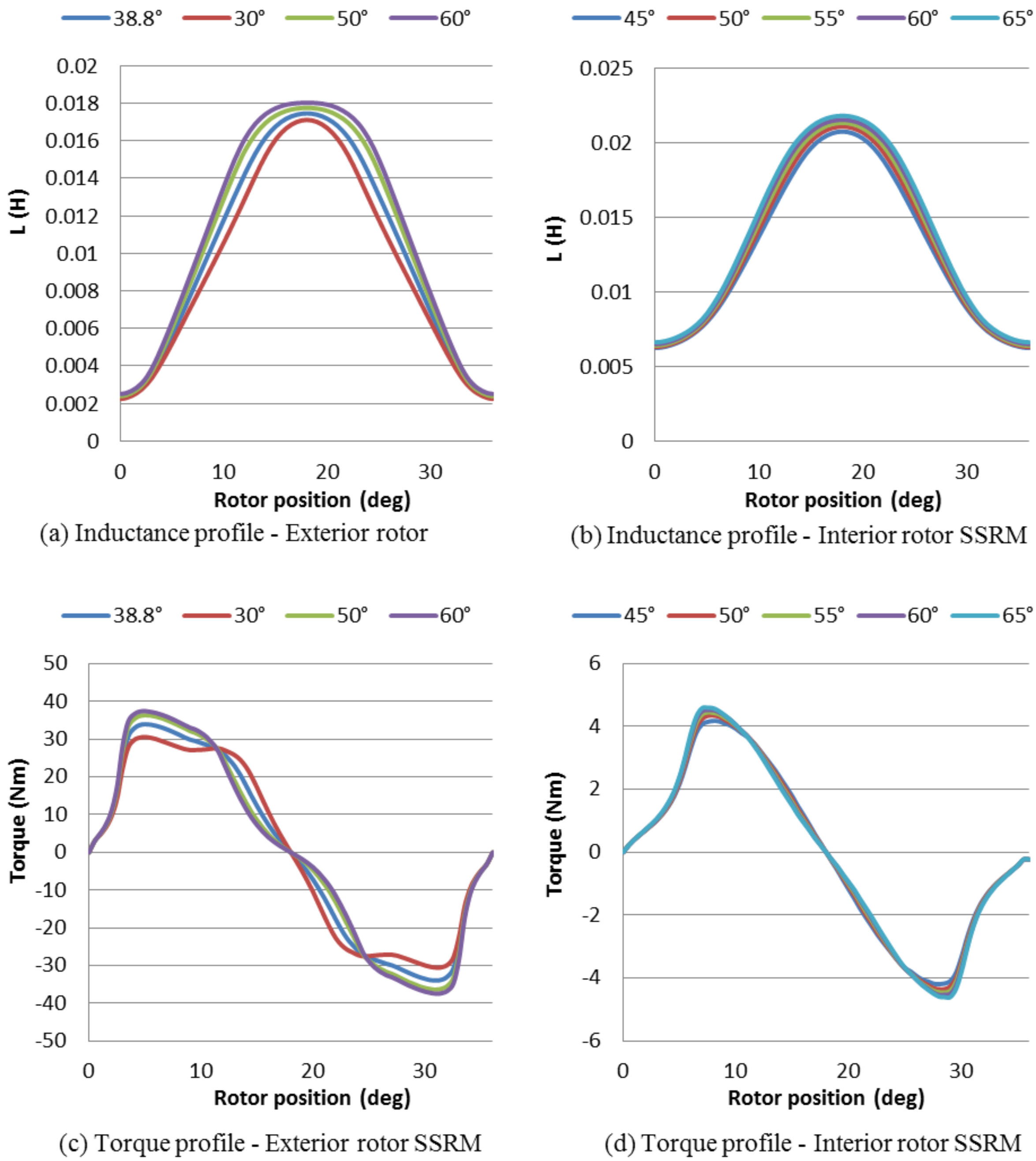

(a) Inductance profile - Exterior rotor

(b) Inductance profile - Interior rotor SSRM

(c) Torque profile - Exterior rotor SSRM

(d) Torque profile - Interior rotor SSRM

Figure 3.46 Torque and inductance profiles of exterior and interior rotor SSRMs with varying stator pole tip taper angle

3.4.3. Steady state torque and ripple estimation

Ideally, to analyze SRM torque characteristics, a true current waveform should be used, which necessitates a complete drive simulation. However, drive simulation is time consuming due to the significant amount of calculation involved in numeric model generation. During the preliminary design parameter selection phase, a fast technique that estimates average torque and torque ripple is needed to analyze the large number of design cases. In the DSRSRM design, a steady state torque estimation scheme based on constant current excitation is used.

To simplify the calculation, the excitation current waveform is approximated as square pulsations, with rise and fall of the excitation current being neglected. The square wave current assumes instantaneous turn-on and turn-off of phase current, which eliminates control circuit dynamics. To give a steady state estimation, first static torque for a single phase at the given excitation level is calculated using FEA at various rotor positions, see Figure 3.47. For a three phase machine, there is a $120°$ electrical lag in current excitation between phases, which equals $24°$ mechanical. Once the torque waveform for one phase is calculated, torque waveforms of other phases can be obtained by shifting the waveform forward and backward by 24 mechanical degrees. Figure 3.48 shows torque waveforms of all three phases.

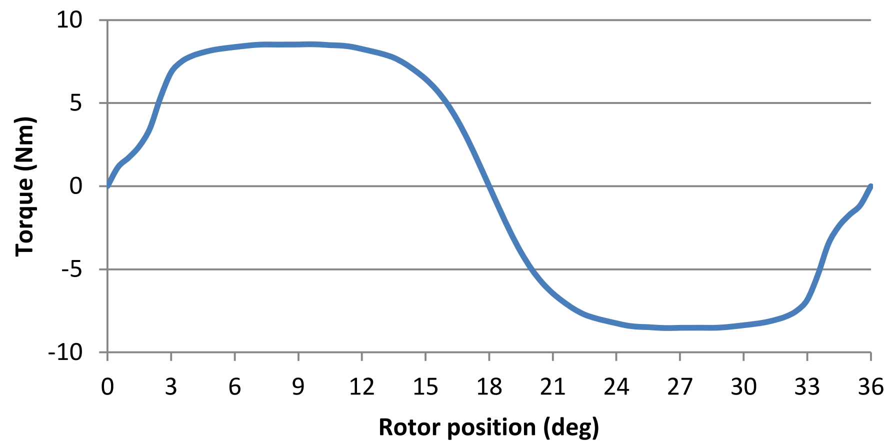

Figure 3.47 Static torque waveform of a single phase

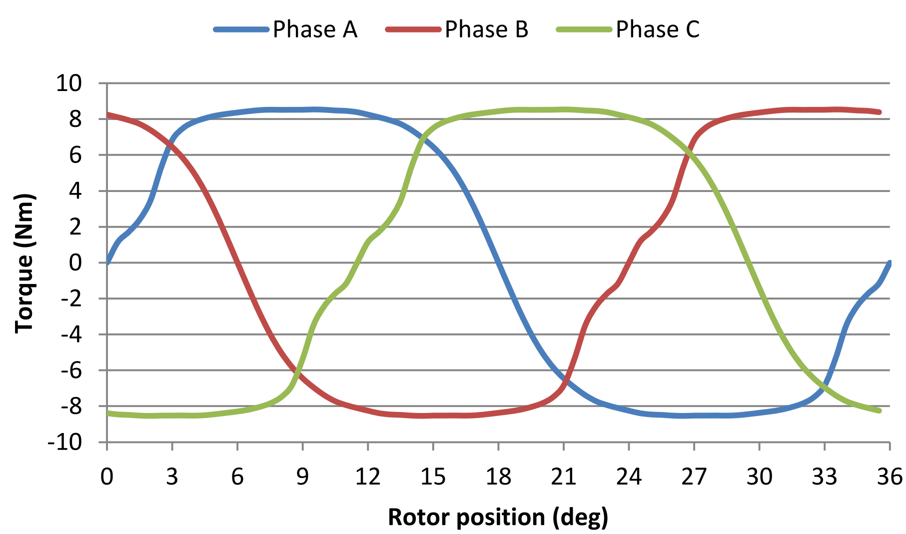

Figure 3.48 Static torque waveforms of all three phases

Note the above torque waveforms assume that excitation current is turned on indefinitely. Torque waveforms for specific current turn-on and turn-off angles can be approximated by truncating off the excitation-off portion of the static waveform (assuming instantaneous current rise and fall). Figure 3.49 shows the torque waveform of a single phase with current turned on at 3 ° and turned off at 15 ° (mechanical).

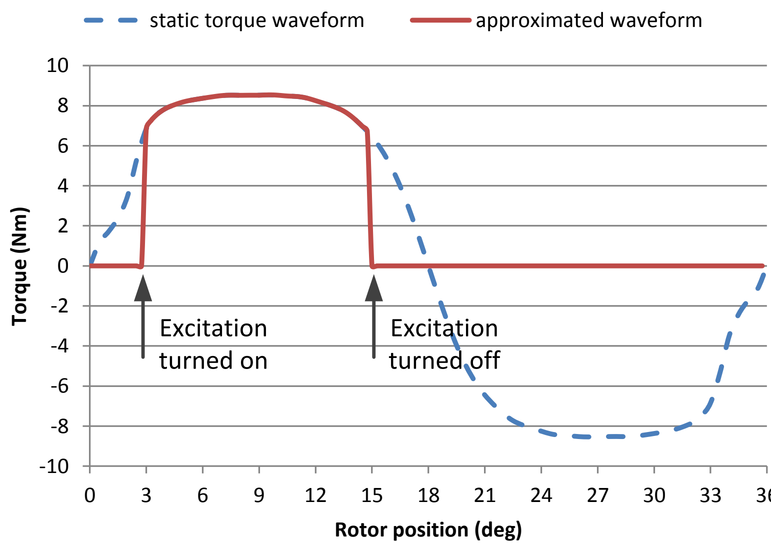

Figure 3.49 Torque waveform estimation considering current turn-on and turn-off

The steady state torque is the summation of torque waveforms of all three phases. Figure 3.50 shows torque waveforms of combined and individual phases. The steady state average torque can be calculated by taking the mean of the combined torque waveform over a complete electrical cycle. And the torque ripple can be calculated by equation 3.22:

$$\%\, torque\ ripple = \left(\frac{T_{max} - T_{min}}{T_{avg}}\right) 100 \qquad (3.22)$$

where T_{max} is maximum torque, T_{min} is minimum torque and T_{avg} is average torque.

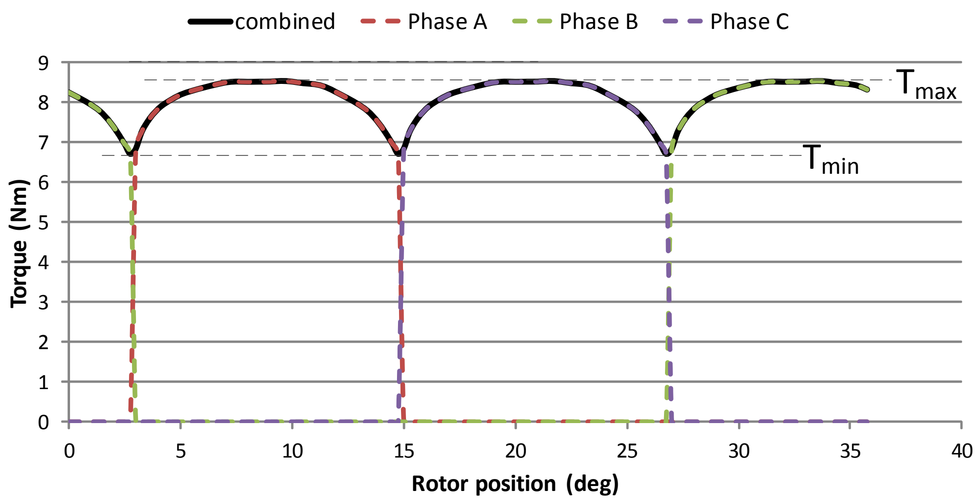

Figure 3.50 Steady state torque estimation

The above torque estimation scheme enables phase current turn-on and turn-off analysis based on only one set of static FEA simulations under constant excitation current, which greatly reduces simulation complexity and calculation time. The assumption of instantaneous rise and fall of excitation current holds well for lower rotational speeds where conduction time is large. This estimation scheme is applied in the DSRSRM design to show more realistic torque characteristics of different design cases. When comparing different designs, first static torque under constant rated current is calculated for all rotor positions. Then the estimation scheme is used to find optimized current turn-on and turn-off angles so that torque ripple is a minimum. This torque ripple optimization can be carried out by a script function that calculates torque ripples for all current turn-on and turn-off angle combinations. The average torque with minimum ripple is selected to represent the steady state torque of a specific design. This optimization runs fast because it requires no FEA simulation. As a result, ripple optimization using the above estimation scheme is applied to the analysis of all design cases in the design parameter study.

3.4.4. Determination of interior machine parameters

The interior SSRM design benchmarks Yang's interior SRM[2]. To give a fair comparison between the two types of machines, a number of design parameters are held constant. Table 3.8 summarises fixed design parameters.

Table 3.8 Fixed design parameters of interior SSRM

Parameter	Description	Value
Lg	Air gap length	0.3mm
D	Air gap diameter	80mm
Lstk	Stack length	50mm
H1	Stator pole height	17mm
H3	Stator yoke thickness	15mm

Refer to Table 3.6: Major geometric parameters of an SSRM, with 5 parameter fixed, there are 9 parameters to be determined. Applying the geometric relationships derived in 3.4.1, independent design parameters reduce to W1 (stator phase pole width) and a1 (stator phase pole top arc). To determine the two parameters, a two dimensional optimization with fixed step change is conducted. Table 3.9 lists selected values of the two parameters. The stator pole width varies between 6 and 15 mm, with center of its range being close to 10mm (half of pole width of benchmark design). The phase pole top arc varies between 29° and 33°, with 1° incremental change (equals about 0.7mm arc length). In section 3.4.2 parameter characteristic analysis, it is shown that generally larger pole top arc leads to higher average torque output and smaller ripple. Here the arc angle is limited to not to exceed 33° due to concerns of a too narrow stator winding slot gap (should be at least 2mm), which could cause problems with winding installation.

Table 3.9 Selected values of parameters – interior SSRM

Parameter	Values
W1	6mm, 7mm, 8mm, 9mm, 10mm, 11mm, 12mm, 13mm, 14mm, 15mm
a1	29°, 30°, 31°, 32°, 33°

The above parameter values generate 50 (5x10) design cases. All design cases are evaluated using FEA with constant current excitation. Static torque and flux linkage of a single phase is calculated for various rotor positions, starting from an unaligned position (0°) to the next unaligned position (36°), with a 0.5° incremental step change. For FEA simulation settings please refer to section 3.3.1. At this design stage, drive characteristic of the machine is not studied. To avoid the determination of turn number (related to machine drive characteristics), the excitation level of a phase is specified by MMF (magneto motive force) which equals the product of current and number of turns. As a starting point, phase MMF of all 50 cases are set to 1000A turns. For each design case, average torque and torque ripple is estimated by applying the method in section 3.4.3 to the calculated static torque waveform. A fixed 120° electrical conduction angle is assumed and the turn-on angle is optimized for minimal torque ripple. Apart from torque information, flux density at stator pole center and copper loss are also used to evaluate different designs. Stator pole center flux density is extracted from the analysis result and copper loss is estimated using the method in section 3.3.2, assuming a 35% slot fill factor. A complete table summarising all 50 design cases is included in APPENDIX A1.

Reviewing the design cases, two general trends are observed for stator phase pole width W1. When pole width increases under same excitation level, both average torque and copper loss increase; flux density in the stator pole center decreases. For small pole width (W1 equals 6mm or 7mm), magnetic flux density in the pole is high while torque output is low. In these cases, average torque output (around 1.5Nm) is far less than the required 2Nm objective, while stator pole center flux density is already over 1.7T. To increase the average torque to demanded level, MMF needs to be increased, which will likely cause stator flux density to exceed the design constraint of 1.8T. Therefore, cases with W1 less than or equal to 7mm can be neglected. On the other hand, when pole width is large both torque ripple and copper loss is high. Cases with W1 equal or greater than 14mm are also neglected for too high torque ripple (over 60%) and copper loss. Another important observation is that phase pole top arc a1 is closely linked to torque ripple, which corresponds to the parameter characteristic study in 3.4.2. Torque ripple is observed to be over 60% for all cases with pole top arc less or equal to 31°. These cases are also neglected.

After screening out cases that do not meet design specifications, there are 12 designs (a1=32° or 33°, W1=8-13mm) under consideration. For each design, phase MMF is adjusted to a level that achieves 2Nm average torque. Torque ripple, stator pole center flux density, copper loss and current density are calculated and tabulated in Table 3.10 to help compare the designs. For the majority of design cases, torque ripple is around 50%, copper loss is around 18W and RMS current density is 3.15A/mm^2. Case 5, 6 and 7 are optimal designs for having the lowest copper loss, current density and torque ripple. Out of the three, case 6 is selected because it has a smaller pole top arc, resulting in a larger winding slot entrance gap, which is very beneficial for coil winding installation.

Table 3.10 Summary of refined design cases of interior SSRM

Case	a1 (deg)	W1 (mm)	MMF (AT)	Torque ripple (%)	Average torque (Nm)	Stator pole center flux density (T)	Copper loss (W)	RMS current density (A/mm^2)
1	33	8	1160	48	2.00	1.76	19.9	3.17
2	32	8	1160	51	2.01	1.75	20.1	3.20
3	33	9	1090	48	2.00	1.71	18.4	3.11
4	32	9	1090	52	1.99	1.7	18.6	3.14
5	33	10	1050	50	2.01	1.67	17.9	3.14
6	**32**	**10**	**1050**	**52**	**2.01**	**1.66**	**18.1**	**3.17**
7	33	11	1010	47	1.99	1.63	17.5	3.16
8	32	11	1020	60	2.00	1.61	18.0	3.23
9	33	12	990	51	2.01	1.59	17.7	3.26
10	32	12	1000	64	2.01	1.58	18.2	3.32
11	33	13	980	57	2.03	1.56	18.3	3.39
12	32	13	1000	70	2.06	1.54	19.2	3.50

Next stator pole tip taper angle and segment tip taper angle are individually optimized. Table 3.11 and Table 3.12 compare design cases with varying stator pole tip taper and segment tip taper, respectively. The simulation results correspond well to the observation in parameter characteristic analysis (see section 3.4.2), where taper angles are shown to have insignificant impact on machine output of interior rotor SSRMs. Here the calculated taper angle based on assumed iron path geometry is 31°. For stator pole tip taper, a smaller angle reduces average torque while a larger angle increases torque ripple and copper loss (due to reduction in slot area). For segment tip taper, increased angle worsens torque ripple but brings no torque capability benefit. A small taper angle even though slightly reduces torque ripple but causes intensified magnetic saturation at the segment tip, resulting in reduced torque output. Therefore, for both pole tip and segment tip taper, the optimized angle is selected to be 31 °.

Table 3.11 Interior SSRM stator pole tip taper optimization

Stator pole tip taper (deg)	Segment tip taper (deg)	Torque ripple (%)	Average torque (Nm)	Stator pole center flux density (T)	Copper loss (W)
26	31	48	1.91	1.6	17.8
31		**52**	**2.01**	**1.66**	**18.1**
36		69	2.05	1.69	18.4
43		79	2.08	1.71	19.0
50		84	2.09	1.74	19.7
60		85	2.12	1.8	21.7

Table 3.12 Interior SSRM segment tip taper optimization

Stator pole tip taper (deg)	Segment tip taper (deg)	Torque ripple (%)	Average torque (Nm)	Stator pole center flux density (T)	Copper loss (W)
31	26	49	1.93	1.64	18.1
	31	**52**	**2.01**	**1.66**	**18.1**
	36	59	2.02	1.67	18.1
	43	64	2.02	1.68	18.1
	50	66	2.01	1.68	18.1
	60	65	1.99	1.68	18.1

With all geometric dimensions of the machine determined, a numeric model that contains static torque and phase inductance information at various current levels and rotor positions can be created. Drive simulations are performed on the numeric model to determine phase coil turn number as well as optimized current turn-on and turn-off angles. Please refer to section 3.3.3 for details of the drive simulation.

Current turn-on and turn-off angles for a given speed are optimized for lowest torque ripple, with a torque output requirement given by the benchmark specification. In the optimization, turn-on angle is varied between -30° and 10° (electrical) with fixed step change of 2° and turn-off angle is varied between 110° and 150° (electrical) with fixed step change of 2°. A total of 400 (20 by 20) current angle combinations are simulated to find optimal switching angles for a certain speed.

The selection of the coil turn number is a more complicated process that involves making a trade-off between small phase current and small phase inductance. On one hand, large turn number is preferred to reduce the phase current (for a certain electric loading, the product of current and number of turns is a constant). On the other hand, higher speed machine operation requires a small phase inductance to reduce back EMF, where small number of turns are preferred. Because turn number is linked to the machine numeric model generation, each time turn number is changed, the numeric model needs to be re-calculated. In the current machine design, turn number selection starts with assuming a turn number and creating the numeric model. Then the excitation is optimized for highest machine operating speed and the output is compared to design objective. If output is below objective, number of turns is reduced to enhance high speed performance; otherwise, turn number is increased to reduce current. The numeric model is updated with a new turn number and the highest speed output is calculated and verified until a satisfying result is achieved. For the interior rotor SSRM design under consideration, a phase turn number of 300 delivers a satisfying output. Table 3.13 summarises drive simulation results of the machine under four critical operating speeds. For all speeds, torque output requirement is met. Note a 10% margin of average torque is kept for 4000 rpm because 2D FEA analysis typically underestimate phase inductance (will be addressed in 3D verification), which results in overestimated output at high speeds.

Table 3.13 Drive simulation results of interior rotor SSRM

Rotational speed (RPM)	Current turn-on angle (deg, elec)	Current turn-off angle (deg, elec)	Average torque (Nm)	Required torque (Nm)	Torque ripple (%)
2000	8	148	2.05	2.00	35
2400	8	148	2.01	1.81	45
3000	-6	144	1.91	1.63	45
4000	-26	130	1.65	1.47	99

Selection of turn number also depends on available winding area, slot fill factor and wire size. The current design has a winding area of 271 mm^2 per slot. And the slot fill factor is limited to 35%. Considering standard wire sizes, actual turn numbers that can be achieved are summarised in Table 3.14.

Table 3.14 Turn number and wire size selection of interior rotor SSRM

Wire gauge	Copper area per strand (mm2)	Number of strands	Number of turns per phase
#20	0.52	1	366
#22	**0.32**	**2**	**292**
#24	0.20	3	308
#26	0.13	4	370
#28	0.08	8	294

The closest turn number achievable is 292 (gauge 22) or 308 (gauge 24). Out of the two, gauge 22 is preferred because it has a smaller number of strands, which makes winding and coil handling easier.

3.4.5. Determination of exterior machine parameters

The exterior SSRM benchmarks Yang's exterior SRM[2]. Again, a number of design parameters are fixed to ensure a fair comparison. Table 3.15 summarises fixed design parameters.

Table 3.15 Fixed design parameters of exterior SSRM

Parameter	Description	Value
Lg	Air gap length	0.3mm
D	Air gap diameter	182mm
Lstk	Stack length	50mm
H1	Stator pole height	19mm
H3	Stator yoke thickness	15mm

Due to the reduced stator back iron thickness of the current design, the exterior SSRM has a smaller stator tooth bottom diameter (144mm) than the benchmarked SRM (182mm). If same stator pole height was set, the SSRM would have smaller active volume (occupied by active material, i.e. copper wire and iron) because of its smaller diameter. To give a fair comparison, a stator pole height is chosen such that the annulus area occupied by winding and stator poles of the exterior SSRM is equal to that of the benchmarked exterior SRM. Figure 3.51 illustrates the exterior annulus area of the two machines. Based on area calculation, stator pole height is determined to be 19mm. The air gap diameter equals pole bottom diameter plus twice of pole height, which is 182mm.

The rest of the parameter selection process is very similar to that of the interior SSRM in the preceding section. First, W1 (stator phase pole width) and a1 (stator phase pole top arc) are optimized by varying both parameters with fixed step changes. Table

3.16 lists selected values of the two parameters. The stator phase pole width is varied between 14mm and 28mm, with center of its range being half of the pole width of the benchmark design. The pole top arc is limited not to exceed 34 ° to ensure enough slot opening for winding installation.

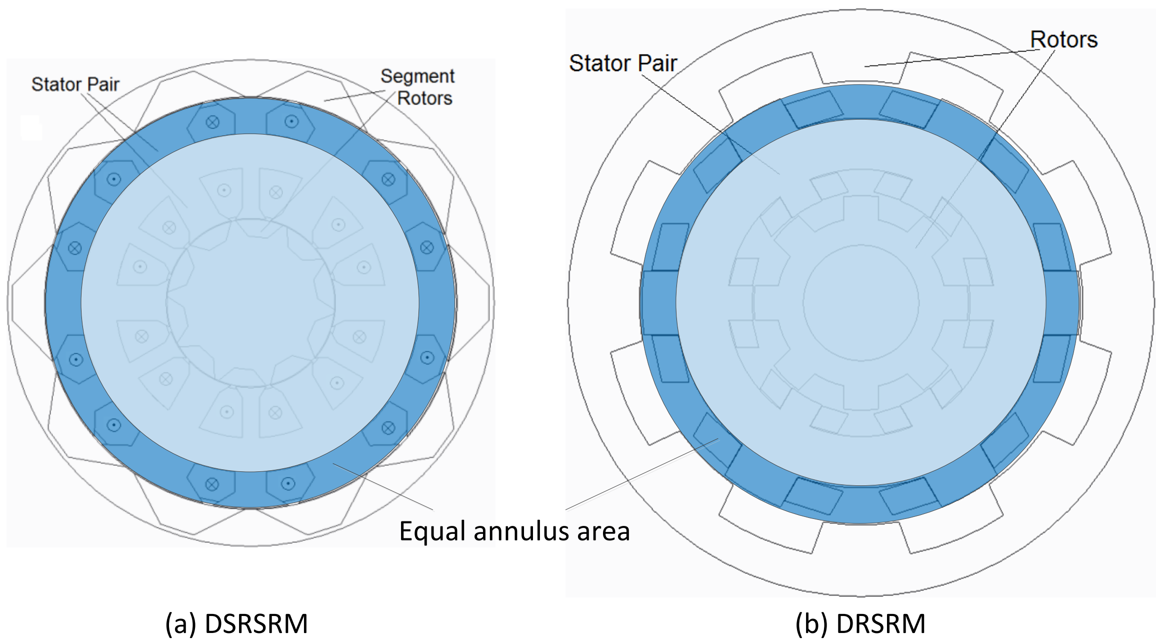

Figure 3.51 Illustration of the annulus area of DSRSRM and DRSRM

Table 3.16 Selected values of parameters – exterior SSRM

Parameter	Values
W1	14mm, 16mm, 18mm, 20mm, 22mm, 24mm, 26mm, 28mm
a1	31 °, 32 °, 33 °, 34 °

The above parameter values generate 32 (8x4) design cases. For each design case, same analysis as described in interior machine parameter selection is performed. Note a 39% slot fill factor is assumed in the copper loss estimation of exterior machine. The results are summarised in APPENDIX A2.

Comparing design cases, small pole width tends to have lower torque ripple and copper loss but suffers from reduced torque capability and flux saturation. Designs with pole width smaller equal or smaller than 16mm cannot meet the torque requirement without exceeding flux density constraint and are therefore neglected. Large pole width, on the other hand, produces higher torque ripple and copper loss. A moderate pole width (20mm and 22mm) achieves the lowest torque ripple for various pole top arc angles. Similar to parameter characteristic analysis result, small pole top arc results in large torque ripple. Pole top arc that is smaller than 32° produces unacceptable torque ripple (higher than 50%) and is therefore neglected in subsequent study.

By screening out designs with unacceptable output, optimization is focused on a smaller range of parameter values. 15 design cases are studied, with W1 being 20, 21 or 22mm; a1 being 32°, 32.5°, 33°, 33.5° or 34°. The simulation results are summarised in Table 3.17. Case 5 achieves both low torque ripple and low copper loss and is therefore selected as optimal design.

With major machine dimensions determined, stator pole tip taper and segment tip taper angles are then individually optimized. The results are tabulated in Table 3.18 and Table 3.19. For both pole tip and segment tip taper, 26.5° yields the lowest torque ripple while satisfying the torque requirement. Hence, the optimal angle is set to 26.5°.

Table 3.17 Summary of refined design cases of exterior SSRM

Case	a1 (deg)	W1 (mm)	MMF (AT)	Torque ripple (%)	Average torque (Nm)	Stator pole center flux density (T)	Copper loss (W)
1	34	20	1740	19	8.05	1.79	37.5
2	34	21	1700	18	8.08	1.76	37.1
3	34	22	1650	19	8.02	1.74	36.2
4	33.5	20	1720	22	8.01	1.76	36.6
5	**33.5**	**21**	**1670**	**20**	**8.00**	**1.74**	**35.8**
6	33.5	22	1620	22	7.98	1.65	35.5
7	33	20	1710	25	8.06	1.75	36.3
8	33	21	1650	27	8.01	1.74	35.0
9	33	22	1600	26	7.99	1.73	34.1
10	32.5	20	1680	31	8.02	1.74	35.0
11	32.5	21	1630	33	8.02	1.73	34.2
12	32.5	22	1590	35	8.04	1.72	33.7
13	32	21	1610	39	8.00	1.72	33.4
14	32	20	1650	38	7.95	1.73	33.9
15	32	22	1570	41	8.01	1.72	32.9

Table 3.18 Exterior SSRM stator pole tip taper optimization

Stator pole tip taper (deg)	Segment tip taper (deg)	Torque ripple (%)	Average torque (Nm)	Stator pole center flux density (T)	Copper loss (W)
18	26.5	14	7.27	1.59	36.3
22		19	7.71	1.66	37.5
26.5		**20**	**8.00**	**1.73**	**38.5**
30		25	7.94	1.76	38.3
35		27	8.33	1.78	42.3
40		27	8.41	1.8	44.9
45		26	8.46	1.83	48.1

Table 3.19 Exterior SSRM segment tip taper optimization

Stator pole tip taper (deg)	Segment tip taper (deg)	Torque ripple (%)	Average torque (Nm)	Stator pole center flux density (T)
26.5	23.5	19	7.54	1.65
	25	20	7.86	1.69
	26.5	**20**	**8.00**	**1.73**
	28	27	8.10	1.74
	30	32	8.44	1.78
	35	46	8.81	1.82
	40	47	9.27	1.83
	48	53	9.35	1.84

A JMAG-RT numeric model is created based on the determined machine geometry, followed by drive simulation to determine coil turn number and current turn-on and turn-off angles. These parameters are determined in the same way as for the interior SSRM. Please refer to section 3.4.4 for details. According to the drive simulation, a phase turn number of 490 will give a satisfying output, shown in Table 3.20. For a winding slot area of 399 mm^2 and a 39% fill factor, the closest achievable turn number is 480 with gauge 22 wires. See Table 3.21 for turn number calculation results.

Table 3.20 Drive simulation results of exterior rotor SSRM

Rotational speed (RPM)	Current turn-on angle (deg, elec)	Current turn-off angle (deg, elec)	Average torque (Nm)	Required torque (Nm)	Torque ripple (%)
500	8	138	8.2	8	24
750	4	136	7.11	6.57	28
837	-6	140	6.37	5.57	43
1000	-8	140	5.03	3.57	85

Table 3.21 Turn number and wire size selection of exterior rotor SSRM

Wire gauge	Copper area per strand (mm2)	Number of strands	Number of turns per phase
#20	0.52	1	600
#22	**0.32**	**2**	**480**
#24	0.20	3	507
#26	0.13	5	486
#28	0.08	8	484

3.4.6. Tip shape study

The segmented rotor SRM has angled tips on both rotor segments and stator poles. These pointy tips are prone to distortion due to high mechanical stress induced by (a) magnetic forces during machine operation (b) machining force during component manufacturing. To increase the mechanical strength of the tips, tip shape is modified to eliminate the thin and pointy nose. Three tip shapes are studied, which includes round tip, extended square tip and truncated square tip, as shown in Figure 3.52. The modified tip shapes introduce an abrupt change of magnetic flux when segment tip and pole tip starts to overlap, causing increased torque ripple. Of the three tip shapes studied, the extended square tip introduces minimal torque waveform changes and is applied in current design. Two parameters that define the tip shape, tip thickness and segment arc, are optimized for minimal torque ripple at rated operation condition, see Figure 3.53. For the interior machine, optimized tip thickness is 0.7mm and segment arc is 31.5°. The exterior machine has same optimized segment arc of 31.5°, the tip thickness is increased to 0.9mm due to higher loading.

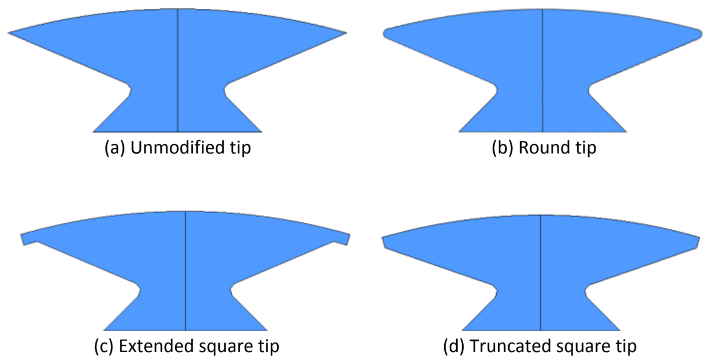

Figure 3.52 Illustration of different tip shapes studied - Interior rotor segment

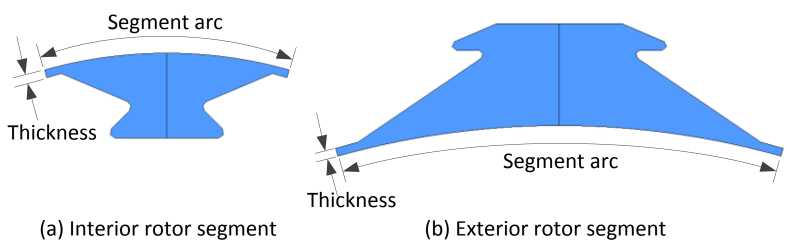

Figure 3.53 Modified tip shape for interior and exterior rotor segments

3.5. Model Verification

A number of simplifications are applied to the machine model in the parameter selection process to speed up the analysis. This includes assuming a 2D model, omitting complicated structural features and neglecting mutual inductance effects. To verify the results obtained from simplified models, more sophisticated models are developed and compared. It has been shown in section 3.2.1 that magnetic coupling between the two machines are negligible, therefore, only isolated machine models are analyzed and compared in this verification study.

Modelling structural details

Three structural features are omitted in the simplified model to reduce model complexity and calculation time. These are mounting holes in the center of the stator yoke, dovetails at the end of rotor segments and slot wedges capping each winding slot. Note the interior machine has a steel shaft in the center, which is also omitted in the simplified model. To evaluate the impact of these features on machine performance, a detailed FEA 2D model with all structural features is created. Figure 3.54 and Figure 3.55 compares the geometry differences.

Static torque and flux linkage under rated operating current are calculated for the detailed model and are compared to the results of the simplified model, see Figure 3.56. For both machines, the structural features introduce negligible impact on torque and flux linkage waveforms. The exterior machine has almost identical curves for both models, giving a 1% difference on average. The interior machine shows slightly bigger difference, at 3% on average.

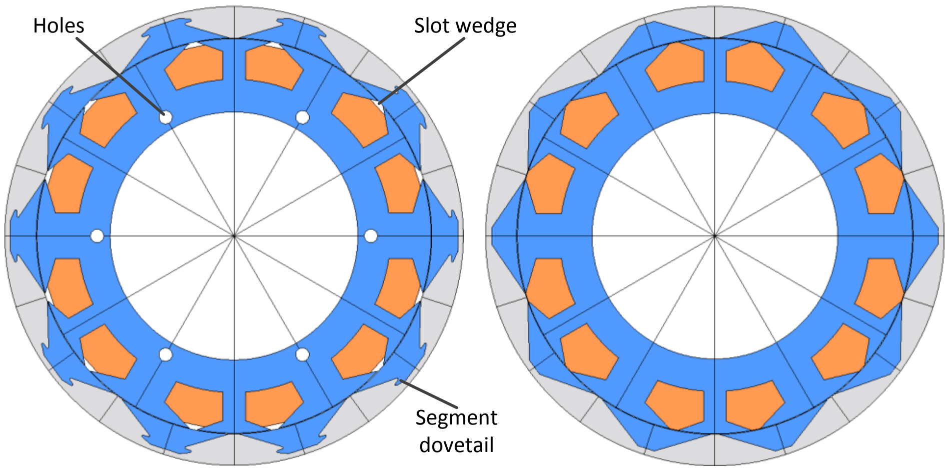

(a) Exterior machine 2D model with structural features

(b) Exterior machine simplified 2D model

Figure 3.54 Comparison of 2D model geometry – exterior machine

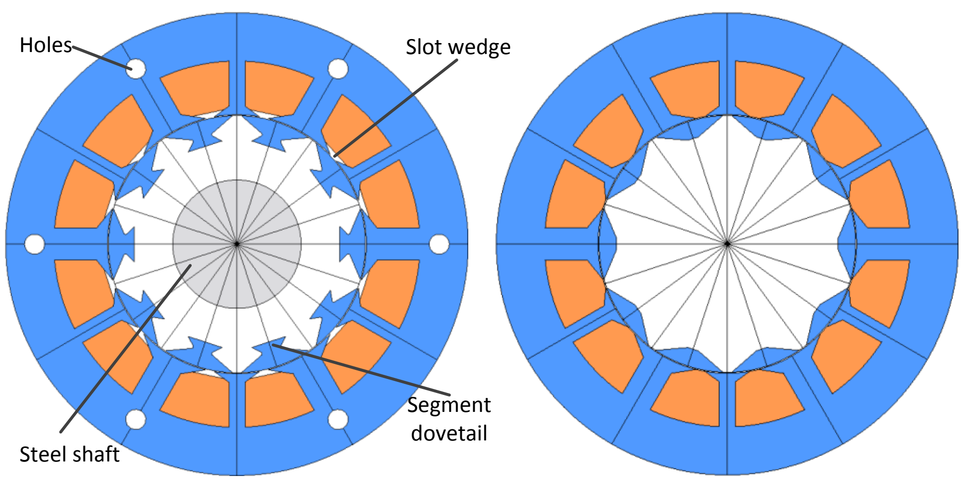

(a) Interior machine 2D model with structural features

(b) Interior machine simplified 2D model

Figure 3.55 Comparison of 2D model geometry – interior machine

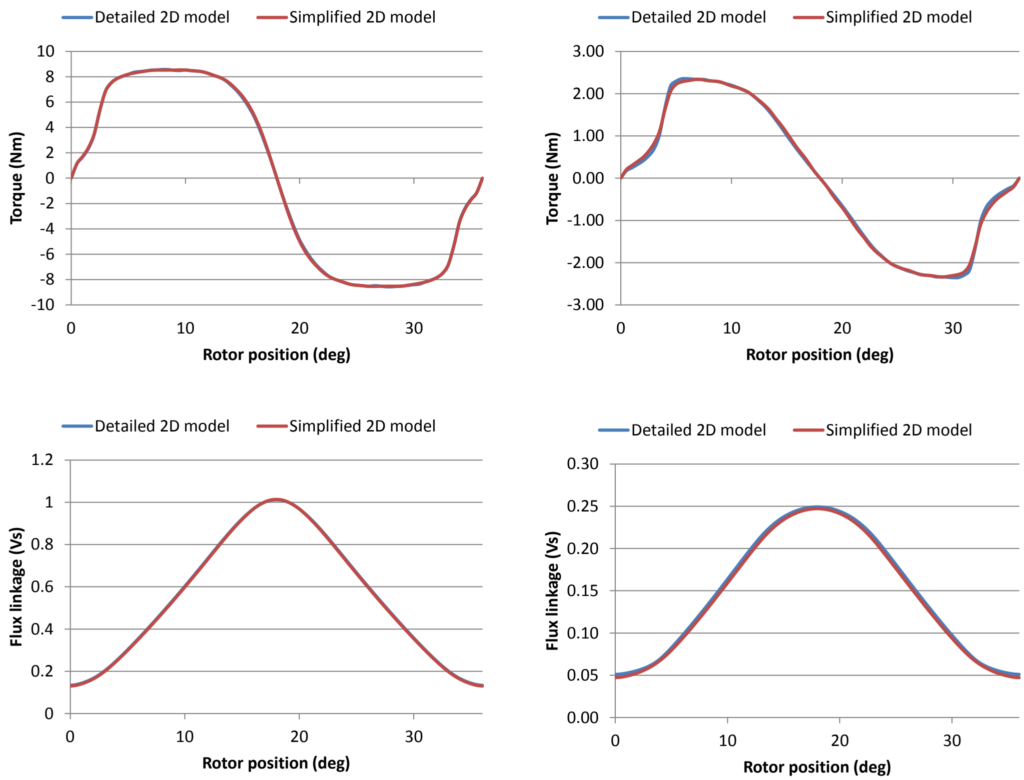

(a) Torque and flux linkage comparison - exterior machine

(b) Torque and flux linkage comparison - interior machine

Figure 3.56 Comparison of torque and flux linkage of different models

Mutual inductance impact

Throughout the parameter selection process, average torque estimation assumes negligible mutual inductance between phases. For a three phase machine, only one phase is excited in the majority of time, during which torque is only affected by the change of self-inductance of the phase. However, during the commutation between phases, there are moments when two phases are excited (one phase experiencing a current rise while the other experiencing a current drop). This introduces a torque component that is contributed by the change of mutual inductance between phases. Like conventional SRMs, segmented rotor SRMs have a relatively insignificant mutual inductance component. Figure 3.57 and Figure 3.58 compare self and mutual inductance of interior and exterior SSRMs under different excitation levels. For both machines, mutual inductance is low for all rotor positions and the curves are difficult to differentiate because inductance values are close to zero. On average, the magnitude of mutual inductance is 4% of the magnitude of self-inductance for the interior machine. The exterior machine has slightly higher mutual inductance, averaging at about 5% of self-inductance. Steady state torque is simulated for the exterior machine at two rated speeds using an RT model (neglecting mutual inductance effect) and an FEA model with incorporated circuit simulation (mutual inductance is accounted for), see Figure 3.59 and Figure 3.60. Small differences in torque are observed comparing the two models, which confirms that mutual inductance has negligible impact on machine performance.

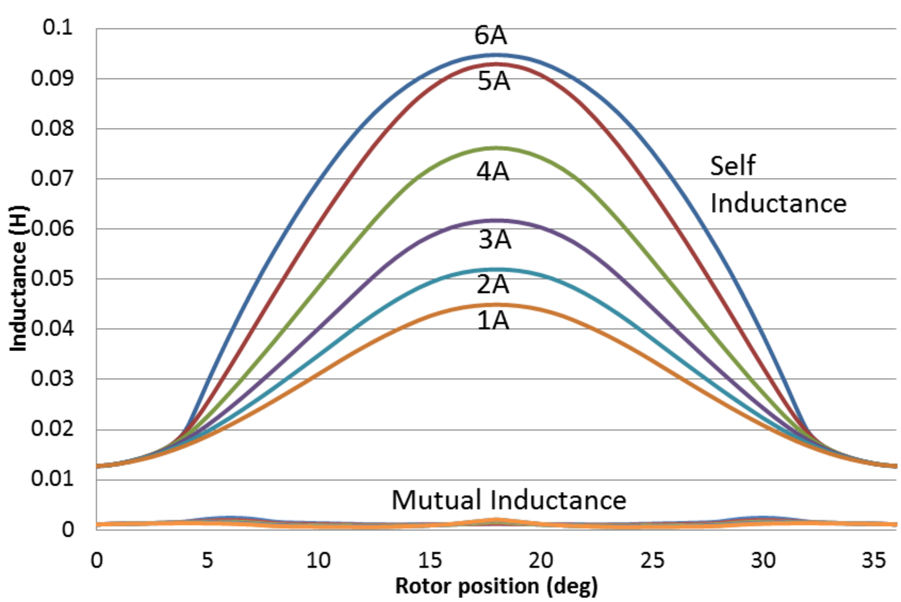

Figure 3.57 Comparison of self and mutual inductance of the interior machine

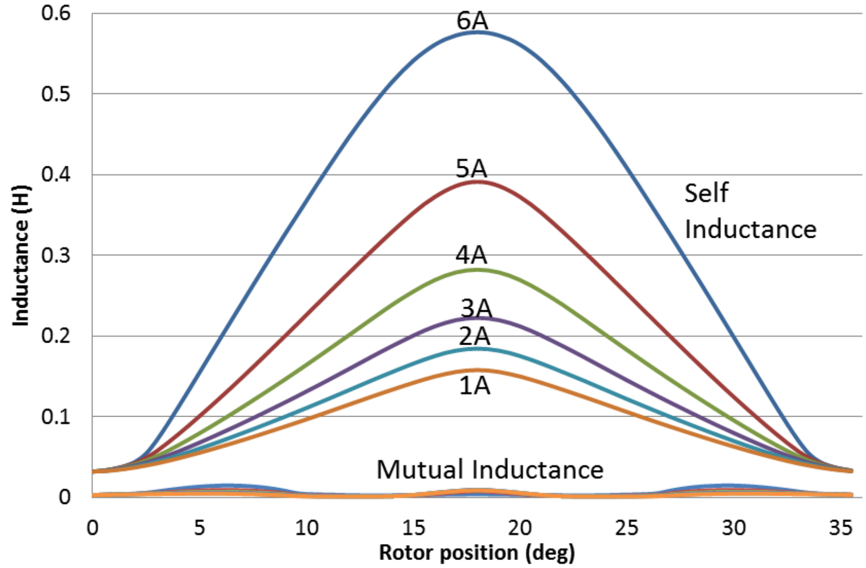

Figure 3.58 Comparison of self and mutual inductance of the exterior machine

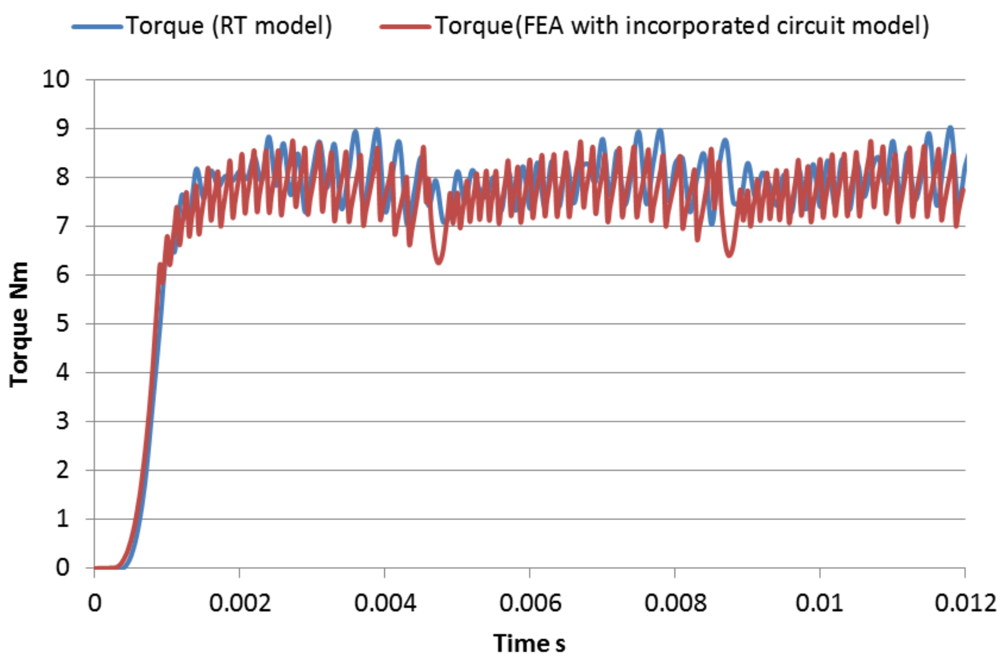

Figure 3.59 Comparison of torque calculation - exterior machine at 500 rpm

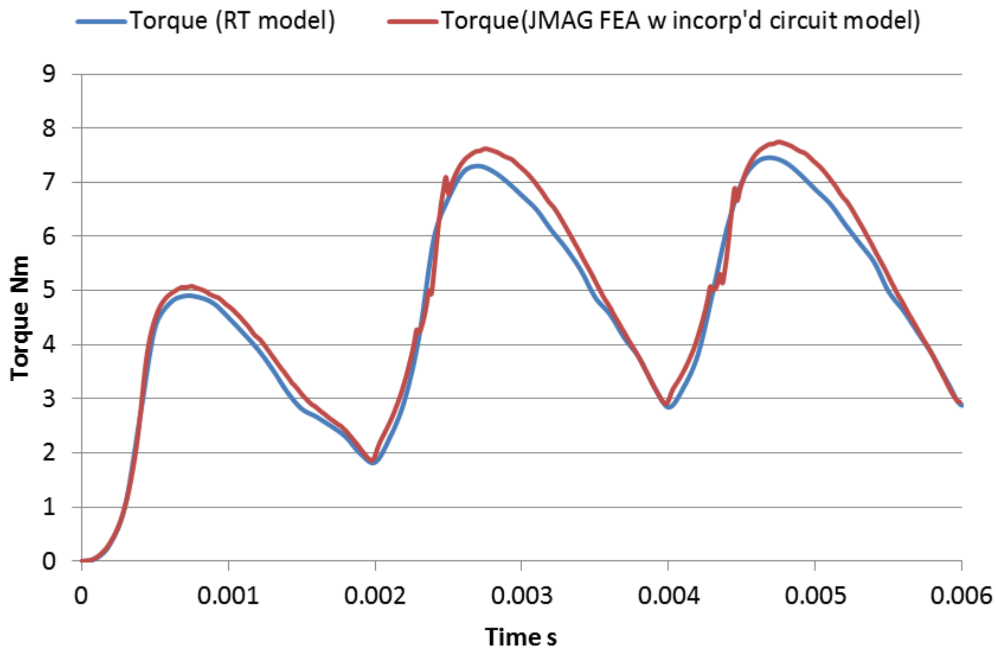

Figure 3.60 Comparison of torque calculation - exterior machine at 1000 rpm

3D effect

2D FEA analysis has been used extensively in the study due to its ability to give faster solution and better convergence than 3D analysis. To investigate the 3D effect on machine performance, a 3D model is created and analyzed for static torque and flux linkage at various rotor positions under rated current. The 3D model is generated by extruding the 2D mesh in the axial direction. For details please refer to section 3.3.1. Figure 3.61 compares torque and flux linkage of both machines between the 2D and 3D models. Torque difference is insignificant with the curves almost being identical between the models. For both the exterior and interior machines, 2D model underestimates flux linkage at all rotor positions. This is mainly due to the fact that flux contributions of the end windings are not accounted in the 2D model. On average, 2D model underestimates flux linkage by 7% for the exterior machine and 10% for the interior machine. Higher flux linkage could result in an extended current rise portion, which may reduce the constant torque operating region of the machine. Recall that in the parameter selection process, a smaller winding turn number is selected to allow a margin on the machine's torque-speed envelope. As a result, the machine design should still satisfy the output objective even though the model underestimates flux linkage.

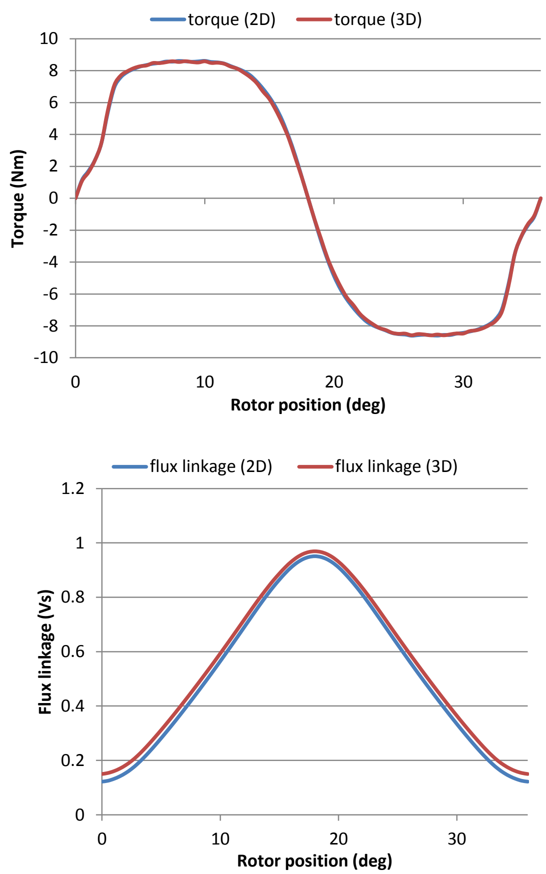

(a) Torque and flux linkage comparison - exterior machine

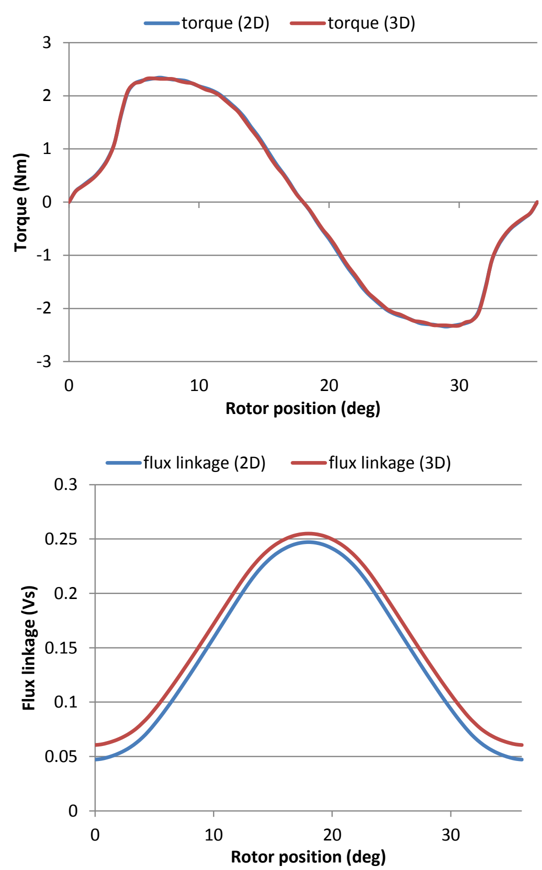

(b) Torque and flux linkage comparison - interior machine

Figure 3.61 Comparison of torque and flux linkage of 2D and 3D models

3.6. Summary

This Chapter presents the design of double segmented rotor SRMs. A family of 8 DSRSRM topologies is proposed and discussed in section 3.1. The central stator DSRSRM design has a compact structure suitable for HEV powertrains and is selected for prototyping. As a unique feature of the prototype design, stator flux path sharing is explained and investigated in detail. Then the prototype machine FEA model is presented, followed by explanation of loss estimation and machine drive simulation. The complete design parameter determination procedure is presented. To allow benchmark comparison of the prototype to a conventionally structured double rotor SRM, some parameters are fixed while the others are locally optimized for performance. A number of geometric simplifications are proposed to reduce model complexity of the design. A design parameter characteristic study is conducted to understand the importance of some unique geometry parameters in an SSRM. Based on the result of the study, high-impact parameters are identified and determined first, followed by other parameters. Finally, the optimized design is verified by comparing the results to more sophisticated models that account for geometric details, mutual inductance and 3D effect.

CHAPTER 4
REALIZATION OF THE DOUBLE SEGMENTED ROTOR SWITCHED RELUCTANCE MACHINE

In this chapter, the mechanical construction of a prototype Double Segmented Rotor Switched Reluctance Machine based on the final design concluded in Chapter 3 will be presented. The overall mechanical design will be introduced first, followed by discussions of the manufacturing processes of major components. The design work is carried out using 3D CAD modelling software.

4.1. Overall Assembly

The DSRSRM consists of three major components: the exterior rotor, the central stator and the interior rotor. Figure 4.1 shows the general layout of the components in an exploded view. The interior rotor is located in the center of the stator assembly through a pair of bearings on its shaft ends. The exterior rotor, which also includes the outside casing of the machine, encloses the stator and interior rotor. The exterior rotor is also supported by two bearings, one large diameter bearing on the rear end of the stator assembly and a standard size bearing on the front shaft end of the interior rotor. The output shaft of the exterior rotor is a stub shaft located on the front end plate of the exterior rotor shell. The machine is mounted to a frame through connection joints on the rear end of the stator, which exits from the exterior rotor through the opening of the large bearing hole. A cross sectional view of the assembly is shown in Figure 4.2.

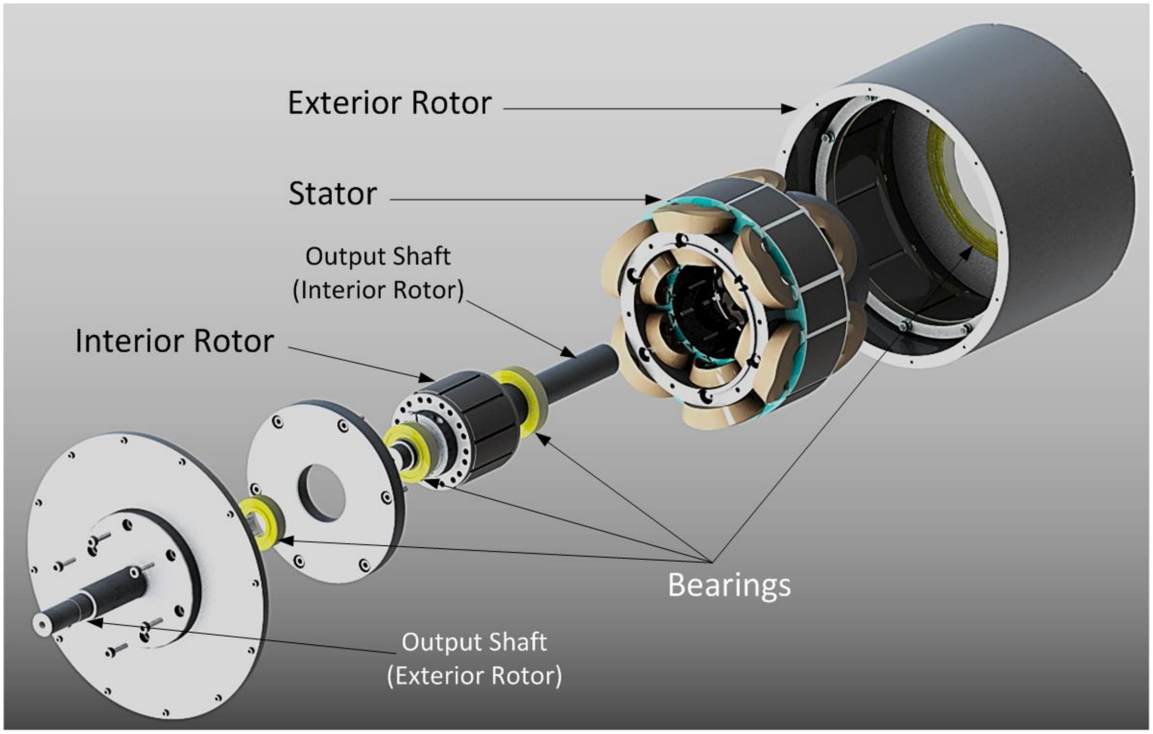

Figure 4.1 Overall exploded view showing relationship between major components

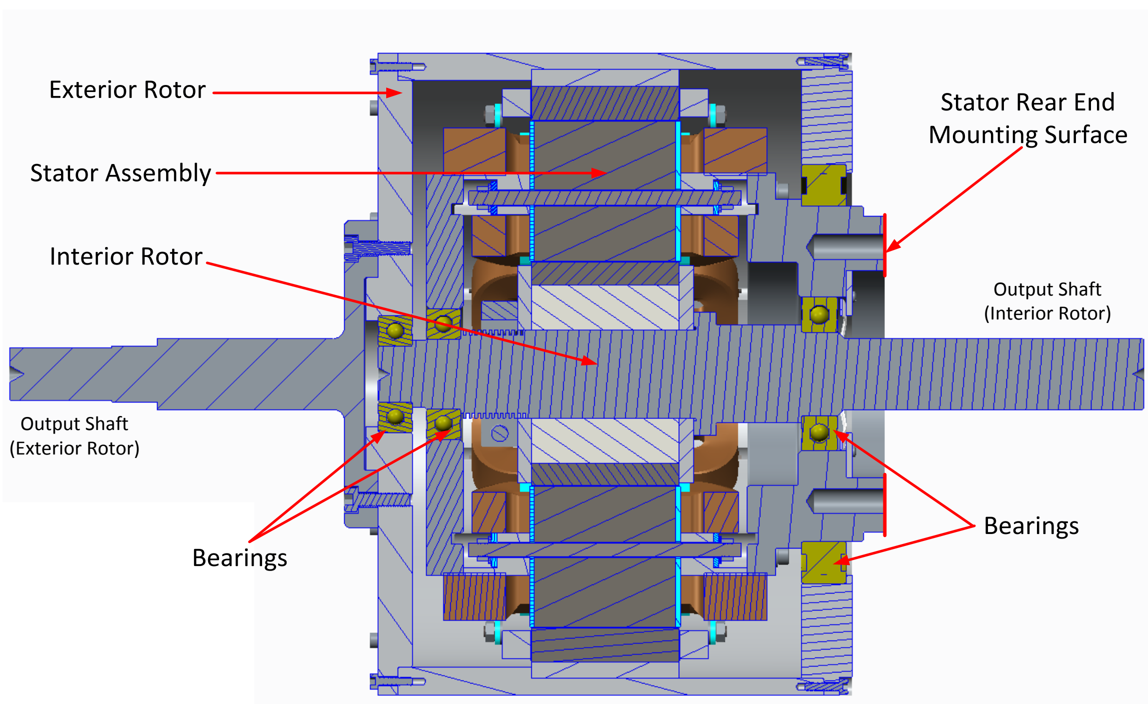

Figure 4.2 Section view showing machine assembly

Note the stator is only fixed at one side, being bolted onto a structure frame as shown in Figure 4.3. This leaves a relatively long unsupported end on the exterior shaft. To reduce deflection at the shaft end, an extra bearing support is added in the left-hand mounting plate such that the machine is supported between two structural plates, as shown in Figure 4.3. Encoders are installed on both shafts to provide positional feedback.

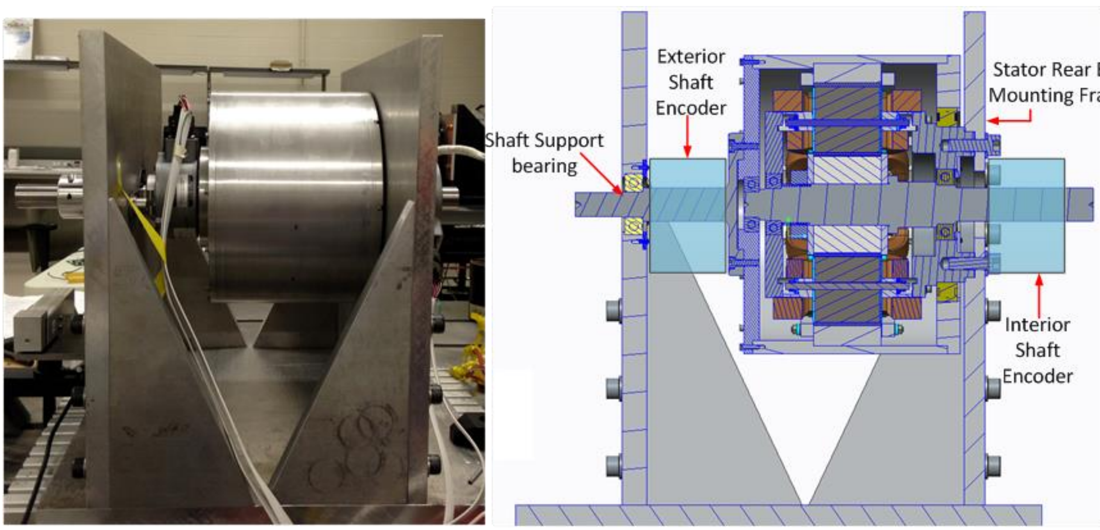

(a) Photograph of total assembly

(b) Section view of total assembly

Figure 4.3 Section view of total assembly with mounting frame

4.2. Lamination

Apart from copper windings, iron cores made of laminated electrical steel sheets make up for the rest of active material of a switched reluctance machine. As the only magnetic conducting material in the machine, lamination dominantly affects machine performance. The majority of electromagnetic analysis conducted in the machine design process is to determine the size and geometry of rotor and stator laminations. The prototype machine uses M15 gauge 29 electric steel, which has a thickness of 0.35mm.

Highest level C5 coating is applied at both sides of the laminations to improve insulation. The laminations are stacked to the required height of 50mm.

Two machining methods, laser cut and wired electrical discharge machining (EDM) are considered for manufacturing the lamination. Laser machining is good for cutting thin material. For the 0.35mm thickness steel lamination, it can achieve a size tolerance of ±0.05mm. The machining process is fairly quick and does not require additional tooling, making laser cutting a popular choice for electric machine prototyping. In comparison, wired EDM is a time consuming machining process due to its low material removal rate. However, tighter tolerance, as small as ±0.01mm can be achieved with wired EDM. And because wired EDM cuts a stack of laminations rather than a single piece (as in laser) each time, machining consistency is better. EDM is not commonly used in machining electric machine laminations due to its high cost. To gain a more realistic measure of cost and accuracy of the process, a sample that contains two stacks of interior rotor segment laminations and a section of the aluminum holder block was made, shown in Figure 4.4.

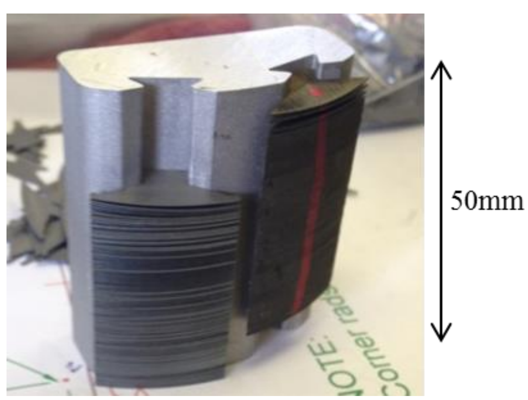

Figure 4.4 Wired EDM machined interior rotor lamination sample

As expected, high part accuracy is achieved; allowing a desirable amount of interference fit between the segment laminations and the dovetail slots. However, it is also found that cutting speed needs to be halved when cutting steel laminations than steel blocks because the insulation on the lamination impedes the electrical discharge process. For the rotor segment lamination machining, wired EDM is estimated to cost three times as much as laser cutting. For this reason, Laser cutting, instead of wired EDM was chosen as the machining method for the laminations. Some additional processes (e.g. post-machining) were introduced to maintain the fit and accuracy of critical dimensions with the enlarged tolerance of laser machining. These processes will be described in detail in following sections on the manufacturing of major components.

4.3. Interior Rotor

The interior rotor assembly, see Figure 4.5 for a photograph, consists of an aluminum holder block inserted with 10 stacks of segment laminations, a shaft, two clamping plates and a threaded collar for locking the clamping plates. Figure 4.6 shows the assembly in an exploded view.

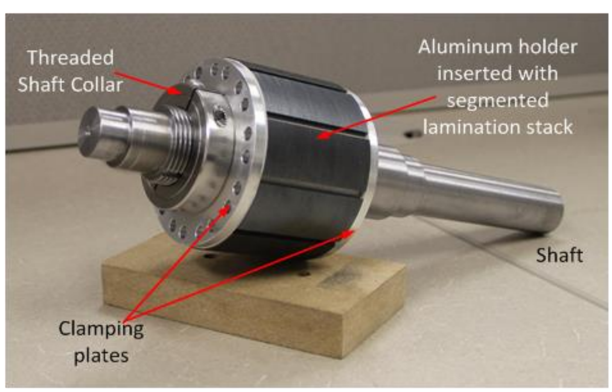

Figure 4.5 Photograph of interior rotor assembly

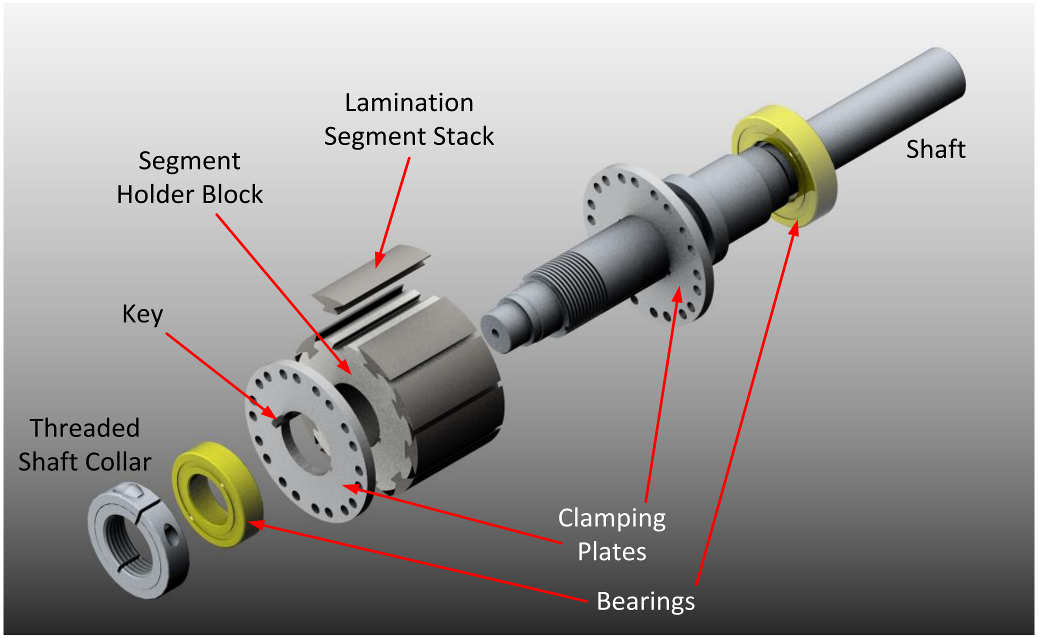

Figure 4.6 Exploded view of interior rotor assembly

The segmented rotor design requires lamination segments be inserted into a holder block made of non-magnetic material. The segments are designed to have a dovetail tip and the aluminum holder is machined to have corresponding dovetail slots, as shown in Figure 4.7 (a) and (b). In SRM rotor manufacturing, the most critical requirement is the accuracy and concentricity of the air gap diameter, or the rotor surface diameter. Normally a tolerance of around ±0.025mm is demanded. The segmented lamination makes things worse because both size and fit of the segments affect the air gap diameter of the assembled rotor. To maintain the desired tolerance, the rotor diameter is cylindrically ground to size after being assembled. As a result, the segments are machined oversize in the laser cutting process, with a 0.4mm allowance on the curved surface, leaving enough extra material for post machining operation. A tiny notch is added near the right side of the segment dovetail to mark the direction of segment placement, see

Figure 4.7(a). The laser machining process leaves burrs on one side of the lamination, which causes damage to the insulation on the same side when later deburred. This is acceptable as long as the segments are stacked in the same orientation so that the insulation damaged sides are not touching, forming an insulation weak spot. To ease segment assembly, a clearance fit was chosen between the segments and holder dovetail slots. Based on the inspection of samples, a 0.025mm oversized dovetail slot ensures a running fit with all segments machined with actual size specification (this indicates that the positive maximum tolerance of the segments is within 0.025mm, even though a 0.05mm tolerance is specified by the manufacturer). A 95% stacking factor was achieved on interior rotor laminations.

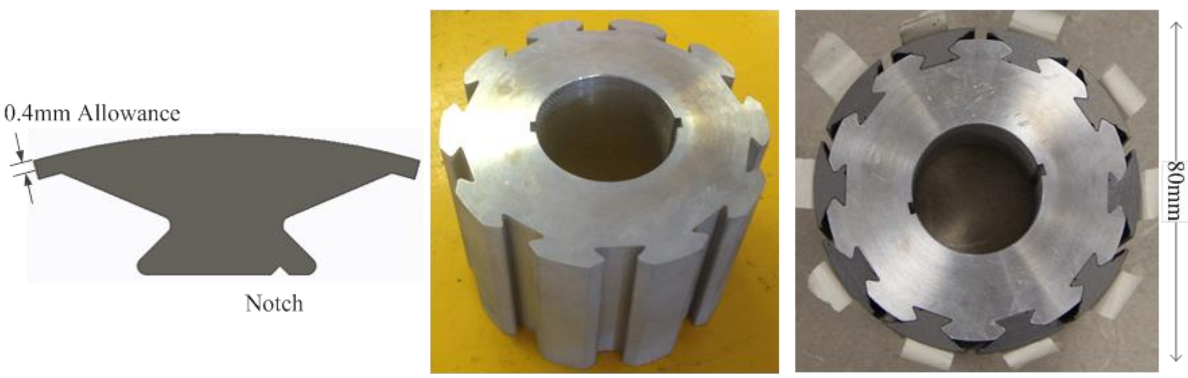

(a) Interior rotor lamination segment (b) Aluminum segment holder block (c) Holder with lamination segments inserted

Figure 4.7 Lamination segment and segment holder

After lamination segments are inserted into the aluminum holder, the assembly is installed on the shaft, with clamping plates on each side. The clamping plates are drilled with 20 holes near the circumferential. These holes align with dovetail tips of the slots, providing passages for epoxy resin to fill the gap between segment and slot in the later resin impregnation process. Nomax insulation paper is applied to the contact surface between clamping plate and holder block to minimize eddy current loss. A clearance fit is specified between the holder block and shaft to avoid distortion to the holder block during assembly. The tangential location of the segment assembly is locked by a pair of keys. Finally, a threaded shaft collar is installed against the outside clamping plate to provide an axial clamping force.

The interior rotor assembly is then treated using VPI (vaccum pressure impregnation). This process is normally only applied to electric machine stators to enhance insulation, thermal conductivity and mechanical strength of the stator windings. Here, the purpose of the VPI treatment is to fill the gaps between segments and holder block with epoxy resin, increasing the rigidness of the assembly as a whole. Release agent is applied to sections of the shaft to avoid leaving resin residuals on critical surfaces, see Figure 4.8(a). The VPI treated rotor outside diameter is then ground to actual size with a 0.01mm tolerance, see Figure 4.8(b) for a photograph of the finished rotor.

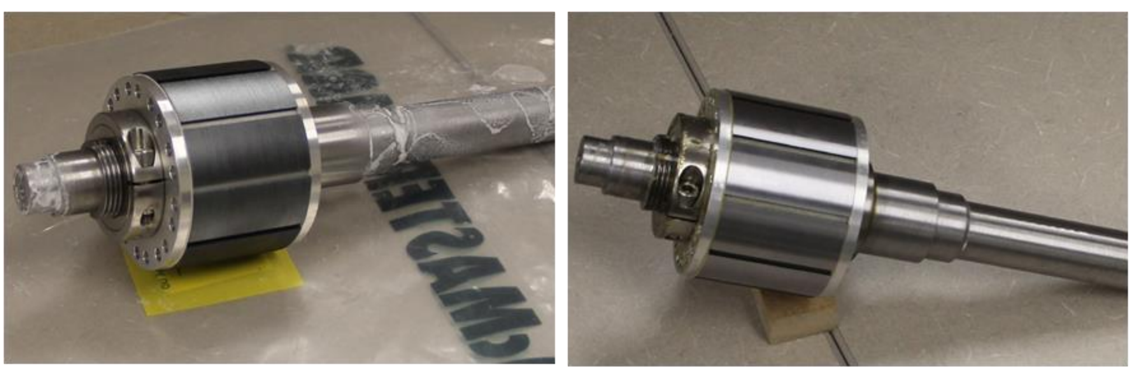

(a) Interior rotor before VPI

(b) Interior rotor after VPI and cylindrical grinding

Figure 4.8 Photographs of interior rotor under different processes

This post-machining process is critical in ensuring a uniform air gap length because it corrects concentricity and roundness errors introduced during assembly.

Finally, before bearings are installed on the shaft, the interior rotor is dynamically balanced under rated maximum rotation speed of 4000 RPM.

4.4. Exterior Rotor

The exterior rotor consists of the machine exterior casing, the segmented lamination assembly and two bearings. Figure 4.9 shows the arrangement of different parts in the exterior rotor. Note the front of the rotor is facing away in the figure.

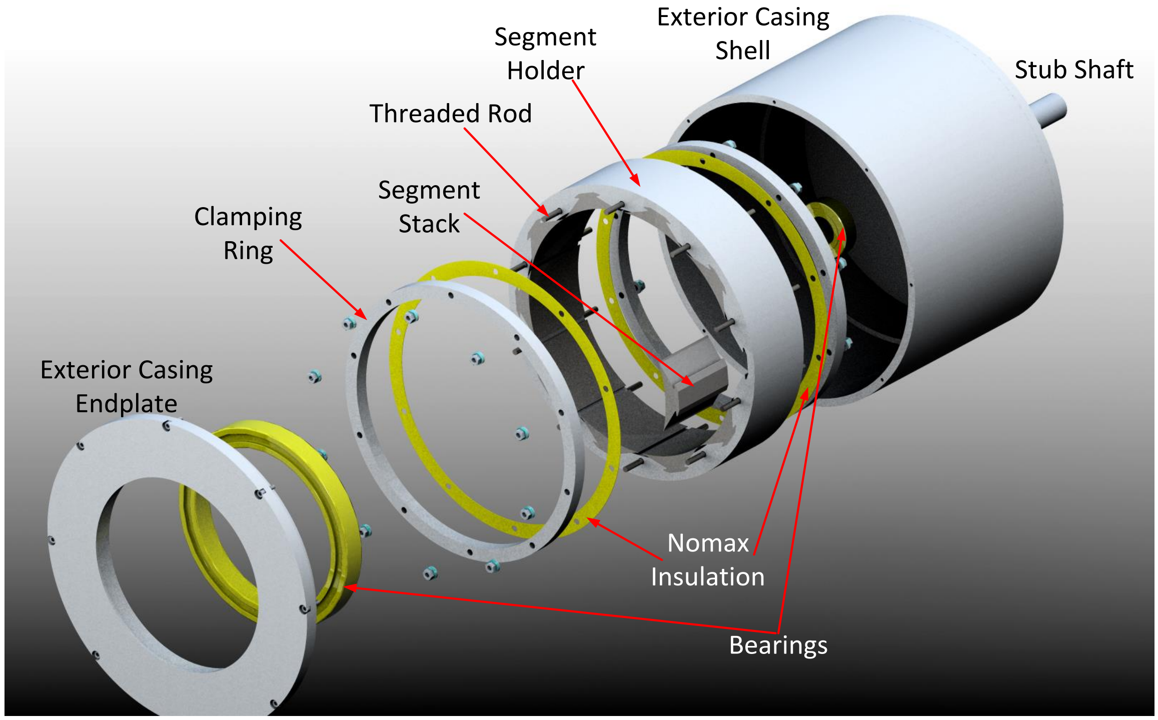

Figure 4.9 Exploded view of the exteior rotor assembly

The segmented lamination assembly, Figure 4.10(c), includes an aluminum segment holder, Figure 4.10(b), inserted with segmented laminations, Figure 4.10(a), and two aluminum clamping rings on both sides. It is housed inside the shell of exterior casing with an interference fit. Similar to the interior rotor design, the segment of the exterior rotor also features a dovetail end (to be fitted into a segment holder with slots of corresponding geometry), a notch marking placement orientation and a 0.4mm allowance for post-machining process. Again, the segment holder is machined from an aluminum plate using wired EDM. Note wired EDM is chosen as the machining process not only because it gives a very tight tolerance but also due to the fact that conventional methods are not available for this work (having an interior profile with a relatively small diameter). Laser and waterjet are also possible alternatives, but they are not as good as wired EDM when cutting thicker materials. The slots are machined oversize by 0.05mm to ensure clearance fit of the segments. 10 stainless steel threaded rods join the two clamping rings and provide clamping force to the segment stacks.

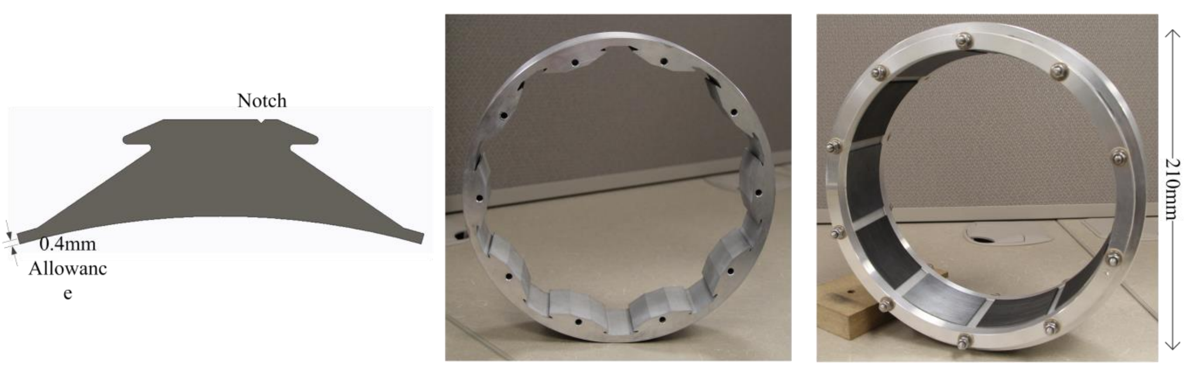

(a) Segmented lamination (b) Aluminum Segment Holder (c) Segment lamination assembly

Figure 4.10 Segment Lamination and segment holder

Special consideration is given on rotor electrical insulation to reduce eddy current loss in the aluminum holder. If not properly insulated, the stainless steel threaded rod, clamping ring and holder can form electrical conducting loops around rotor segments, resembling the squirrel cage in induction machines, which may cause significant loss due to induced magnetic field change. Therefore, insulation is applied to the threaded rods, Figure 4.11(a), and the clamping surfaces, Figure 4.11 (b) and (c). Nomex insulation paper is wrapped around the threaded rods so that there is no electrical connection between the rod and the aluminum holder. The PEEK washers insulate the rods from the clamping rings. Between the holder and the ring, there is also insulation paper applied. The assembled exterior rotor is VPI treated (see Figure 4.12) in the same way as the interior rotor to increase the rigidness of the assembly.

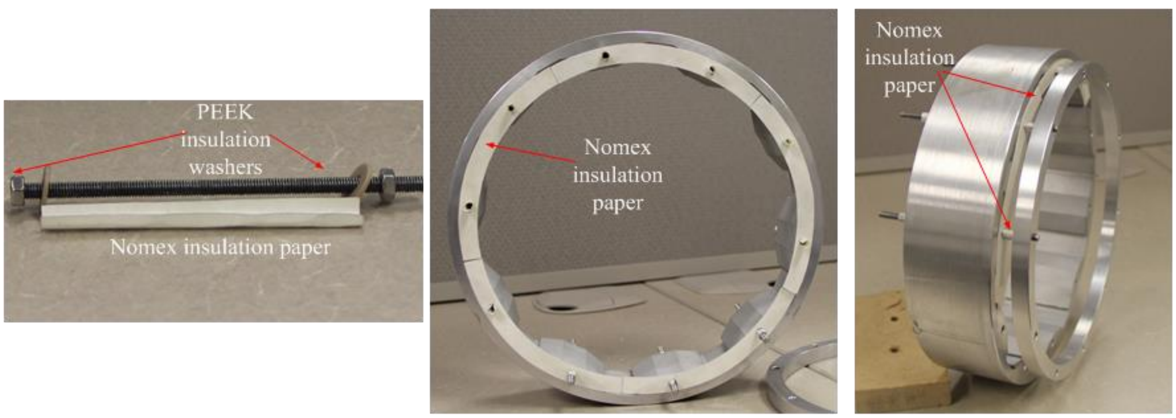

(a) Insulation on threaded rod (b) Insulation on clamping ring (c) Insulation in assembly

Figure 4.11 Electrical insulation on exterior rotor

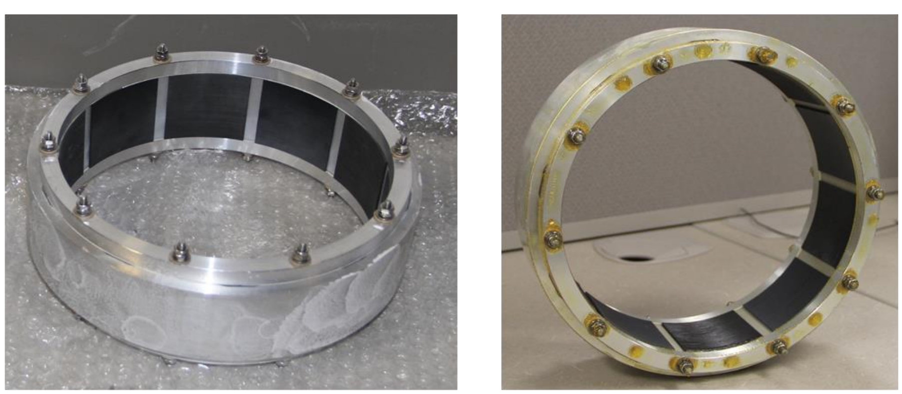

(a) Outer surface coated with release agent before VPI (b) Exterior rotor after VPI

Figure 4.12 Segmented lamination assembly before and after VPI treatment

The exterior casing is machined from aluminum and includes a tube housing the lamination segment assembly, a front endplate connecting to a stub shaft and a rear endplate. According to stress calculation, a 0.1mm interference fit is applied between the segment holder outside diameter and casing tube interior diameter. Figure 4.13(a) shows the exterior casing being heated to 250 ℃ for a shrink fit. To minimize distortion during the shrink fit, a thicker rotor casing tube is kept by leaving the outside diameter unfinished at the time of assembly and is machined to actual size, see Figure 4.13(b), after segment holder is inserted in. The alignment diameters of the two endplates are machined last to account for dimension changes of the casing interior due to shrink fit. Figure 4.13(c) shows the assembled exterior rotor.

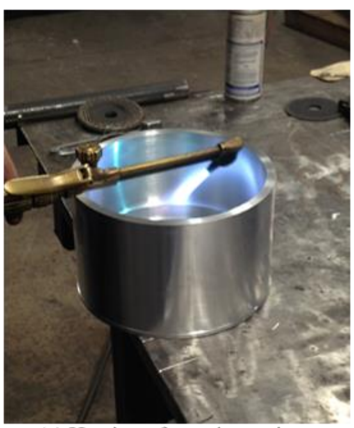

(a) Heating of exterior casing (shrink fit)

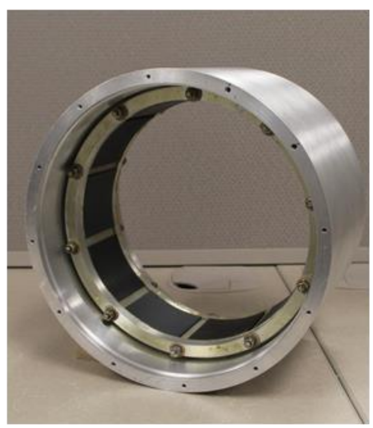

(b) Exterior casing machined to actual size after shrink fit

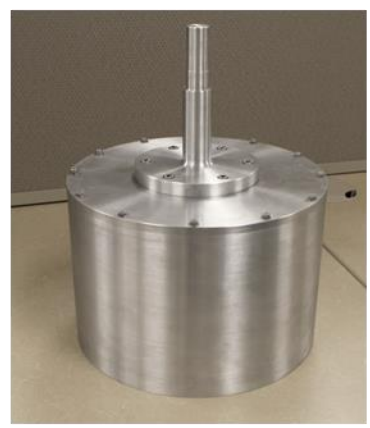

(c) Exterior rotor assembled

Figure 4.13: Exterior rotor shrink fit and assembly

To ensure concentricity, the air gap diameter (interior diameter of the segment assembly) is ground on a cylindrical grinding machine. Grinding is performed with all rotor parts assembled (except the endplate at back, which leaves an opening for the grinding wheel to enter). The rotor is chucked on the stub shaft and centered on shaft axis.

Like the interior rotor, this post-machining operation corrects misalignment introduced during component assembly, which helps to maintain a uniform air gap. Because the exterior rotor is designed to be running at low speeds (maximum1000 RPM), rotor balancing is not performed.

4.5. Stator

The stator is the most complicated component in the DSRSRM. It includes the iron core lamination stack, exterior and interior machine coil windings, clamps and endplates, as well as insulation sheets and wedges. Figure 4.14 shows a photograph of the assembled stator.

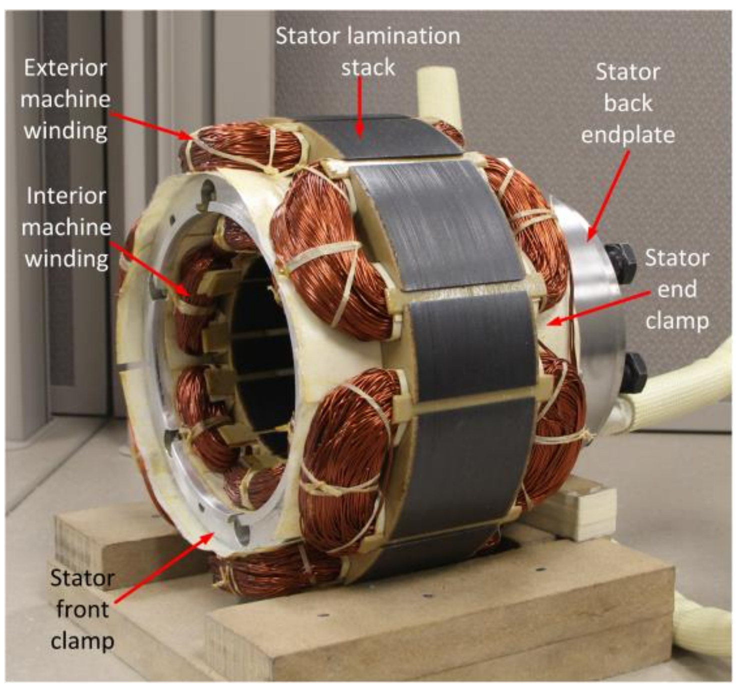

Figure 4.14 Photograph of stator assembly (front endplate removed)

At the center of stator are stacked electric steel laminations, sandwiched by two insulation sheets cut to the same geometry as the stator cross section. Two ring shaped aluminum clamps are placed on the two sides of the lamination stack, aligned with the stator yoke and jointed by six stainless steel threaded rods. The assembly is terminated at the two ends by two mild steel endplates, which house bearings for the interior rotor. Figure 4.15 shows the stator assembly in an exploded view.

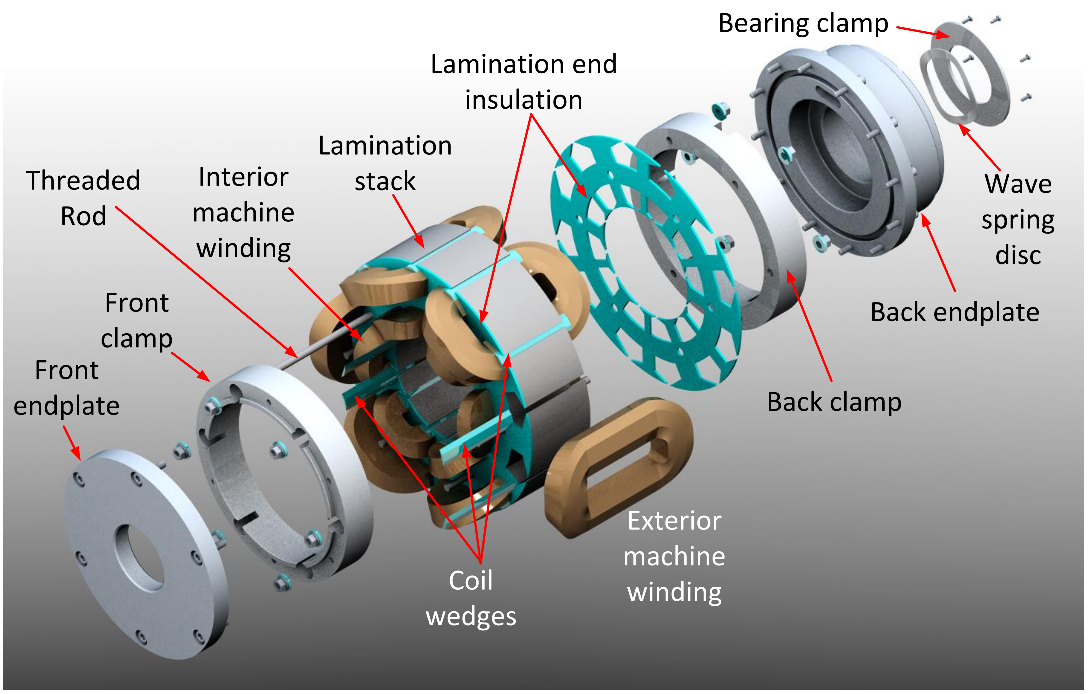

Figure 4.15 Exploded view of the stator assembly

The stator laminations are also manufactured by laser machining. Unlike rotor laminations, which are handled individually for flexibility during segment insertion, the stator laminations are glued together to form a single stack. Figure 4.16(a) shows a photograph of the bonded stator lamination stack. Bonding eliminates movement of individual laminations during assembly, improving alignment accuracy. In addition, the thin laminations form into a single solid piece, which has improved mechanical strength and is more resilient to tear and deformation during assembly and winding installation.

On the two ends of the stack are two 1/16 inch thick glastic insulation sheets, laser cut to the same dimension as the steel lamination. These sheets electrically insulate the iron core from coil windings. They are also softer, which protect the coil insulation from being scratched by sharp edges of the lamination.

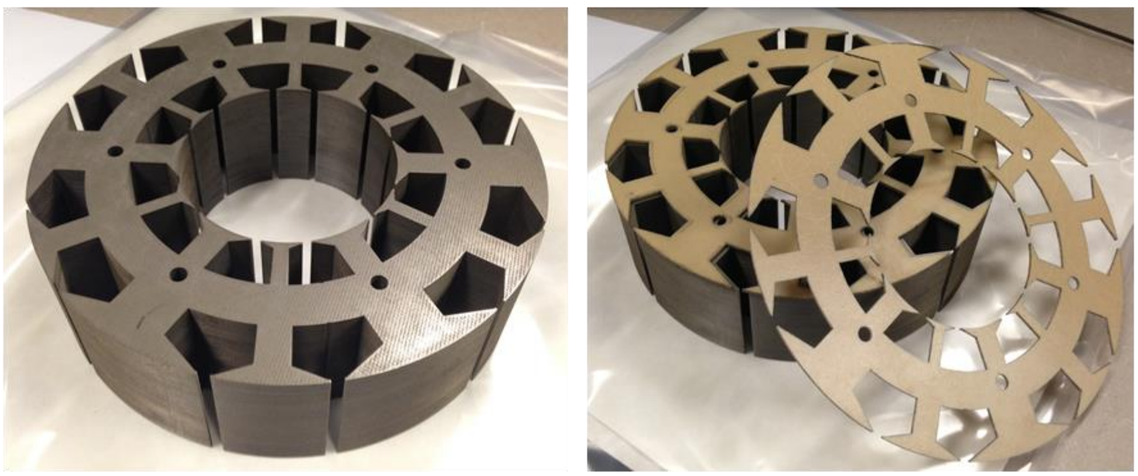

(a) Bonded stator lamination stack (b) Stator lamination end insulation

Figure 4.16 Stator lamination and end insulation

Six non-magnetic conductive stainless steel threaded rods go through the holes on stator yoke, connecting the two aluminum clamps. To avoid the rods and aluminum clamps forming electrical conducting loops, which could increase eddy current loss, insulation is required. Similar to the exterior rotor construction, insulation paper is wrapped around the threaded rod and non-metallic washers made of PEEK are used, see Figure 4.17. Because of the laminated construction of the stator core, it is difficult to rely on alignment features such as grooves or spigots. Alignment tooling is used to ensure the concentricity between the back clamp and stator air gap diameter, see Figure 4.18 (a) and (b). The front clamp is not aligned using tooling. Concentricity error is corrected by a post-machining process that grinds the bearing housing diameter of the front endplate, see

Figure 4.18 (c). The bearing housing is ground with front endplate assembled and is centered with reference to the stator air gap diameter, which ensures concentricity between the shaft and the air gaps.

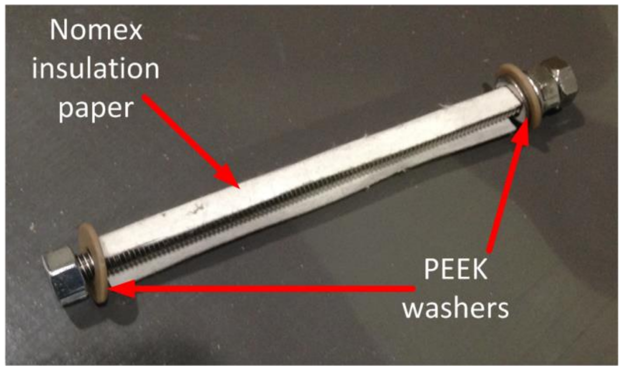

Figure 4.17 Insulation of threaded rods

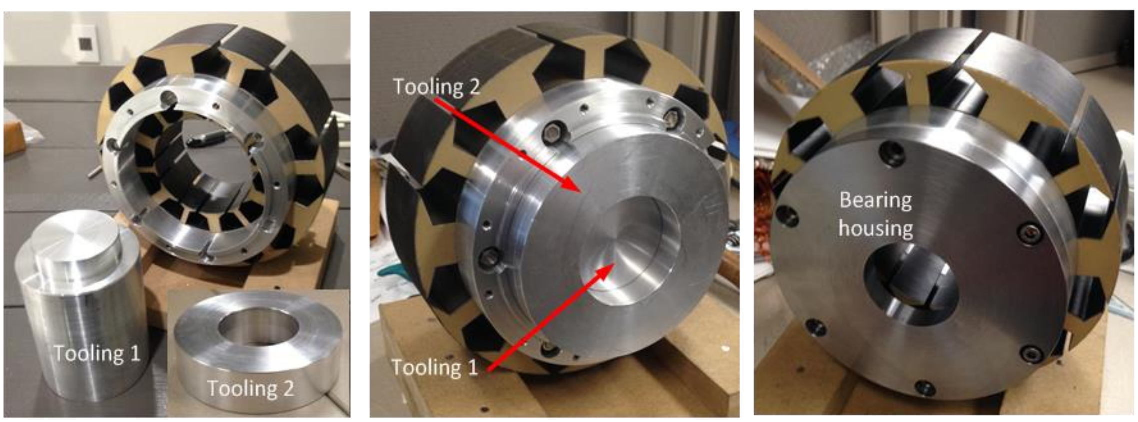

(a) Tooling for back clamp alignment

b) Back clamp assembled with tooling

(c) Grinding of front endplate bearing housing diameter

Figure 4.18 Alignment control of stator components

Once the two clamps are assembled, the stator core is ready to be wound with coils. In order to achieve a high packing factor and uniform winding size, coils for each pole are axially wound on a winding tooling, shown in Figure 4.19 (a). The completed coil windings are then installed on the stator core. A wooden 1:1 duplicate of the stator slot is produced using water jet machining, see Figure 4.19(c). The desired filling factor is tested on the slot duplicate. Both the interior and exterior windings are wound with two passes of AWG #22 (0.32mm^2 cross sectional area) size wires, i.e. two wires paralleled together to form one turn. The exterior windings achieve a 39% slot fill factor and the interior windings achieve a 35% slot fill factor.

(a) Winding tooling (b) Completed coil windings (c) Wood stator slot duplicate

Figure 4.19 Making coil windings

Before coils are installed on the stator, all stator core surfaces that may come into contact with coils are insulated with Nomex insulation paper, see Figure 4.20(a). The slot liners insulate coils from stator laminations and the end winding insulation separates coil end winding with the clamp. Coils for each stator pole are then inserted into the slots through the two slot openings, see Figure 4.20(b). Lacing ties are passed through the end winding section of the coils and are later tightened to restrain movement of wires. Upon complete insertion of a coil winding, slot wedges, see Figure 4.20(c), made of Delmart (high temperature and non-electric conductive plastic) are added so that wires are contained within the slots.

In the meantime of coil winding installation, sensors are inserted at various locations on the stator. Both the exterior and interior machines have 6 sensors, which include 5 5kΩ thermistors for temperature measurement and one search coil for flux linkage measurement. The search coils are wound on stator phase poles, with 10 turns of AWG #32 wires. The locations of the thermistors are summarised in Table 4.1 and are also illustrated in Figure 4.21.

(a) Slot liners and insulation (b) Insertion of wound coils (c) Installed coil winding

Figure 4.20 Installing wound coils on the stator

Table 4.1 Sensor locations of thermistors

Thermistor	Sensor location	Description
1	Back iron	In the middle of a slot, against back iron
2	Termination coil	Embedded in end winding, on the termination side
3	Non-termination coil	Embedded in end winding, on the non-termination side
4	Coil center	Embedded in coil center, middle of a slot
5	Stator pole	In the middle of a slot, against stator pole

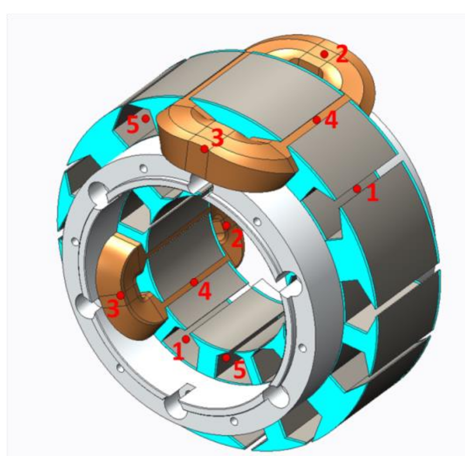

Figure 4.21 Diagram of thermistor locations

With all coils installed, lead wires on the termination end of the coil are organized and numbered. Lead wires of all six phases and 12 sensors are bundled and passed through a wiring opening on the stator back endplate, see Figure 4.22(a). Again, all contacting surfaces with the wires on the stator are insulated with Nomex insulation paper. The assembly is then VPI (vacuum pressure impregnation) treated. In the VPI process, the stator assembly is first submerged in a vacuum chamber filled with epoxy fluid. The vacuum pressure empties air in the gaps of windings and fills the gaps with epoxy. The epoxy coated stator is then baked in an oven to let the epoxy solidify. This process improves the thermal conductivity, electrical insulation and mechanical strength of the windings. Figure 4.22(b) shows the stator assembly after VPI treatment. Note the front endplate is removed during the VPI process to avoid forming permanent bonding with the clamp, making it difficult to disassemble the plate when installing the interior rotor.

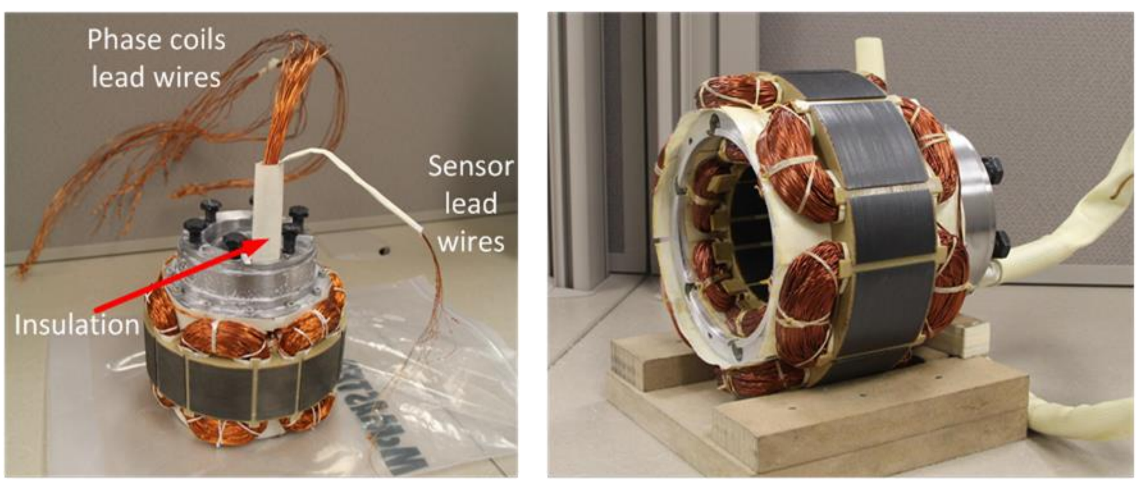

(a) Lead wires in stator assembly

(b) Stator assembly after VPI treatment

Figure 4.22 Lead wire arrangement and assembling of back endplate

4.6. Summary

This Chapter explains the manufacturing details associated with the DSRSRM prototype construction. The Chapter starts with an explanation of the overall mechanical structure of the prototype, and then continues on with discussion of the construction process of each machine sub-assembly. Both the stator laminations and rotor segment laminations are produced by laser cutting. The stator laminations are bonded with epoxy glue to form the stator iron core while the rotor segments are held in place through dovetail slots in wired electrical discharge machined aluminum holders. Concentricity of the assembly is maintained through the use of alignment tooling and cylindrical grinding of critical diameters. Electrical insulation is required at a number of locations and is discussed throughout the Chapter. The rotor and stator assemblies are treated with the VPI process to improve the electric insulation, mechanical rigidness and heat conduction capability of the prototype.

CHAPTER 5
EXPERIMENTAL VALIDATION OF DSRSRM

5.1. Static Tests

Both static and dynamic experiments are conducted on the DSRSRM prototype machine to comprehensively evaluate the machine performance. Static refers to the fact that tests are conducted with fixed rotor position. Because of the limitation of test equipment, it is difficult to obtain accurate instantaneous measurements of torque and flux linkage while the machine is operating. Static tests, on the other hand, are good at capturing these rotor position dependent parameters. Rotors of both interior and exterior machines are locked at pre-defined positions, and static torque and flux linkage are measured under different excitation current levels.

5.1.1. Apparatus

Figure 5.1 illustrates the simple mechanism used for locking rotor position as well as taking torque measurements. The rotor shaft is joined together with a rectangular arm through an aluminum shaft holder. At the end of the arm, there is a threaded rod, the height of which can be adjusted by rotation. The rod is held perpendicular to a loadcell measurement surface. Torque on the rotor shaft is simply the product of rod end force and horizontal length between shaft center and rod center. Because the arm length is fixed, the apparatus effectively turns torque measurement into force measurement. Clamping force on the rotor shaft is adjustable through a setscrew on the shaft holder. By unscrewing the setscrew, rotor position can be changed. An optical encoder mounted on the rotor shaft returns rotor position, which has a minimal resolution of less than 0.1 degree. The same apparatus are used for both interior and exterior machine static tests, see Figure 5.2.

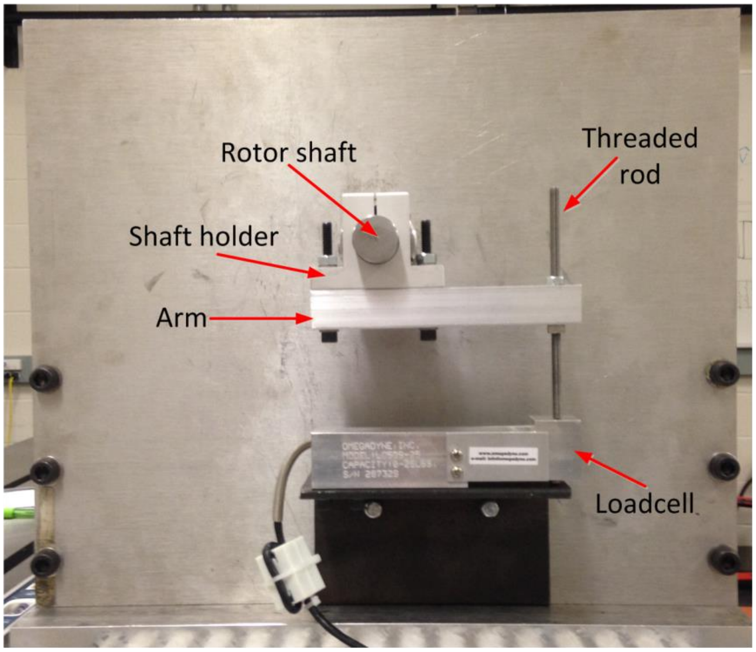

Figure 5.1 Simple mechanism for torque measurement

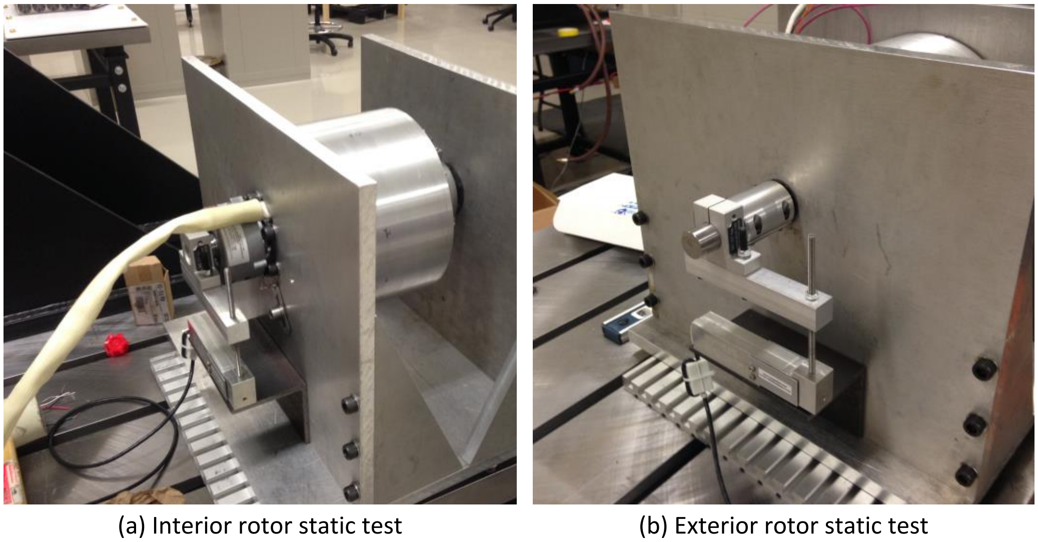

Figure 5.2 Static tests of interior and exterior machines

5.1.2. Flux linkage

Flux linkage is a key magnetic performance indicator of switched reluctance machine. For both the interior and exterior machines, flux linkage loci, which represent the relationship between flux linkage and excitation current, at various rotor positions, are recorded. Note magnetic flux is not a quantity that can be directly measured. It is calculated based on voltage and current measurements. Recall in chapter 2, equation 2.11 gives the voltage across an electric conductor:

$$V = iR + \frac{d\lambda(\theta, i)}{dt} \tag{2.11}$$

Take the integral of above equation, we have

$$\lambda(\theta, i) = \int V dt - R \int i dt \tag{5.1}$$

where λ is flux linkage, V is voltage, i is current and R is conductor resistance.

To obtain flux loci for a single phase at a certain rotor position, a DC step voltage is applied across the phase coil and both voltage and current history of the phase coil is recorded, see Figure 5.3 for a typical plot obtained from an oscilloscope. Note the slight drop of voltage is due to the discharging of the capacitor in the circuit. The flux linkage is then calculated using equation 5.1 and is plotted against current to represent the flux linkage loci, see Figure 5.4 for an example. Note a small amount of fluctuation is observed which is possibly due to the noise in voltage and current measurements. To give a better representation of the loci, a 6th degree polynomial spline is fitted to the data. This operation is used in all charts in this Chapter to treat the flux loci data unless otherwise noted.

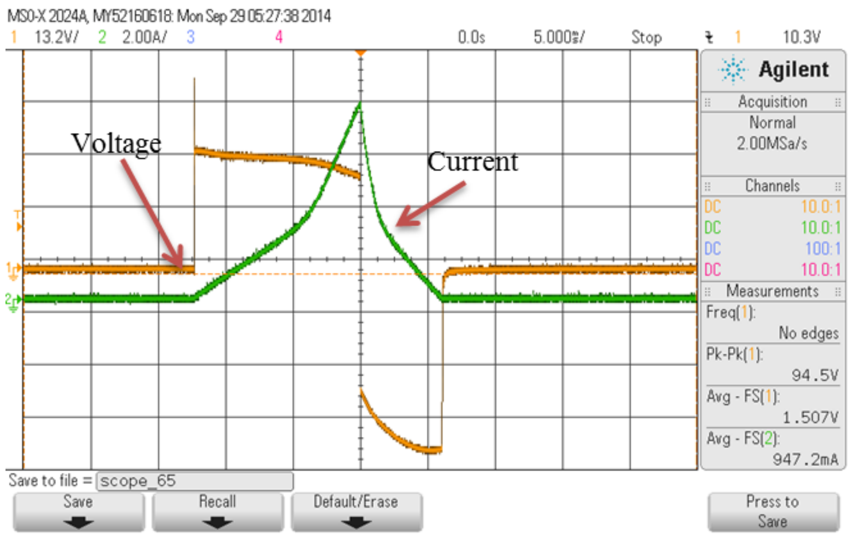

Figure 5.3 Example of phase coil current and voltage recorded on an oscilloscope with step excitation

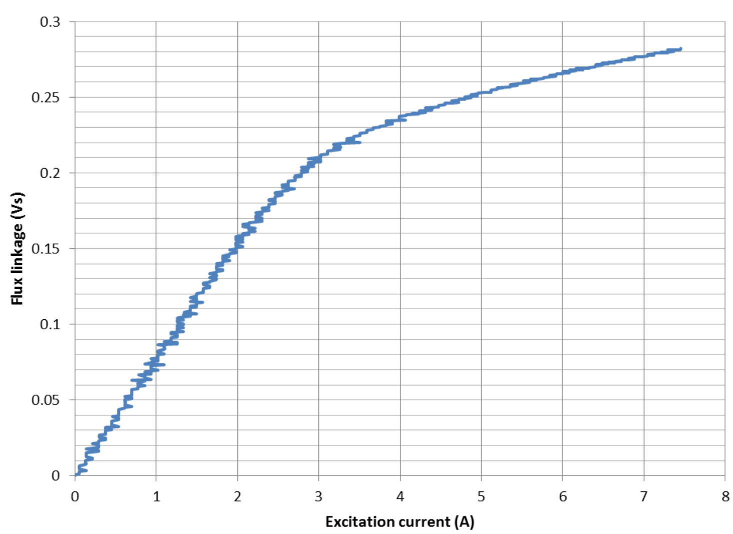

Figure 5.4 Typical plot of flux linkage loci (aligned rotor position)

As a concentricity check, flux linkage loci are measured at aligned and unaligned rotor positions with various rotor pole and stator pole combinations. The results are plotted in Figure 5.5(a) for the interior machine and in Figure 5.5(b) for the exterior machine. Ideally, one should expect all flux linkage curves overlap with each other, indicating perfectly uniform and concentric machine construction. The plots show that while variations do exist (may be due to non-uniformity of machine air gap, variations of coil winding and machining tolerances, etc), they are typically small and can be neglected. The small variations of flux linkage curves also indicate that the mechanical construction of the prototype machine is reasonably accurate.

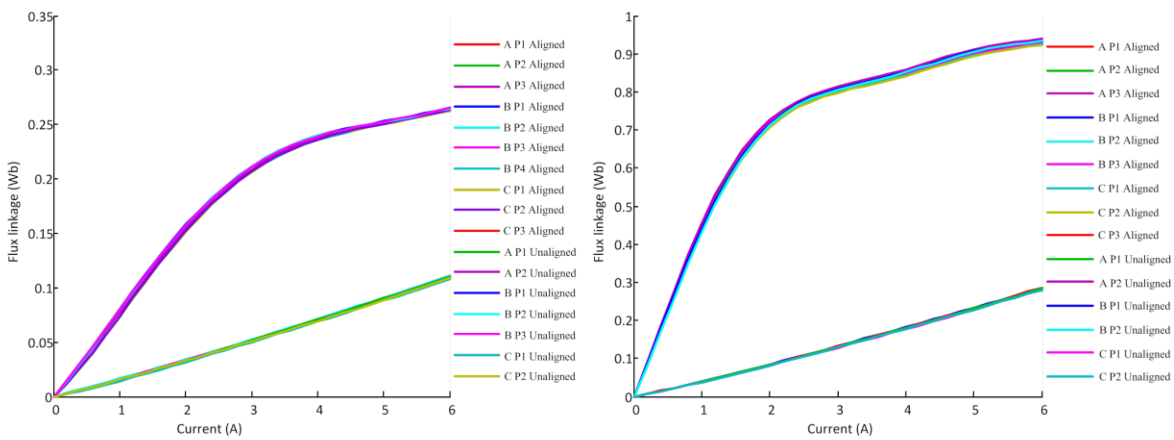

(a) Interior machine flux linkage (b) Exterior machine flux linkage

Figure 5.5 Flux linkage at aligned and unaligned positions with varying pole and phase combinations

To examine the flux linkage characteristics of both machines, measurements are taken at 10 rotor positions, equally spaced between the aligned and unaligned positions. Figure 5.6 shows flux linkage plots of the exterior machine and Figure 5.7 shows plots of the interior machine. The experiment determined flux linkage plots, shown in solid lines, are compared to FEA calculated values, shown in dashed lines.

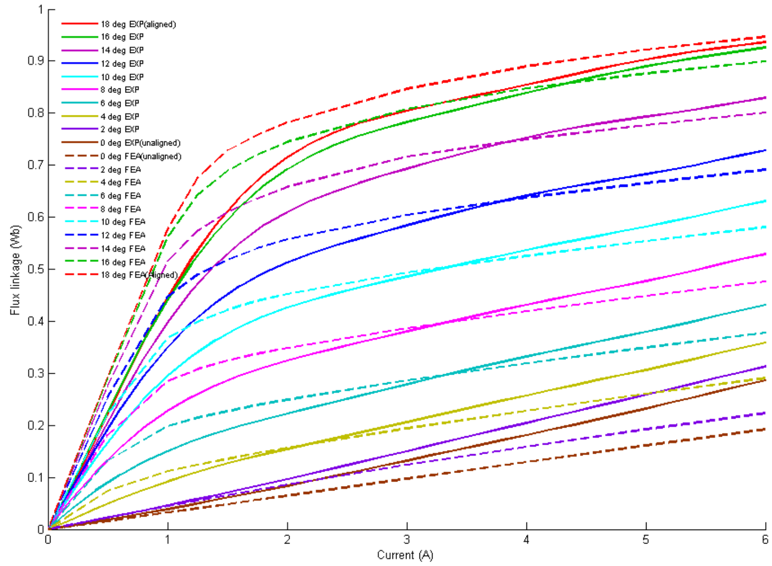

Figure 5.6 Exterior machine flux linkage plots

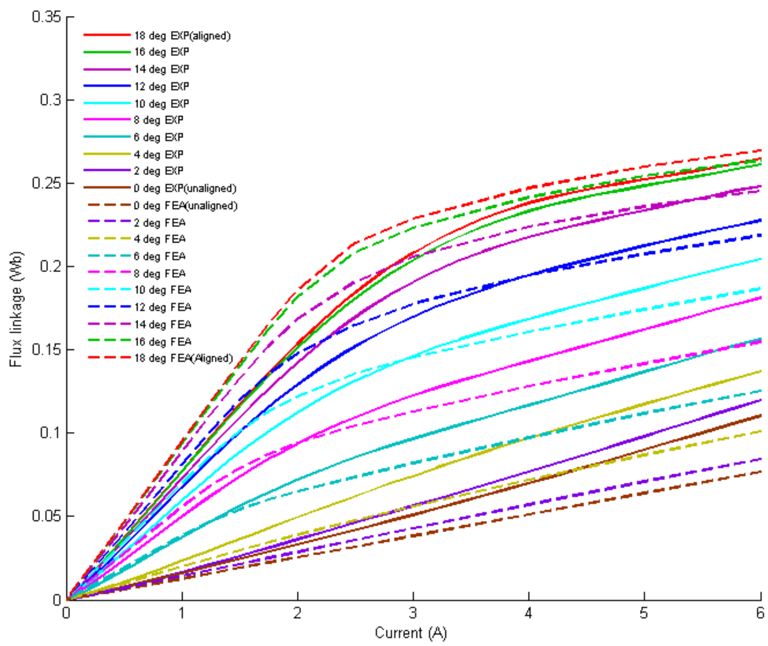

Figure 5.7 Interior machine flux linkage plots

For both the exterior and interior machines, the flux linkage comparisons show that FEA simulations over predict flux linkage near aligned positions and under predict flux linkage near unaligned positions, resulting in reduced area enclosed by the loci and hence a smaller average torque output. The discrepancy between measured and FEA simulation will be discussed in the next section.

5.1.3. Torque

As described in 5.1.1, static torque is determined from force measurement on a loadcell. A loadcell, sometimes called a strain gauge, has a linear relationship between load and strain and outputs a DC voltage for a given load. Before the static torque tests, the loadcell is calibrated using standard laboratory weights (2000g±1g). The calibration showed the error is within 2.5% for both hysteresis and linearity, see Table 5.1 for calibration result.

Table 5.1 Loadcell calibration result

Weight (g)	Voltage reading Adding weights (V)	Voltage reading Reducing weights (V)
0	0.514	0.52
2000	2.095	2.101
4000	3.682	3.693
6000	5.273	5.281
8000	6.86	6.87
10000	8.45	8.46
12000	10.04	10.04

Torque measurements are taken at the same rotor positions as in flux linkage measurements, which include 10 evenly spaced positions between the aligned and unaligned position. Especially for the exterior machine, two extra measurements are taken at 3 and 5 degrees (mechanical) to give finer detail of the torque waveform. For each rotor position, static torque is measured at 5 different current levels, from 1A to 5A. A constant current is maintained by pulse width modulated (PWM) chopping control of the power electronic switching unit. The results are plotted using square markers in Figure 5.8 for the exterior machine and in Figure 5.9 for the interior machine. As a comparison, FEA calculated static torque values are also shown in the diagrams, which are designated by solid lines. In the diagrams, zero degree corresponds to unaligned rotor position whereas 18 degree corresponds to aligned position.

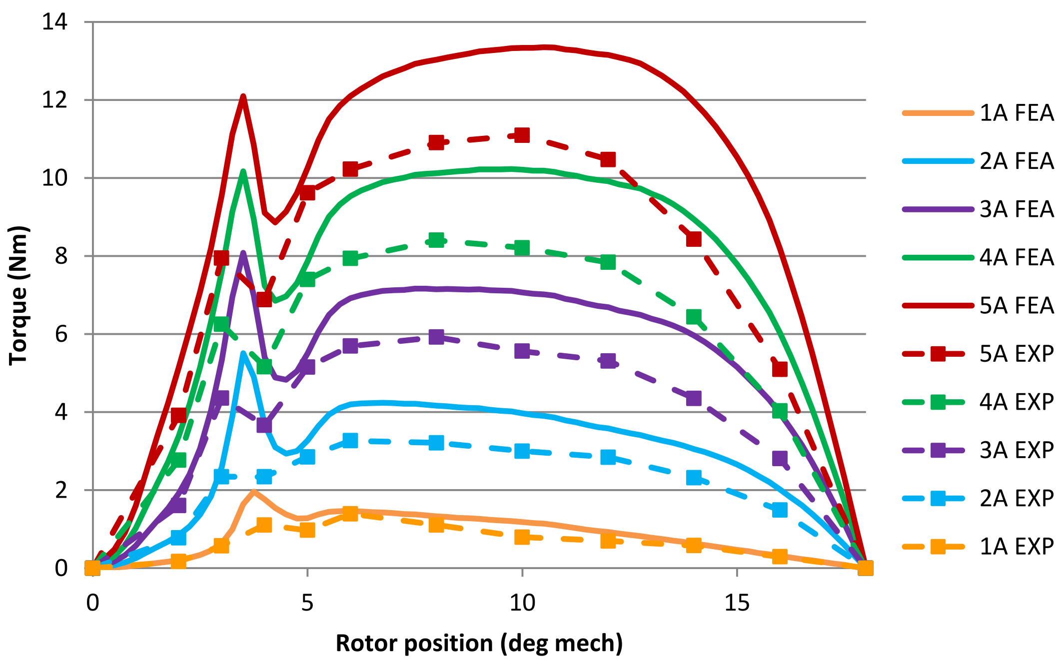

Figure 5.8 Exterior machine static torque comparison

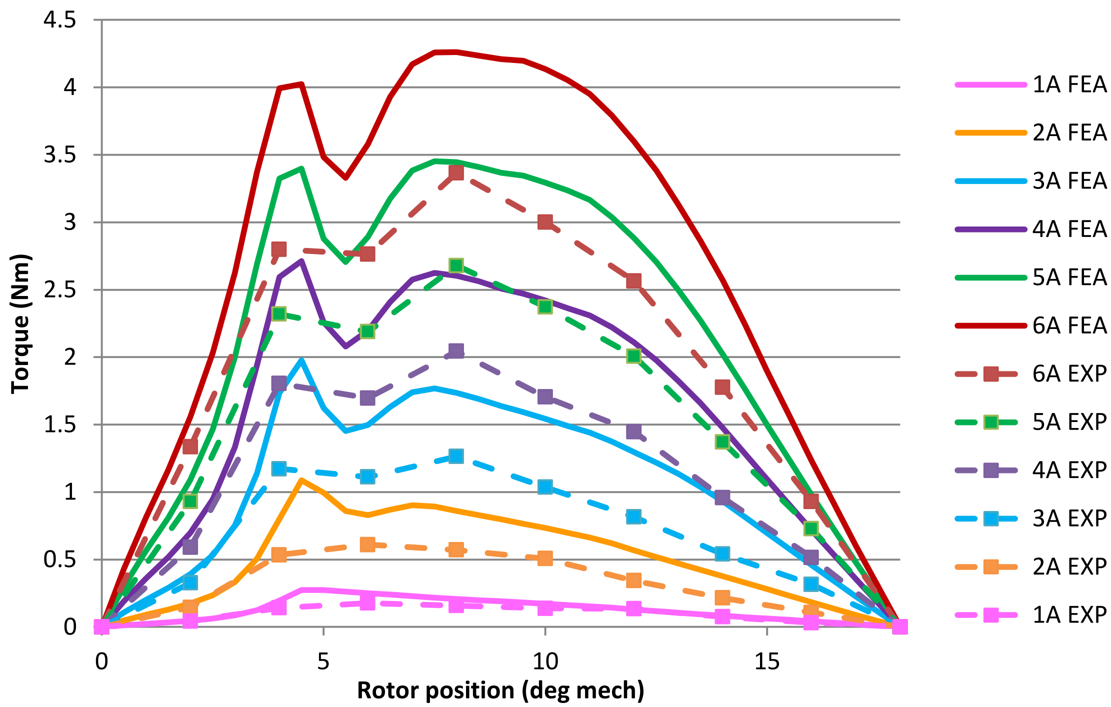

Figure 5.9 Interior machine static torque comparison

For both exterior and interior machines, FEA simulation overestimates static torque at all rotor positions. This can be foreseen by the fact that flux linkage loci measured in section 5.1.2 are smaller in area, which relates to average torque, than FEA prediction. Torque differences are larger for higher currents where flux linkage loci area differences are also greater. Apart from the torque difference, the general trend of torque waveform is well reflected in the FEA simulation result. Starting from the unaligned position, torque increases steeply with increasing rotor position angle. Then right after the first peak, there is a small drop in torque, followed by a plateau region. Torque gradually decreases to zero afterwards till the aligned rotor position.

The difference of flux linkage and torque between measurement and FEA simulation indicates that there are errors in the FEA model. One possible cause of model error is discrepancy in iron core magnetic property. As the major active component in an SRM, the magnetic property of the lamination material directly affects magnetic characteristics of the machine, as well as machine performance. To make sure that the FEA simulation is based on true material characteristics, the B-H curve of lamination samples of the same type as used in the prototype is measured and compared to the B-H data of the model in the simulation software, see Figure 5.10. Only slight difference is seen between the curves, which should only result in minor contribution to the observed discrepancy.

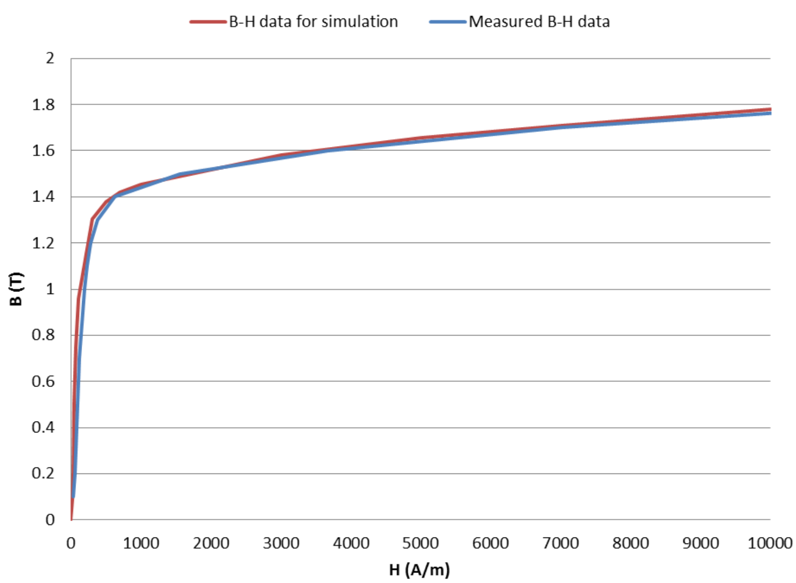

Figure 5.10 Comparison of BH characteristic between simulation and true measurement

A number of studies[80]-[84] have found that machining technique could have big impact on the magnetic characteristics of steel laminations near the machined surface.

Laser cutting, which is used extensively in the manufacturing of the prototype machine, is known to leave a HAZ (heat affected zone) on the boundary of cut laminations. In the HAZ, magnetic property is permanently changed due to the high temperature involved in the laser cutting process. The impact on machine performance is most significant on air gap boundaries where the HAZ directly affects effective air gap length and permeability.

A design parameter study is conducted that varies air gap length and lamination magnetic saturation point to replicate the deterioration of magnetic property at the air gap boundary. Figure 5.11 and Figure 5.12 plots FEA simulated torque waveforms of exterior and interior machines, respectively, under varying air gap length and saturation condition. For comparison, the torque waveforms measured in static tests are shown in solid lines with markers. The results show that while both lowering saturation and increasing air gap length suppress torque output at higher excitation current, the torque waveform at low excitation is only affected by air gap length. To replicate the measured torque waveform would require both an increase in air gap length and a decrease in magnetic saturation point in the FEA model. A close match of the experiment result, see Figure 5.13, can be obtained by setting a 0.4mm air gap length and an 85% magnetic saturation in the FEA model.

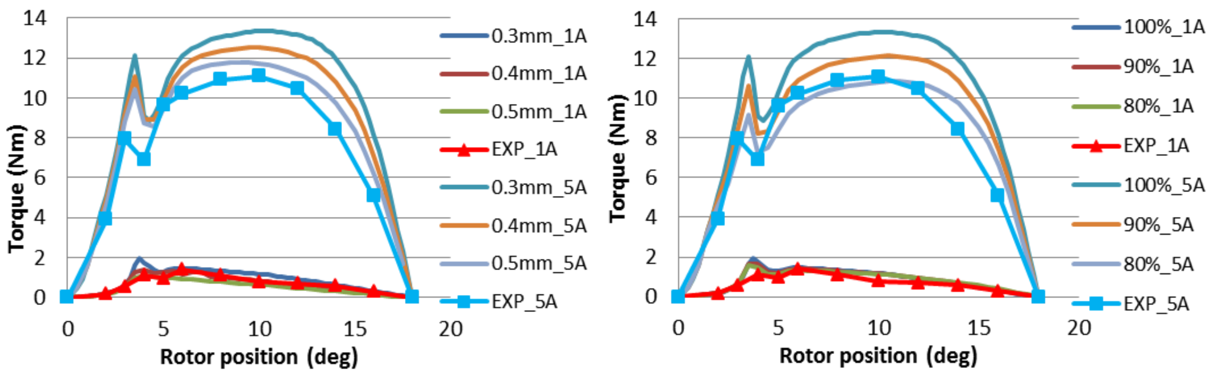

(a) Change of air gap length (b) Change of saturation

Figure 5.11 Exterior machine parameter study

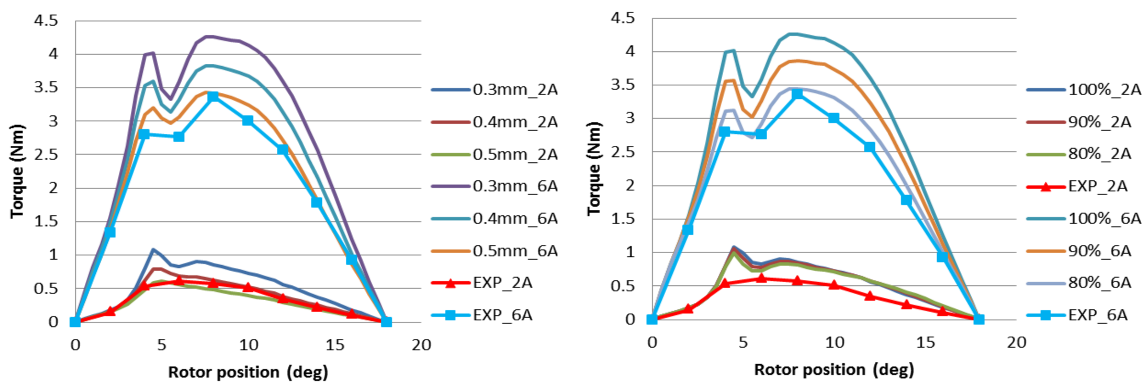

(a) Change of air gap length (b) Change of saturation

Figure 5.12 Interior machine parameter study

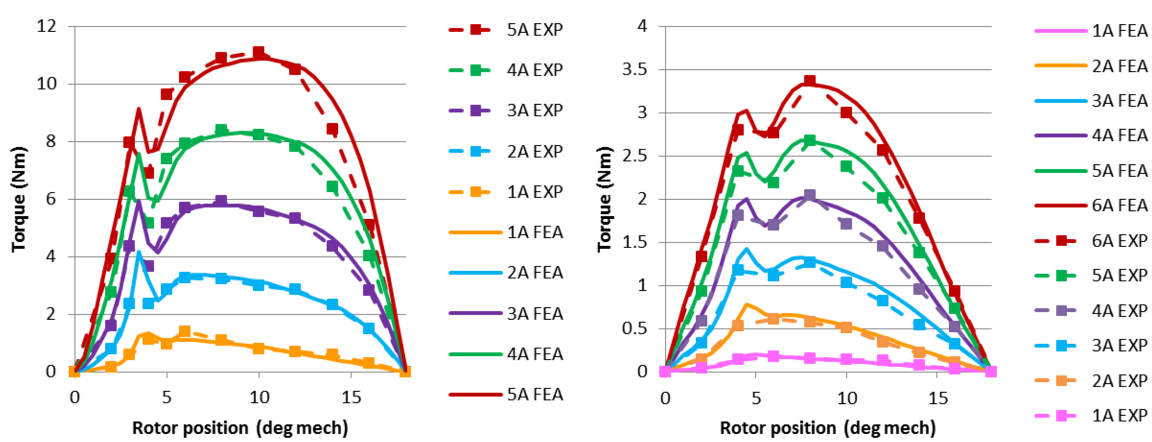

(a) Exterior machine torque waveform (b) Interior machine torque waveform

Figure 5.13 Altered FEA simulation compared to experiment measurements

5.1.4. Coupling effect

Coupling effect is of great concern in a double rotor machine because it determines the ability of the machines to operate independently without interference. In Chapter 3, magnetic coupling is studied thoroughly using FEA simulations. It is validated here with static tests. In this experiment, one phase of either the interior or the exterior machine is turned on and given a constant excitation current (4A as the rated current level). The rotor of this excited machine is locked at aligned position ensuring maximum magnetic flux, hence worst coupling scenario in the stator back iron. Then flux linkage of the other machine is measured for various rotor positions, following the same procedure of single machine flux linkage measurement described in section 5.1.2. The flux linkage loci are compared to previous isolated tests to show the impact of coupling. Because both machines have three phases and same phases are aligned, there are two coupling modes:

(a) same phase coupling

(b) adjacent phase coupling

Figure 5.14(a) compares same phase coupling of the interior machine. Flux linkage of the interior machine phase A is compared with and without exterior machine phase A excitation. Figure 5.14(b) compares adjacent phase coupling of the interior machine, where flux linkage of the interior machine phase B is compared with and without exterior phase A excitation. Similarly, Figure 5.15(a) and Figure 5.15(b) show same phase coupling and adjacent phase coupling, respectively, of the exterior machine. For all the diagrams, flux linkage loci under coupling condition are represented by dashed lines whereas uncoupled cases are represented by solid lines.

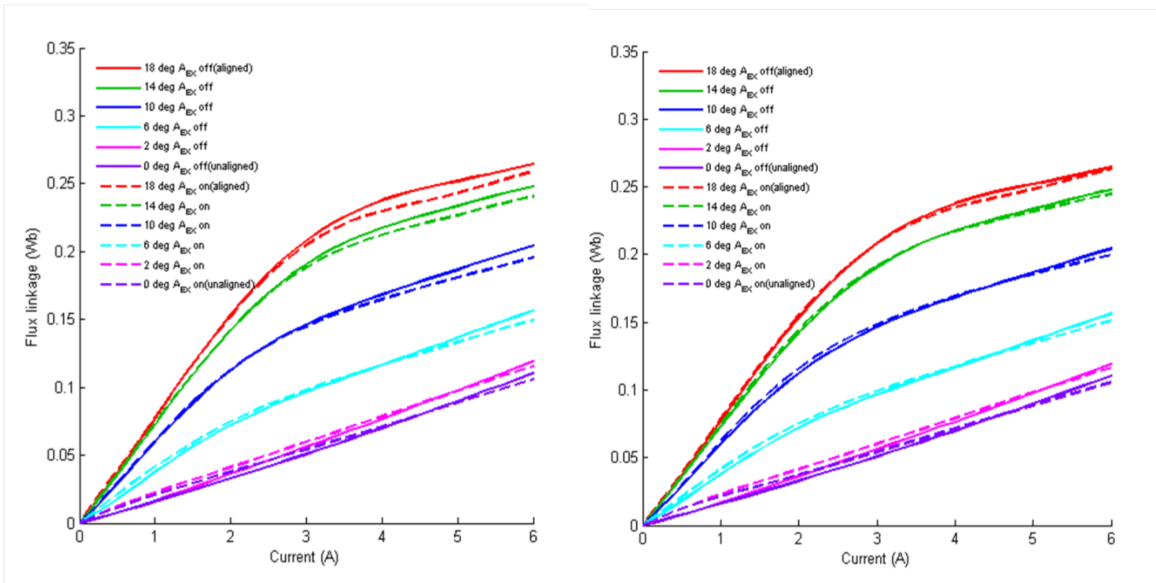

(a) Interior phase A – same phase coupling

(b) Interior phase B – adjacent phase coupling

Figure 5.14 Interior machine flux linkage comparison – coupling analysis

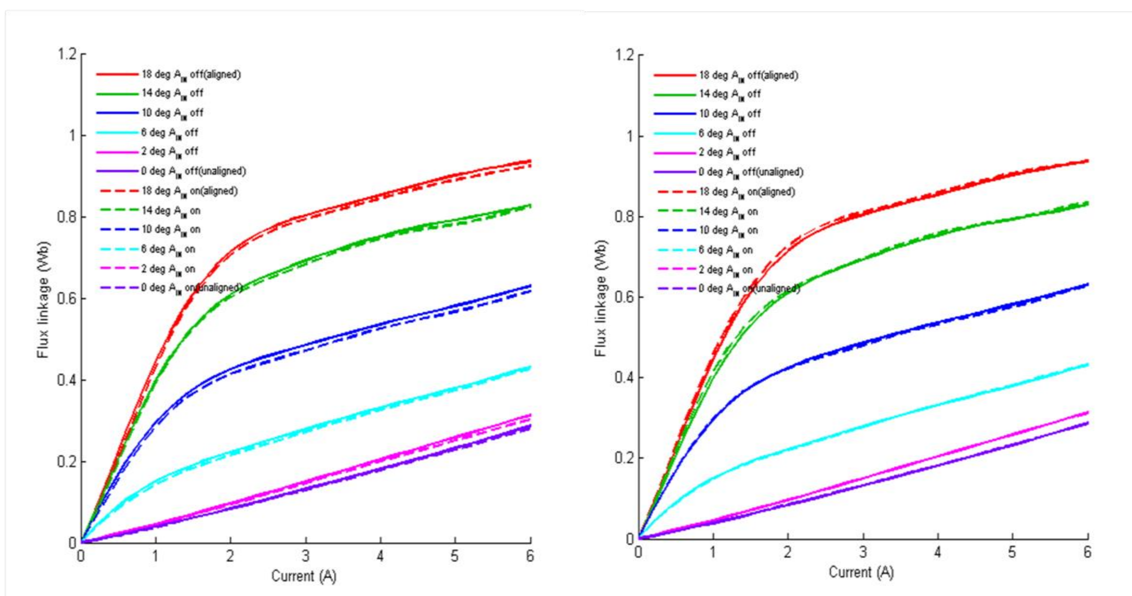

(a) Exterior phase A – same phase coupling

(b) Exterior phase B – adjacent phase coupling

Figure 5.15 Exterior machine flux linkage comparison – coupling analysis

The diagrams show that difference in flux linkage due to coupling between the machines is negligible for both the exterior and interior machines. This agrees well with FEA simulation results in section 3.2.1, which also predict insignificant coupling effect on flux linkage. The flux linkage comparison indicate that coupling between the machines has negligible impact on the magnetic characteristics and hence the operation of each individual machine. In later dynamic tests, the two machines are controlled to operate together to examine any dynamics induced coupling effect.

5.2. Dynamic Tests

5.2.1. Apparatus

In the dynamic tests, the prototype double rotor machine is axially connected to two brushed DC machine dynamometers. The two dynamometers are located at the front and back of the DSRSRM, connected with shaft couplers to the exterior rotor shaft and interior rotor shaft, respectively. See Figure 5.16 for a photograph of the test bench set-up. Horizontal 90 degree iron angles connect the two dynamometers, forming a base that is bolted onto the bottom plate of the DSRSRM frame. The shafts are aligned properly between the dynamometers and DSRSRM by adjusting screw jacks that fasten the DC machines onto the dynamometer frame. In the experiment, the two brushed DC machines operate as generators which provide mechanical loads to the DSRSRM. Resistors are connected to the armatures of the DC machines, consuming the electricity generated as heat. The stator fields of the DC machines are excited through external DC power supplies, where machine load can be adjusted by varying the excitation current. The dynamometers are equipped with loadcells that give torque measurements of the

DSRSRM shaft end output. Output speeds are monitored from the rotor shaft encoder readings.

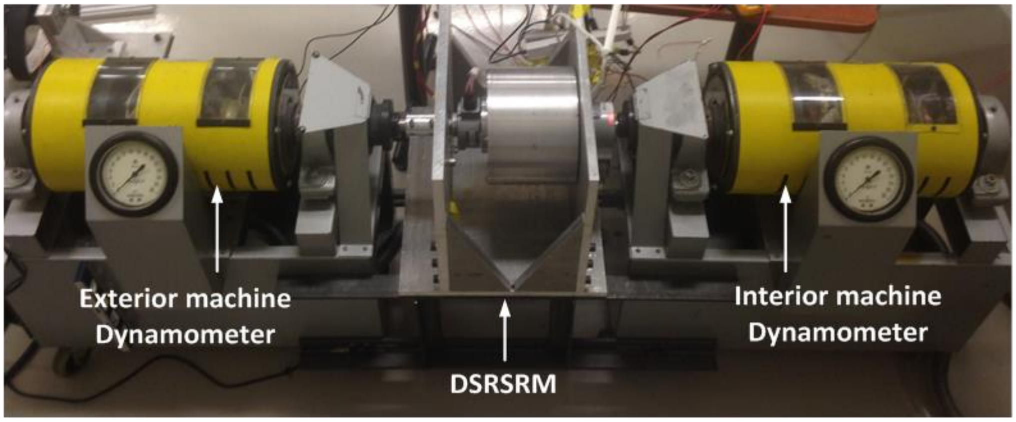

Figure 5.16 Photograph of DSRSRM test bench

The machine drive of the DSRSRM consists of two power stage boards for power electronic switching of the two machines and a processor board for real time processing of feedback data and execution of operation commands. The circuit boards are shown in Figure 5.17. The power stage uses the typical asymmetric bridge design, the operation principle of which is explained in section 2.1.3 of Chapter 2.

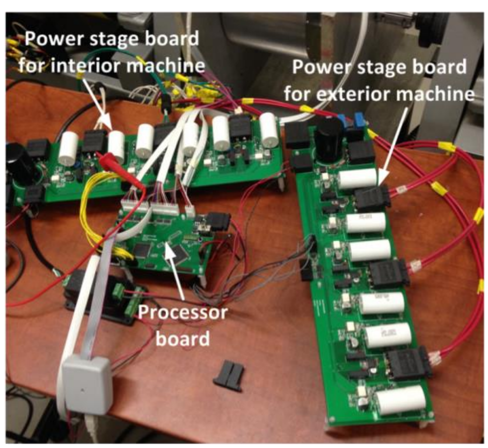

Figure 5.17 Photograph of machine drive of the DSRSRM

Apart from torque and speed, phase voltage and current are measured using an oscilloscope through a voltage probe and a Hall Effect sensor, respectively. The electric power in the machine drive is provided by a 300V laboratory DC power supply (primary power supply). DC current and voltage inputs into the machine drive are monitored by taking measurements from the power supply digital read-out. The primary power supply also outputs a DC current to the exterior machine dynamometer for field excitation. The field excitation of the interior machine dynamometer is provided by an auxiliary DC power supply. Figure 5.18 shows a photograph of all the experiment apparatus during a dynamic test.

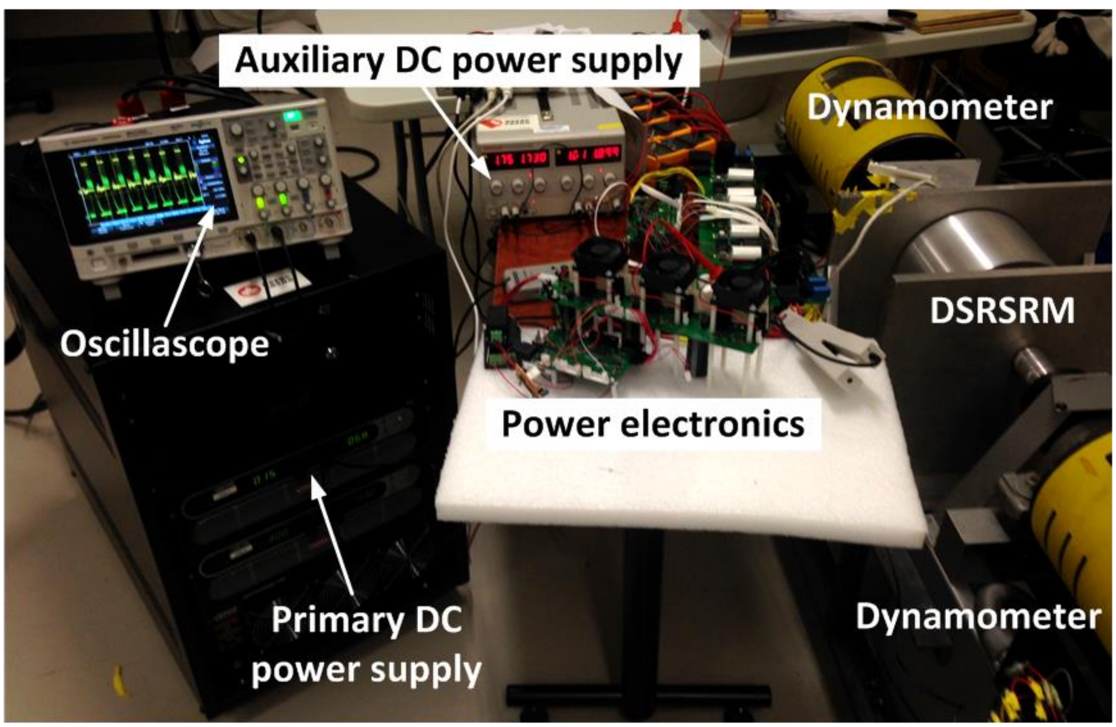

Figure 5.18 Photograph of all apparatus during an experiment

In the dynamometer, the DC machine stator is not mechanically grounded to the frame, but rather supported in a pair of gimbal bearings, which makes the stator free to rotate. A loadcell measures the torque needed to stop the stator from rotating. Because any force interaction between the rotor and stator is within the gimbal system, the total torque on the rotor should equal the total torque on the stator, which includes magnetic torque and frictional torque. This means the dynamometer loadcell is able to capture the total torque delivered at the shaft end. The loadcells on both dynamometers are calibrated to ensure accuracy of the measurements. Figure 5.19 shows the set-up of the calibration test where an overhang beam and a set of laboratory weights are used to compare torque measurements at a series of loads. The actual torque applied onto the loadcell equals the gravitational force of the weights multiplied by horizontal distance from the shaft axis to the center of the weights, plus torque produced by the beam, which is the weight of the beam times horizontal distance between its center to shaft axis. The calibration results are tabulated in Table 5.2 for the exterior machine dynamometer and Table 5.3 for the interior machine dynamometer.

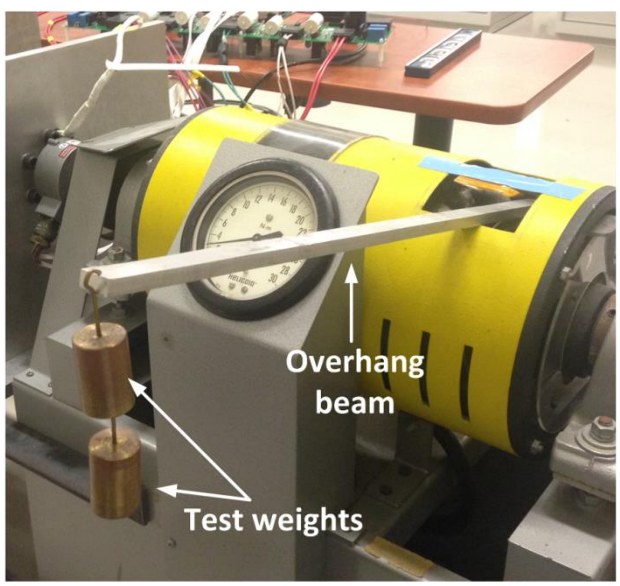

Figure 5.19 Calibration of dynamometer loadcell

Table 5.2 Dynamometer loadcell calibration result for the exterior machine

Weight added (g)	Loadcell torque reading (Nm)	Actual torque (Nm)	Error (Nm)
0	1.2	1.32	-0.12
100	1.8	1.94	-0.14
200	2.35	2.57	-0.22
300	2.9	3.19	-0.29
400	3.5	3.81	-0.31
500	4.1	4.44	-0.34
600	4.7	5.06	-0.36
700	5.5	5.68	-0.18
800	5.8	6.31	-0.51
900	6.2	6.93	-0.73
1000	6.8	7.55	-0.75
1100	7.4	8.17	-0.77
1200	7.9	8.80	-0.90
1300	8.4	9.42	-1.02
1400	8.9	10.04	-1.14

Table 5.3 Dynamometer loadcell calibration result for the interior machine

	Weight added (g)	Loadcell torque reading (Nm)	Actual torque (Nm)	Error (Nm)
Shorter beam	0	0.8	0.55	0.25
	50	0.9	0.78	0.12
	100	1.1	1.02	0.08
	150	1.3	1.25	0.05
Longer beam	0	1.35	1.32	0.03
	50	1.6	1.63	-0.03
	100	1.8	1.94	-0.14
	150	2.1	2.26	-0.16
	200	2.4	2.57	-0.17

Note that only torque ranges of interest, i.e. within 10Nm for exterior and within 2.5Nm for interior, are calibrated. The calibration shows that errors are not consistent at various load conditions; therefore a fixed correction cannot be applied. Instead, torque correction is calculated based on the above tables, with intermediate readings interpolated. The correction is applied to all dynamometer readings in this experiment.

5.2.2. Interior machine

The interior machine is designed for a rated speed of 2000 RPM and a rated output torque of 2Nm, which produces a mechanical output of 420W. The interior machine is tested under various loads and speeds to evaluate its performance. Before connecting to the dynamometer, the interior machine is tested under no-load condition to measure the mechanical loss within the machine. During the no-load test, the dynamometer is decoupled from the rotor shaft and all rotor mechanical power output is consumed within the machine as electrical and mechanical losses. The mechanical loss is estimated by subtracting electrical loss from total electrical power input, which is the integral average of instantaneous line voltage and current product. In the test, the machine is operated under current control to reach a desired steady state speed, phase voltage and current are recorded for power calculation. Note that iron loss is assumed negligible and only copper loss is accounted for in the estimation of electrical loss because of the low current levels and hence low magnetic fields induced in the no-load tests. With phase current measurements, copper loss can be easily obtained from Ohm's Law equation. Figure 5.20 shows phase voltage and current plots for the interior machine operating at no-load 4000 RPM. In order to achieve a single pulse excitation without current chopping, full voltage is not applied. This is to reduce iron loss associated with higher frequency magnetic field changes due to chopping.

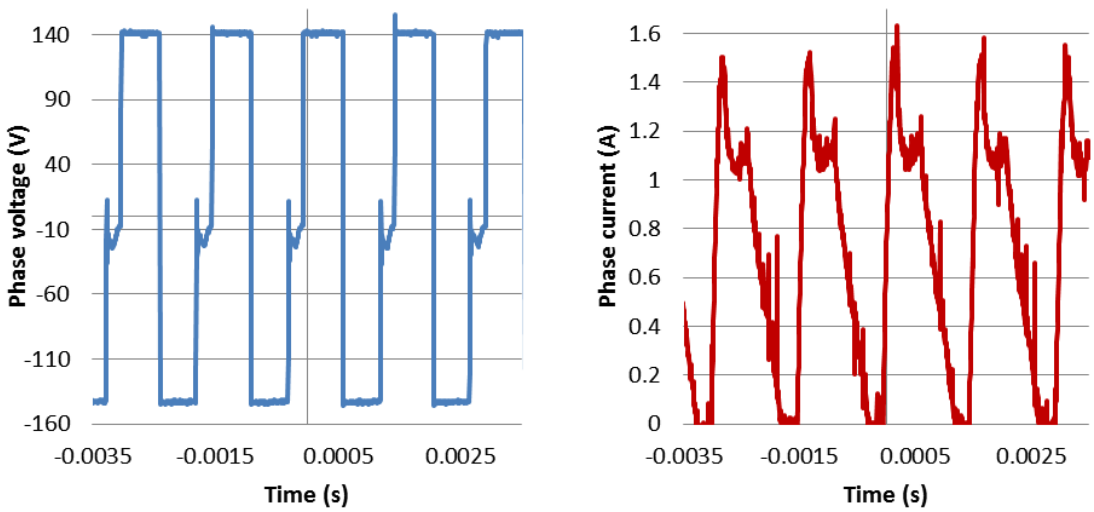

(a) Phase voltage waveform (b) Phase current waveform

Figure 5.20 Interior machine phase voltage and current waveforms at no-load 4000 RPM

Table 5.4 summarises no-load test result of the interior machine. The results show that mechanical loss is significant for the interior machine. On average, a 0.2 Nm resistance torque is expected, which is 10% of the rated output torque of the machine. The high resistance is mainly attributed to the high friction of output shaft encoder, which employs a through-shaft design and relies on contact with shaft surface for alignment. The resistance torque measurements are included as a correction to interior machine total mechanical output in all the experiments.

Table 5.4 No-load test result of the interior machine

Speed (rpm)	4000	3000	2400	2000	1500	1000	500
Electrical input power (W)	106.2	76.4	45.8	31.7	32.9	20.9	11.2
Copper loss (W)	3.6	3.1	2.4	2.0	2.6	2.4	2.3
Mechanical loss (W)	102.6	73.4	43.4	29.7	30.2	18.6	8.9
Resistance torque (Nm)	0.24	0.23	0.17	0.14	0.19	0.18	0.17

Loaded tests are conducted by coupling rotor shaft with the dynamometer and exciting the brushed DC machine stator winding to produce a field for inducing back EMF on the dynamometer rotor. The induced back EMF creates current flow in the rotor armature winding, which produces a magnetic force on the rotor and thus load on the drive shaft. The load can be adjusted by controlling the magnitude of excitation current. From the static tests, it is observed that the measured flux linkage loci area is smaller than simulation prediction, which indicates reduced torque capability at designed current rating. To meet the simulated design target points, phase current limit is increased while same current conduction angles are maintained, as determined in section 3.4.4. Table 5.5 compares machine performance with designed operating points. "SIM" in the table denotes results are from simulation and "EXP" denotes the results are experiment measurements. The results show that even though the machine is able to produce desired torque output at rated speeds, the efficiency is lower for all cases. As mentioned before, this is due to increased phase current and hence increased loss. For the majority of the operational speed range, peak phase current needs to be increased by 1A to deliver the same output, which results in about 25% increase in root-mean-square (RMS) current.

Table 5.5 Interior machine performance comparison with simulation results

Speed (RPM)	Torque (Nm)	DC input current (A)		Phase current limit (A)		Phase RMS current (A)		Efficiency (%)	
		SIM	EXP	SIM	EXP	SIM	EXP	SIM	EXP
1500	2	1.22	1.3	3.5	4.2	2.20	2.63	81.2	75.2
2000	2.05	1.64	1.7	3.5	4.5	2.21	2.68	86.1	83.5
2400	2.01	1.95	2.0	3.5	4.5	2.19	2.83	89.5	85.1
3000	1.91	2.26	2.3	3.5	4.5	2.22	2.84	92.2	84.6
4000	1.65	2.58	2.6	3.5	4	2.11	2.46	92.7	85.5

Figure 5.21 shows phase current waveforms of the interior machine at different speeds.

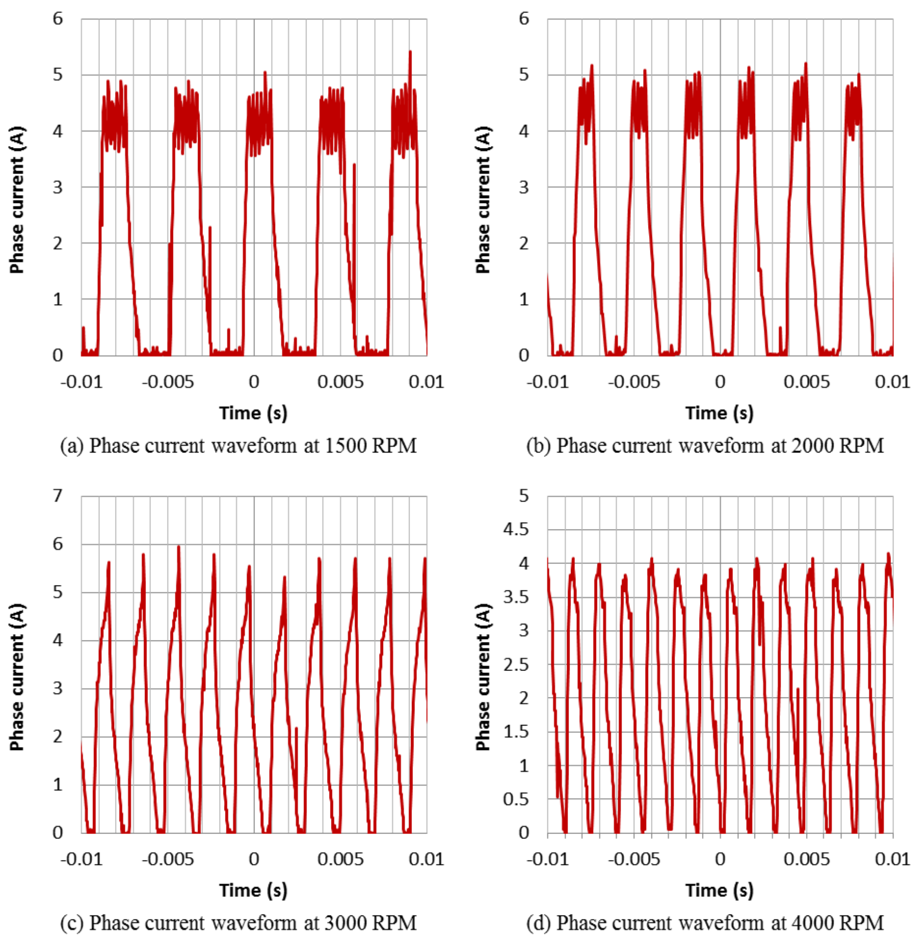

Figure 5.21 Measured interior machine phase current waveforms under different speeds

At (a) 1500 and (b) 2000 RPM, current chopping is executed at around 4.5A with a bandwidth of 0.4A. Due to the relatively long conduction period, the waveform resembles square pulses. As the rotor speed increases, so does excitation frequency. In this speed range, the machine output torque stays almost constant because same peak phase current is maintained through chopping. At (c) 3000 RPM, chopping is no longer needed and the waveform is in a triangular shape. The machine operates under single pulse excitation. Torque can still be increased at this speed because there is still room for turn-on angle advance. At (d) 4000 RPM, phase current switching reaches very high frequency and current turn-on angle cannot be further advanced. Phase current is limited to be within 4A due to the limited time for current rise. Above this speed, machine output power begins to decrease with further increase of speed.

As one objective of the thesis, the interior segmented rotor SRM is compared to a benchmark machine (for details and specifications see section 3.1.10) in another set of experiments. Again the machine is operated to deliver same output while parameters such as line DC current, phase current limit and efficiency are compared. See Table 5.6 for a summary of the comparison. Note the benchmark specifications generally require lower output than the design target in Table 5.5. This is because a design margin is kept to allow for errors in modelling and prototype manufacturing that may result in reduced machine output. The comparison shows that the interior segmented rotor SRM generally performs with higher efficiency than the benchmark machine, except for 4000 RPM operation, where the benchmark machine efficiency is higher. For the same output condition and supply voltage, the segmented rotor SRM requires lower current. Note that at 2000 RPM, the benchmark machine has lower DC input current, which contradicts with the fact that the benchmark efficiency is lower. This indicates a potential error in the acquired benchmark machine data.

Table 5.6 Interior machine performance comparison with benchmark

Speed (RPM)	Torque (Nm)	DC input current (A)		Phase current limit (A)		Efficiency (%)	
		Benchmark	DSRSRM	Benchmark	DSRSRM	Benchmark	DSRSRM
2000	2	1.6	1.7	6	4.4	82.9	85.8
2400	1.81	1.8	1.7	6	4.5	84.24	93.3
3000	1.63	2.1	2	6	4	81.28	88.6
4000	1.47	2.3	2.5	6	4	89.24	82.9

5.2.3. Exterior machine

The exterior machine is rated for 8Nm output torque at 500 RPM, which equals 420W mechanical output power, same as the interior machine. The exterior machine experiment follows the same procedure as the interior machine tests. First, the exterior machine is decoupled from the dynamometer for a no-load test to determine the mechanical losses within the machine. The result is summarized in Table 5.7. Compared to the interior machine, the exterior machine has higher resistance torque. This is probably due to the fact that the rotor mass is bigger and larger bearings are used, which results in higher frictional torque. As an example, phase voltage and current waveform of the exterior machine at no-load 1000 RPM is shown in Figure 5.22. Again, in order to minimize iron loss, reduced phase voltage is used to maintain single pulse excitation to eliminate current chopping. The resistance torque measurements are applied as a correction to exterior machine total mechanical output in all the experiments.

Table 5.7 No-load test result of the exterior machine

Speed (rpm)	1000	850	750	625	500	250	100
Electrical input power (W)	55.1	40.0	28.7	22.6	23.7	17.4	7.2
Copper loss (W)	2.0	1.6	1.3	1.2	1.6	2.3	1.7
Mechanical loss (W)	53.1	38.4	27.4	21.4	22.1	15.1	5.6
Resistance torque (Nm)	0.51	0.42	0.34	0.33	0.42	0.58	0.46

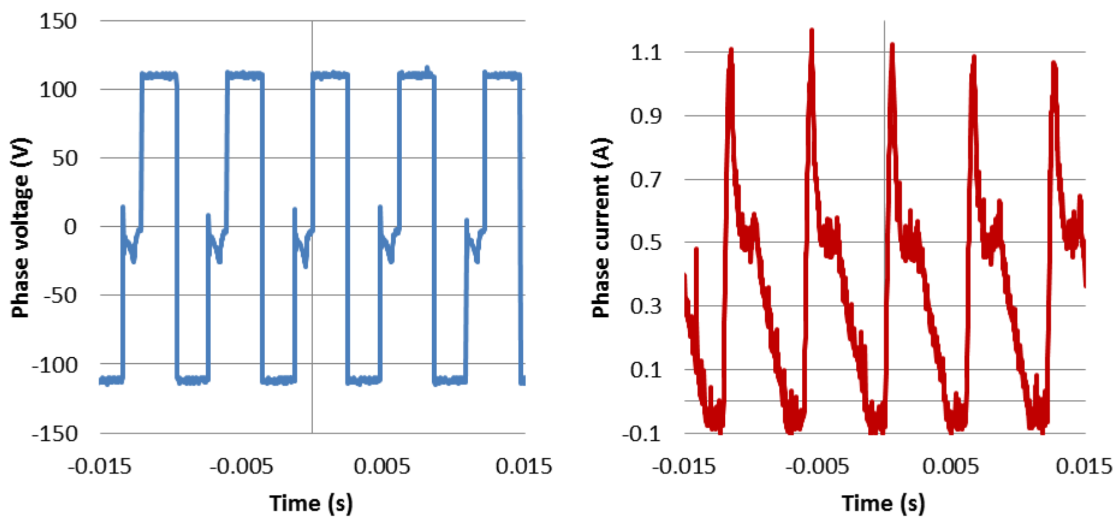

(a) Phase voltage waveform (b) Phase current waveform

Figure 5.22 Exterior machine voltage and current waveforms at no-load 1000 RPM

Similar as in the interior machine loaded tests, the exterior machine is operated at target outputs determined by design simulations. The input parameters are compared to see the difference in performance. The results are tabulated in Table 5.8, where "SIM" designates simulation results and "EXP" designates experiment results. Compared to simulation results, higher phase current is demanded to meet the same output requirement. This is mainly due to the difference between simulated and measured flux linkage, as first noted in the static tests. To achieve the required output torque, an increase of phase peak current of 0.5A is needed at lower speeds. As a result, higher current and lower efficiency than simulation results are observed in the experiments. Apart from the differences in phase current, the experiment result agrees well with simulation in terms of general trend of parameters. For example, RMS current reduces as speed increases and efficiency is also higher at higher speeds.

Table 5.8 Exterior machine performance comparison with simulation results

Speed (RPM)	Torque (Nm)	DC input current (A)		Phase current limit (A)		Phase RMS current (A)		Efficiency (%)	
		SIM	EXP	SIM	EXP	SIM	EXP	SIM	EXP
275	8.15	0.96	1.1	3.4	3.9	2	2.33	81.2	75.2
500	8.2	1.66	1.7	3.4	3.8	1.98	2.23	86.1	83.5
750	7.11	2.08	2.1	3.4	3.5	1.78	2.07	89.5	85.1
850	6.37	2.05	2.1	3.4	3.5	1.73	1.99	92.2	84.6
1000	5.03	1.89	2.0	3.4	3.5	1.54	1.76	92.7	85.5

Figure 5.23 plots phase current waveforms of the exterior machine at different speeds. For the majority of its speed range, from (a) 275 RPM to (c) 750 RPM, the exterior machine operates in constant torque region, with machine torque controlled mainly by the current chopping level. At (d) 1000 RPM, excitation frequency is higher and current chopping is only performed once in each stroke.

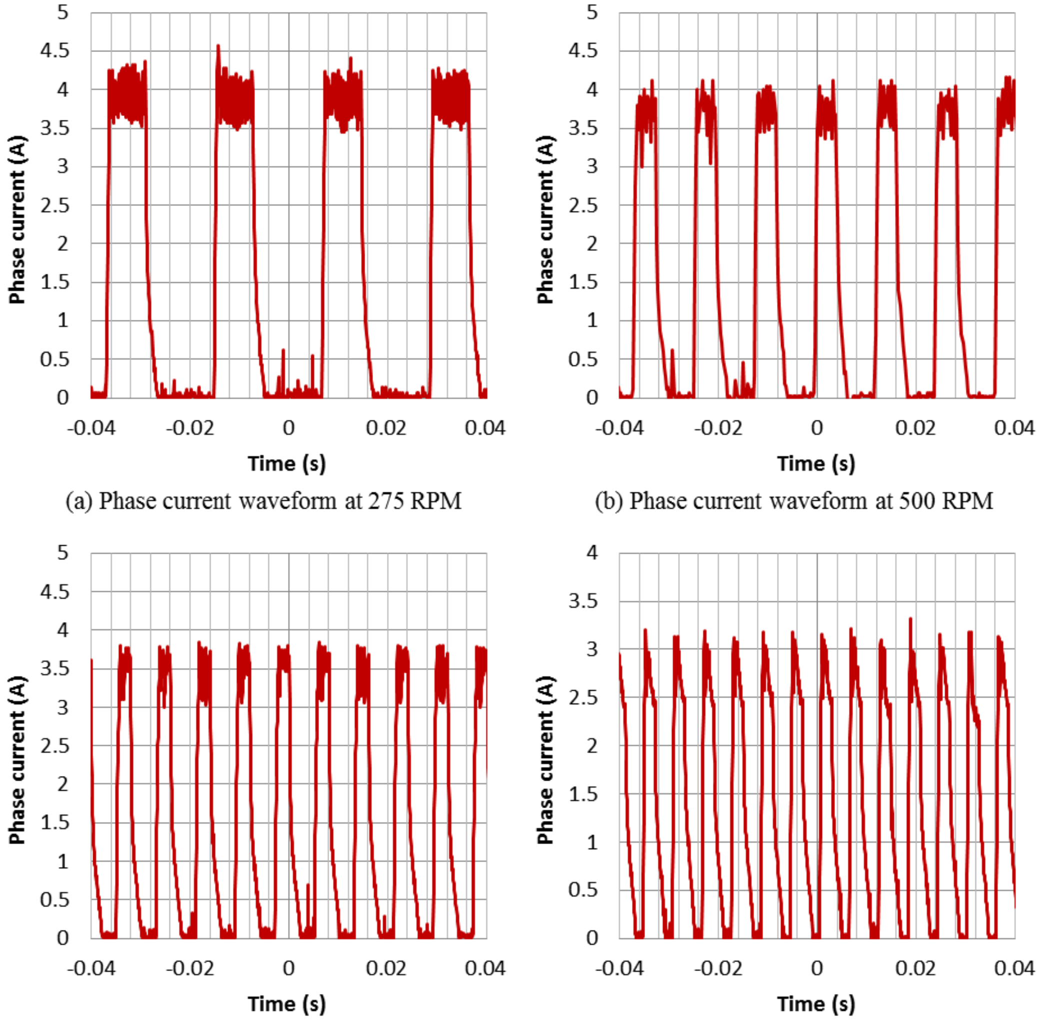

(a) Phase current waveform at 275 RPM

(b) Phase current waveform at 500 RPM

(c) Phase current waveform at 750 RPM

(d) Phase current waveform at 1000 RPM

Figure 5.23 Exterior machine phase current waveforms at different speeds

The exterior machine is also tested at benchmark machine operating points to compare the performance. Table 5.9 summarises the comparison results. For all tested speeds, the segmented rotor SRM achieves higher efficiency than the benchmark machine. This is corresponded by the fact that both the DC input current and phase current limit of the machine is smaller than the benchmark.

Table 5.9 Exterior machine performance comparison with benchmark

Speed (RPM)	Torque (Nm)	DC input current (A)		Phase current limit (A)		Efficiency (%)	
		Benchmark	DSRSRM	Benchmark	DSRSRM	Benchmark	DSRSRM
500	8	1.7	1.6	5	3.7	81.41	81.5
750	6.57	2.1	1.9	5	3.5	81.91	82.7
850	5.57	2.1	1.8	5	3	77.49	83.7
1000	3.57	1.6	1.4	5	2.3	77.89	80.3

5.2.4. Combined operation

Finally, the two machines are operated together to validate the double rotor machine topology. Both machines are controlled at rated torque and speed: 8Nm at 500 RPM for exterior machine and 2Nm at 2000 RPM for interior machine. Two separate tests were conducted with the two machines rotating in the same direction and in the opposite direction. The phase current waveforms are plotted, together with the waveform of uncoupled operation, in Figure 5.24 for the exterior machine and in Figure 5.25 for the interior machine.

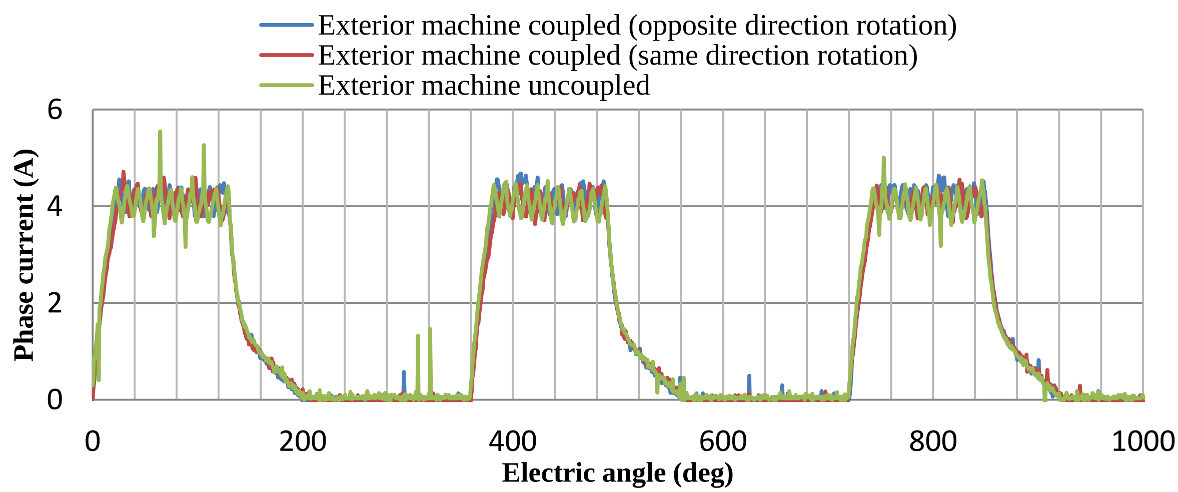

Figure 5.24 Phase current comparison coupled experiment – Exterior machine

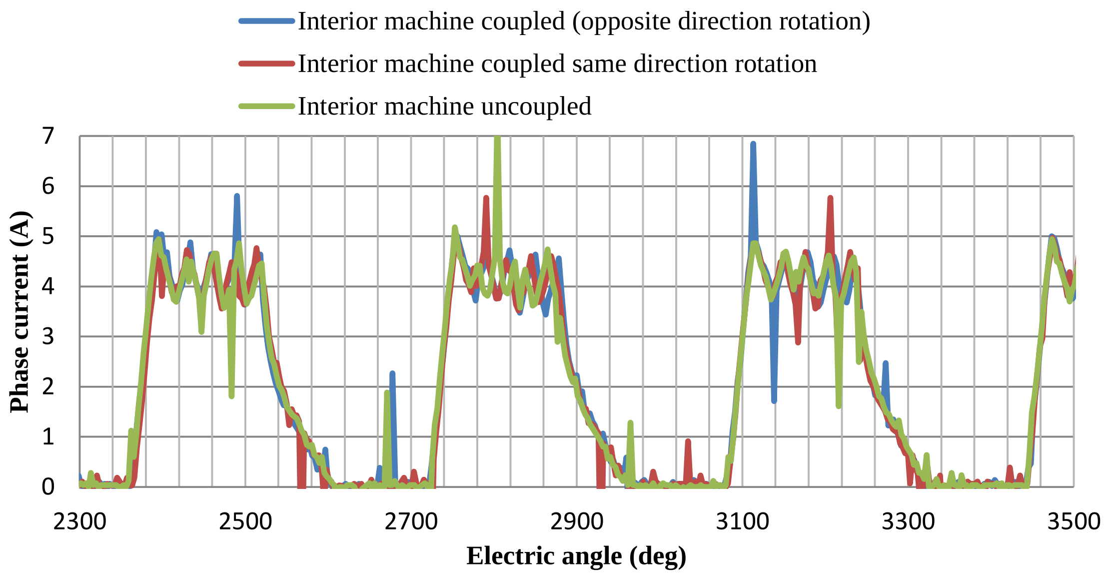

Figure 5.25 Phase current comparison coupled experiment - Interior machine

No noticeable difference can be identified in phase current waveforms of both the interior and exterior machines, regardless of the rotation direction. Once again, coupling between the two machines are proved to have negligible impact on machine performance, which agrees with the conclusion from FEA coupling analysis.

To validate if the DSRSRM can operate continuously within its thermal limit at rated operation condition, both machines are run together at rated speeds and output torque, with temperature at various locations within the DSRSRM measured. After 150 minutes of continuous operation, an equilibrium temperature is reached, which is approximately 85 ℃, much below the 150 ℃ temperature limit defined by insulation breakdown temperature. Figure 5.26 plots temperature readings at three critical locations in the machine: interior machine coil center, exterior machine coil center and stator yoke. Because of the enclosed structure, heating of the interior machine is more significant than other components. As a result, the interior machine coil center has the highest temperature due to difficulty in heat dissipation. Table 5.10 summarises temperature measurements from all sensors installed in the DSRSRM.

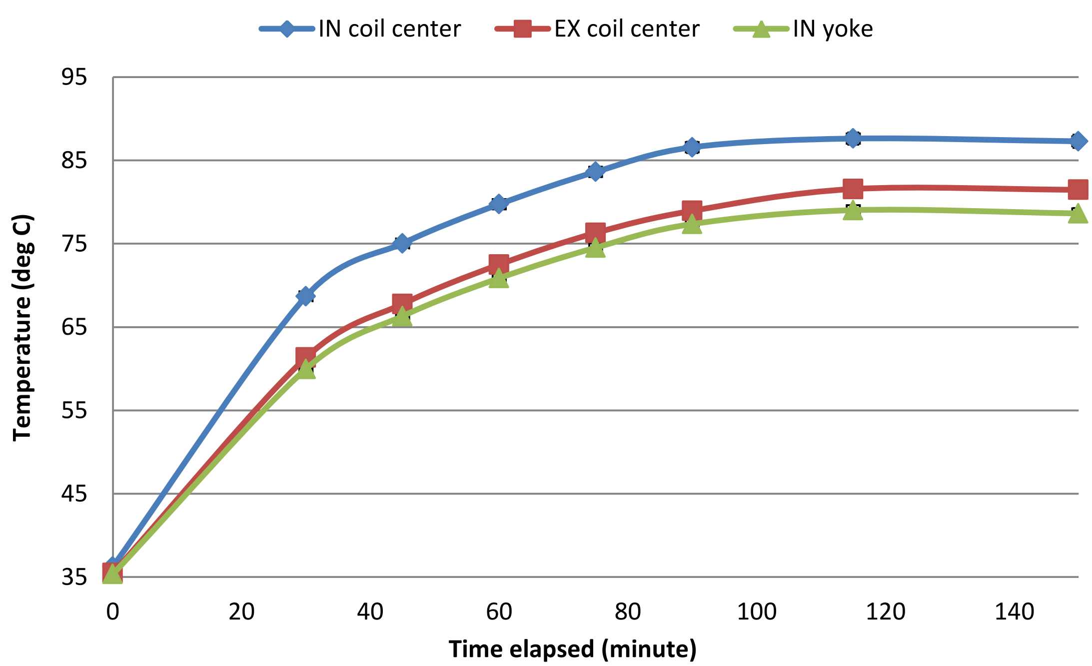

Figure 5.26 Plot of DSRSRM temperature measurements

Table 5.10 DSRSRM temperature measurements under rated operation

Location	Temperature (℃)							
	0 min	30 min	45 min	60 min	75 min	90 min	115 min	150 min
IN coil center	36.3	68.7	75.0	79.7	83.6	86.6	87.6	87.3
EX coil center	35.5	61.3	67.8	72.5	76.3	78.9	81.6	81.5
IN yoke	35.4	60.0	66.3	70.9	74.5	77.4	79.0	78.6
EX yoke	35.0	59.5	65.8	70.4	74.2	77.0	78.9	78.7
EX tooth	35.4	57.0	63.7	68.7	73.0	75.2	77.2	77.0
IN tooth	35.4	61.8	69.2	74.6	77.9	80.7	82.2	81.2
EX winding front	35.4	61.4	68.7	73.4	76.7	78.9	81.6	81.9
IN winding front	35.4	66.4	73.8	78.8	82.5	84.6	85.7	86.2
EX winding back	35.4	60.4	68.0	72.7	76.0	78.3	81.2	81.6
IN winding back	35.4	66.6	74.3	79.5	82.9	85.8	86.7	86.5

5.3. Summary

This Chapter presents experiment results of the DSRSRM prototype. Two types of tests: static and dynamic are separately conducted. The static tests provide rotor position dependent measurements, such as torque waveform and flux linkage plot. The flux linkage measurements at various aligned and unaligned rotor position show good consistency, indicating a well maintained air gap in the prototype construction. Discrepancies between measured flux linkage and FEA simulation are observed, which result in reduced torque output. This discrepancy is further investigated and material deterioration due to machining technique is identified as one possible cause. The dynamic tests evaluate machine performance under various loading conditions. Generally, machine performance shows good agreement with simulation, however, higher current is required to deliver required output due to a shrinked flux linkage loci, which decreases efficiency. Compared to the benchmark machine, the DSRSRM performs better with lower current input and higher efficiency for most operating points. In addition, coupling of the two machines are tested in both static and dynamic scenarios. The results agree with previous FEA simulation conclusion that coupling effect between the machines is negligible.

CHAPTER 6 CONCLUSIONS

6.1. Review and Summary

This thesis proposed and studied double rotor SRMs with segmented rotors. A prototype electric machine based on one of the proposed topologies was constructed and tested. Compared to double rotor SRM with a conventional rotor structure, the prototype achieves significant reduction in external diameter, demonstrating compactness improvement.

Chapter 1 reviews past research on double rotor electric machines. Different applications are discussed with a focus on advanced hybrid electric vehicle powertrains. Double rotor machines demonstrate potential in improving system integration of two types of HEV powertrain architectures, the complex power split topology and the EVT topology, both of which rely on two electric machines. The switched reluctance machine, featuring high efficiency and a simple structure with no permanent magnet, appears to be a promising candidate for realizing double rotor topologies.

In Chapter 2, fundamental knowledge on switched reluctance machine is introduced to set the stage for the discussion of machine designs. As a key element in the proposed machine designs, SRM with segmented rotor is thoroughly explained. A total of 16 radial flux double rotor SRM topologies are identified based on all possible rotor/stator arrangements.

Chapter 3 proposes 8 interesting double segmented rotor SRM (DSRSRM) designs. Of the proposed topologies, two are beneficial for HEV powertrain applications. The DSRSRM with central stator offers two independent rotor outputs, which is suitable for a complex powersplit type HEV powertrain. The DSRSRM with external stator and inner wound rotor is suitable for an EVT powertrain where the two rotors are coupled. The central stator design features a shared stator offering substantial compactness improvement. It is selected for prototype validation. As a key novelty of the proposed design, stator yoke flux path sharing is investigated with winding scheme proposed. FEA analysis is conducted to study the effect of flux path sharing and it is found that coupling between the two machines is negligible. The chapter continues on with details on machine modelling and simulation, followed by parameter selection and optimization of the DSRSRM. A number of design parameters are kept constant to allow fair comparison of the prototype to a benchmark double rotor SRM. Other design parameters are determined based on a parameter characteristic study. Apart from meeting design objectives and constraints laid out by the benchmark, design parameters are optimized for minimal torque ripple. Rotor segment tip shape is also studied to ensure adequate tip mechanical strength while minimizing effects on torque output. Finally, the design based on 2D simplified model is verified with more sophisticated models, considering added structural geometry details, mutual inductance and 3D effects.

The mechanical construction of the prototype machine is described in Chapter 4. Both stator and rotor laminations are laser cut and stacked to form the iron cores of the machine. The stator lamination stack is bonded with epoxy to ensure alignment. The rotor lamination segments are held together by electrical discharge machined aluminum holders. Dovetail slots are machined on the holders which are later inserted with lamination segments. The assembled rotors and stator are vacuum pressure impregnated to enhance electrical insulation, heat conduction and mechanical strength of the assemblies. The two rotors are cylindrically ground on the air gap diameters for better concentricity and size accuracy.

In Chapter 5, results of the DSRSRM validation experiments are discussed , which consist of both static and dynamic tests. The static tests measure static torque and flux linkage of the machine with the rotor locked at various positions. Flux linkage loci comparison between different phases and rotor poles show that difference is insignificant, implying the machine construction is concentric and uniform. However, compared to FEA solutions, even though the general trend is similar, the measured flux linkage is lower near aligned position and higher near unaligned position for both interior and exterior machines. This results in a shrinked flux linkage loci and hence reduced torque output, which is confirmed by the fact that torque measurements are typically 15% lower than the FEA predictions. The discrepancy may be largely due to heat induced magnetic characteristic deterioration at the air gap resulted from laser cutting. This corresponds to findings from further FEA parameter study that increasing model air gap length and reducing model saturation limit together lead to a much closer estimation. To see the coupling effect, flux linkage loci of each machine are measured with and without magnetic coupling and are compared to isolated conditions. Again, difference is negligible as predicted by FEA analysis. In the dynamic tests, the DSRSRM is loaded with dynamometers to evaluate machine performance under various speeds and loads. Both the interior and exterior machines are able to deliver required torque at various rated speeds. Because of the difference between measured and predicted flux linkage, phase current needs to be increased to achieve designed output, this results in 5%~10% drop in efficiency compared to design prediction. However, compared to the benchmark machine, the DSRSRM prototype still achieves similar or higher efficiencies for the same output requirements. Magnetic coupling between exterior and interior machines is verified to be negligible by operating both machines simultaneously. The thermal capability of the DSRSRM is tested by operating both machines at rated outputs and measuring temperature change. After 150 minutes of continuous operation, the machine reaches an equilibrium temperature of 85 ℃, which is much lower than the thermal limit of 150 ℃.

The prototype machine demonstrates that the DSRSRM design is able to reduce machine overall diameter from 300mm to 230mm, equalling 41.2% total volume reduction, while maintaining similar or higher operation efficiencies of both rotors. The substantial machine size reduction achieved by DSRSRM design leads to lighter weight, less material usage and higher torque and power density, which are critical characteristics for high performance machines.

6.2. Novelties and Contributions

The thesis focuses on the design and application of a novel group of double segmented rotor switched reluctance machines, which leads to several original developments and electric machine design novelties.

Various applications of double rotor electric machines are investigated. Of which, applications on advanced HEV powertrain seems promising because of the requirement of two electric machines in such systems. Applications on two types of powertrain architectures are identified: a) complex power split, requiring two independent rotor outputs; b) EVT without planetary gearing, requiring two coupled rotors.

The segmented rotor structure is applied to the design of double rotor SRM for the first time. All possible radial flux rotor/stator arrangements are investigated and a family of double segmented rotor SRM is established. Compared to conventional SRM rotor designs, the segmented rotor eliminates rotor back iron, which contributes to size and weight reduction of the rotor. 8 DSRSRM topologies are proposed, of which two are suitable for HEV powertrains. The central stator DSRSRM topology can be used to integrate a complex power split type drivetrain and the external stator and inner wound rotor DSRSRM topology can be used in an EVT.

Stator yoke flux path sharing is implemented as another novelty of the DSRSRM. Flux path sharing allows the two magnetic paths in a double rotor machine use same sections of back iron rather than having separate path, which reduces material usage and increases compactness. As a new design concept, flux path sharing is first time proposed in the design of double rotor machines. This feature is thoroughly investigated in the thesis and is validated for negligible magnetic coupling effect through both static and dynamic experiments.

The prototyped novel central stator DSRSRM design effectively combines the compactness benefit of both segmented rotor and stator yoke flux path sharing. Compared to the benchmark design, the prototype achieves a machine volume reduction of as much as 41.2% while maintaining uncompromised peformance.

6.3. Future Work

As a new member of the double rotor SRM family, double segmented rotor SRMs present good potential for high performance applications. More work is needed to further improve the DSRSRM.

As a proof-of-concept design, the prototype machine was designed for a low power rating of 1kW so as to reduce requirement on power electronics and mechanical construction. However, real traction applications typically require electric machines with at least 30kW power output, which demands larger and scaled-up versions of DSRSRM to be developed. Two major aspects are to be addressed in scaling up the design, thermal and vibration. Because of the heavily enclosed interior stator structure, cooling will be a big concern for the interior machine. High fidelity thermal modelling of the machine is required. For very high power operations, forced fluid cooling may be necessary and cooling system designs should be studied and optimized. To increase the machine power density, the DSRSRM is expected to be operated at higher speeds, which often results in increased vibration and noise. Modal analysis is to be performed to avoid operating the DSRSRM at resonant frequencies. The mechanical structure of the machine should also be optimized from a vibration reduction perspective.

Variations of the prototype design can be studied. For example, different stator and rotor pole combinations can be investigated. New stator pole and rotor segment geometries can be studied. Different winding schemes, e.g. full pitched winding, may also be explored. The prototype design is not globally optimized in the current research. A global optimization algorithm can be developed, based on stochastic optimization methods. The design can then be optimized for application specific attributes.

More work is to be carried out on integrated DSRSRM HEV powertrains. This includes system optimization, component sizing, packaging and assembly design and optimization. The external stator wound inner rotor DSRSRM for EVT application should also be prototyped and evaluated. Even though this design is not studied in detail in this thesis, it is of great interest for HEV applications due to its simple structure that eliminates planetary gearing.

The group of DSRSRMs proposed in this thesis can also be further studied for opportunities to be used in other applications.

REFERENCES

[1] D. H. Kelly, "Double-Rotor Induction Motor," *IEEE Transactions on Power Apparatus and Systems*, vol. 10, no. 7, 1969.

[2] Y. Yang, "Double-rotor Switched Reluctance Machine for Integrated Electro-mechanical Transmission in Hybrid Electric Vehicles," McMaster University, 2013.

[3] E. Nordlund and C. Sadarangani, "The four-quadrant energy transducer," *Conference Record of the 2002 IEEE Industry Applications Conference*, vol. 1, pp. 390–397, 2002.

[4] R. Qu and T. A. Lipo, "Dual-Rotor, Radial-Flux, Toroidally Wound, Permanent-Magnet Machines," *IEEE Transactions on Industry Applications*, vol. 39, no. 6, pp. 1665–1673, 2003.

[5] Y. Yeh, M. Hsieh, and D. G. Dorrell, "Different Arrangements for Dual-Rotor Dual-Output Radial-Flux Motors," *IEEE Transactions on Industry Applications*, vol. 48, no. 2, pp. 612–622, 2012.

[6] National Highway Traffic Safety Administration, *2017 and Later Model Year Light-Duty Vehicle Greenhouse Gas Emissions and Corporate Average Fuel Economy Standards; Final Rule*, vol. 77, no. 199. United States Federal Register, 2012, pp. 4–8.

[7] Toyota Motor Sales U.S.A. Inc., "Toyota is Global Hybrid Leader with Sales of 7 Million," *Toyota USA Newsroom*, 2014. [Online]. Available: http://pressroom.toyota.com/releases/toyota+global+hybrid+leader+sales+7mm.htm. [Accessed: 21-Oct-2014].

[8] A. Emadi, K. Rajashekara, S. S. Williamson, and S. Lukic, "Topological Overview of Hybrid Electric and Fuel Cell Vehicular Power System Architectures and Configurations," *IEEE Transactions on Vehicular Technology*, vol. 54, no. 3, pp. 763–770, 2005.

[9] M. Ehsani, Y. Gao, and J. M. Miller, "Hybrid Electric Vehicles: Architecture and Motor Drives," *Proceedings of the IEEE*, vol. 95, no. 4, pp. 719–728, Apr. 2007.

[10] J. M. Miller, "Hybrid Electric Vehicle Propulsion System Architectures of the e-CVT Type," *IEEE Transactions on Power Electronics*, vol. 21, no. 3, pp. 756–767, 2006.

[11] Wikipedia, “Hybrid Synergy Drive,” 2010. [Online]. Available: http://commons.wikimedia.org/wiki/File:Toyota_electronic_continuously_variable_transmission_(2010-10-16)_02.jpg. [Accessed: 10-Nov-2014].

[12] Allpar, “Dodge Durango 2007 - 2009, including the Dodge Durango Hybrid,” 2010. [Online]. Available: http://www.allpar.com/trucks/durango.html. [Accessed: 10-Nov-2014].

[13] Y. Yang and A. Emadi, “Integrated Electro-Mechanical Transmission Systems in Hybrid Electric Vehicles,” in *IEEE Vehicle Power and Propulsioin Conference*, 2011.

[14] P. Thelin and E. Nordlund, “Influence of saturation and saliency on the inductance of a four-quadrant transducer prototype machine,” *IEEE Transactions on Magnetics*, vol. 42, no. 4, pp. 1319–1322, Apr. 2006.

[15] P. Zheng, R. Liu, P. Thelin, E. Nordlund, and C. Sadarangani, “Research on the Parameters and Performances of a 4QT Prototype Machine Used for HEV,” *IEEE Transactions on Magnetics*, vol. 43, no. 1, pp. 443–446, Jan. 2007.

[16] R. Liu, H. Zhao, C. Tong, G. Chen, P. Zheng, and G. Gu, “Experimental Evaluation of a Radial-Radial-Flux Compound-Structure,” *IEEE Transactions on Magnetics*, vol. 45, no. 1, pp. 645–649, 2009.

[17] X. Sun and M. Cheng, “Application of Electrical Variable Transmission in Wind Power Generation System,” *IEEE Transactions on Industry Applications*, vol. 49, no. 3, pp. 1299–1307, 2013.

[18] Y. Cheng, S. Cui, L. Song, and C. C. Chan, “The Study of the Operation Modes and Control Strategies of an Advanced Electromechanical Converter for Automobiles,” *IEEE Transactions on Magnetics*, vol. 43, no. 1, pp. 430–433, Jan. 2007.

[19] P. Zheng, R. Liu, Q. Wu, J. Zhao, and Z. Yao, “Magnetic Coupling Analysis of Four-Quadrant,” *IEEE Transactions on Magnetics*, vol. 43, no. 6, pp. 2597–2599, 2007.

[20] P. Zheng, R. Liu, P. Thelin, and E. Nordlund, “Research on the Cooling System of a 4QT Prototype Machine Used for HEV,” *IEEE Transactions on Energy Conversion*, vol. 23, no. 1, pp. 61–67, 2008.

[21] Y. Cheng, R. Trigui, C. Espanet, A. Bouscayrol, and S. Cui, “Specifications and Design of a PM Electric Variable Transmission for Toyota Prius II,” *IEEE Transactions on Vehicular Technology*, vol. 60, no. 9, pp. 4106–4114, Nov. 2011.

[22] M. J. Hoeijmakers and J. A. Ferreira, “The Electric Variable Transmission,” *IEEE Transactions on Industry Applications*, vol. 42, no. 4, pp. 1092–1100, 2006.

[23] P. Pišek, B. Štumberger, T. Mar, and P. Virti, “Design Analysis and Experimental Validation of a Double Rotor Synchronous PM Machine Used for HEV,” *IEEE Transactions on Magnetics*, vol. 49, no. 1, pp. 152–155, 2013.

[24] S. Niu, S. L. Ho, and W. N. Fu, “A Novel Double-Stator Double-Rotor Brushless Electrical Continuously Variable Transmission System,” *IEEE Transactions on Magnetics*, vol. 49, no. 7, pp. 3909–3912, Jul. 2013.

[25] C. Tong, P. Zheng, Q. Wu, J. Bai, and Q. Zhao, “A Brushless Claw-Pole Double-Rotor Machine for Power-Split Hybrid Electric Vehicles,” *IEEE Transactions on Industrial Electronics*, vol. 61, no. 8, pp. 4295–4305, 2014.

[26] P. Zheng, J. Zhao, R. Liu, C. Tong, and Q. Wu, “Magnetic Characteristics Investigation of an Axial-Axial Flux Compound-Structure PMSM Used for HEVs,” *IEEE Transactions on Magnetics*, vol. 46, no. 6, pp. 2191–2194, 2010.

[27] P. Zheng, J. Bai, C. Tong, Y. Sui, Z. Song, and Q. Zhao, “Investigation of a Novel Radial Magnetic-Field-Modulated Brushless Double-Rotor Machine Used for HEVs,” *IEEE Transactions on Magnetics*, vol. 49, no. 3, pp. 1231–1241, Mar. 2013.

[28] C. Yunyun, Q. Li, Z. Xiaoyong, W. Hua, and Z. Wang, “Electromagnetic Performance Analysis of Double-Rotor Stator Permanent Magnet Motor for Hybrid Electric Vehicle,” *IEEE Transactions on Magnetics*, vol. 48, no. 11, pp. 4204–4207, Nov. 2012.

[29] R. Qu and T. A. Lipo, “Design and Parameter Effect Analysis of Dual-Rotor , Permanent-Magnet Machines,” *IEEE Transactions on Industry Applications*, vol. 40, no. 3, pp. 771–779, 2004.

[30] J. Wang, R. Qu, and L. Zhou, “Dual-Rotor Multiphase Permanent Magnet Machine With Harmonic Injection to Enhance Torque Density,” *IEEE Transactions on Applied Superconductivity*, vol. 22, no. 3, pp. 3–6, 2012.

[31] J. A. Stegmann and M. J. Kamper, “Design Aspects of Double-Sided Rotor Radial Flux Air-Cored Permanent-Magnet Wind Generator,” *IEEE Transactions on Industry Applications*, vol. 47, no. 2, pp. 767–778, 2011.

[32] S. Mohammadi and M. Mirsalim, “Analytical Design Framework for Torque and Back-EMF Optimization, and Inductance Calculation in Double-Rotor Radial-Flux

Air-Cored Permanent-Magnet Synchronous Machines," *IEEE Transactions on Magnetics*, vol. 50, no. 1, pp. 1–16, Jan. 2014.

[33] K. Atallah and D. Howe, "A novel high-performance magnetic gear," *IEEE Transactions on Magnetics*, vol. 37, no. 4, pp. 2844–2846, Jul. 2001.

[34] P. O. Rasmussen, T. O. Andersen, F. T. Jørgensen, and O. Nielsen, "Development of a High-Performance Magnetic Gear," *IEEE Transactions on Industry Applications*, vol. 41, no. 3, pp. 764–770, 2005.

[35] C.-T. Liu, H.-Y. Chung, and C.-C. Hwang, "Design Assessments of a Magnetic-Geared Double-Rotor Permanent Magnet Generator," *IEEE Transactions on Magnetics*, vol. 50, no. 1, pp. 1–4, Jan. 2014.

[36] A. Emadi, "Transportation 2.0," *IEEE Power & Energy Magazine*, vol. 9, no. 4, 2011.

[37] M. Krishnamurthy, C. S. Edrington, A. Emadi, P. Asadi, and M. Ehsani, "Making the Case for Applications of Switched Reluctance Motor Technology in Automotive Products," *IEEE Transactions on Power Electronics*, vol. 21, no. 3, pp. 659–675, 2006.

[38] K. M. Rahman, B. Fahimi, G. Suresh, A. V. Rajarathnam, and M. Ehsani, "Advantages of switched reluctance motor applications to EV and HEV: design and control issues," *IEEE Transactions on Industry Applications*, vol. 36, no. 1, pp. 111–121, 2000.

[39] H. Chen and J. J. Gu, "Implementation of the Three-Phase Switched Reluctance Machine System for Motors and Generators," *IEEE/ASME Transactions on Mechatronics*, vol. 15, no. 3, pp. 421–432, 2010.

[40] K. M. Rahman, "PERFORMANCE ANALYSIS OF ELECTRIC MOTOR DRIVES FOR ELECTRIC AND HYBRID ELECTRIC VEHICLE APPLICATIONS," in *Power Electronics in Transportation*, 1998, pp. 49–56.

[41] W. Peng, F. Zhang, and J. Ahn, "Design and control of a novel bearingless SRM with double stator," *2012 IEEE International Symposium on Industrial Electronics*, pp. 1928–1933, May 2012.

[42] M. Abbasian, M. Moallem, and B. Fahimi, "Double-Stator Switched Reluctance Machines (DSSRM): Fundamentals and Magnetic Force Analysis," *IEEE Transactions on Energy Conversion*, vol. 25, no. 3, pp. 589–597, Sep. 2010.

[43] M. Abbasian, B. Fahimi, and M. Moallem, “High torque double-stator switched reluctance machine for electric vehicle propulsion,” in *2010 IEEE Vehicle Power and Propulsion Conference*, 2010, vol. 2, no. 1, pp. 1–5.

[44] S. Cui, Y. Yuan, and T. Wang, “Research on Switched Reluctance Double-rotor Motor Used for Hybrid Electric Vehicle,” in *International Conference on Electrical Machines and Systems*, 2008, pp. 3393–3396.

[45] T. J. E. Miller, *Switched Reluctance Motors and Their Control*. Magna Physics, 1993.

[46] R. Krishnan, *Switched Reluctance Motor Drives: Modeling, Simulation, Analysis, Design, and Applications*. CRC Press, 2001.

[47] J. Ahn, “Switched Reluctance Motor,” in *Torque Control*, InTech, 2011, pp. 201–252.

[48] B. C. Mecrow, J. W. Finch, E. a. El-Kharashi, and A. G. Jack, “Switched reluctance motors with segmental rotors,” *IEE Proceedings - Electric Power Applications*, vol. 149, no. 4, pp. 245–254, 2002.

[49] R. Vandana, N. Vattikuti, and B. G. Fernandes, “A Novel High Power Density Segmented Switched Reluctance Machine,” *2008 IEEE Industry Applications Society Annual Meeting*, pp. 1–7, Oct. 2008.

[50] J. Oyama, T. Higuchi, T. Abe, and K. Tanaka, “The fundamental characteristics of novel switched reluctance motor with segment core embedded in aluminum rotor block,” *2005 International Conference on Electrical Machines and Systems*, pp. 515–519 Vol. 1, 2005.

[51] J.-W. Ahn, “A novel 6/5 segmental rotor type switched reluctance motor: Concept, design and analysis,” *2013 International Conference on Electrical Machines and Systems (ICEMS)*, pp. 582–585, Oct. 2013.

[52] B. Mecrow, E. El-Kharashi, J. W. Finch, and A. G. Jack, “Preliminary Performance Evaluation of Switched Reluctance Motors With Segmental Rotors,” *IEEE Transactions on Energy Conversion*, vol. 19, no. 4, pp. 679–686, Dec. 2004.

[53] T. Higuchi, K. Suenaga, and T. Abe, “Torque ripple reduction of novel segment type Switched reluctance motor by increasing phase number,” *2009 International Conference on Electrical Machines and Systems*, pp. 1–4, Nov. 2009.

[54] T. Higuchi, Y. Nakao, and T. Abe, “Characteristics of a novel segment type SRM with 2-step slide rotor,” *2009 International Conference on Electrical Machines and Systems*, pp. 1–4, Nov. 2009.

[55] Y. Matsuo, T. Higuchi, and T. Abe, “Characteristics of a Novel Segment Type Switched Reluctance Motor using Grain - Oriented Electric Steel,” in *International Conference on Electrical Machines and Systems*, 2011, pp. 1–4.

[56] B. C. Mecrow, J. W. Finch, and A. G. Jack, “Segmental rotor switched reluctance motors with single-tooth windings,” *IEE Proceedings - Electric Power Applications*, vol. 150, no. 5, pp. 591–599, 2003.

[57] M. B. Belhadi, A. Kolli, G. Krebs, and C. Marchand, “Evaluation of torque-speed curve of switched reluctance motor with segmental rotor,” in *2012 XXth International Conference on Electrical Machines*, 2012, pp. 250–255.

[58] N. Vattikuti, V. Rallabandi, and B. G. Fernandes, “A novel high torque and low weight segmented switched reluctance motor,” *2008 IEEE Power Electronics Specialists Conference*, pp. 1223–1228, Jun. 2008.

[59] B. C. Mecrow, C. Weiner, and A. C. Clothier, “The Modeling of Switched Reluctance Machines With Magnetically Coupled Windings,” *IEEE Transactions on Industry Applications*, vol. 37, no. 6, pp. 1675–1683, 2001.

[60] J. D. Widmer, R. Martin, and B. C. Mecrow, “Optimisation of an 80kW Segmental Rotor Switched Reluctance Machine for automotive traction,” *2013 International Electric Machines & Drives Conference*, pp. 427–433, May 2013.

[61] R. Vandana and B. G. Fernandes, “Segmented switched reluctance motor with novel winding and excitation strategy,” *The XIX International Conference on Electrical Machines - ICEM 2010*, pp. 1–4, Sep. 2010.

[62] S. P. Nikam, V. Rallabandi, and B. G. Fernandes, “A High-Torque-Density Permanent-Magnet Free Motor for in-Wheel Electric Vehicle Application,” *IEEE Transactions on Industry Applications*, vol. 48, no. 6, pp. 2287–2295, Nov. 2012.

[63] R. Vandana, S. Nikam, and B. G. Fernandes, “High torque polyphase segmented switched reluctance motor with novel excitation strategy,” *IET Electric Power Applications*, vol. 6, no. 7, p. 375, 2012.

[64] J. D. Widmer and B. C. Mecrow, “Optimized Segmental Rotor Switched Reluctance Machines With a Greater Number of Rotor Segments Than Stator Slots,” *IEEE Transactions on Industry Applications*, vol. 49, no. 4, pp. 1491–1498, Jul. 2013.

[65] R. Madhavan and B. G. Fernandes, “A Novel Axial Flux Segmented SRM for Electric Vehicle Application,” in *International Conference on Electrical Machines*, 2010.

[66] R. Madhavan and B. G. Fernandes, “A novel technique for minimizing torque ripple in axial flux segmented rotor SRM,” in *2011 IEEE Energy Conversion Congress and Exposition*, 2011, pp. 3383–3390.

[67] R. Madhavan and B. G. Fernandes, “Axial Flux Segmented SRM With a Higher Number of Rotor Segments for Electric Vehicles,” *IEEE Transactions on Energy Conversion*, vol. 28, no. 1, pp. 203–213, 2013.

[68] Y. Yoshimaru, T. Higuchi, Y. Yokoi, and T. Abe, “On the improvement performance of a dual rotor segment type SRM,” in *2013 IEEE 10th International Conference on Power Electronics and Drive Systems (PEDS)*, 2013, pp. 1045–1048.

[69] B. Fahimi, “Optimal design of double stator switched reluctance machine (DSSRM),” *2012 IEEE International Symposium on Industrial Electronics*, no. 1, pp. 719–724, May 2012.

[70] C. Liu, K. T. Chau, and Z. Zhang, “Novel Design of Double-Stator Single-Rotor Magnetic-Geared Machines,” *IEEE Transactions on Magnetics*, vol. 48, no. 11, pp. 4180–4183, Nov. 2012.

[71] A. Radun, “Analytically computing the flux linked by a switched reluctance motor phase when the stator and rotor poles overlap,” *IEEE Transactions on Magnetics*, vol. 36, no. 4, pp. 1996–2003, Jul. 2000.

[72] H. C. Lovatt, “Analytical model of a classical switched-reluctance motor,” *IEE Proceedings - Electric Power Applications*, vol. 152, no. 2, pp. 352–358, 2005.

[73] S. A. Hossain and I. Husain, “A Geometry Based Simplified Analytical Model of Switched Reluctance Machines for Real-Time Controller Implementation,” *IEEE Transactions on Power Electronics*, vol. 18, no. 6, pp. 1384–1389, 2003.

[74] A. Khalil and I. Husain, “A Fourier Series Generalized Geometry-Based Analytical Model of Switched Reluctance Machines,” *IEEE Transactions on Industry Applications*, vol. 43, no. 3, pp. 673–684, 2007.

[75] JSOL Corporation, “JMAG.” .

[76] G. Say, *Alternating Current Machines*, 5th ed. Wiley, 1983.

[77] P. N. Materu and R. Krishnan, “Estimation of Switched Reluctance Motor Losses,” *IEEE Transactions on Industry Applications*, vol. 28, no. 3, pp. 668–679, 1992.

[78] JSOL Corporation, “Drive Simulation of an SR Motor Using a Control Simulator and the JMAG-RT System.” 2011.

[79] V. Rallabandi and B. G. Fernandes, “Design procedure of segmented rotor switched reluctance motor for direct drive applications,” *IET Electric Power Applications*, vol. 8, no. 3, pp. 77–88, Mar. 2014.

[80] a Belhadj, P. Baudouin, F. Breaban, a Deffontaine, M. Dewulf, and Y. Houbaert, “Effect of laser cutting on microstructure and on magnetic properties of grain non-oriented electrical steels,” *Journal of Magnetism and Magnetic Materials*, vol. 256, no. 1–3, pp. 20–31, Jan. 2003.

[81] R. Siebert, J. Schneider, and E. Beyer, “Laser Cutting and Mechanical Cutting of Electrical Steels and its Effect on the Magnetic Properties,” *IEEE Transactions on Magnetics*, vol. 50, no. 4, pp. 3–6, 2014.

[82] a Belhadj, P. Baudouin, and Y. Houbaert, “Simulation of the HAZ and magnetic properties of laser cut non-oriented electrical steels,” *Journal of Magnetism and Magnetic Materials*, vol. 248, no. 1, pp. 34–44, Jul. 2002.

[83] M. Emura, F. J. . Landgraf, W. Ross, and J. . Barreta, “The influence of cutting technique on the magnetic properties of electrical steels,” *Journal of Magnetism and Magnetic Materials*, vol. 254–255, pp. 358–360, Jan. 2003.

[84] N. E. Evine and D. S. Petrovi, “NON-ORIENTED ELECTRICAL STEEL SHEETS,” *Materials and technology*, vol. 44, no. 6, pp. 317–325, 2010.

APPENDIX

A1 Summary of Interior Machine Design Cases

Case	MMF (AT)	a1 (deg)	W1 (mm)	a5 (deg)	Available winding area per slot (mm^2)	Torque ripple (%)	Average torque (Nm)	Stator pole center flux density (T)	Copper loss estimate (W)
1	1000	33	6	16.6	329	47	1.33	1.77	13.5
2	1000	32	6	17.9	327	55	1.34	1.75	13.6
3	1000	31	6	19.3	324	69	1.34	1.73	13.7
4	1000	30	6	21.0	322	82	1.32	1.72	13.8
5	1000	29	6	23.0	319	95	1.30	1.7	13.9
6	1000	33	7	19.5	315	47	1.50	1.74	14.1
7	1000	32	7	21.0	313	53	1.50	1.72	14.2
8	1000	31	7	22.7	310	68	1.49	1.7	14.3
9	1000	30	7	24.7	308	82	1.47	1.68	14.4
10	1000	29	7	27.1	305	98	1.45	1.67	14.6
11	1000	33	8	22.5	302	46	1.64	1.71	14.8
12	1000	32	8	24.2	299	53	1.64	1.69	14.9
13	1000	31	8	26.2	297	69	1.63	1.67	15.0
14	1000	30	8	28.5	294	84	1.60	1.65	15.2
15	1000	29	8	31.4	292	102	1.56	1.64	15.3
16	1000	33	9	25.4	289	49	1.77	1.67	15.5
17	1000	32	9	27.4	286	54	1.76	1.66	15.6
18	1000	31	9	29.7	284	71	1.74	1.64	15.8
19	1000	30	9	32.5	281	88	1.70	1.63	15.9
20	1000	29	9	35.9	279	106	1.64	1.6	16.1
21	1000	33	10	28.5	276	49	1.87	1.65	16.3
22	1000	32	10	30.8	274	58	1.86	1.64	16.4
23	1000	31	10	33.4	271	74	1.83	1.62	16.6
24	1000	30	10	36.6	269	92	1.78	1.6	16.7
25	1000	29	10	40.6	266	110	1.70	1.57	16.9

Case	MMF (AT)	a1 (deg)	W1 (mm)	a5 (deg)	Available winding area per slot (mm^2)	Torque ripple (%)	Average torque (Nm)	Stator pole center flux density (T)	Copper loss estimate (W)
26	1000	33	11	31.7	263	47	1.96	1.62	17.1
27	1000	32	11	34.2	261	60	1.95	1.6	17.3
28	1000	31	11	37.3	258	77	1.90	1.58	17.5
29	1000	30	11	41.0	256	95	1.84	1.56	17.6
30	1000	29	11	45.7	253	116	1.74	1.53	17.8
31	1000	33	12	35.0	251	50	2.04	1.6	18.0
32	1000	32	12	37.9	248	64	2.01	1.58	18.2
33	1000	31	12	41.4	246	82	1.95	1.55	18.4
34	1000	30	12	45.7	243	100	1.87	1.52	18.6
35	1000	29	12	51.4	240	120	1.76	1.48	18.9
36	1000	33	13	38.4	238	56	2.10	1.57	19.0
37	1000	32	13	41.7	236	70	2.06	1.54	19.2
38	1000	31	13	45.7	233	87	1.99	1.51	19.5
39	1000	30	13	50.9	230	106	1.89	1.47	19.7
40	1000	29	13	57.8	226	128	1.77	1.42	20.1
41	1000	33	14	41.9	226	62	2.15	1.54	20.2
42	1000	32	14	45.7	224	74	2.09	1.51	20.4
43	1000	31	14	50.5	221	90	2.01	1.47	20.6
44	1000	30	14	56.7	217	111	1.90	1.42	21.0
45	1000	29	14	65.7	210	131	1.76	1.36	21.7
46	1000	33	15	45.7	214	64	2.18	1.5	21.4
47	1000	32	15	50.1	212	79	2.11	1.47	21.6
48	1000	31	15	55.7	208	97	2.01	1.42	21.9
49	1000	30	15	63.5	203	116	1.89	1.36	22.5

A2 Summary of Exterior Machine Design Cases

Case	MMF (AT)	a1 (deg)	W1 (mm)	a5 (deg)	Available winding area per slot (mm^2)	Torque ripple (%)	Average torque (Nm)	Stator pole center flux density (T)	Copper loss estimate (W)
1	1700	34	14	16.7	353	27	5.99	1.86	29.0
2	1700	33	14	17.9	352	32	6.10	1.83	29.1
3	1700	32	14	19.2	350	38	6.21	1.8	29.3
4	1700	31	14	20.8	347	39	6.45	1.77	29.4
5	1700	34	16	19.2	329	23	6.65	1.83	31.1
6	1700	33	16	20.6	328	29	6.78	1.8	31.2
7	1700	32	16	22.1	326	36	6.88	1.76	31.3
8	1700	31	16	23.9	324	41	7.25	1.76	31.5
9	1650	34	18	21.7	306	21	6.99	1.8	31.4
10	1650	33	18	23.3	305	25	7.12	1.76	31.5
11	1770	32	18	25.0	303	37	7.97	1.76	36.4
12	1710	31	18	27.1	302	38	8.06	1.75	34.1
13	1740	34	20	24.3	285	19	8.05	1.79	37.5
14	1710	33	20	26.0	284	25	8.06	1.75	36.3
15	1650	32	20	28.1	282	38	7.95	1.73	33.9
16	1600	31	20	30.4	281	45	8.01	1.72	32.0
17	1650	34	22	26.9	264	19	8.02	1.74	36.2
18	1600	33	22	28.9	264	26	7.99	1.73	34.1
19	1570	32	22	31.2	262	41	8.01	1.72	32.9
20	1520	31	22	33.9	261	51	7.98	1.69	31.0
21	1560	34	24	29.6	245	22	7.99	1.72	34.8
22	1520	33	24	31.8	244	33	7.96	1.71	33.1
23	1480	32	24	34.4	243	47	8.07	1.7	31.5
24	1460	31	24	37.4	242	54	7.93	1.66	30.8
25	1490	34	26	32.4	226	25	7.97	1.68	34.3
26	1466	33	26	34.8	226	37	8.00	1.66	33.3
27	1420	32	26	37.7	225	48	7.98	1.64	31.3
28	1420	31	26	41.2	223	61	7.95	1.63	31.4
29	1440	34	28	35.2	208	32	7.99	1.64	34.7
30	1420	33	28	37.9	208	43	8.00	1.63	33.8
31	1380	32	28	41.2	207	51	7.96	1.61	32.0
32	1390	31	28	45.2	205	69	7.96	1.6	32.6

A3 Drawings of Machined Components

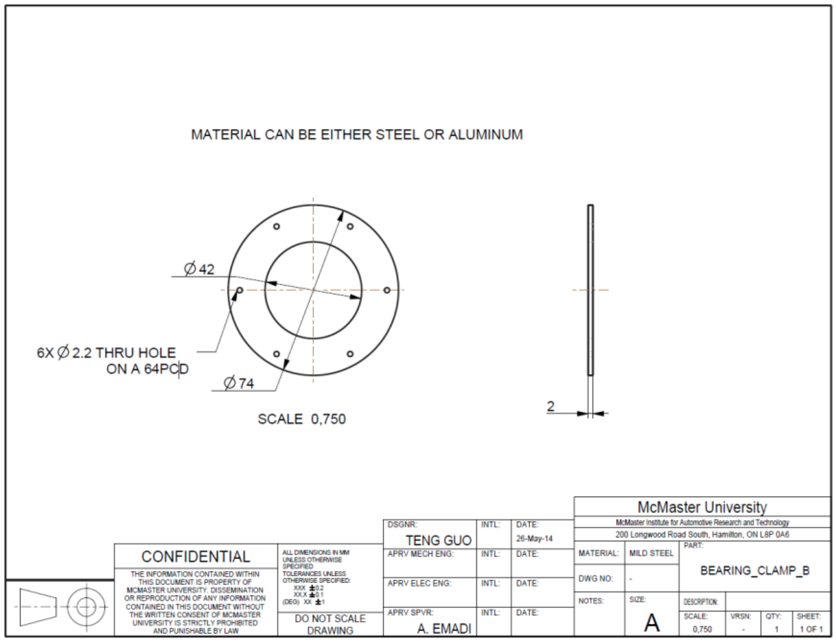

Figure A1 Drawing of bearing clamp

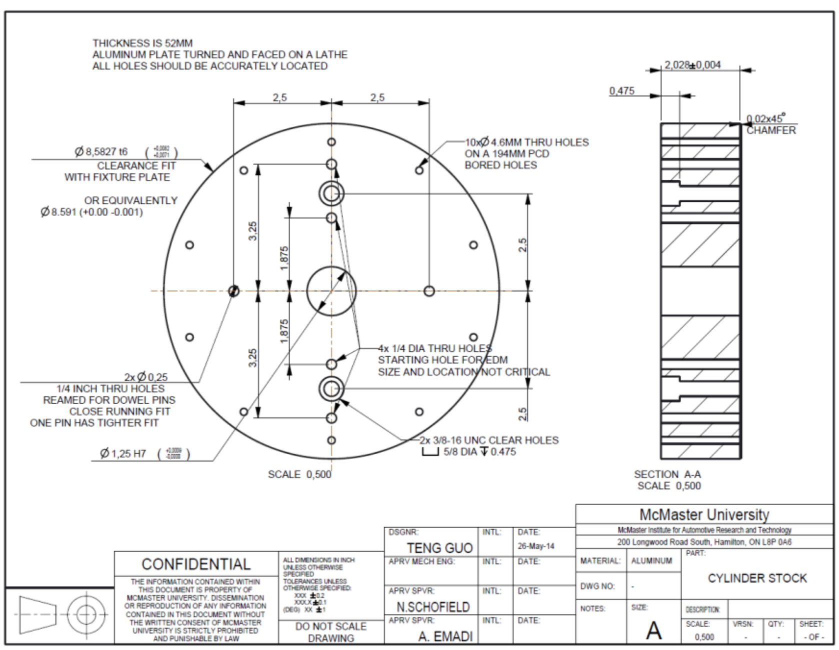

Figure A2 Drawing of cylinder stock for wired electrical discharge machining

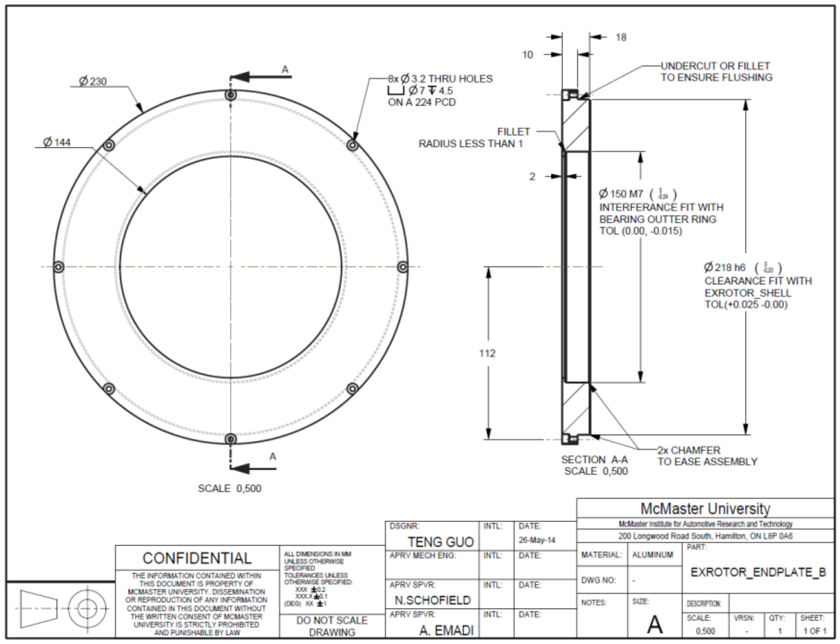

Figure A3 Drawing of exterior rotor rear endplate

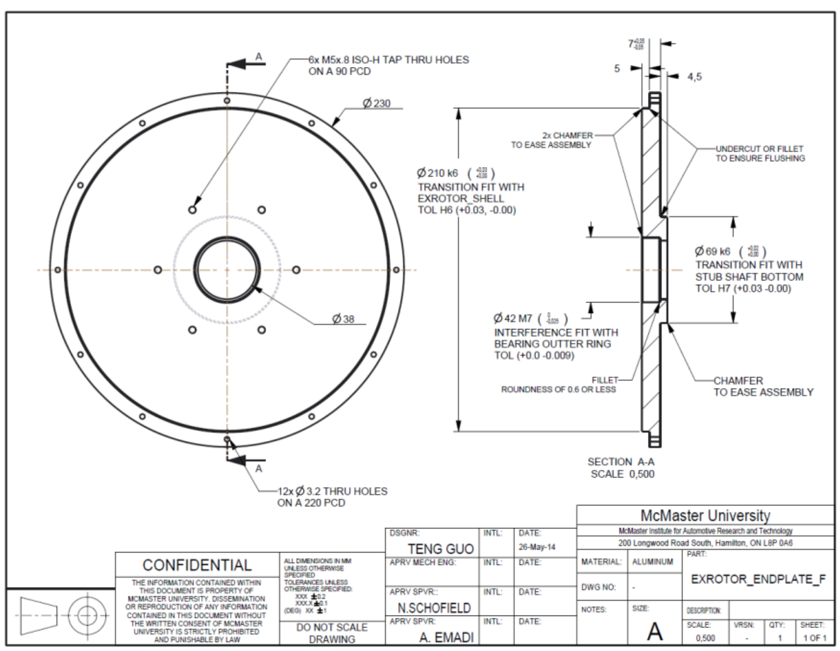

Figure A4 Drawing of exterior rotor front endplate

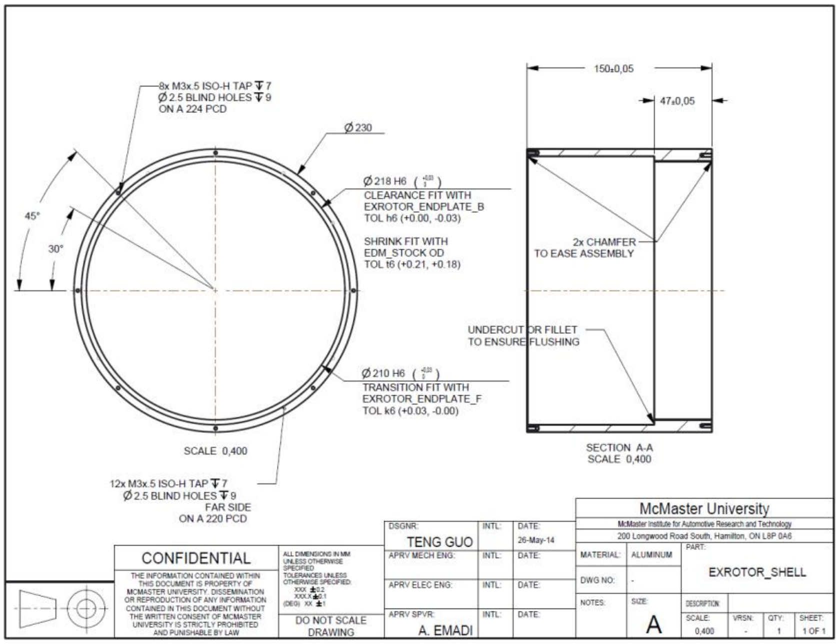

Figure A5 Drawing of exterior rotor shell

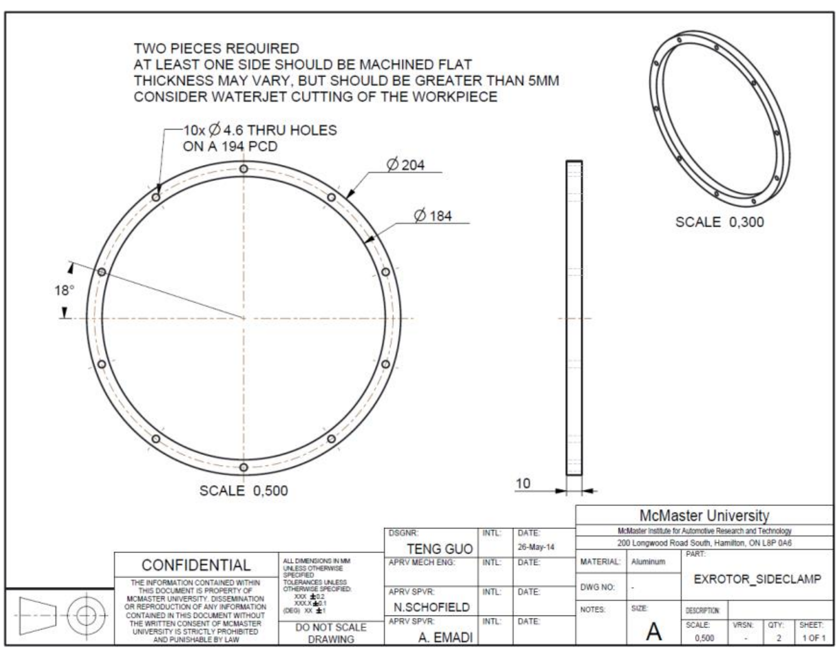

Figure A6 Drawing of exterior rotor side clamp

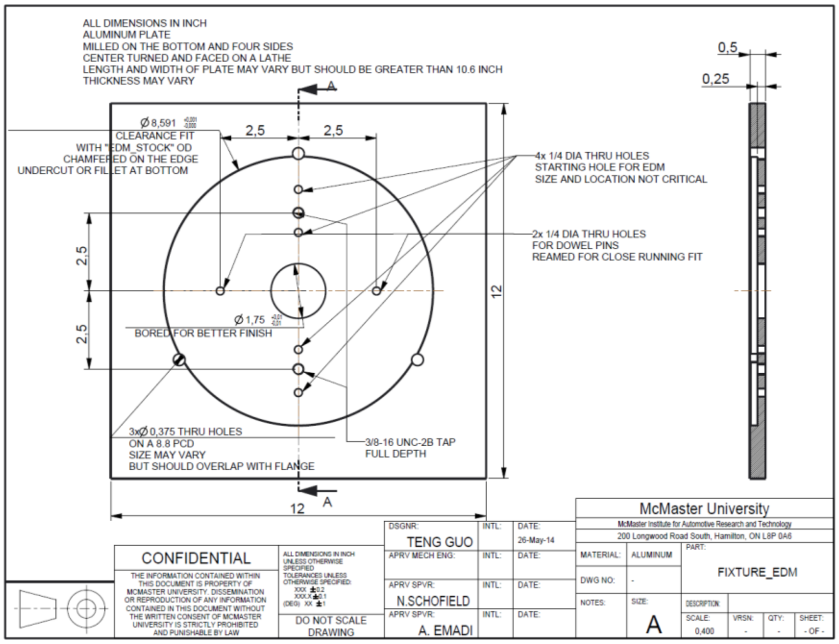

Figure A7 Drawing of fixture plate for wired electrical discharge machining

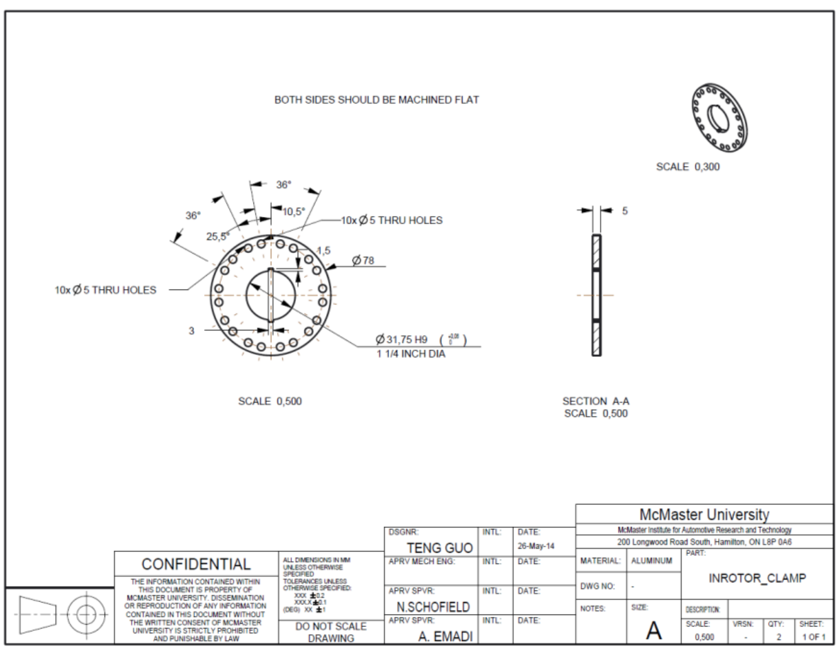

Figure A8 Drawing of interior rotor side clamp

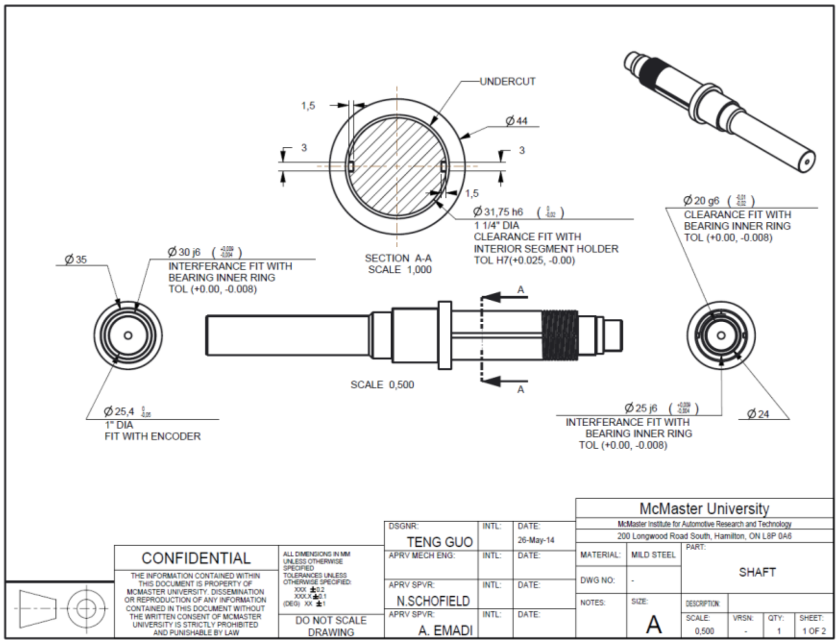

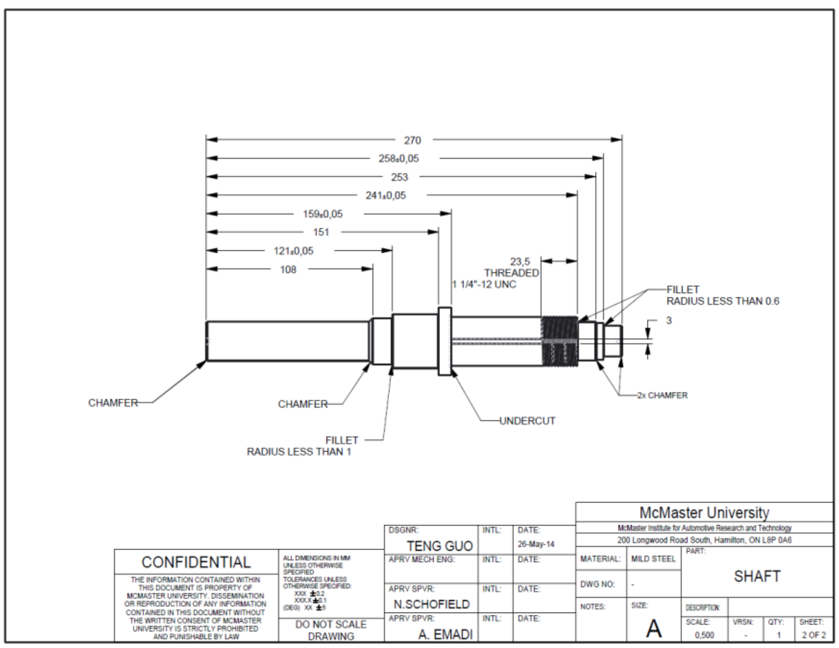

Figure A9 Drawing of interior rotor shaft

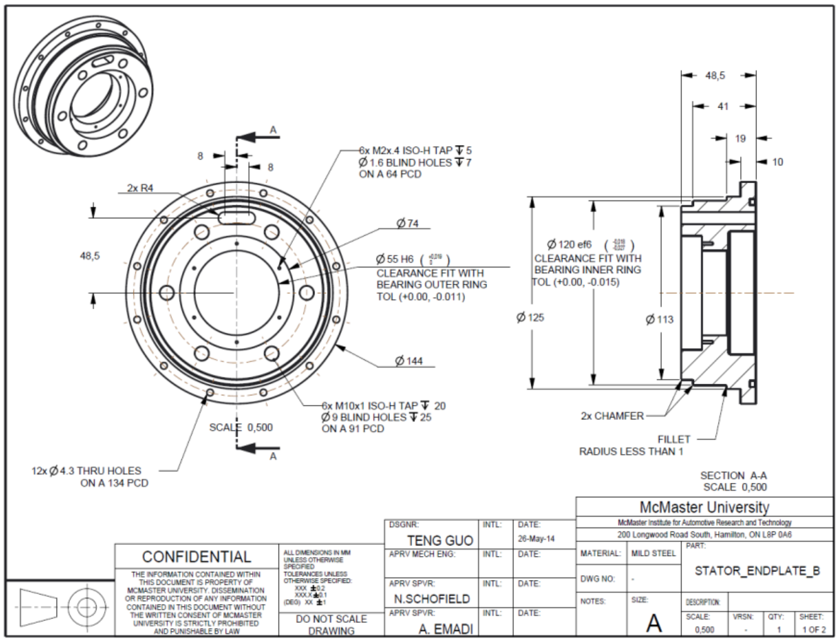

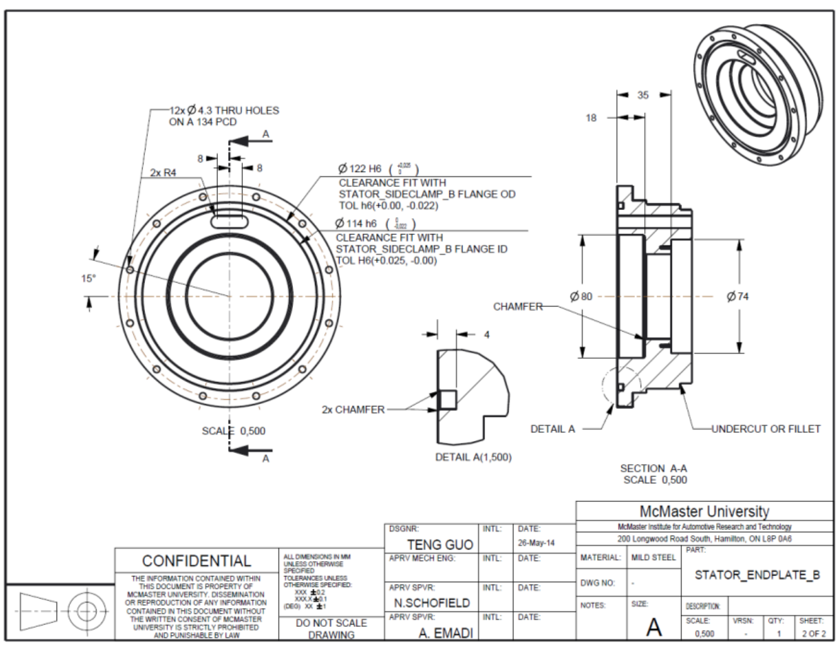

Figure A10 Drawing of stator rear endplate

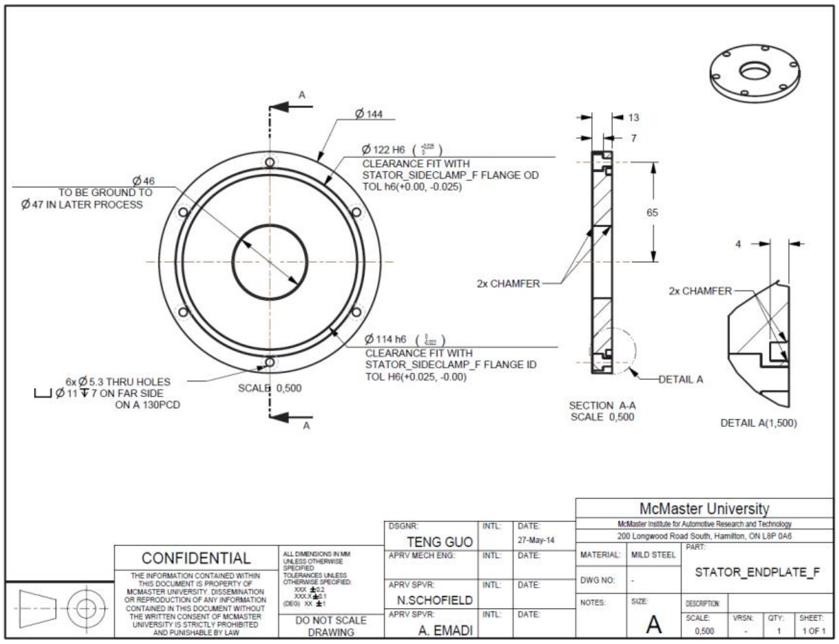

Figure A11 Drawing of stator front endplate

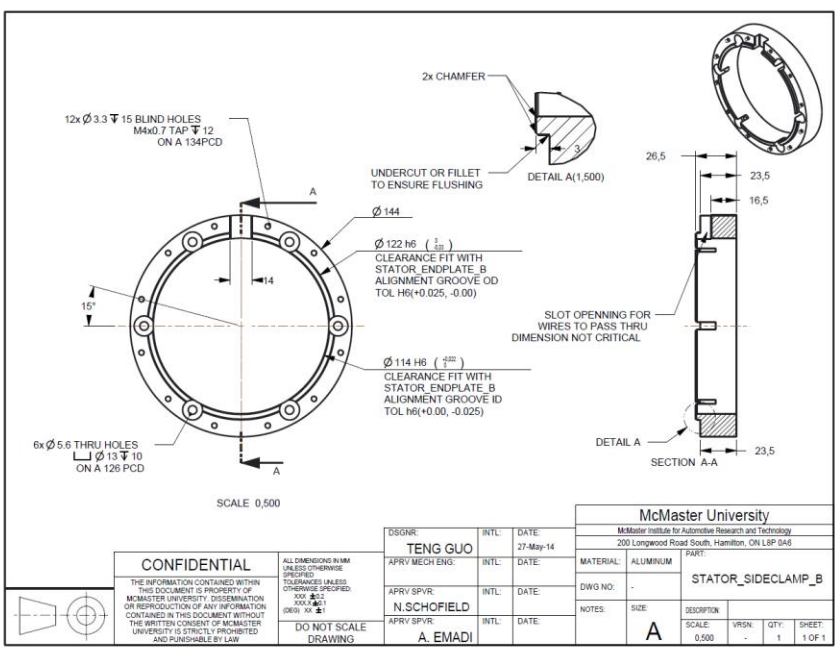

Figure A12 Drawing of stator rear side clamp

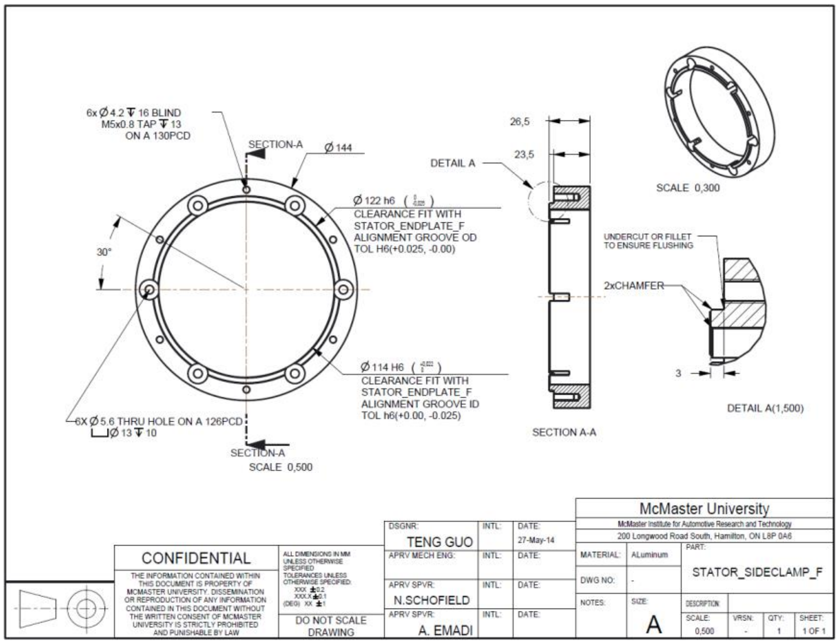

Figure A13 Drawing of stator front side clamp

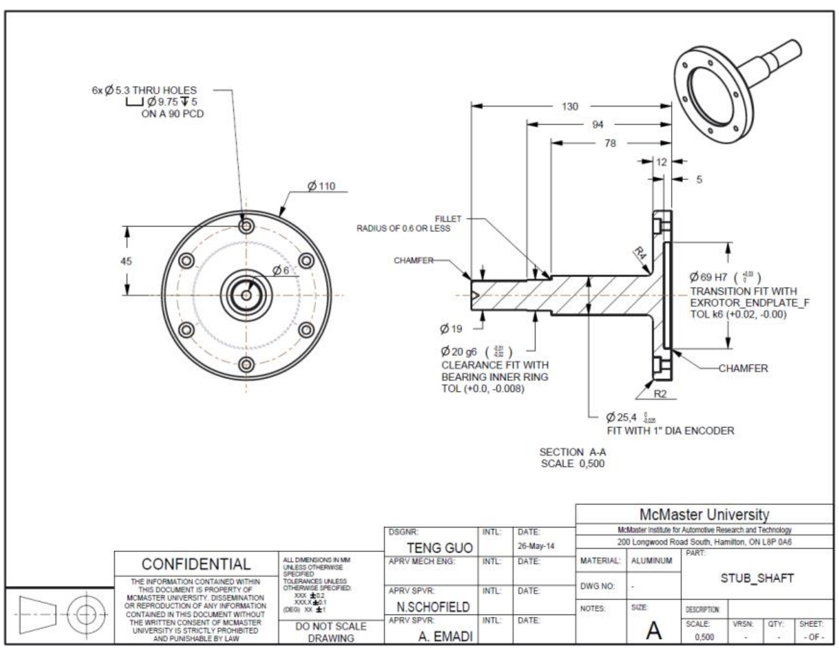

Figure A14 Drawing of exterior rotor stub shaft